SAPIENZA
UNIVERSITÀ DI ROMA

Gravitational wave signatures of scalarized black holes and horizonless compact objects

Scuola di Dottorato in scienze astronomiche, chimiche, fisiche, matematiche e della terra "Vito Volterra"
Dottorato di Ricerca in Fisica (XXXVIII cycle)

Marco Melis
ID number 2077211

Advisor
Prof. Paolo Pani

Academic Year 2025/2026

Gravitational wave signatures of scalarized black holes and horizonless compact objects

PhD thesis. Sapienza University of Rome

This thesis has been typeset by LaTeX and the Sapthesis class.

Version: October 30, 2025

Author's email: marco.melis@uniroma1.it

Abstract

Black holes are among the simplest objects in the universe, yet they serve as one of the most powerful testbeds for probing some of the deepest puzzles in physics, such as the curvature singularity, the information loss paradox and other fundamental challenges within general relativity. These unresolved issues motivated the investigation of alternative models of compact objects. Among the various proposals, the Fuzzball program stands out as one of the most promising top-down approaches to resolving these problems in one coherent picture, as it describes the black hole as an ensemble of smooth and horizonless geometries representing its microstates with the same mass and charge.

The flourishing field of gravitational waves research provides an excellent avenue for investigating the phenomenology of these objects. This thesis focuses on the study of toy models whose simplified yet physically motivated solutions, involving gravity coupled with additional degrees of freedom, effectively capture key properties of Fuzzballs. We investigate the perturbative response of these objects by computing their oscillatory modes and highlighting the presence of echo patterns in the ringdown signal. Moreover, we analyze extreme-mass-ratio inspirals as a promising probe to differentiate classical black holes from horizonless compact objects in these toy models.

Preface

The research work forming the basis of this thesis was conducted at Sapienza University of Rome, within the Gravity Theory and Gravitational Wave Phenomenology Group. Part of this work was also carried out during a visiting period at the Instituto Superior Técnico (IST) in Lisbon, within the Center for Astrophysics and Gravitation (CENTRA) group. I am grateful to Prof. Richard Brito for his collaboration and kind hospitality during my stay.

List of publications

The work presented in this thesis is based on the following publications:

- Title: Spectroscopy of magnetized black holes and topological stars
  Journal: Phys. Rev. D 110 (2024) 8, 084067; arXiv:2406.19327 [gr-qc]
  Authors: Alexandru Dima, **Marco Melis**, Paolo Pani

- Title: Black hole spectroscopy and nonlinear echoes in Einstein-Maxwell-scalar theory
  Journal: Phys. Rev. D 111 (2025) 6, 064072; arXiv:2412.14259 [gr-qc]
  Authors: **Marco Melis**, Fabrizio Corelli, Robin Croft, Paolo Pani

- Title: Nonradial stability of topological stars
  Journal: Phys. Rev. D 111 (2025) 10, 104001; arXiv:2502.04444 [gr-qc]
  Authors: Alexandru Dima, **Marco Melis**, Paolo Pani

- Title: Extreme mass ratio inspirals around topological stars
  Journal: Phys. Rev. D 111 (2025) 12, 124043; arXiv:2504.16156 [gr-qc]
  Authors: **Marco Melis**, Richard Brito, Paolo Pani

- Title: The Great Impersonation: $\mathcal{W}$-Solitons as Prototypical Black Hole Microstates
  Journal: arXiv:2509.18245 [gr-qc]
  Authors: Alexandru Dima, Pierre Heidmann, **Marco Melis**, Paolo Pani, Gela Patashuri

Acronyms

ADM: Arnowitt–Deser–Misner
BH: black hole
ECO: exotic compact object
EHT: Event Horizon Telescope
EM: electromagnetic
EMRI: extreme mass ratio inspiral
EMS: Einstein-Maxwell-scalar
ET: Einstein Telescope
GW: gravitational wave
GR: General Relativity
ISCO: innermost stable circular orbit
KAGRA: Kamioka Gravitational Wave Detector
LIGO: Laser Interferometer Gravitational-Wave Observatory
LISA: Laser Interferometer Space Antenna
LVK: LIGO-Virgo-KAGRA collaboration
NS: neutron star
ODE: ordinary differential equation
PDE: partial differential equation
PN: post-Newtonian
QNEF: quasi-normal excitation factor
QNM: quasi-normal mode
SM: Standard Model
TLN: tidal Love number
TS: topological star

Contents

Introduction

The first direct detection of gravitational waves (GWs) in September 2015 [1], produced by the coalescence of a binary system of black holes (BHs), opened a new era of BH physics and paved the way for GW astronomy. To date, more than 300 GW events have been collected by the LIGO - Virgo - KAGRA (LVK) collaboration [2–6], with the current fourth observing run (O4) expected to significantly expand the event catalog. The majority of these detected signals originate from the merger of binary systems of BHs. A smaller but significant portion of these events come from neutron stars (NSs) binaries, of which it is also possible to detect the electromagnetic counterpart, making them essential targets for multi-messenger astronomy, which began with the first detection in August 2017 [7, 8]. The remaining fraction of these events is instead produced by mixed binaries of NSs and BHs.

The rapidly growing research field of GW astronomy constitutes the most promising avenue to study the gravitational interaction in its highly dynamical and strong-field regime, and to test with high precision the predictions of Einstein's theory of general relativity (GR). Moreover, the study of GW signals collected by current and future interferometers enables us to infer the nature and intrinsic properties of the compact objects originating them. This analysis can potentially signal departures from GR, thus providing critical insights into new physics and the fundamental behavior of gravity in the extreme regime.

Such GW observations, combined with the high-resolution images of BH accretion disks obtained by the Event Horizon Telescope (EHT) [9, 10], represent not only a direct measurement of the existence and properties of the latter, but also a remarkable validation of GR. Despite all these direct evidences of the existence of BHs, their underlying physics still suffers from profound foundational issues, which arise either from the theory of GR itself or when one tries to introduce quantum effects into it.

One of the most critical issues affecting BHs in GR is the existence of curvature singularities, regions of spacetime where the curvature diverges and the theory of relativity breaks down. These singularities are conjectured to be hidden by an event horizon [11, 12], a surface of no return that prevents any matter or information from escaping once it has crossed the boundary of the BH. As a consequence, the region inside the event horizon is causally disconnected from the exterior spacetime. Moreover, since, according to the no-hair theorem [13–17], the exterior is fully characterized by at most three parameters (the BH mass, charge and angular momentum) it remains entirely independent of the specific details of the matter and processes that formed it.

In 1975 Hawking showed that a semiclassical treatment of the vacuum spacetime

outside the event horizon leads to the emission of thermal radiation from the BH [18, 19]. As a result, the BH gradually evaporates, making it impossible to reconstruct its interior from exterior information, in a process that violates the unitarity of quantum mechanics. This is known as the *information loss paradox*.

Additionally, the BH is characterized by an entropy that is proportional to the area of its event horizon [20], thus extremely large. According to statistical mechanics, the entropy of a system is related to the number of accessible microstates by the Boltzmann formula

$$S = k_{\mathrm{B}} \ln \Omega \,,$$

where Ω denotes the number of microscopic configurations compatible with a given macroscopic state. In this sense, the enormous BH entropy suggests an exponentially large number of underlying microstates. However, as previously stated, the spacetime outside the event horizon (parametrized in terms of mass, charge and angular momentum) is described by a single classical state, leading to a significant mismatch.

The open problems of GR and semiclassical gravity mentioned above, along with the lack of a coherent quantum description of the gravitational interaction, have opened the landscape to a plethora of exotic compact objects (ECOs) [21, 22]: astrophysical objects that, differently than classical BHs, are regular and horizonless. They arise as solutions of theories beyond GR or modified gravity; however, they are typically constructed using a bottom-up approach, namely they are phenomenological models designed to capture deviations from classical BHs without necessarily deriving directly from a fundamental underlying theory.

Among the wide variety of ECOs, String Theory, with the *Fuzzball proposal* [23–25], provides a top-down approach that is able to fully solve the challenging problems of classical BHs by replacing the latter with a horizon-scale microstructure: an ensemble of regular and horizonless geometries representing the microstates of the BH. To prevent collapse, these microstates are topologically non-trivial geometries existing in a higher-dimensional space.

However, the lack of symmetries in Fuzzball microstates (which are instead a typical feature of GR solutions) and their intrinsic complexity make the study of their dynamics a particularly difficult task. In light of these challenges, one fruitful approach is to investigate simplified yet physically motivated models whose solutions are both more tractable and preserve certain symmetries, while still sharing some ingredients with Fuzzballs: like existing in higher-dimensional spacetimes and involving gravity coupled with other fields or extra degrees of freedom. Thanks to the shared ingredients, these solutions are able to capture many of the essential aspects and phenomenological properties of the Fuzzball microstates.

Among such solutions, two recently discovered families have attracted considerable interest: topological stars (TS) [26] and $\mathcal{W}$-solitons [27]. Both represent smooth, horizonless and non-extremal geometries in five-dimensional theories of gravity. In particular, TSs are solutions of the five-dimensional Einstein-Maxwell theory and in order to prevent the gravitational collapse they are supported by a magnetic flux. On the other hand, $\mathcal{W}$-solitons come from minimal five-dimensional supergravity and possess the same mass and charges as four-dimensional charged black holes, but cap off smoothly due to a topological bubble supported by electromagnetic flux and an axion field. Thanks to their symmetry and tractability, these solutions provide

an ideal framework for exploring the behavior and observable features of black hole microstructure.

The analysis of the GWs produced by binary systems or by mergers involving such exotic objects currently provides the best opportunity to investigate their phenomenology and to identify potential deviations from GR. The GW signal originated by the coalescence of a compact binary system can be divided into three main phases: the inspiral, during which the two widely separated objects gradually spiral toward each other due to the emission of gravitational radiation; the merger, where the two bodies collide and form a single remnant dominated by strong nonlinear effects; and the ringdown, during which the final object settles into its equilibrium configuration.

One of the most effective and widely used methods to investigate the phenomenological properties of ECOs as the end-products of a binary coalescence, is the study of the ringdown signal. For standard BHs, the latter is accurately described by the so-called quasi-normal modes (QNMs): characteristic damped oscillation modes of the object with complex frequency that can be computed by analyzing small perturbations around the background solution. According to the no-hair theorem, the QNMs of a BH are fully determined by its three parameters: mass, charge and angular momentum. Moreover, these modes strongly depend on the nature of the compact object under study, and the presence or absence (as in the case of ECOs) of the event horizon can drastically affect them. Therefore, computing and comparing the QNMs spectrum with that of standard BHs represents a valuable way to infer the nature of the final compact objects produced in the coalescence of binaries.

Unlike standard BHs within GR, many ECOs exhibit a richer set of null geodesics, often featuring both the usual unstable photon orbit and an additional stable photon sphere. The presence of a stable photon sphere can support long-lived modes (QNMs with a long damping time) that give rise to a train of modulated pulses, known as *echoes*, in the late-time ringdown signal [22, 28, 29].

The presence of a stable photon sphere is a feature that not only characterizes many ECOs, but also appears in certain BH solutions with scalar hair, known as scalarized BHs [30–34]. The emergence of an additional stable photon sphere, or more generally a richer photon sphere structure compared to that of standard BHs without scalar hair, provides a compelling framework to explore long-lived QNMs and late-time features in the gravitational wave signal [35].

Over the past years several distinct groups have claimed evidence for post-merger repeating damped echoes in the signal of many GWs [36–38]. However, subsequent analyses by independent groups have found that the evidence for such events is weak and likely attributable to noise [39–43].

Beyond the ringdown signal, further insights into the nature of ECOs can be gained by studying the inspiral dynamics of extreme mass ratio systems. Extreme mass ratio inspirals (EMRIs) are binaries in which a stellar-mass compact object (the secondary) orbits around a much heavier one (the primary). Due to the large mass ratio, the secondary object completes a large number of orbital cycles before plunging into the primary. The long timescale of the inspiral dynamics allows deviations from GR, such as the absence of an event horizon or the presence of long-lived modes, to leave observable imprints on the GW signal. In particular, if the central object possesses long-lived QNMs, these modes can be resonantly excited

during the inspiral, leaving observable signatures in the GW [44–48]. Even when such resonances are not present, absence of the event horizon in the geometry can lead to an accumulated dephasing of the signal with respect to the BH case [48, 49].

The next generation of gravitational wave detectors both ground-based and space-based, such as Einstein Telescope (ET) [50], Cosmic Explorer [51] and Laser Interferometer Space Antenna (LISA) [52], will enhance our possibility to probe the nature of compact objects and potentially detect the phenomenological signatures discussed above. In particular, ET and the Cosmic Explorer will be able to detect high-frequency signals with greater sensitivity, potentially detecting post-merger features such as gravitational echoes or deviations in the ringdown. On the other hand LISA, with its sensitivity in the millihertz band, is particularly suited to observe long timescale signals like those produced by EMRIs [53].

The aim of this thesis is to explore how horizonless and regular spacetimes, motivated by top-down models like the Fuzzball proposal, can mimic or deviate from classical BH behavior in GW observables. We study simplified but analytically tractable solutions (such as scalarized BHs, TSs, and $\mathcal{W}$-solitons) that incorporate key features of BH microstates, including additional degrees of freedom and nontrivial topological structure. By analyzing their perturbative response and the dynamics of extreme-mass-ratio inspirals in these backgrounds, we identify phenomenological signatures that could help distinguish such exotic compact objects from standard BHs in upcoming GW observations.

The thesis is organized as follows.

Chapter 1 introduces the fundamental conceptual issues affecting BH physics in GR. These long-standing problems motivate the search for horizonless models of compact objects, among which the Fuzzball program of String Theory is one of the most promising top-down approaches. The chapter reviews the concept of Fuzzballs and presents explicit solutions within supergravity, namely the microstate geometries, together with illustrative examples. The final part of the chapter is devoted to their phenomenology, focusing on potential observational signatures that could distinguish them from classical BHs.

Chapter 2 presents the theoretical framework of BH perturbation theory and the associated QNMs. After a brief overview of GW emission from compact binaries, the chapter presents the formalism of linear perturbations in Schwarzschild spacetimes, with particular focus on scalar and gravitational perturbations. The QNMs are then introduced formally as the poles of the Green function, and different computational techniques to extract their frequencies, such as direct integration and the continued fraction method, are explored. Finally the phenomenological implications in the ringdown signal of ECOs are examined. Particular attention is given to long-lived QNMs and GW echoes, and the discussion concludes by connecting these general features to the case of Fuzzball microstate geometries.

Chapter 3 is devoted to EMRIs, long-lived binary systems in which a stellar-mass compact object spirals around a (super)massive one. After introducing the basic features of EMRIs, their perturbative treatment is outlined. The final part instead discusses the phenomenology that arises when the central object is an ECO rather than a BH, highlighting potential observable imprints such as resonant excitations and dephasing in the emitted GW signal.

Chapter 4 presents the mechanism of spontaneous scalarization. After introducing the tachyonic instability that underlies this mechanism, the chapter reviews the main classes of scalarization, driven by compactness, spin, or couplings to matter and other fields. Some specific models, such as the scalar-Gauss-Bonnet and the Einstein-Maxwell-scalar theory, are discussed as illustrative examples.

Chapter 5 is devoted to hairy BHs in the Einstein–Maxwell–scalar (EMS) theory, a framework that allows for spontaneous scalarization via a non–minimal coupling between scalar and electromagnetic fields. Static scalarized BH solutions are presented and analyzed, showing that in certain regions of their parameter space these configurations develop both stable and unstable photon spheres. The resulting effective potentials support long-lived QNMs and echo-like features in the ringdown signal.

Chapter 6 explores the topological star (TS), a novel smooth and horizonless soliton supported by magnetic flux in five-dimensional Einstein–Maxwell theory, together with the corresponding magnetized BH. After presenting their construction and perturbative dynamics, we compare their QNM spectra and ringdown signals,

showing that TSs can sustain long-lived modes and echo features absent in the BH case.

Chapter 7 studies the dynamics of EMRIs when the central object is a TS instead of a BH. The chapter investigates the scalar radiation emitted by a test charge orbiting circularly around TSs and magnetized BHs, highlighting the phenomenological consequences of the absence of an event horizon. The study reveals the appearance of sharp resonances in the TS case, associated with long–lived QNMs, and estimates the dephasing between inspirals around TSs and BHs, discussing its potential detectability with future space-based GW detectors such as LISA.

Chapter 8 presents the analysis of the $\mathcal{W}$-soliton, a smooth, horizonless solution of minimal five-dimensional supergravity, and its corresponding charged BH with the same mass and charge. Differently than usual ECOs, the $\mathcal{W}$-soliton possesses a single unstable photon sphere, much similar to a standard BH, thus preventing the formation of long-lived QNMs and echoes in the ringdown. The full QNM spectrum is then studied, together with a time domain analysis, highlighting the features in common and the differences between the soliton and the corresponding BH.

Chapter 1

BH conundrums and the Fuzzball program

BHs occupy a unique place in modern physics: they are not only fundamental theoretical solutions of GR, but their role has expanded in recent years thanks to the direct observation of GWs. At the same time they represent the source of profound conceptual issues whose understanding would clarify the role of gravity in its strong field regime and its interplay with quantum mechanics.

In this chapter we recall the most significant issues that have long puzzled the BH physics community, and introduce a promising top-down approach derived from String Theory that aims to resolve them all at once.

1.1 Challenges in BH physics

BHs have accompanied the development of GR since its very beginnings. Only two months after that Einstein presented his field equations, Schwarzschild discovered the first exact solution that describes the gravitational field exterior to a static, spherically symmetric, uncharged and non-rotating body [54]. Such remarkable and exotic result was soon followed by important generalizations: the Reissner–Nordström solution, accounting for charge [55, 56]; the Kerr metric, including rotation [57]; and finally the Kerr–Newman geometry, incorporating both charge and spin [58]. The surprising mathematical structure of these solutions set the stage for the so-called *no-hair theorem* [13–17], according to which stationary BHs in GR are uniquely characterized by three macroscopic parameters: their mass, charge and angular momentum.

Despite their elegant mathematical structure, BHs have faced considerable skepticism over the years, to the point that even Einstein himself argued against the physical reality of such solutions in nature [59]. As a consequence, BHs, together with their event horizons and singularities, were for a long time regarded as mere artifacts of the theory of GR, rather than compact objects with astrophysical relevance.

The first indirect evidence supporting the existence of BHs comes from the discovery of compact X-ray binaries in the 1960s and 1970s, in particular of Cygnus X-1 [60, 61]. Decades later astronomers were able to track the motion of individual stars near the center of the Milky Way. Their orbits revealed the presence of an

invisible but enormously massive object, now identified as the supermassive BH Sagittarius A* [62, 63]. In the present century the detections of GWs from the LVK collaboration have offered a remarkable confirmation of merging compact objects with masses and dynamics fully consistent with BHs. Finally, the first direct images of the shadows of M87* and Sagittarius A* have provided striking confirmation of the physical reality of BHs, settling long-standing doubts about the viability of their existence.

Despite the compelling indirect and direct observational evidences of the existence of BHs, their theoretical description still suffers from profound conceptual challenges. In GR the event horizon of the BH traps matter, light and any form of information within the interior region. As a consequence, the exterior is uniquely determined by a small set of long range parameters (mass, charge and angular momentum), while the spacetime region close to the horizon is vacuum, since any form of matter crossing the horizon is inevitably drawn toward the singularity. Hawking found that this vacuum region is unstable to the quantum creation of entangled particles [18, 19]. One component of the pair carries positive energy and escapes to infinity in the form of the so-called *Hawking radiation*, which is universal and thermal as a consequence of the uniqueness of BHs in GR. The other component with negative energy is captured by the BH, thereby reducing its mass. The two components define a pair in entanglement, whose state can be written as [24, 25, 64]

$$|\psi\rangle_{\text{pair}} = \frac{1}{\sqrt{2}}(|0\rangle_a\,|0\rangle_b + |1\rangle_a\,|1\rangle_b)\,, \tag{1.1}$$

where a and b denote the two components of the pair. By considering semi-classical back-reaction of the Hawking radiation it is possible to show that the BH will slowly evaporate. This process of evaporation gives rise to the *information loss paradox*: the thermal nature of the Hawking radiation implies that the final state carries no imprint of the BH initial configuration, making it impossible to recover the information about the matter that formed it. Therefore the evaporation process is not represented by a unitary transformation of states in a Hilbert space [24, 25]. Thus, once the BH has completely evaporated, the outgoing radiation remains in an entangled state, yet nothing appears to exist for it to be entangled with.

One possible way to address the information loss paradox is through the existence of long-lived remnants: when the BH shrinks to Planck-scale size, quantum-gravitational effects halt the evaporation process, leaving a stable object that stores the information. However, remnants do not appear to be possible in String Theory for two main reasons: first, this scenario leads to a necessarily infinite degeneracy of states for Planck-scale energies; second, the AdS/CFT duality rules it out [65].

Another proposed resolution to the problem of the monotonically increasing entanglement is the so-called *small corrections* scenario. The idea is that since the BH evaporation time is extremely long, the information about its formation could leak out through tiny corrections to the state of each emitted pair [64]

$$|\psi\rangle_{\text{pair}} = \frac{1}{\sqrt{2}}(|0\rangle_a\,|0\rangle_b + |1\rangle_a\,|1\rangle_b) + |\delta\psi\rangle\ , \qquad \Big||\delta\psi\rangle\Big| < \epsilon\,, \qquad \epsilon \ll 1\,, \tag{1.2}$$

arising from quantum gravity effects. Although the corrections to each created pair are individually very small, the total number of emitted quanta, N_{quanta}, is large

enough that $N_{\text{quanta}}\,\epsilon \geq 1$. In this way, correlations among the quanta could in principle prevent the entanglement from growing monotonically. However a theorem [66] proves that such small corrections are not enough to solve such problem. Indeed, if one assumes that each radiated quantum undergoes no significant change, the entanglement entropy $S_{\text{ent}}(N)$ of the radiation with the BH at step N continues to grow monotonically, as

$$S_{\text{ent}}(N+1) > S_{\text{ent}}(N) + \log 2 - 2\epsilon\,. \tag{1.3}$$

Therefore, the problem cannot be resolved by small corrections, it requires corrections of order unity.

Another puzzle affecting BH physics regards its entropy, which according to Bekenstein [20] is proportional to the horizon area A

$$S_{\text{BH}} = \frac{A}{4}\,, \tag{1.4}$$

where we used Planck units (i.e. $G = c = \hbar = \kappa_B = 1$). The *no-hair theorem* states that, from the perspective of an external observer, the BH is described by a single classical state. This simple description is in contradiction with the BH entropy that, if interpreted in terms of the Boltzmann formula, is connected to the number of available microstates. The puzzle is therefore evident: on the one hand, the *no-hair theorem* implies a unique exterior state, while on the other, BH thermodynamics assigns an enormous entropy (for example, Sagittarius A* has $S_{\text{BH}} \sim e^{10^{90}}$), pointing to an exponentially large number of underlying microstates.

The common expectation is that quantum gravity corrections become relevant only in the spacetime regions where the curvature reaches the Planck scale, typically in the deep interior of the BH, where the singularity lives. Conversely, in the near horizon region, where the curvature is small, physics should be accurately described by low-energy semiclassical physics. Contrary to this belief, in order to resolve the information paradox new physics cannot be confined to the singularity, but it must already appear at the horizon scale. If we consider a shell of mass M that is collapsing to form a BH we get that the curvature at the horizon is very small [64]

$$R \sim \frac{1}{(GM)^2} \ll \frac{1}{l_p^2}\,, \tag{1.5}$$

where we have reintroduced the gravitational constant G and where l_p is the Planck length. Under this condition, one expects that low energy semiclassical dynamics holds, therefore, the shell will smoothly cross the horizon radius and pair creation proceed in the exterior vacuum. The outgoing quanta of Hawking radiation are then entangled with negative energy particles inside the horizon, and by causality any quantum gravity effect from the interior (or the singularity) cannot alter this mechanism. A viable resolution instead requires order-unity departures from the Hawking vacuum at the horizon scale, namely a breakdown of semiclassical physics precisely where the curvature remains small, and not where the curvature is large, as it is close to the singularity. The next section presents the Fuzzball program, providing a concrete scenario that resolves the challenges outlined above.

1.2 From BHs to Fuzzballs

In the Fuzzball paradigm, the usual description of a BH endowed with a smooth event horizon is replaced by a horizon-scale microstructure: from far away the geometry matches the BH it is supposed to replace, but at the would-be horizon it shows order unity deviations. In this sense a Fuzzball is a BH microstate whose near-horizon structure is non-trivial, while its asymptotics coincide with those of the corresponding BH [23]. Therefore BH microstates, replacing an arbitrary BH, are highly complex quantum objects, realized as solutions of String Theory, including string or brane condensates with a wave-function that extends over the horizon scale, and whose degrees of freedom provide the microscopic accounting of the BH entropy [25].

The appeal of the Fuzzball program is that it provides a natural and conceptually straightforward resolution of the information problem, accounts for the large BH entropy and removes curvature singularities all at once. Following [25], one can view Fuzzballs as a new quantum phase that appears when matter is compressed to BH densities. In this case the gravitational collapse and the subsequent appearance of a horizon and a singularity is prevented with the formation of a horizon scale microstructure.

The information problem is solved because the internal degrees of freedom of the Fuzzball are in causal contact with an exterior observer. Indeed the absence of a horizon implies that the usual mechanism of Hawking pair creation does not take place and therefore the information loss problem never arises. Instead, the Fuzzball can emit radiation directly from its surface, exactly like an ordinary star, though with an emission rate that matches the Hawking rate [67]. According to this program the curvature singularities and event horizons appear only when one tries to describe the gravitational interaction by using a theory with not sufficiently many degrees of freedom.

1.2.1 Microstate Geometries

While a general Fuzzball construction for arbitrary BHs remains still an open problem, for certain classes of BHs one can explicitly build well-behaved solutions within supergravity, the low-energy effective theory of String Theory. Such solutions are known as *microstate geometries* and, as explicit realizations of Fuzzballs, they are smooth and regular everywhere and possess no horizon. Although the general property of microstate geometries is to be regular everywhere, there exist some five-dimensional solutions that upon a dimensional compactification to four dimensions show well-understood singularities and are called *microstate solutions* [68]. Moreover microstate geometries are constructed to have the same mass and charges as the corresponding BH they are meant to replace. In this way they reproduce the correct asymptotic behavior of the classical BH solution while differing drastically in their near-horizon structure, where they are smooth and horizonless.

One should emphasize that microstate geometries are Fuzzballs solutions of the effective long-wavelength approximation to String Theory, therefore they are valid within the supergravity regime. In this sense higher order quantum stringy corrections can be neglected up to the Planck or string scale [69, 70].

The known microstate geometries can be divided into two main classes: *multi-centered bubbled* geometries and *superstrata* geometries.

Multicentered bubbled geometries

The multicentered bubbled geometries are regular and horizonless solutions of five-dimensional supergravity [71], that can have $\mathbb{R}^{4,1}$ or $\mathbb{R}^{3,1} \times (S^1)_\psi$ asymptotics. Those with $\mathbb{R}^{4,1}$ asymptotics represent the microstates of a five-dimensional, three-charge supersymmetric BMPV BH [72]. The others, with $\mathbb{R}^{3,1} \times (S^1)_\psi$ asymptotics, can be dimensionally reduced along the $(S^1)_\psi$ circle to four dimensions and represent the microstates of a supersymmetric, static and four-dimensional BH.

These solutions are defined by the presence of several distinct *centers* which correspond to points in a three-dimensional subspace where the $(S^1)_\psi$ circle smoothly shrinks to zero leaving the overall spacetime regular. Their name derives from the fact that each pair of centers is connected by a non-trivial two-sphere, or *bubble*, whose collapse is prevented by a magnetic flux. In this sense the role of extra dimensions with non-trivial topology is a key aspect to avoid the collapse.

As already anticipated, when one performs a dimensional reduction to four dimensions over the $(S^1)_\psi$ circle, the centers give rise to singularities which, not being hidden behind a horizon, are naked.

An explicit example of such configurations is provided by the *scaling solutions*, a family characterized by a continuous parameter λ such that in the scaling limit $(\lambda \to 0)$ the centers approach zero separation, yielding a microstate geometry that asymptotically approaches the corresponding BH. In this limit the redshift throat of the bubbled solution becomes deeper and deeper, reaching the one of the BH horizon.

For more details and explicit examples of these solutions see [68, 71, 73–88].

Superstrata geometries

The multicentered bubbled geometries account for only a small subset of the full set of microstates associated with the BMPV BH [80]. A much broader class of microstates of the same BMPV BH is instead captured by the *superstrata* geometries. Even though they correspond to a larger fraction of these BH microstates, they still do not account for the full BMPV entropy [89–92].

The superstrata geometries are solutions of six-dimensional supergravity, with a non-trivial momentum along the sixth extra dimension. They can be pictured as having a single S^2 topological bubble, similarly to a two-centered bubbled geometry [23].

For more details about the superstrata geometries see [93–103].

Beyond supersymmetry: other microstate geometries

Both the multicentered bubbled geometries and the superstrata geometries are only possible within supersymmetry, therefore the microstates they capture are just of supersymmetric BHs. The supersymmetric microstate geometries can be constructed by solving the simpler first-order supersymmetry equations, rather than the full

equations of motion of supergravity, that are necessary for non-supersymmetric solutions, and this is the reason why the latter are much more difficult to investigate.

Over the last years, some non-supersymmetric microstate solutions have been constructed [104–114], however, they suffer from the drawback of being overspinning and therefore cannot match the charges of the corresponding BHs.

1.2.2 Fuzzball formation

A natural issue of the Fuzzball program at this stage is to understand how the collapse of a star can lead to an object different from a BH, thereby evading or generalizing Birkhoff's theorem. In an idealized scenario, if we consider a spherical shell of matter with sufficiently large total mass, it will inevitably collapse under its own gravitational pull, eventually forming an event horizon and giving rise to a Schwarzschild BH. The Fuzzball program must also account for how horizon formation can be dynamically prevented, so that the collapse results in a Fuzzball rather than in a classical BH. Since for a shell of mass M the curvature close to the horizon goes like Eq. (1.5), and therefore no large curvatures are involved, one might expect that quantum corrections would not be sufficient to prevent the shell from collapsing into a horizon. This problem, together with the seemingly inevitable collapse leading to horizon formation, is addressed by the enormous entropy of the BH and the correspondingly vast number of available microstates [115, 116].

The idea for resolving the problem of horizon formation is that gravitational collapse can undergo a tunneling process from the shell state to a Fuzzball configuration. One can show that for Fuzzballs there is a non-zero probability of tunneling given by

$$P = |\mathcal{A}|^2 \,, \qquad \mathcal{A} \sim e^{-S_{\rm cl}} \,, \tag{1.6}$$

where $\mathcal{A}$ is the tunneling amplitude and $S_{\rm cl}$ is the classical gravitational action that can be estimated by considering all the involved length scales to be of the order of the BH radius $\sim GM$, i.e.

$$S_{\rm cl} \sim \frac{1}{G}\int d^4x\, R \sim \frac{1}{G}(GM)^4\frac{1}{(GM)^2} \sim GM^2 \sim \left(\frac{M}{m_p}\right)^2 \,, \tag{1.7}$$

where m_p is the Planck mass. It is straightforward to see that if the BH is sufficiently large, i.e. for $M \gg m_p$, the tunneling probability P is extremely small. Such small probability is consistent with the fact that the evolution of macroscopic objects is perfectly described by classical dynamics, and the probability of tunneling between two distinct macroscopic configurations is completely negligible. However, in this case, to obtain the total tunneling probability $\mathcal{P}$, one must multiply the single-state probability P by the number $\mathcal{N}$ of Fuzzball states accessible to the shell, and this number is enormously large

$$\mathcal{N} \sim e^{S_{\rm BH}} \sim e^{\frac{A}{4G}} = e^{4\pi GM^2} \,. \tag{1.8}$$

The extremely small probability of tunneling into a single state is counterbalanced by the enormous number of available Fuzzball microstates, so that the total tunneling probability can effectively become of order unity

$$\mathcal{P} = P\mathcal{N} \sim 1 \,. \tag{1.9}$$

In this scenario the shell of matter, or in the realistic case the star, will tunnel into a linear combination of Fuzzball states, instead of forming a horizon.

The heuristic argument outlined above can be made more rigorous through the so-called VECRO hypothesis (see [117] for further details).

1.2.3 The issue of typicality

As described above, microstate geometries are solutions of supergravity and represent the microstates of the corresponding BH. However, these known solutions constitute only a small subset of the full phase space of microstates required to account for the Bekenstein–Hawking entropy of BHs [70, 118]. This issue in the context of microstate geometries is known as *typicality*, and concerns the question of whether these geometries efficiently represent and share properties with most BH microstates (*typical*), or whether they instead capture only atypical features (*atypical*). In the latter case they would correspond to only a marginal sector of the full phase space of BH microstates [70]. Conversely, some works have showed how some interesting features of microstate geometries are actually typical [77, 78, 119, 120]. In this sense and in a much broader perspective, microstate geometries serve as a valuable framework to probe the microscopic structure of BHs and to study possible observational features of horizon-scale structures.

1.3 Phenomenology of Fuzzballs

In order to test the Fuzzball program we must focus on distinct phenomenological features that would differentiate these horizonless microstate structures from classical BHs within GR. Fuzzballs indeed provide a top-down model to analyze horizonless objects and explore possible quantum gravity signatures in observable phenomena. The study of the observable features produced by such objects is referred to as *Fuzzball phenomenology* and has several different applications.

In the present work we will focus on the GW signatures of Fuzzballs, with a particular attention to the perturbative response. For a more detailed discussion on how the Fuzzball phenomenology fit into the broader ECOs landscape we refer the reader to Sec. 2.5. In the present section, however, we will also briefly mention other interesting phenomenological features for completeness.

1.3.1 QNMs and echo pattern in Fuzzballs

One of the most promising observational channels to test the Fuzzball proposal is the study of GW perturbations.

BHs in GR are characterized by a discrete spectrum of quasi-normal modes (QNMs), which describe the GW signal associated with the late time relaxation of the BH following a perturbation. As a direct consequence of the *no-hair* theorem, these modes only depend on mass, charge and spin of the BH. The absence of an event horizon in microstate geometries, and more generally in the Fuzzball program, modifies the boundary conditions that must be imposed when solving the eigenvalue problem to determine the QNMs. Additionally to a modified QNMs spectrum, some modes of the perturbation can be trapped in the potential well between the

photon sphere and the effective reflective surface replacing the horizon in microstate geometries. Such modes can leak through the potential barrier at late times in the GW signal, giving rise to a series of repeated peaks known as *echoes* [23, 121–123] (a more detailed discussion is provided in Sec. 2.5).

1.3.2 Multipolar structure

Besides the modifications of the QNMs spectrum and the possible presence of an echo pattern in the ringdown GW signal, another noteworthy phenomenological feature that differentiates Fuzzballs from classical BHs regards their multipoles [124–127]. According to the *no-hair* theorem, the multipoles of a Kerr BH are uniquely defined by its two parameters, mass M and angular momentum $J = Ma$

$$M_l + iS_l = M(ia)^l \,, \tag{1.10}$$

where l is the angular momentum number, while M_l and S_l are the mass and current (or angular momentum) multipoles, respectively. The above relation is fulfilled also by the Kerr-Newman BH, showing that the electric charge Q does not play any role in the multipolar structure [128].

On the other hand, Fuzzballs violate the *no-hair* theorem, and as a consequence they exhibit a non trivial multipoles set, depending on the complicated microstate structure. Asymptotically flat supersymmetric BHs in four dimensions are static and therefore all their multipoles, except the mass $M = M_0$, vanish. However, it has been shown that dimensionless ratios of multipoles show an interesting structure. Since ratios of multipoles is in general not well-defined for supersymmetric BHs, it is necessary to deform the BH under study to a non-extremal charged BH of maximal supergravity in four dimensions. In this way it is possible to compute the multipoles for these deformed BHs and consequently evaluate their ratios. By taking the limit of these multipoles ratios as the deformation is turned off one can construct well-defined ratios. Such a procedure is called *indirect* method [129, 130].

As stated above, any Fuzzball, and therefore any multicentered bubbled geometry, will have non-vanishing multipoles. However, in the scaling limit $\lambda \to 0$ the microstate geometry becomes the same of the associated BH. In this way, one can compute the relevant ratios for BHs in terms of the multipoles of four-dimensional microstate geometries by taking the scaling limit, through a procedure known as the *direct* method.

The *indirect* method can be applied also to non-static BHs, like the Kerr BH. A noteworthy multipoles ratio for the Kerr BH is

$$\frac{M_2 S_l}{M_{l+1} S_1} = 1 \,, \tag{1.11}$$

that is well defined using the *indirect* method and serves as a useful quantity to constrain possible deviations from the Kerr geometry. Additionally it is possible to compare the multipoles and multipoles ratios between multicentered bubbled geometries and Kerr BHs [131, 132]. In [132] it was shown that for several families of three-centered bubbled solutions, more than the 90% have shown multipole ratios such as

$$\mathfrak{M}_l = \left| \frac{M_l \, M_0^{l-1}}{S_1^l} \right| \tag{1.12}$$

higher than the ones of the Kerr BH. Moreover the ratios $\mathfrak{M}_l$ are monotonically increasing with the intercenter distance, reaching the minimum value at the $\lambda \to 0$.

The four-dimensional three-center bubbled geometries discussed in [132] are supersymmetric solutions. In [133] the gravitational multipole structure of four-dimensional non-supersymmetric extremal black holes (almost BPS-BHs) and their horizonless microstate geometries has been computed and compared to that of the Kerr BHs, showing that almost-BPS BHs possess a much richer multipolar structure than Kerr BHs, with non-vanishing odd-parity moments and a dependence on additional parameters such as the charge to mass ratio; moreover, their corresponding microstate geometries reproduce the BH multipoles to leading order while exhibiting microstructure-dependent departures.

1.3.3 Tidal Love numbers

Another important phenomenological feature of Fuzzballs concerns their tidal response. The tidal Love numbers (TLNs) quantify how a compact object deforms under the influence of an external tidal force [134]. Within classical GR, TLNs of BHs are zero [22]. By contrast, horizonless compact objects (or more general ECOs) possess non-vanishing TLNs. This is true for boson stars, gravastars, wormholes, and other ECO models [135], and it is expected to hold as well for Fuzzball microstate geometries. The computation of TLNs for microstate geometries, in contrast with their BH counterparts, represents a particularly promising observable that has so far remained unexplored because of the complexity of the task.

1.3.4 Other experimental observables: geodetic motion, shadows and EMRIs phenomenology

Beyond QNMs, echoes, multipolar structure, and tidal responses, several additional phenomenological features of Fuzzballs can be probed through their geodetic motion and associated astrophysical signatures.

Microstate geometries may exhibit richer geodesic structure than Kerr BHs, with additional photon spheres or stable orbits. Moreover the absence of a horizon means that microstate geometries do not absorb all the incident light rays, resulting in possible large differences in the shadows compared to the BH case [23].

A particularly promising observable for future interferometers is provided by EMRIs. In these binary systems the secondary probes the horizon-scale structure of the primary object, orbiting around it for many cycles. Horizonless geometries, such as Fuzzballs, can provide several smoking-guns through EMRIs. Long-lived QNMs may be resonantly excited during the inspiral, producing phase shifts or bursts in the waveform. In the absence of resonances, the lack of an event horizon leads to a cumulative dephasing relative to the BH case, see Sec. 3.3. The millihertz sensitivity of future space-based detectors like LISA makes them well suited to detect such signatures, defining EMRIs as one of the most powerful probes for Fuzzball phenomenology.

Chapter 2

Black hole perturbation theory and QNMs

2.1 Gravitational waves from compact binaries

Since the first direct measurement of a GW produced by the merger of two BHs on September 14, 2015, GW astronomy has become one of the most promising avenues to probe the strong-field regime of gravity and experimentally test the theory of GR with unprecedented accuracy. This event, famously known as GW150914 [1], constitutes the oscillations of the gravitational field emitted by two coalescing compact objects, specifically two BHs with masses

$$m_1 = 34.6^{+4.4}_{-2.6}\, M_\odot\,, \qquad m_2 = 30.0^{+2.9}_{-4.6}\, M_\odot\,, \tag{2.1}$$

finally merging into a remnant BH of mass $M = 61.5^{+3.4}_{-2.9}\, M_\odot$ and dimensionless spin $a = 0.68^{+0.05}_{-0.05}$. By comparing the total mass of the binary system with the mass of the final object it turns out that $\sim 3.1 M_\odot$ has been radiated away in the form of waves of the gravitational field, an enormous amount of energy corresponding to $\sim 5.5 \times 10^{54}$ erg. The signal has been collected by the interferometric antennas of LIGO, both in Livingston (Louisiana, USA) and in Hanford (Washington, USA), and has proven to be fully consistent with GR predictions [136].

As can be seen from Fig. 2.1, the signal of GW150914, as well as the GW produced by any other BHs binary system, can be split into three distinct phases, depending on the distance between the two components, their inspiral motion, and the corresponding features of the waveform:

- ***Inspiral phase***: It represents the first part of the coalescence dynamics, where the two binary components are relatively far away from each other. The emission of GWs causes the system to lose energy and angular momentum, leading to a gradual reduction of the orbital separation and a progressive increase of the orbital frequency.

  The gravitational interaction pulling one compact object into the other is still relatively weak, the relative velocity remains small compared to the speed of light, and perturbation theory of GR can be applied. Indeed the GW signal can be accurately described in terms of the so-called *post-Newtonian*

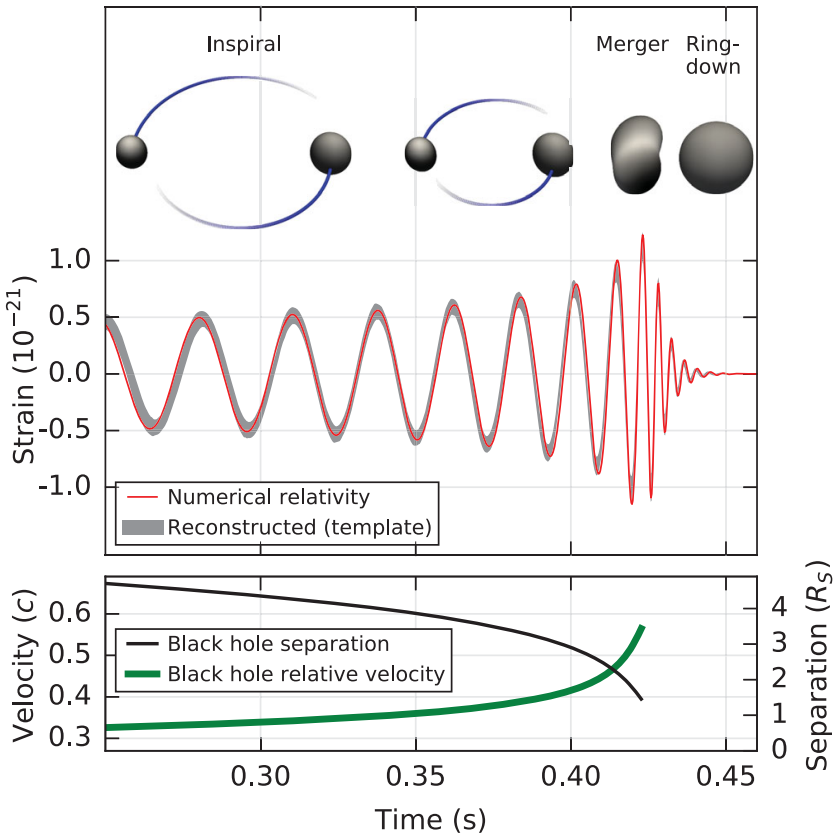

Figure 2.1. The top panel shows the pictorial representation of the different stages of a GW signal from a binary BH coalescence, together with the comparison between the observed strain amplitude of GW150914 and the numerical waveform of a binary BH merger. The bottom panel displays the Keplerian effective BH separation in units of Schwarzschild radii $R_S = 2M$ and the effective relative velocity between the two components of the binary system [1].

(PN) expansion, that brings corrections to the Newtonian dynamics with an expansion in terms of the velocity parameter v/c [137–141].

- ***Merger phase***: In this phase the two objects are very close and eventually plunge one into the other to form a final remnant. Due to the very strong gravitational interaction involved in the process, the dynamics is highly non-linear and only Numerical Relativity simulations are able to correctly describe the evolution. During this extremely short stage, the amplitude of the gravitational radiation reaches its maximum, and the largest fraction of the total energy is released.

- ***Ringdown phase***: It defines the last stage of the GW signal, where the final object has been formed and relaxes towards its equilibrium configuration. The waveform can be described with perturbation theory in terms of characterized damped sinusoids of the final object called quasi-normal modes (QNMs) as

follows [142–148]

$$h = \sum_{lmn} A_{lmn}(r)\, \sin(\omega_{R,lmn} t + \phi_{lmn})\, e^{-t/\tau_{lmn}}\, {}_{-2}S_{lm}(\theta, \phi)\,, \tag{2.2}$$

where $\omega_{R,lmn}$ is the real part of the associated complex frequencies of the QNMs $\omega_{lmn} = \omega_{R,lmn} + i\,\omega_{I,lmn}$, with damping time $\tau_{lmn} \equiv -1/\omega_{I,lmn}$, $A_{lmn}(r)$ is the amplitude, ϕ_{lmn} is the phase, and ${}_sS_{lm}(\theta, \phi)$ are the so-called spin-weighted spheroidal harmonics. The characteristic QNMs define an infinite set labeled by the so-called *overtone number* $n \geq 0$, which orders the modes hierarchically according to their damping times. The integers $l \geq 0$ and m, with $|m| \leq l$, are the *angular number* and *azimuthal number*, respectively.

2.2 Linear perturbations of BHs

The study of BH perturbations provides a crucial framework to study the response of such spacetimes under small disturbances. In the present thesis we will focus on the use of BH perturbation theory as a powerful tool to analyze the stability of BH spacetimes and other ECOs, and to describe the ringdown phase generated by these objects after a binary merger [146–153]. Nevertheless, BH perturbation theory also represents a powerful tool for investigating GWs arising from a variety of astrophysical processes, as well as in applications related to the gauge/gravity duality [147, 153].

The birth of BH perturbation theory can be traced back to 1957, when Regge and Wheeler studied a specific class of gravitational perturbations (*axial* perturbations) propagating on the background of the Schwarzschild BH [154]. In 1970, Zerilli further developed the analysis of Regge and Wheeler by investigating *polar* gravitational perturbations of the Schwarzschild geometry [155]. A few years after, in 1973, by using the Newman-Penrose formalism [156], Teukolsky has been able to decouple the gravitational perturbations of the Kerr background [157]. These seminal works defined the foundations of BH perturbation theory, showing that the dynamics of small disturbances on the background of BH geometries can be described by solving wave equations with an effective gravitational potential. For a broader and more detailed review see [147].

Before addressing gravitational perturbations of BH spacetimes, it is instructive to begin with the simpler case of scalar perturbations on the Schwarzschild geometry, as it already captures several essential aspects of the perturbative framework.

2.2.1 Scalar perturbation on Schwarzschild BH

Let us first consider an instructive example, namely that of a test scalar field propagating on the background geometry of a Schwarzschild BH. The test field assumption means that the scalar field is treated as a small perturbation that propagates on a fixed background, without modifying the geometry. In other words we want to solve the field equations to the linear order, therefore the scalar field does not contribute to the Einstein field equations via the stress-energy tensor, where it enters with quadratic terms in the field (and its derivative).

To begin with we recall the line element of the Schwarzschild BH, that is given by

$$ds^2 = -f(r)\,dt^2 + f(r)^{-1}\,dr^2 + r^2\,d\Omega_2^2\,, \tag{2.3}$$

where $d\Omega_2^2 = d\theta^2 + \sin^2\theta\,d\phi^2$ is the metric on the two-sphere, and $f(r) \equiv (1-2M/r)$, with M that represents the mass of the BH. The evolution of the scalar field Φ is encoded in the Klein-Gordon equation

$$\Box\,\Phi \equiv \nabla_\mu \nabla^\mu \Phi = 0\,, \tag{2.4}$$

which can be written in terms of partial derivatives in a more convenient form

$$\frac{1}{\sqrt{-g}}\partial_\mu(\sqrt{-g}\,g^{\mu\nu}\,\partial_\nu\Phi) = 0\,, \tag{2.5}$$

where g is the determinant of the metric tensor $g_{\mu\nu}$.

Thanks to the spherical symmetry of the background geometry, it is possible to decompose the scalar field in *spherical harmonics* $Y_{lm}(\theta,\phi)$. Moreover, since the Schwarzschild spacetime is static, it is convenient to Fourier transform as follows

$$\Phi = \Phi(t,r,\theta,\phi) = \sum_{lm}\int \frac{d\omega}{2\pi}\,e^{-i\omega t}\,\psi_{lm}(r)\,Y_{lm}(\theta,\phi)\,, \tag{2.6}$$

where $\psi_{lm}(r)$ represents the radial component of the scalar field. Using the spherical harmonics decomposition and the Fourier transform in Eq. (2.6), together with the eigenvalue equation

$$\left(\partial_\theta^2 + \cot\theta\,\partial_\theta + \frac{1}{\sin^2\theta}\partial_\phi^2\right) Y_{lm} = -l(l+1)\,Y_{lm}\,, \tag{2.7}$$

we can separate the radial from the angular components of the scalar field, to get an ordinary differential equation in r

$$f\frac{d^2\psi_l(r)}{dr^2} + \left(\frac{2f}{r} + \frac{df}{dr}\right)\frac{d\psi_l(r)}{dr} + \left(\frac{\omega^2}{f} - \frac{l(l+1)}{r^2}\right)\psi_l(r) = 0\,, \tag{2.8}$$

where we have omitted the index m, since the equation does not depend on it owing to spherical symmetry. By performing a field redefinition $\psi_l(r) \equiv \Psi_l(r)/r$ and introducing a *tortoise coordinate* r_* with $dr/dr_* = f^{-1}$, we can recast Eq. (2.8) in the form of a one-dimensional wave equation

$$\frac{d^2}{dr_*^2}\Psi_l(r) + (\omega^2 - V_l^{\rm scal})\Psi_l(r) = 0\,, \tag{2.9}$$

where $V_l^{\rm scal}$ is the gravitational effective potential given by

$$V_l^{\rm scal}(r) = \left(1 - \frac{2M}{r}\right)\left[\frac{l(l+1)}{r^2} + \frac{2M}{r^3}\right]\,, \tag{2.10}$$

where we used $f(r) = 1 - 2M/r$. It is worth noting that Eq. (2.9) has the same form of the time-independent Schrödinger equation in one dimension, as can be verified by replacing ω^2 with the energy of the quantum mechanical system under

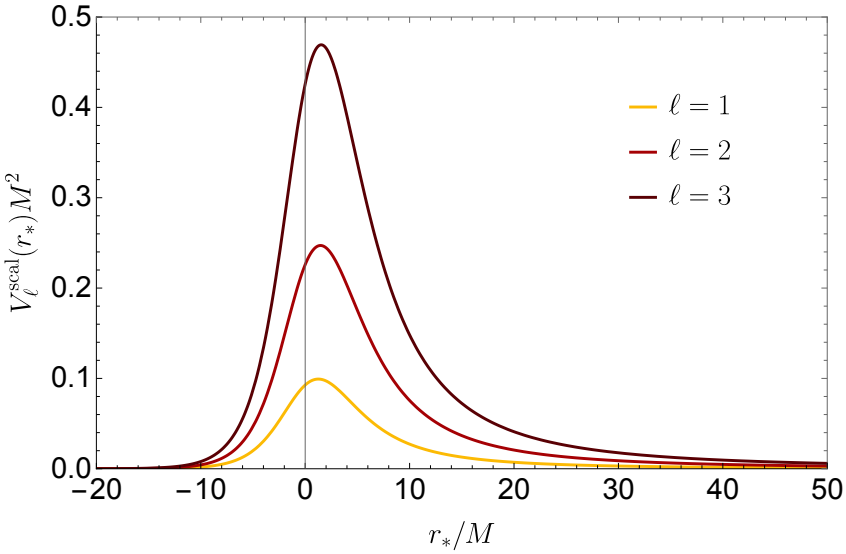

Figure 2.2. Effective potential $V_l^{\rm scal}$ for a test scalar field perturbation on the background of the Schwarzschild BH, for different values of $l = 1, 2, 3$.

study. This correspondence proves particularly useful for studying wave equations in BH perturbation theory, as it enables the application of well-known methods from quantum mechanics.

The effective potential of Eq. (2.10) is plotted in Fig. 2.2, which shows how $V_l^{\rm scal} \to 0$ in both the limits $r_* \to -\infty$ ($r \to 2M$) and $r_* \to +\infty$ ($r \to +\infty$), at the horizon and at infinity, respectively. It presents a maximum which depends on the value of l and approaches the location of the photon sphere ($r = 3M$) in the eikonal limit $l \to +\infty$.

2.2.2 Regge-Wheeler and Zerilli equations

We now move on to the more relevant case of gravitational perturbations in the Schwarzschild geometry. In this case the disturbances of the spacetime are encoded by $h_{\mu\nu}$ on the background spacetime $\bar{g}_{\mu\nu}$, while the full metric tensor $g_{\mu\nu}$ is given by

$$g_{\mu\nu} = \bar{g}_{\mu\nu} + h_{\mu\nu}\,, \tag{2.11}$$

with condition $|h_{\mu\nu}| \ll |\bar{g}_{\mu\nu}|$. In order to find the wave equations describing the gravitational perturbations we need to linearize, in terms of the metric of Eq. (2.11), the Einstein's field equations in vacuum

$$G_{\mu\nu} = R_{\mu\nu} - \frac{1}{2} g_{\mu\nu} R = 0\,, \tag{2.12}$$

where $R_{\mu\nu}$ is the Ricci tensor, that written in terms of the affine connection $\Gamma^\rho_{\mu\nu}$ is given by

$$R_{\mu\nu} = \partial_\rho \Gamma^\rho_{\mu\nu} - \partial_\nu \Gamma^\rho_{\mu\rho} + \Gamma^\rho_{\sigma\rho}\Gamma^\sigma_{\mu\nu} - \Gamma^\rho_{\sigma\nu}\Gamma^\sigma_{\mu\rho}\,, \tag{2.13}$$

with

$$\Gamma^\rho_{\mu\nu} = \frac{1}{2} g^{\rho\sigma}(\partial_\nu g_{\sigma\mu} + \partial_\mu g_{\sigma\nu} - \partial_\sigma g_{\mu\nu})\,. \tag{2.14}$$

If we expand up to the first order in $h_{\mu\nu}$ the Eq. (2.12) we get

$$G_{\mu\nu}[g_{\mu\nu}] = \bar{G}_{\mu\nu}[\bar{g}_{\mu\nu}] + \delta G_{\mu\nu}[h_{\mu\nu}] + \mathcal{O}(h^2_{\mu\nu})\,. \tag{2.15}$$

The term $\bar{G}_{\mu\nu}[\bar{g}_{\mu\nu}]$, that represents the Einstein's tensor for the background metric vanish identically, namely $\bar{G}_{\mu\nu}[\bar{g}_{\mu\nu}] = 0$. If we expand the affine connection we get

$$\Gamma^{\rho}_{\mu\nu}(g_{\mu\nu}) = \Gamma^{\rho}_{\mu\nu}(\bar{g}_{\mu\nu}) + \delta\Gamma^{\rho}_{\mu\nu}(\bar{g}_{\mu\nu}, h_{\mu\nu}) + \mathcal{O}(h^2_{\mu\nu})\,, \tag{2.16}$$

with

$$\delta\Gamma^{\rho}_{\mu\nu}(\bar{g}_{\mu\nu}, h_{\mu\nu}) = \frac{1}{2}\bar{g}^{\rho\sigma}(\nabla_\nu h_{\sigma\mu} + \nabla_\mu h_{\sigma\nu} - \nabla_\sigma h_{\mu\nu})\,. \tag{2.17}$$

By replacing Eq. (2.16) in the definition of the Ricci tensor of Eq. (2.13) we get the expanded expression

$$R_{\mu\nu}(g_{\mu\nu}) \equiv \bar{R}_{\mu\nu}(\bar{g}_{\mu\nu}) + \delta R_{\mu\nu}(\bar{g}_{\mu\nu}, h_{\mu\nu}) + \mathcal{O}(h^2_{\mu\nu})\,, \tag{2.18}$$

with the linearized Ricci tensor

$$\begin{aligned}\delta R_{\mu\nu}(\bar{g}_{\mu\nu}, h_{\mu\nu}) &= \nabla_\rho \delta\Gamma^{\rho}_{\mu\nu} - \nabla_\nu \delta\Gamma^{\rho}_{\mu\rho} \\ &= \frac{1}{2}(\nabla_\rho\nabla_\mu h^{\rho}{}_{\nu} + \nabla_\rho\nabla_\nu h^{\rho}{}_{\mu} - \nabla_\nu\nabla_\mu h^{\rho}{}_{\rho} - \nabla_\rho\nabla^\rho h_{\mu\nu})\,.\end{aligned} \tag{2.19}$$

The linearized Einstein's field equations are given by

$$\delta G_{\mu\nu}[h_{\mu\nu}] = \delta R_{\mu\nu} - \frac{1}{2}(\bar{g}_{\mu\nu}\delta R - h_{\mu\nu}\bar{R}) = 0\,. \tag{2.20}$$

However, since the Schwarzschild spacetime is Ricci flat, i.e. $\bar{R}(\bar{g}_{\mu\nu}) = 0$, and that $\delta R = 0$ (as can be verified by taking the trace of Eq. (2.20)) the study of the linearized Einstein equations in vacuum reduces to the study of

$$\delta R_{\mu\nu}(\bar{g}_{\mu\nu}, h_{\mu\nu}) = 0\,. \tag{2.21}$$

Since the Schwarzschild BH is spherically symmetric it is useful to perform a spherical harmonics decomposition. In this case, however, the procedure is considerably more involved than for simple scalar perturbations, as the decomposition must account for the full tensorial structure of $h_{\mu\nu}$. In particular, one must employ scalar, vector, and tensor spherical harmonics (see Appendix A for a more detailed discussion).

The so-called Regge–Wheeler gauge [154] provides a natural framework for the decomposition, enabling us to factorize the (t, r) dependence from the angular (θ, ϕ) dependence of the gravitational perturbations as follows

$$h_{\mu\nu}(t, r, \theta, \phi) = h^{\text{axial}}_{\mu\nu}(t, r, \theta, \phi) + h^{\text{polar}}_{\mu\nu}(t, r, \theta, \phi)\,, \tag{2.22}$$

with

$$h^{\rm axial}_{\mu\nu} = \sum_{lm} \begin{pmatrix} 0 & 0 & -h_{0\,lm}(r)/\sin\theta\,\partial_\phi & h_{0\,lm}(r)\sin\theta\,\partial_\theta \\ * & 0 & -h_{1\,lm}(r)/\sin\theta\,\partial_\phi & h_{1\,lm}(r)\sin\theta\,\partial_\theta \\ * & * & 0 & 0 \\ * & * & * & 0 \end{pmatrix} Y_{lm}(\theta,\phi)\, e^{-i\omega t}\,, \tag{2.23}$$

$$h^{\rm polar}_{\mu\nu} = \sum_{lm} \begin{pmatrix} f(r)H_{0\,lm}(r) & H_{1\,lm}(r) & 0 & 0 \\ * & f(r)^{-1}H_{2\,lm}(r) & 0 & 0 \\ * & * & r^2 K_{lm}(r) & 0 \\ * & * & * & r^2\sin^2\theta K_{lm}(r) \end{pmatrix} \times \tag{2.24}$$

$$\times\, Y_{lm}(\theta,\phi)\, e^{-i\omega t}\,,$$

where the asterisk denotes the symmetric components of the metric. The metric perturbations $h_{\mu\nu}$ are split into an *axial* and a *polar* part (also commonly referred to as *odd* and *even*, respectively), according to their behavior under parity inversion (see Appendix A for a broader discussion). Furthermore, the static nature of the background geometry allows us to separate the time dependence of the perturbations, which can be expressed as a Fourier mode $e^{-i\omega t}$, so that the problem reduces to solving for the radial and angular components.

By inserting the perturbed metric of Eqs. (2.22)- (2.24) into the linearized Einstein's equations (2.21) one can decouple the axial from the polar perturbations and derive two single Schrödinger-like master differential equations.

Axial perturbations: Regge-Wheeler equations

The axial perturbations are governed by the so-called Regge-Wheeler master equation

$$\frac{d^2 Q_l}{dr_*^2} + [\omega^2 - V_l^{\rm axial}(r)]Q_l = 0\,, \tag{2.25}$$

with effective potential given by

$$V_l^{\rm axial}(r) = \left(1 - \frac{2M}{r}\right)\left[\frac{l(l+1)}{r^2} - \frac{6M}{r^3}\right]. \tag{2.26}$$

Polar perturbations: Zerilli equation

On the other hand the polar perturbations are given by solving the Zerilli master equation

$$\frac{d^2 Z_l}{dr_*^2} + [\omega^2 - V_l^{\rm polar}(r)]Z_l = 0\,, \tag{2.27}$$

whose potential is

$$V_l^{\rm polar}(r) = \left(1 - \frac{2M}{r}\right)\left[\frac{(l-1)(l+2)}{3}\left(\frac{1}{r^2} + \frac{2(l-1)(l+2)(l^2+l+1)}{(6M + r(l-1)(l+2))^2}\right)\right]. \tag{2.28}$$

The Regge-Wheeler (*axial*) and Zerilli (*polar*) gravitational potentials of Eq. (2.26) and Eq. (2.28) are plotted in Fig. 2.3 , together with the potential of scalar perturbations of Eq. (2.10) , for $l = 2$. As can be seen, the *axial* and *polar* potentials exhibit a very similar profile, despite their analytical expressions is different. This close resemble is not accidental, but reflects a remarkable property that characterizes the Regge-Wheeler and Zerilli equations. Indeed, Chandrasekhar proved that the two effective potentials can be recovered by [158]

$$V_l^{\text{polar, axial}}(r) = \pm 6M \frac{dh}{dr_*} + (6M)^2 h^2 + l(l+2)(l+1)(l-1)h\,, \tag{2.29}$$

where the plus and minus signs are for *polar* and *axial* cases, respectively, and we defined the function $h = h(r)$ as

$$h(r) \equiv \frac{1}{r}\left(1 - \frac{2M}{r}\right) \frac{1}{r(l-1)(l+2) + 6M}\,. \tag{2.30}$$

Such a connection has direct implications for the computation of QNMs in the *axial* and *polar* sectors, that reduces to solving an eigenvalue problem for Eq. (2.25) and Eq. (2.27) with appropriate boundary conditions. Indeed, the two QNM spectra coincide, giving rise to a peculiar property of GR known as *isospectrality* (for further details see [144, 159–161]).

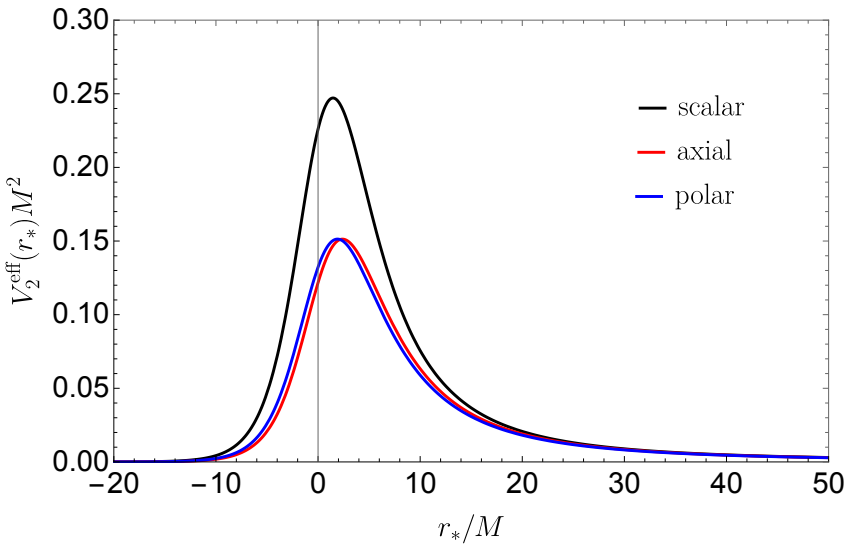

Figure 2.3. Effective potentials V_2^{eff} for scalar and gravitational field (*axial* and *polar*) perturbations on the background of the Schwarzschild BH, for $l = 2$.

It is noteworthy to mention that one can recast into a single unified form the Eq. (2.9) for scalar perturbations (for $s = 0$) and Eq. (2.25) for gravitational axial perturbations (for $s = \pm 2$), together with the equation describing electromagnetic (EM) perturbations (for $s = \pm 1$) on the background of the Schwarzschild BH [147]

$$\frac{d^2\Psi_s}{dr_*^2} + \left[\omega^2 - V_s(r)\right]\Psi_s = 0\,, \tag{2.31}$$

where the effective potential is

$$V_s(r) = \left(1 - \frac{2M}{r}\right)\left[\frac{l(l+1)}{r^2} + (1-s^2)\frac{2M}{r^3}\right] . \tag{2.32}$$

Although this master equation explicitly captures only the *axial* sector of gravitational perturbations, the existence of the Chandrasekhar transformation guarantees a correspondence with the *polar* sector, and therefore *isospectrality*. This property ensures that solving the eigenvalue problem for the axial perturbations is sufficient to determine the complete QNM spectrum of the Schwarzschild BH.

In four dimensions, the most general vacuum and asymptotically flat BH solutions is axisymmetric and is described by the Kerr spacetime [57]. However, when passing from the study of gravitational perturbations on the Schwarzschild BH to the Kerr background the situation becomes considerably more intricate. The axial-polar decomposition that greatly simplifies the non-rotating case no longer applies, since rotation breaks the spherical symmetry and the perturbations do not possesses a definite parity. The separability of the radial and angular dependence of scalar, electromagnetic and gravitational perturbations on the Kerr background was achieved by Teukolsky [157], using a decomposition in spin-weighted spheroidal harmonics and the Newman-Penrose formalism [156]. A remarkable consequence of the breaking of spherical symmetry is that the potential in this case depends both on the angular number l and the azimuthal number m.

2.3 Quasi-normal modes

As previously stated, the ringdown, which constitutes the final stage of the GW signal from a binary BH coalescence, corresponds to the perturbed remnant relaxing toward its stationary equilibrium state. Once the remnant has formed, after a transient, it reaches a quasi-stationary configuration in which it vibrates according to its characteristic modes, until it settles into the stationary (or static) state. Unlike other ideal physical systems that approach equilibrium through *normal modes*, like vibrating strings, a BH constitutes an open system, as its gravitational oscillations can either be absorbed by the event horizon or radiated away to infinity in the form of GWs detectable by interferometers. Therefore, the intrinsic oscillation modes are damped and for this reason are called *quasi-normal modes* (QNMs).

The issue of boundary conditions

The computation of the QNMs of a BH can be achieved in terms of the perturbative approach that we discussed in Sec. 2.2. In particular, within GR, the study of the BH QNM spectrum corresponds to solving a second-order ODE of the form of Eq. (2.31) for ω, subject to the boundary conditions appropriate to the problem at the horizon ($r_* \to -\infty$) and at infinity ($r_* \to +\infty$). In all BH spacetimes in GR, the gravitational effective potential $V \to 0$ at the inner boundary, namely the horizon for $r_* \to -\infty$. Therefore, in this limit the solution of the wave equation behaves like $\Psi \sim e^{-i\omega(t \pm r_*)}$. Since nothing can escape the pulling force of the BH once it crosses the horizon, only ingoing waves must be considered, therefore

$$\Psi \sim e^{-i\omega(t+r_*)} , \quad r_* \to -\infty . \tag{2.33}$$

Conversely, in an asymptotically flat BH spacetime, at spatial infinity the metric is given by the Minkowski metric. Also in this case the potential $V \to 0$ at the outer boundary, namely at spatial infinity for $r_* \to +\infty$. Since we are interested in the free oscillations of the final object we want to discard incoming waves from infinity, to select only

$$\Psi \sim e^{-i\omega(t-r_*)}\,, \qquad r_* \to +\infty\,. \tag{2.34}$$

2.3.1 QNMs as poles of the Green function

Computing the QNM spectrum of a perturbed BH reduces to the study of an eigenvalue problem with the mentioned boundary conditions, for a master wave equation of the following form

$$\frac{d^2\Psi}{dr_*^2} + (\omega^2 - V)\Psi = S(\omega, r)\,, \tag{2.35}$$

where we introduce $S(\omega, r)$ that represents the source inducing the perturbation. The Green functions method provides a standard framework for the computation of QNMs [162–166].

The homogeneous version of Eq. (2.35) has two linearly independent solutions, $\Psi_-(r)$ and $\Psi_+(r)$, whose boundary conditions are the following

$$\Psi_- \sim e^{-i\omega r_*}\,, \qquad (r_* \to -\infty) \tag{2.36}$$

$$\Psi_- \sim A_{\rm in}(\omega)e^{-i\omega r_*} + A_{\rm out}(\omega)e^{i\omega r_*}\,, \qquad (r_* \to +\infty) \tag{2.37}$$

$$\Psi_+ \sim B_{\rm in}(\omega)e^{-i\omega r_*} + B_{\rm out}(\omega)e^{i\omega r_*}\,, \qquad (r_* \to -\infty) \tag{2.38}$$

$$\Psi_+ \sim e^{i\omega r_*}\,, \qquad (r_* \to +\infty) \tag{2.39}$$

$$\tag{2.40}$$

where we introduce $A_{\rm in}(\omega)$, $A_{\rm out}(\omega)$ and $B_{\rm in}(\omega)$, $B_{\rm out}(\omega)$ as the amplitudes of ingoing and outgoing wave components for the two independent solutions Ψ_- and Ψ_+, respectively. Note that only the asymptotic behavior at the horizon of Ψ_- and at infinity of Ψ_+ provide the correct boundary conditions to identify the QNMs. The general solution of Eq. (2.35) is a combination of the two independent solutions as follows

$$\Psi(\omega, r) = \frac{\Psi_+}{W}\int_{-\infty}^{r_*} S(\omega, r)\Psi_- dr_* + \frac{\Psi_-}{W}\int_{r_*}^{+\infty} S(\omega, r)\Psi_+ dr_*\,, \tag{2.41}$$

where W is the Wronskian of the two wavefunctions, defined by

$$W = \Psi_-\frac{d\Psi_+}{dr} - \Psi_+\frac{d\Psi_-}{dr}\,. \tag{2.42}$$

Using the property that the Wronskian does not depend on r, i.e. $dW/dr = 0$, we can rewrite it in terms of the asymptotic behavior of the two independent solutions, namely $W = 2i\omega A_{\rm in}$.

Since the general solution $\Psi(\omega, r)$ in the frequency domain can be connected to the time domain solution $\Psi(t, r)$ via a Laplace transform

$$\Psi(\omega, r) = \int_0^{\infty} dt\, e^{i\omega t}\, \Psi(t, x)\,, \tag{2.43}$$

one can recover the $\Psi(t,x)$ via the inverse of the Laplace transform

$$\Psi(t,x) = \int_{-i\epsilon+\infty}^{i\epsilon+\infty} \frac{d\omega}{2\pi}\, e^{-i\omega t}\, \Psi(\omega, r)\,, \tag{2.44}$$

that represents an integral over a contour parallel to the real axis in the complex ω-plane, and displaced into the upper half plane with an infinitesimal ϵ, as depicted in Fig. 2.4. As can be seen from Fig. 2.4 , the contour is closed in the lower half plane of complex ω, namely for $\mathrm{Im}(\omega) < 0$, since for large $\mathrm{Im}(\omega) > 0$ the exponential $e^{-i\omega t}$ of the inverse Laplace transform diverges. Moreover, since the solution $\Psi_+(\omega, r)$ has a branch cut in the ω-complex plane [162, 166, 167], along the negative imaginary axis, we must go around this branch cut. The integral has therefore three distinct contributions: the poles inside the contour, the two quarter-circles at infinity, and the branch cut.

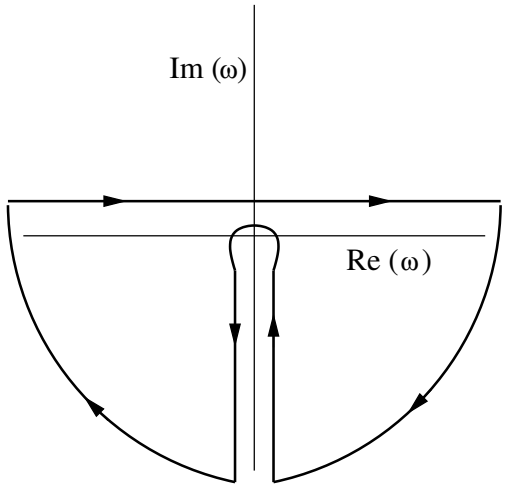

Figure 2.4. Integration contour in the complex ω-plane for Eq. (2.44). The contour is closed in the lower half plane and presents a branch cut for negative values of the imaginary part of ω [166]. The poles inside the contour are the characteristic QNMs of the background spacetime. The two quarter-circles contribute to the prompt signal (*precursor*). Finally, the branch cut gives rise to the *late-time tail* of the signal, which is dominated by the back scattering of waves off the spacetime curvature at large distances.

The poles inside the contour coincide with the zeros of the Wronskian W, and the sum over their residues represents exactly the set of QNMs. The poles indeed represent the perturbations that satisfy both the conditions of ingoing waves at the horizon and outgoing waves at spatial infinity, the boundary conditions defining the QNMs. Being damped modes, their frequency is complex

$$\omega_j = \omega_{R,j} + i\omega_{I,j}\,, \tag{2.45}$$

where $j = lmn$, $\omega_{R,j}$ is the real oscillation frequency of the mode, and $\omega_{I,j}$ is the damping rate. Since $\Psi \sim e^{-i\omega t}$, modes with $\omega_{I,j} < 0$ are damped, modes with $\omega_{I,j} > 0$ are unstable. One should highlight that they do not depend on the specific way the background geometry is perturbed. Thus, QNMs are completely determined

by the BH parameters and for this reason may constitute its fingerprints. Some of the most powerful techniques to practically compute the QNMs of a given BH will be discussed in the next section. In asymptotically flat spacetime and far from the source, the contributions from the QNM spectrum can be written as [164, 168]

$$\Psi(t,r) = -\mathrm{Re}\left[\sum_j C_j e^{-i\omega_j(t-r_*)}\right] , \tag{2.46}$$

where the index j identifies the poles in the complex plane. The coefficients C_j are called *quasi-normal excitation coefficients*, they are fixed by the initial data and measure the extent to which each QNM is excited in the waveform. They are related to the so-called *quasi-normal excitation factors* (QNEFs) B_j as follows

$$C_j = B_j \int_{-\infty}^{+\infty} \frac{S(\omega,r)\Psi_-}{A_{\mathrm{out}}} dr'_* , \tag{2.47}$$

with

$$B_j = \frac{A_{\mathrm{out}}}{2\omega}\left(\frac{dA_{\mathrm{in}}}{d\omega}\right)^{-1}_{\omega=\omega_j} . \tag{2.48}$$

The QNEFs only depend on the background geometry, and, together with the information of specific initial data (encoded by the source $S(\omega, r)$), they allow to determine the QNM content of the signal.

In the spectrum of BH QNMs not all modes contribute equally to the observed signal. The dominant excitation is given by the so-called *fundamental mode* ($n = 0$), which is the least damped and therefore the longest lived. Since quadrupolar radiation is the leading channel for GW emission, the quadrupolar mode with $l = m = 2$ dominates the ringdown. Higher overtones ($n > 0$) are typically suppressed because of their stronger damping. Moreover, subdominant modes such $(l, m) = (3, 3)$, $(2, 1)$ or $(4, 4)$ may also be excited depending on the mass ratio and spin of the binary, but their relative amplitudes are generally suppressed.

The contribution coming from the two quarter-circles would be the prompt response in flat space, namely in the limit in which the mass of the BH goes to zero [162]. In our case it represents waves propagating directly from the source to the observer at spatial infinity and we call it *precursor* signal [166].

The third and final contribution is provided by the branch cut and gives rise to *late-time tails* [162, 169], generated by back-scattering off the spacetime curvature at large distances, and as a consequence depend on the asymptotic behavior of the background.

Incompleteness of the QNM spectrum

The full response of the BH to a small perturbation is described by all these three distinct components. As a consequence, it is clear that the entire signal cannot be described solely in terms of the QNMs, as in Eq. (2.46). For this reason, QNMs are said not to form a complete set. This aspect is closely connected to the dissipative nature of perturbed BHs, which are intrinsically non-conservative systems. Indeed, unlike conservative systems where the equations of motion are Hermitian and the

eigenfunctions correspond to orthogonal normal modes forming a complete basis, the perturbation equations of BHs are intrinsically non-Hermitian. Further discussion of this issue can be found in [148] and references therein.

While the non-self-adjoint nature of the problem prevents QNMs from forming a complete basis, a linear superposition of damped sinusoids reproduces the waveform with high accuracy during the intermediate ringdown phase, as proved by simulations and observational evidence.

Beyond the linear regime: nonlinear QNMs

The discussion so far was limited to the linear regime of perturbations, where the QNMs arise as the intrinsic eigenmodes of the system. Nevertheless, studies on the limitations of the linear regime [170, 171] have motivated investigations into nonlinear effects, such as quadratic mode excitation. This family of higher order modes in perturbation theory has not only been studied extensively in recent years [172–177], but has also been extracted from nonlinear binary merger simulations [171, 178–181].

2.4 Computational methods for QNMS

As discussed in Sec. 2.3, the determination of the QNM spectrum of a BH spacetime requires solving an eigenvalue problem with appropriate boundary conditions. Over the years a large variety of analytical, semi-analytical and numerical techniques have been developed to tackle this problem, for which there is not a unique and straightforward procedure to apply. Depending on the background under consideration, whether it is a BH spacetime or the geometry of a more exotic object (which may require different boundary conditions), and on the specific form of the master equations to be solved, one method may turn out to be more useful than another. For this reason, each computational approach has its own range of applicability and inherent limitations.

In this section we focus on two widely used approaches, *direct integration* and the *continued fraction method*, which will also be employed in the context of the original work presented in this thesis.

2.4.1 Direct integration

One of the most powerful techniques for the computation of the QNMs is the so-called *direct integration shooting* method (see [153, 182–185] for some applications). Being conceptually simple, this method is straightforward to implement numerically. Moreover, since it does not rely on any special properties of the effective potential in the perturbation equations, it can be applied to a wide range of backgrounds, including ECOs, modified gravity theories, and even systems governed by coupled equations. It typically provides accurate results for the fundamental QNM and sometimes the first few overtones, especially when the imaginary part of the frequency is not too large compared to the real part. Its application is usually demanded for scenarios in which it is not possible to get a single master equation for the perturbation, as in Eq. (2.31). When dealing with modified theories of gravity or

with ECOs, one frequently encounters systems of coupled second-order differential equations. For this reason let us consider a system of N second order ODEs for N perturbation functions that can be written together in an N-dimensional vector $\mathbf{\Psi} = (\Psi^{(1)}, \dots, \Psi^{(N)})$

$$\frac{d^2\mathbf{\Psi}}{dr_*^2} + [\omega^2 - \hat{\mathbf{V}}(r)]\mathbf{\Psi} = 0\,, \tag{2.49}$$

where $\hat{\mathbf{V}}(r)$ is an N × N matrix depending on r [1] . We can expand the array of perturbations near the horizon (or more generally the inner boundary $r_{\rm in}$) as follows

$$\Psi^{(j)} \sim (r - r_{\rm in})^{\lambda} \sum_{i=0}^{N_{\rm in}} \Psi^{(j)}_{{\rm in},i} (r - r_{\rm in})^i\,, \tag{2.51}$$

where $N_{\rm in}$ is the order of the series expansion. By solving the perturbation equations with the ansatz of the Frobenius series of Eq. (2.51) we get the exponent λ and the expansion coefficients $\Psi^{(j)}_{{\rm in},i}$ with $i > 0$ in terms of $\Psi^{(j)}_{{\rm in},0}$. Since the perturbation equations are linear, without loss of generality we can choose an orthogonal basis of unit vectors for the N-dimensional space

$$\begin{aligned}
\Psi^{(1)}_{{\rm in},0} &= (1, 0, 0, \dots, 0)\,,\\
\Psi^{(2)}_{{\rm in},0} &= (0, 1, 0, \dots, 0)\,,\\
&\vdots\\
\Psi^{({\rm N})}_{{\rm in},0} &= (0, 0, 0, \dots, 1)\,.
\end{aligned}$$

At infinity the solutions are given by a linear combination of ingoing ($e^{-i\omega r}$) and outgoing ($e^{i\omega r}$) waves, whose amplitudes can be written in terms of an expansion in $1/r$ as follows

$$\Psi^{(j)} \sim \left(B^{(j)}(\omega) + \sum_{k=1}^{N_\infty} \Psi^{{\rm ing},(j)}_{\infty,k} \frac{1}{r^k}\right) e^{-i\omega r}\, r^{\bar{\lambda}} + \left(C^{(j)}(\omega) + \sum_{k=1}^{N_\infty} \Psi^{{\rm out},(j)}_{\infty,k} \frac{1}{r^k}\right) e^{i\omega r}\, r^{-\bar{\lambda}}\,, \tag{2.52}$$

where $\Psi^{{\rm ing},(j)}_{\infty,k}$ and $\Psi^{{\rm out},(j)}_{\infty,k}$ are the expansion coefficients for ingoing and outgoing waves, respectively, while $B^{(j)}(\omega)$ and $C^{(j)}(\omega)$ are the leading order of the amplitudes. By solving order by order the perturbation equations at infinity, independently for the ingoing and the outgoing waves, we get the exponent $\bar{\lambda}$, the coefficients $\Psi^{{\rm ing},(j)}_{\infty,k}$ in terms of $B^{(j)}(\omega)$ and $\Psi^{{\rm out},(j)}_{\infty,k}$ in terms of $C^{(j)}(\omega)$. N_∞ is the order of the series expansion at spatial infinity.

We can then use the boundary conditions of Eq. (2.51) to perform N integrations from the inner boundary to infinity, at an arbitrarily large distance. The perturbation

[1] The direct integration technique described in this section can be straightforwardly applied also to more general systems of the form

$$\left(\frac{d^2}{dr^2} + \frac{d}{dr} + \hat{\mathbf{V}}(\omega, r)\right)\mathbf{\Psi} = 0\,, \tag{2.50}$$

where now $\hat{\mathbf{V}}(\omega, r)$ depends both on r and ω.

equation can be numerically integrated from a point near the inner boundary $\bar{r}_{\rm in} = r_{\rm in}(1+\epsilon)$, with $\epsilon \ll 1$ to avoid numerical divergences. We can now construct the following N × N matrix

$$\hat{\mathbf{S}}_{\rm QNM}(\omega) = \begin{pmatrix} B_1^{(1)} & B_1^{(2)} & \dots & B_1^{(\rm N)} \\ B_2^{(1)} & B_2^{(2)} & \dots & B_2^{(\rm N)} \\ \dots & \dots & \dots & \dots \\ \dots & \dots & \dots & \dots \\ B_{\rm N}^{(1)} & B_{\rm N}^{(2)} & \dots & B_{\rm N}^{(\rm N)} \end{pmatrix} . \tag{2.53}$$

In order to find the QNMs we need to impose the boundary condition of only outgoing waves at infinity, that in this case is fulfilled by requiring $\det \hat{\mathbf{S}}_{\rm QNM}(\omega) = 0$. Since the matrix $\hat{\mathbf{S}}_{\rm QNM}(\omega)$ is constructed with complex functions of ω, namely $B_k^{(j)} = B_k^{(j)}(\omega)$ (with $k, j = 1, \dots, \rm N$), imposing $\det \hat{\mathbf{S}}_{\rm QNM}(\omega) = 0$ is achieved through a shooting procedure in the complex ω plane providing a guess $\omega_{\rm guess}$ to start with.

In the case of massive perturbations with mass μ, the potential does not vanish at spatial infinity (as instead occurs for massless scalar and gravitational perturbations in Fig. 2.2 and Fig. 2.3), but instead the components of the matrix-valued effective potential $\hat{\mathbf{V}}(r)$ asymptotically behave as $V_{ij} \to \mu^2 \delta_{ij}$. As a consequence the ω in the expansion at infinity of Eq. (2.52) must be replaced by $k_\infty = \sqrt{\mu^2 - \omega^2}$. In this scenario the boundary condition at infinity of pure ingoing waves has a physical motivation since it defines *quasi-bound states* (QBSs): states that live close to the BH and decay exponentially at spatial infinity [184, 186]. In order to compute them one can construct the following N × N matrix

$$\hat{\mathbf{S}}_{\rm QBS}(\omega) = \begin{pmatrix} C_1^{(1)} & C_1^{(2)} & \dots & C_1^{(\rm N)} \\ C_2^{(1)} & C_2^{(2)} & \dots & C_2^{(\rm N)} \\ \dots & \dots & \dots & \dots \\ \dots & \dots & \dots & \dots \\ C_{\rm N}^{(1)} & C_{\rm N}^{(2)} & \dots & C_{\rm N}^{(\rm N)} \end{pmatrix} , \tag{2.54}$$

and ask for the condition $\det \hat{\mathbf{S}}_{\rm QBS}(\omega) = 0$ to be fulfilled.

The main limitation of the direct integration method is its susceptibility to numerical errors in certain scenarios. Indeed QNMs are characterized by a negative imaginary part $\omega_I < 0$ to guarantee stability, that generates a spatial divergence in the spatial part of the outgoing wave, i.e. $e^{i\omega r} = e^{i\omega_R r} e^{-\omega_I r}$, with $e^{-\omega_I r} \to \infty$ for $r \to +\infty$. Although this divergent behavior is not physical, since in the time domain it is compensated by the exponential factor $e^{-i\omega t}$, it can nevertheless cause difficulties in the numerical integration, particularly in those cases in which $\omega_R/|\omega_I| \sim \mathcal{O}(1)$. A way to prevent such problems is to use an high order of the expansion at infinity N_∞ to reduce truncation errors, and consider moderately large values for numerical infinity.

For the reasons mentioned above, the direct integration method is not well suited to compute QNMs with very short timescales, or in other words those that are strongly damped. Therefore its applicability is limited when it comes to identifying higher overtones. Conversely, this method proves especially effective in the computation of long-lived QNMs, as will be discussed later.

2.4.2 Continued fraction method

The *continued fraction* (or Leaver) method is generally considered as the most accurate algorithm for the computation of QNMs. It has been developed by Leaver [145] and it is ideal for effective potentials that contain only (fractions of) powers of $1/r$. The idea is to find a guess for the eigenfunction that simultaneously capture the behavior both at the inner boundary and at spatial infinity. Moreover, this ansatz must involve a function that vanishes at the inner boundary, which can be expressed as a series expansion. By substituting this ansatz into the perturbation equation, one derives a finite-term recurrence relation for the series coefficients. The method was originally developed for solving single equations but it has been generalized to handle systems of coupled equations [184, 187]. Following [153], in this section we present the method generalized to a system of differential equations.

Let us consider the case in which the background geometry possess a single horizon at r_H. In this case we can consider the following ansatz

$$\Psi^{(j)} \sim e^{-i\omega r_*}\, r^{-\nu} e^{kr} \sum_{n=0}^{N_{\rm CF}} a_n^{(j)} F(r)^n \,, \tag{2.55}$$

where ν depends on the studied background, the function $F(r) \sim (r - r_H)$ has to vanish at the horizon (i.e. $F(r_H) = 0$), and the exponent $k = \pm\sqrt{\mu^2 - \omega^2}$. The sign of the exponent k defines the boundary condition at infinity: for $k > 0$ we find the QNMs, while for $k < 0$ we search for the quasi-bound states. $N_{\rm CF}$ represents the order of the expansion. Inserting the ansatz into the system of Eq. (2.49) we get a finite-term matrix-valued recurrence relation for the vectors $\mathbf{a}_n = (a_n^{(1)}, \ldots, a_n^{(\rm N)})$. In the simplest case it is a three-term recurrence relation, however, any higher order recurrence relation can be reduced via Gaussian elimination techniques [147]. The three-term matrix-valued recurrence relation has the following form

$$\boldsymbol{\alpha}_0 \mathbf{a}_1 + \boldsymbol{\beta}_0 \mathbf{a}_0 = 0 \qquad n = 0 \,, \tag{2.56}$$

$$\boldsymbol{\alpha}_n \mathbf{a}_{n+1} + \boldsymbol{\beta}_n \mathbf{a_n} + \boldsymbol{\gamma}_n \mathbf{a}_{n-1} = 0 \quad n > 0 \,, \tag{2.57}$$

where $\boldsymbol{\alpha}_n$, $\boldsymbol{\beta}_n$ and $\boldsymbol{\gamma}_n$ are non-diagonal matrices for the system of coupled equations.

In order to solve the three-term recurrence relation let us define a ladder matrix operator R_n^+ as follows

$$\mathbf{a}_{n+1} = \mathbf{R}_n^+ \mathbf{a}_n \,. \tag{2.58}$$

By making use of Eq. (2.57) we can get the following expression for the ladder matrix

$$\mathbf{R}_n^+ = -[\boldsymbol{\beta}_{n+1} + \boldsymbol{\alpha}_{n+1}\mathbf{R}_{n+1}^+]^{-1}\boldsymbol{\gamma}_{n+1} \,. \tag{2.59}$$

By making use of Eq. (2.56), solving the recurrence relation reduces to searching the roots of

$$\mathbf{M}\, a_0 = 0 \,, \tag{2.60}$$

with

$$\mathbf{M} \equiv \boldsymbol{\beta}_0 - \boldsymbol{\alpha}_0[\boldsymbol{\beta}_1 - \boldsymbol{\alpha}_1(\boldsymbol{\beta}_2 + \boldsymbol{\alpha}_2\mathbf{R}_2^+)\boldsymbol{\gamma}_2]^{-1}\boldsymbol{\gamma}_1 \,, \tag{2.61}$$

where $\mathbf{R}_2^+$ can be obtained by Eq. (2.59). More specifically, one choose a large enough order expansion $N_{\rm CF}$ and defines arbitrarily the ladder matrix $\mathbf{R}_{N_{\rm CF}}^+$. The

other matrices, $\mathbf{R}^{+}_{N_{\rm CF}-1}$, $\mathbf{R}^{+}_{N_{\rm CF}-2}$, ..., $\mathbf{R}^{+}_{2}$, are determined using Eq. (2.59). In order to find the frequencies of the modes we require the determinant of $\mathbf{M}$ to vanish

$$\det \mathbf{M} = 0\,. \tag{2.62}$$

The continued fraction method turns out to be extremely efficient and accurate since it converges rapidly and allows the calculation of QNMs with very high precision. Moreover, unlike direct integration, it works reliably for very damped modes.

2.5 Phenomenology of ECOs in the ringdown

The central role of BHs as astrophysical objects living in our universe and their unique place in gravitational physics has been increasingly confirmed over the past years by multiple observational confirmations. Starting from the detection of numerous GW events [2–6], and including the electromagnetic observations of the accretion disks around M87 and Sagittarius A* [9, 10], the Kerr hypothesis [15, 16], according to which any sufficiently compact and isolated object is described by the Kerr geometry, has been strongly supported.

The LVK Collaboration recently performed the first robust spectroscopy test using the exceptional GW250114 event [188, 189], the loudest GW detected to date. The dominant quadrupolar $lm = 22$ mode of GW250114 has been measured with great accuracy, with uncertainties of about 6% in its real part and 10% in its imaginary part. Moreover, they measured the first overtone with an accuracy of approximately 30%. These results represent the most stringent single event confirmation to date of the Kerr nature of astrophysical BHs.

Nevertheless, the gravity and quantum gravity communities have devoted considerable effort to investigating models of compact objects that might evade the BH description. Many models of exotic compact objects (ECOs) have been explored over the last years as possible alternatives or extensions to classical BHs [22]. Examples include boson stars, gravastars, and wormholes, as well as more string-inspired constructions such as the aforementioned Fuzzballs.

In what follows we review their phenomenology in the ringdown phase: first recalling general properties of ECOs, then discussing the emergence of long-lived modes and echoes, and finally connecting to the case of microstate geometries.

2.5.1 Exotic compact objects

ECOs are compact objects without an event horizon that deviate from the BH description predicted by GR. They may be motivated by quantum gravity theories [190–193] or allowed by the inclusion of exotic matter content in GR [194–196]. Among the most notable and mentioned ones we can recall *gravastars* [197, 198], *boson stars* [199–202], *wormholes* [203–205], Fuzzballs and microstate geometries (see Chapter 1), and many other examples [206–209]. Because of their extreme compactness [22], ECOs can reproduce much of the dynamics and observational appearance of BHs. Since for a distant observer their electromagnetic features and the gravitational field are indistinguishable from those of a BH, they are also commonly dubbed *BH mimickers*. As such they can either serve as alternatives to

BHs, effectively replacing them, or coexist with them as a broader class of compact objects in the universe.

In the following, we highlight a few of the most representative examples.

Gravastars

"Gravitational-vacuum stars", commonly referred to as *gravastars* [197, 198] are ECOs supported by a negative pressure [210, 211], which can be interpreted as the effective outcome of one-loop QFT corrections in curved spacetime, thereby avoiding the need for exotic matter. Since the negative pressure violates some energy conditions, and because the internal effective fluid is anisotropic [212], gravastars evade the Buchdahl limit [213]. Depending on their specific construction and on the model describing the negative pressure, gravastars belong to a broad class of objects with arbitrary compactness. The original gravastar construction has five layers: an internal de Sitter core, a thin shell separating it from a perfect-fluid region, and finally another thin-shell that connects to the external Schwarzschild geometry. A simple construction, dubbed thin-shell gravastar [210], is instead given by a de Sitter core connected to the Schwarzschild exterior via a thin-shell of perfect fluid. The formation channel is represented by gravitational collapse undergoing a quantum gravitational vacuum phase transition to prevent the formation of the horizon. The gravastar is free of singularities and no information paradox is present.

Boson stars

When one considers a massive scalar field minimally coupled to gravity, it is possible to obtain a self-gravitating compact object called *boson star* [194, 214, 215]. The action of the theory is given by

$$S = \int d^4x\sqrt{-g}\left(\frac{R}{16\pi} + \mathcal{L}_M\right) , \tag{2.63}$$

where the matter Lagrangian $\mathcal{L}_M$ of the scalar field Φ is

$$\mathcal{L}_M = -\frac{1}{2}\left[g^{\mu\nu}\nabla_\mu\Phi^*\nabla_\nu\Phi + V(|\Phi|^2)\right] , \tag{2.64}$$

where $V(|\Phi|^2)$ is the potential of the scalar field. If in GR a crucial property of BHs is that the mass is a free parameter, for boson stars it has a maximum value, depending on the mass μ of the bosonic scalar field and by its potential. Their formation has been widely studied because they can be the end-state of the gravitational collapse in presence of this extra scalar field [216, 217]. If the latter is complex the boson star is a static spherically symmetric solution [200, 201], otherwise, if it is real, the solution is an oscillating geometry called "oscillaton" [202]. Over the last years the stability and the binary coalescence of boson stars have been deeply studied [218–220].

Wormholes

Wormholes were originally introduced by Einstein and Rosen [203] to describe particles. They can be constructed by connecting two spacetime regions that are usually static, spherically symmetric and asymptotically flat [204, 221]. The region

connecting the two spacetimes is the throat. If the two asymptotically flat spacetime can be solutions of vacuum Einstein's equations, the throat, where the connection occurs, requires a thin shell of matter with negative energy density that violates the energy conditions. Nevertheless, some studies on how to construct wormholes that do no violate the energy conditions have been conducted [221–224].

The simplest wormhole construction is given by two Schwarzschild solutions of mass M with metric

$$ds^2 = -\left(1-\frac{2M}{r}\right)dt^2 + \left(1-\frac{2M}{r}\right)^{-1}dr^2 + r^2 d\Omega_2^2 \tag{2.65}$$

glued at a fixed distance $r_0 > 2M$. The radial coordinate of the full spacetime is given by the tortoise coordinate r_*, defined by $dr/dr_* = \pm(1-2M/r)$, with positive and negative sign associated to the two glued regions. By properly fixing the integration constant we set $r_*(r_0) = 0$, in such a way that one spacetime region is described by $r_* > 0$, while the other one by $r_* < 0$. The connection is allowed by a thin shell of matter with surface density σ and surface pressure ρ respectively given by

$$\sigma = -\frac{1}{2\pi r_0}\sqrt{1-\frac{2M}{r_0}}\,, \qquad p = \frac{1}{4\pi r_0}\frac{1-M/r_0}{\sqrt{1-\frac{2M}{r_0}}}\,. \tag{2.66}$$

Even though in general wormholes are linearly unstable [225–228], they can be characterized by an arbitrary mass and compactness.

2.5.2 Ringdown features and echoes

Due to the lack of an event horizon and to the presence of a reflective surface, the ringdown stage of an ECO departs in several key aspects from the standard BH case in GR. The QNM spectrum, which is typically used to model this part of the signal, can deviate substantially (depending on the specific ECO) from the BH case. Computing the QNMs of ECOs therefore provides a quantitative estimate of these deviations and, as a consequence, offers a way to constrain the possible absence of an event horizon in the merger remnant. In ECOs, the characteristic property of isospectrality that is present in GR is broken, or, in other words, the axial and polar sector of QNMs receive different corrections to the BH case. The absence of a horizon modifies the boundary conditions, allowing for the appearance of additional families of modes. In particular they can be associated either with internal structure (as in gravastars or wormholes) or with extra degrees of freedom arising in modified theories of gravity.

Following [22], a spherically symmetric ECO that mimics a BH of mass M can be modeled as having a reflective surface located at a fixed radial distance

$$r_0 = 2M(1+\epsilon)\,, \tag{2.67}$$

which replaces the event horizon at $r_H = 2M$. The quantity ϵ is commonly dubbed "closeness" parameter, and it measures how close one is to the BH spacetime (whose limit is $\epsilon \to 0$). As a consequence, when computing the QNM spectrum the boundary conditions differ from those of the BH case, and one must impose (for instance)

Dirichlet or Neumann conditions at the surface, which completely alters the spectrum. In particular, in the $\epsilon \to 0$, low-frequency limit the modes read [229–231]

$$M\omega_R \simeq -\frac{M\pi}{2|z_0|}\left(q+\frac{s(s+1)}{2}\right) \sim |\log\epsilon|^{-1}\,, \tag{2.68}$$

$$M\omega_I \simeq -\beta_{ls}\frac{M}{|z_0|}(2M\omega_R)^{2l+2} \sim -|\log\epsilon|^{-2l+3} \tag{2.69}$$

where $z_0 \equiv z(r_0) \sim 2M\log\epsilon$, with z being the tortoise coordinate defined by

$$z = r + 2M\log\left(\frac{r}{2M}-1\right)\,, \tag{2.70}$$

q is a positive even (odd) integer for polar (axial) modes, s is the spin of the perturbation ($s = 0, \pm 1, \pm 2$ for scalar, vector and axial tensor modes, respectively), and finally

$$\beta_{ls} = \left(\frac{(l-s)!(l+s)!}{(2l)!(2l+1)!!}\right)^2\,, \tag{2.71}$$

from [231, 232]. The first feature that emerges is the aforementioned breaking of isospectrality. Moreover, the frequencies of this modes are much less damped, depending on how small the closeness parameter ϵ is. This is an expected consequence of the dissipation channel provided by the horizon in the BH case. By studying the effective potential one can explain these *long-lived* (small damping rate) frequencies as trapped modes between the reflective inner boundary and the peak of the potential at $r \sim 3M$ [28, 231, 233–235]. As shown in Fig. 2.5, although both the Schwarzschild BH and a horizonless ECO share the same boundary condition at spatial infinity (purely outgoing waves), since their asymptotic geometry is identical, they differ at the inner boundary. In the BH case, one imposes purely ingoing waves at the horizon, whereas for an ECO this condition is replaced by a reflective surface located just outside the would-be horizon. The presence of this surface, together with the potential barrier associated with the photon sphere, creates an effective cavity. Within such a cavity, low-frequency modes with a wavelength comparable to the cavity size ($\omega_R \sim 1/z_0$) can become trapped. Eventually they can leak out, tunneling through the potential barrier and reach infinity, thus becoming long-lived modes with a small imaginary part of the frequency. Remaining in the low-frequency limit, their tunneling probability can be computed and is given by $|\mathcal{A}|^2 \sim (M\omega_R)^{2l+2} \ll 1$ [232]. By considering that after a time t the modes trapped inside of the cavity of size z_0 get reflected $N = t/z_0$ times, their amplitude is modulated as follows

$$A(t) \sim (1-|\mathcal{A}|^2)^N \sim (1-t|\mathcal{A}|^2/z_0). \tag{2.72}$$

The amplitude is also damped in time as follows

$$A(t) \sim e^{\omega_I t} \sim (1+\omega_I t)\,, \tag{2.73}$$

with $\omega_I < 0$. Therefore we obtain

$$\omega_R \sim \frac{1}{z_0}\,, \qquad\qquad \omega_I \sim \frac{|\mathcal{A}|^2}{z_0} \sim \omega_R^{2l+3}\,. \tag{2.74}$$

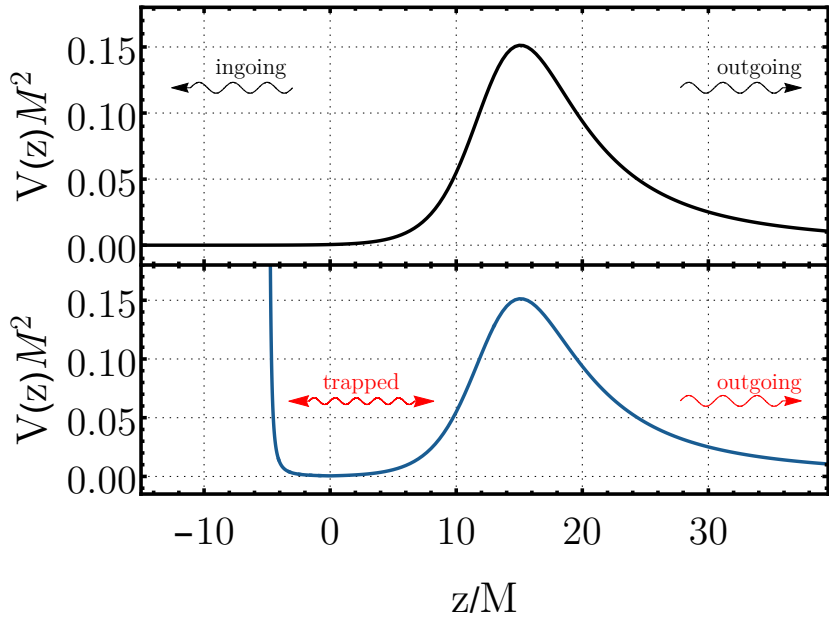

Figure 2.5. Effective potentials for perturbations on the Schwarzschild BH background (top panel) and an ECO without the horizon (bottom panel) [22]. Both potentials are characterized by a maximum that in the eikonal limit ($l \to +\infty$) coincide with the position of the unstable photon sphere at $r = 3M$ for the Schwarzschild BH.

In the case of BHs the QNMs are connected to excitations of the photon sphere [236–238]. These modes can either propagate toward the horizon and be absorbed by the BH, or travel outward to the observer at infinity. As a consequence the ringdown signal of a BH in the intermediate time is dominated by the QNMs that are generated at the unstable photon sphere. Conversely, for compact enough ECOs the response to perturbations is different. As shown in Fig. 2.6, after a prompt response associated to the modes produces at the photon sphere, that is identical to the BH case, at later time the modes traveling towards the inner boundary get reflected by it. After the reflection they are quasi-trapped by the cavity of the potential and after each interaction with the photon sphere they can leak out producing a series of repeated pulses in the signal that are commonly dubbed as *echoes*. Echoes are separated by a fixed delay time given by

$$\tau_{\text{echo}} \sim 4M|\log\epsilon|\,, \tag{2.75}$$

and after the first pulse each subsequent echo has a smaller amplitude than the previous one. Therefore, while in ECOs the early part of the ringdown signal is identical to that of a BH, being dominated by high-frequency modes generated at the photon sphere and scattered back to the observer, the late-time behavior displays a distinctive echo pattern, which can be regarded as a powerful smoking gun of horizonless ECOs. Repeated echoes are a characteristic feature of many ECOs and, as we will see in the next section, Fuzzballs provide a particularly notable example.

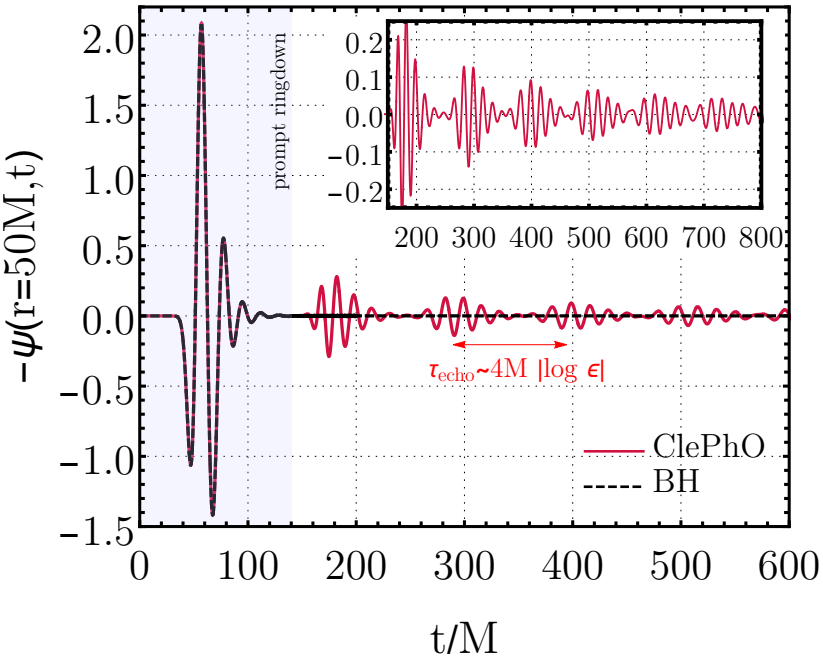

Figure 2.6. Comparison between the ringdown waveforms of a BH (dashed black line) and of an ultra-compact (ClePhO, see [22] for more details) ECO. The initial part of the signal is the same in both cases, whereas at late times the ECO case deviates exhibiting repeated GW echoes. [22].

2.5.3 Microstate geometries as ECOs

Among the wide zoo of ECO models, Fuzzballs stand out as the only class of objects explicitly constructed in string theory, and therefore, as a top-down approach, they represent the most concrete realization of horizon-scale structure. Owing to the absence of an event horizon, Fuzzballs are expected to exhibit the same phenomenology common to other ECOs, namely deviations in their QNM spectrum, the presence of long-lived modes, and the appearance of echoes in the late-time ringdown signal. As we will see in the following chapters, simplified effective models provide a powerful framework to explore the observational consequences of microstate geometries and constitute a central part of the work developed in this thesis.

These expectations were recently substantiated by a detailed numerical study of scalar perturbations on explicit Fuzzball microstate geometries [123]. The analysis revealed that the early part of the signal is essentially indistinguishable from the BH case, being dominated by the photon sphere modes. However, at later times the response shows a clear sequence of echoes, in full analogy with the generic phenomenology of ECOs discussed above. This result provides the first explicit demonstration that Fuzzball microstates can naturally produce echo signals, thereby strengthening their role as concrete realizations of horizonless ECOs with potentially observable signatures in the ringdown phase of GWs.

At present, this remains the only study of perturbations on explicit Fuzzball backgrounds. Given the complexity and lack of symmetries of microstate geometries, further progress in their direct analysis is extremely challenging. For this reason, it

is useful to rely on simplified toy models that capture the essential phenomenological features of Fuzzballs, such as cavities in the effective potential, long lived modes, and echoes, and can thus serve as effective proxies.

Chapter 3

Extreme Mass-Ratio Inspirals

The future space-based interferometer LISA [52], planned to be launched in 2035, represents a promising experiment for BH physics at the horizon scale and possible deviations from the GR picture. This GW detector will access frequency bands much lower than those of ground-based detectors, making it the most suitable instrument to detect and study EMRIs. Extreme mass-ratio inspirals (EMRIs) are highly asymmetric binaries that occur when a stellar-mass compact object spirals into a much heavier compact object located at the center of a galaxy. Because of this extreme asymmetry, EMRIs provide one of the most promising testbeds to probe the phenomenology of ECOs, as the small companion effectively scans the near-horizon spacetime region of the central body over many orbital cycles.

In this section we will introduce EMRIs, outlining their main features and their relevance as GWs sources for future space-based detectors, before turning to their phenomenology in the context of ECOs.

3.1 Introduction to EMRIs

EMRIs consist of binary systems of compact objects characterized by orders of magnitude difference in their masses. Within GR, the primary object, a (super)massive compact object of mass M, is typically assumed to be a Kerr BH, placed at the center of a galaxy. The less massive compact object, referred to as the secondary and typically of stellar mass m, orbits around the primary until the final plunge.

Such phenomenologically interesting systems can form because (super)massive BHs are in general surrounded by a nuclear star cluster. Therefore it may happen that a stellar compact object is captured by this cluster and starts to spiral around the primary, defining, in the most general case, inclined and eccentric orbits [239, 240]. The more compact objects there are in the nuclear star cluster distribution the higher the probability to form an EMRI will be. Another proposed formation channel comes from the tidal disruption of binaries around a massive BH [241]. According to this idea, one of the binary components, after it is tidally disrupted, gets captured on a bound orbit around the massive BH. Conversely, the other component of the binary is ejected away.

The usual mass ratio of EMRIs, defined as $q = m/M \ll 1$, belongs to the range $10^{-6} \leq q \leq 10^{-4}$, and due to this asymmetry the dynamics of the evolution

and the details of the emitted GWs are highly complex. Fig. 3.1 shows a pictorial

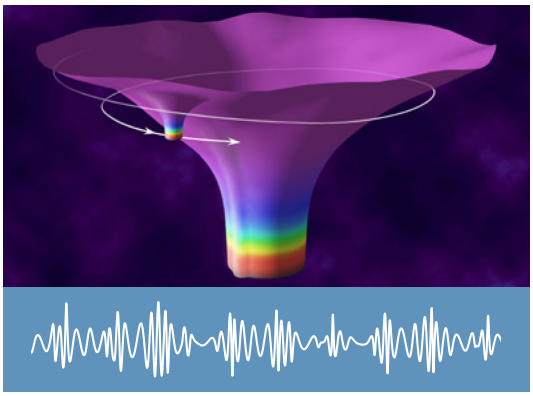

Figure 3.1. Pictorial impression of the spacetime of an EMRI, together with the expected waveform of the emitted GW (NASA and [242]).

representation of an EMRI with the associated typical waveform of the GW. As a binary system, the GW is emitted as the system loses energy and angular momentum during the inspiral. However, because of the huge difference in the involved masses, in the last year of inspiral preceding the plunge, the stellar mass object may complete up to 10^5 orbital cycles, much more than a typical binary with comparable masses. Notably, most of these cycles take place when the secondary is very close to the primary, where the gravitational interaction lies in the strong-field regime [243].

Another important consequence of the big mass asymmetry is given by the typical frequencies of GWs emitted by EMRIs. The latter, indeed, represent one of the main sources of gravitational radiation belonging to the low-frequency band, between 10^{-4}Hz and 1Hz. Such low-frequency waves make the ground-based detectors of the LVK Collaboration unsuitable for probing the existence and population of EMRIs, since this part of the spectrum is strongly affected by Newtonian noise. On the contrary, space-based interferometers like LISA, for which EMRIs are one of the target sources, are able to provide valuable scientific data. In particular, LISA will be able to detect from a few to a few thousand (according to the most optimistic projections) events per year [244]. Moreover, it will be possible to make very precise estimates of the physical parameters, particularly of intrinsic parameters like the redshifted masses, the spin of the primary and the eccentricity.

Other notable promising experiments that will be able to probe the GWs emitted by EMRIs are the future space-based interferometers TianQin [245] and Taiji [246].

3.2 Perturbative treatment

The standard framework for studying asymmetric binaries, and EMRIs in particular, is relativistic perturbation theory, formulated as an expansion in the small mass ratio $q \ll 1$ of the binary [247]. It is exactly the smallness of the mass ratio q that allows us to study the first order approximation, that ignore the internal structure of the secondary and describes it as a point particle spiraling around the primary and moving in its background spacetime. In this approximation, the stellar-mass object

is modeled as an energy–momentum distribution moving along a timelike curve and characterized by its physical parameters (mass, spin, etc.). The orbit evolves adiabatically considering a sequence of geodesics. If the *adiabatic* approximation is useful to tackle the problem of the EMRI dynamics in a simple way, in order to provide accurate waveforms modeling for the LISA data analysis the next order of the approximation is necessary. At the next order the finite structure of the secondary is taken into account, together with the interaction with its own perturbation, the *self-force* [247–252]. The self-force approach is nowadays considered the best way to model the EMRI dynamics and can be described as follows. The spacetime geometry produced by the EMRI system is given by the metric of the primary object, plus the perturbations generated by the motion of the secondary, that in the simplest picture can still be considered as a point-particle. The perturbations of the spacetime will affect the motion of the secondary itself, through gravitational backreaction. This backreaction acts as a force vector, known as the self-force, which drives the motion of the secondary away from the geodesic dictated by the background spacetime of the primary. This backreaction effect has to be computed at each perturbative order, giving the corrected gravitational waveform at the next order.

3.3 Phenomenology of ECOs in EMRIs

If we move beyond the standard EMRI scenario, where these asymmetric systems are composed solely of compact objects predicted by GR, we can instead consider the possibility that ECOs form the central body in EMRIs.

Depending on the nature of the ECO, there are several ways in which the GW signal produced by an exotic EMRI can deviate from the standard scenario. In the latter case indeed, the primary, being a Kerr BH, in the most general case, constitutes a dissipative object: the loss of energy and angular momentum of the system does not occur only through gravitational radiation reaching the distant observer, but also by BH absorption via the horizon. Such a process takes the name of *tidal heating* [253–255]. When the primary is replaced by an ECO, that does not possesses a horizon but a (partially) reflective surface, the dissipation channel represented by absorption across the inner boundary is weakened or totally absent. In the most extreme case of total reflection by the inner boundary, the secondary performs many more cycles during the spiraling, bringing additional phase to the emitted GW. The dephasing between the GW produced by a standard EMRI and the one where the primary is replaced by a horizonless ECO can be detectable and would allow us to distinguish between the two cases [48, 49, 256, 257].

Another interesting phenomenological property of EMRIs with ECOs regards the possibility of the secondary of exciting the QNMs of the primary object [44, 45, 47, 48]. If we consider the ideal case of circular orbit, with zero eccentricity, it is possible that the compact object spiraling around the primary excites its QNMs whenever the following condition is satisfied

$$\omega_R = m\Omega\,, \tag{3.1}$$

where ω_R is the real part of the complex frequency of the QNM, Ω is the orbital frequency of the secondary, while m is the azimuthal number. In GR, when the

primary is a Kerr BH, such excitation never occurs: the real frequency of the fundamental QNM of a Kerr BH is always higher than the orbital frequency $\Omega_{\rm ISCO}$ at the innermost stable circular orbit. Since this represents the circular orbit with the highest possible orbital frequency, no resonant coupling between the orbital motion and the QNM spectrum of the primary can take place. This result also applies to all the other BHs within GR. For ECOs, on the other hand, the situation is different. As discussed in Sec. 2.5, the absence of an event horizon allows for the formation of an effective cavity that can sustain long-lived modes. These long-lived modes are also characterized by a small real part of the frequency and can therefore fall within the range of orbital frequencies spanned during the inspiral. This makes resonant excitation possible, in stark contrast with the BH case in GR. The presence of such a resonance has direct consequences for the emitted energy flux. When the orbital frequency approaches that of a long-lived mode of the ECO, the mode can be resonantly excited, producing a sharp peak in the flux. Such a peak would eventually lead to a significant energy loss of the system, accompanied by a phase shift in the emitted GW. If detected, this would provide a clear signature of horizon scale modifications. However, the strength and width of the resonance are determined by the imaginary part of the QNM. If this quantity is too small, as can occur for certain long-lived modes, the resulting peak in the energy flux becomes extremely narrow, so that the EMRI crosses it very quickly during the inspiral. In [46], the role of such resonances in EMRI dynamics was analyzed in the low-frequency approximation for a non-spinning horizonless object with a perfectly reflective surface. They showed that in these conditions the resonances are too narrow to produce a detectable dephasing in the GW signal. Subsequent studies have shown that, for partially absorbing compact objects with generic spin, resonances can be excited with a sufficiently large width to have a significant impact on the EMRI dynamics [48].

EMRIs offer a powerful probe of horizon-scale physics, since the presence of ECOs can imprint resonances, modified absorption, and other distinctive signatures, making them prime targets for future space-based detectors.

Chapter 4

Spontaneous scalarization

In this chapter we introduce the concept of *spontaneous scalarization*, a mechanism by which compact objects develop nontrivial scalar hair once certain thresholds in curvature, compactness, or spin are exceeded. After a brief overview of the underlying mechanism and of the different types of scalarization, we focus on scalarized BHs that arise in scalar-tensor extensions of GR, namely the Einstein–Maxwell–scalar (EMS) theory.

A distinctive feature of scalarized BHs in EMS is the emergence of effective potentials of perturbations that eventually resemble those of ECOs in some features. In particular, the existence of potential wells can trap perturbations, leading to long-lived QNMs and to echo-like patterns in the ringdown signal. These phenomenological signatures establish a direct connection between scalarized BHs in EMS and the broader ECO landscape.

The present chapter provides the theoretical and conceptual background needed to understand these solutions: their onset and end state. A more detailed discussion of their phenomenology, including the QNM spectrum and the appearance of linear and nonlinear echoes in the ringdown signal, will be presented in the Chapter 5.

4.1 Spontaneous scalarization mechanism

Among the several avenues in the study of possible deviations from the GR picture there is the possibility of the existence of some elusive fundamental fields, that, if detected, would represent signatures of new physics beyond the Standard Model (SM) or GR. In light of all the outstanding confirmations of GR, one possible reason why such new fundamental fields have remained undetected so far is the existence of a nontrivial mechanism that suppresses them in weak or moderately strong gravitational regimes. One fundamental field that has attracted considerable attention over the years in GR, cosmology, and beyond the SM physics is the scalar field.

In 1993, Damour and Esposito-Farèse proposed for the first time a promising mechanism, dubbed *spontaneous scalarization* (see [32] for an extensive review on the subject), able to hide the presence of the scalar field in weak field scenarios of gravity [258]. By introducing an appropriate non-minimal coupling function between the scalar field and gravity in the action of the theory, the latter will be indistinguishable

from GR in the weak field limit but will show some notable differences in the strong regime. According to such a theory, these differences are compatible with the appearance of a non-trivial scalar field surrounding the NSs that are solutions of the theory. The process, known as scalarization, has garnered significant interest in recent years and has been extended from NSs to other compact objects, including BHs. More in detail, the mechanism of spontaneous scalarization can be described as resembling a phase transition where the scalar field cloud forms only when a property of the compact object, such as its compactness or spin, exceeds a certain threshold. This occurs because, in these configurations, the linear approximation of the scalar field shows a peculiar instability known as *tachyonic instability*. This instability is quenched in the nonlinear regime, where the scalar field endows the compact object with a nontrivial structure.

4.1.1 Tachyonic instability in Minkowski spacetime

In order to introduce the concept of tachyonic instability, let us consider the simple case of a real scalar field ϕ in the Minkowski spacetime, with Lagrangian given by

$$\mathcal{L} = \frac{1}{2}\partial_\mu\phi\partial^\mu\phi + V(\phi)\,, \tag{4.1}$$

where the potential $V(\phi)$ contains a bare mass μ term and a quartic self-interaction with coupling λ

$$V(\phi) = \frac{1}{2}\mu^2\phi^2 + \frac{1}{4}\lambda\phi^4\,. \tag{4.2}$$

By denoting the d'Alambertian in Minkowski spacetime as $\Box_\eta = \eta^{\mu\nu}\partial_\mu\partial_\nu$, we can write the scalar field equation below

$$\Box_\eta\phi - \mu^2\phi - \lambda\phi^3 = 0\,, \tag{4.3}$$

of which $\phi = 0$ is a solution. The linearized scalar field equation around the trivial solution $\phi = 0$ is

$$\Box_\eta\delta\phi - \mu^2\delta\phi = 0\,, \tag{4.4}$$

where $\delta\phi$ is a small perturbation. The solutions of Eq. (4.4) are plane waves with dispersion relation $\omega^2 = k^2 + \mu^2$, where ω is the frequency and k is the wavenumber. For $\mu^2 > 0$ the perturbations will exponentially decay, on the contrary, for $\mu^2 < 0$ and a sufficiently small k, they will grow defining a so-called *tachyonic instability*. However, such a picture is valid only within the linear approximation, because as the scalar field ϕ grows the nonlinear effect become non-negligible and the self-interaction term $\lambda\phi^3$ starts to be important. In this scenario, namely for $\mu^2 < 0$ and $\lambda > 0$, the potential of Eq. (4.2) has the famous "Mexican hat" shape displayed in Fig. 4.1. Such potential has a local maximum at $\phi_{\max} = 0$ and two minima at $\phi_{\min}$ defined by $\phi^2_{\min} = -\mu^2/\lambda$. The tachyonic instability dynamically evolves the scalar field from the unstable local maximum to a stable minimum, in a process that can be seen as a phase transition of the system. The instability, captured at the linear approximation, is then quenched by the nonlinear interaction.

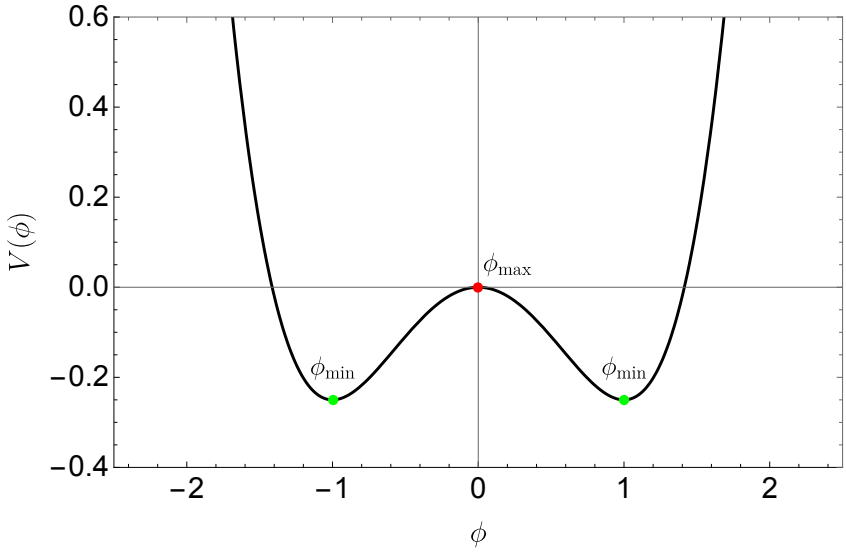

Figure 4.1. Potential $V(\phi)$ of Eq (4.2) for $\lambda = 1$ and $\mu^2 = -1$. The potential presents the well-known "Mexican hat" shape with an unstable local maximum for $\phi_{\rm max} = 0$ and two stable minima for $\phi_{\rm min} = \pm 1$.

4.1.2 Tachyonic instability in curved spacetime

While the mechanism described above in Minkowski spacetime becomes somewhat more intricate in curved spacetime, it also gives rise to interesting consequences. Let us consider a general curved spacetime described by the metric $g_{\mu\nu}$. In this case the linearized scalar field equation becomes

$$\Box\delta\phi - \mu^2\delta\phi = 0\,, \tag{4.5}$$

where $\Box = g^{\mu\nu}\nabla_\mu\nabla_\nu$. Let us now restrict ourselves to the case where $g_{\mu\nu}$ represents the Schwarzschild metric of a compact object of mass M. Following the same procedure of Sec. 2.2.1, if we decompose the scalar field perturbation in spherical harmonics, introducing an exponential time dependence, we get the following Schrödinger-like equation

$$\frac{d^2\Psi}{dr_*^2} + [\omega^2 - V_{\rm eff}(r)]\Psi = 0\,, \tag{4.6}$$

where r_* is the usual tortoise coordinate defined by $dr/dr_* = 1 - 2M/r$, and the effective potential is

$$V_{\rm eff} = \left(1 - \frac{2M}{r}\right)\left[\frac{2M}{r^3} + \frac{l(l+1)}{r^2} + \mu^2\right]\,. \tag{4.7}$$

A sufficient, but non necessary, condition to have an instability is

$$\int_{-\infty}^{\infty} dr_* V_{\rm eff}(r) \leq 0\,. \tag{4.8}$$

One can easily note that the above condition is always satisfied whenever $M = 0$, namely in Minkowski spacetime, for $\mu^2 < 0$. On the other hand, the condition is not

guaranteed for $M \neq 0$. In particular, μ^2 has to be sufficiently negative, depending on the particular spacetime under consideration.

In addition to the bare mass of the scalar field, further contributions from non-minimal couplings between the scalar field and gravity can enter the effective mass squared $\mu^2_{\rm eff}$. Let us consider the simple case in which the scalar field is non-minimally coupled to gravity by means of a term $\phi^2 R$ present in the action of the theory. The scalar field equation will contain also a term proportional to ϕR, that will contribute to the effective mass squared as $\mu^2_{\rm eff} \sim \mu^2 + R$. In a general curved spacetime the sign and the magnitude of R are position dependent, and, as a consequence, also $\mu^2_{\rm eff}$ does as well. This tells us that there will be regions of the studied spacetime in which $\mu^2_{\rm eff}$ is sufficiently negative to induce a tachyonic instability that is quenched at the non-linear level via a scalarization process.

It is important to note that spontaneous scalarization is a sharp transition, the onset of which depends on the specific threshold of the parameter controlling the tachyonic instability.

4.2 Different types of scalarization

In addition to possible non-minimal coupling terms of the form $\phi^2 R$ in the action, other non-minimal couplings to gravity or to matter fields can be introduced, which may contribute to the effective mass squared. Consequently, scalarization can be triggered in several ways, which may be classified by the mechanism responsible for the tachyonic instability. Following [32] three distinct types of scalarization can be identified: compactness-induced scalarization, spin-induced scalarization, and scalarization triggered by matter effects or couplings to additional fields. In the following sections these three possibilities are introduced, mentioning some notable specific examples.

4.2.1 Compactness-induced scalarization

For models in which the scalar field couples non-minimally to gravity, the onset of the tachyonic instability is determined not by the magnitude of the spacetime curvature invariants, but by the compactness of the object, which depends on whether the object is a BH or a NS.

Scalar-Gauss-Bonnet theory

A notable model is provided by the scalar-Gauss-Bonnet theory, whose action is given by

$$S = \frac{1}{16\pi G}\int d^4x\sqrt{-g}\left(R - \frac{1}{2}\nabla_\mu\phi\nabla^\mu\phi + f(\phi)\mathcal{G}\right) + S_{\rm m}(\Psi_m; g_{\mu\nu})\,, \qquad (4.9)$$

where $\mathcal{G} = R^{\mu\nu\rho\sigma}R_{\mu\nu\rho\sigma} - 4R^{\mu\nu}R_{\mu\nu} + R^2$ is the Gauss-Bonnet invariant, $f(\phi)$ is the non-minimal coupling function, and $S_{\rm m}$ is the matter action with matter fields given by $\Psi_{\rm m}$. In [259, 260] it was shown that the theory with action (4.9) can exhibit scalarized BHs. The coupling function $f(\phi)$ must satisfy the condition $(df/d\phi)_{\phi=\phi_0} = 0$ for some constant field ϕ_0, in order to guarantee that the trivial

constant scalar field configurations are solutions of GR. If we vary the action with respect to ϕ we find the scalar field equation

$$\Box\phi + \frac{df(\phi)}{d\phi}\mathcal{G} = 0\,. \tag{4.10}$$

By considering a small perturbation $\delta\phi$ on the background of the trivial solution $\phi = \phi_0$ we get the following linearized equation

$$\Box\delta\phi - \mu^2_{\rm eff}\delta\phi = 0\,, \tag{4.11}$$

where, in this case, the effective mass squared is

$$\mu^2_{\rm eff} = -\left(\frac{d^2 f(\phi)}{d\phi^2}\right)_{\phi=\phi_0}\mathcal{G}\,. \tag{4.12}$$

As long as the condition $\mu^2_{\rm eff} > 0$ is fulfilled, according to a no-hair theorem, the BH solutions of GR with constant scalar profile ϕ_0 are the only admissible ones in the theory [260]. On the contrary, for $\mu^2_{\rm eff} < 0$, the scalar field perturbation can become unstable, leading to a scalarized BH [261]. In particular, in [262] it was shown that scalarized BHs can form dynamically from the core collapse of an unscalarized star. One should note that, in the simple case of a Schwarzschild BH, the Gauss-Bonnet invariant is $\mathcal{G} = 48M^2/r^6$. Therefore, the greater the compactness of the BH, the more prone it is to develop a tachyonic instability that may trigger scalarization.

4.2.2 Spin-induced scalarization

Within gravity, without involving any other matter field, compactness is not the only parameter that can trigger the scalarization mechanism. Another important feature of compact objects that plays a role in this sense is provided by the spin. For a Schwarzschild BH, the Gauss–Bonnet invariant $\mathcal{G}$ is positive definite everywhere. In contrast, for a Kerr BH, $\mathcal{G}$ can take negative values outside the horizon when the spin is sufficiently large. In theories where the coupling function $f(\phi)$ fulfills the condition $(d^2 f/d\phi^2)_{\phi=\phi_0} < 0$, a sufficiently negative Gauss–Bonnet invariant can trigger scalarization. Evidence for scalarized BHs in the parameter regions where linear theory signals a tachyonic instability has been provided in [263–266].

Additionally, in [267] it was shown that in Damour-Esposito-Farèse-like models high spins can increase the parameter space where rotating NSs can scalarize.

4.2.3 Scalarization induced by matter or couplings with other fields

Besides compactness-induced and spin-induced mechanisms, scalarization can also be triggered by the presence of matter distributions or by additional couplings of the scalar field to other fields. A notable example is the Damour-Esposito-Farèse model [258], where the scalar field is minimally coupled to gravity, but non-minimally coupled to matter fields [1] .

[1] It is important to note that the Damour-Esposito-Farèse model where the scalar field is non-minimally coupled to matter is written in the so-called Jordan frame. By means of a proper metric redefinition it is possible to move to the so-called Einstein frame where the non-minimal coupling occurs with gravity [268].

Over the years, many studies have investigated alternative scalarization mechanisms involving couplings to matter. Among them there is also the first model that introduced scalarization of BHs, namely a Damour-Esposito-Farèse model coupled with non-linear electromagnetism [269–271]. The scalarized BHs presented in [271] violate the no-hair theorems for scalar fields of [272, 273].

Similarly to how the Schwarzschild BH can scalarize in scalar-Gauss-Bonnet gravity, the same may happen to charged BHs described by the Reissner–Nordström solution, as proved in [274, 275].

A model that has attracted significant attention is the Einstein–Maxwell–scalar (EMS) theory, with the first study of BH scalarization presented in [30]. In this case, matter is introduced in terms of the Maxwell invariant $F_{\mu\nu}F^{\mu\nu}$, and the scalar field is non-minimally coupled to it. In contrast to the scalar–Gauss–Bonnet model, EMS theory has no higher curvature corrections, and this represents a major technical simplification. The latter permitted to investigate the model fully non-linearly and to perform numerical simulations in spherical symmetry, showing that the Reissner–Nordström BH evolves dynamically into a perturbatively stable scalarized charged BH [30]. Moreover, in [30] non-spherical, static, scalarized solutions have been studied, showing that they are thermodynamically preferred over the electrovacuum spherical BH. This model has been further investigated in [31, 276–279].

Another possibility has been discussed in [280, 281], where it was shown that matter in the vicinity of BHs can trigger scalarization, posing some interesting questions on the possibility of such mechanism in more realistic and involved configurations like accretion disks or dark matter halos.

Chapter 5

Scalarized BHs in Einstein-Maxwell-scalar theory

In this chapter we focus on BHs in EMS theory, a framework where a real scalar field is minimally coupled to gravity and non–minimally coupled to the electromagnetic field through a coupling function. Depending on the choice of this function and on the parameters of the solutions, the theory admits scalarized BHs that can exhibit qualitatively new phenomenology compared to the standard Reissner–Nordström family.

A particularly intriguing feature arises in a specific region of the parameter space: scalarized BHs can develop, besides the usual *unstable* photon sphere, an additional *stable* one. This richer geodesic structure has direct consequences on the dynamics of perturbations. In fact, the effective potential for linear perturbations acquires multiple maxima and minima, presenting cavities where waves can become temporarily trapped. The associated QNM spectrum therefore contains long–lived modes, and the time domain response of the system displays repeated, delayed echoes analogous to those previously observed for horizonless ultracompact objects. This phenomenon provides a remarkable example of how scalarized BHs, which still possess a horizon, can mimic features usually associated with ECOs. Moreover, in EMS theory the nonlinear dynamics can be investigated beyond the perturbative level, allowing us to verify the presence of echoes in fully nonlinear evolutions.

This chapter is devoted to a detailed discussion of these results, largely based on the original work [35].

5.1 EMS action and scalarized BH solutions

As mentioned in Chapter 4, the EMS theory that presents a non-minimal coupling between the electromagnetic field and the scalar field is prone to a tachyonic instability that defines the onset of a scalarization process. To this end, let us consider the following EMS theory that describes a real scalar field ϕ minimally coupled to Einstein's gravity and non-minimally coupled to the electromagnetic Maxwell's field:

$$S = \frac{1}{16\pi}\int d^4x\sqrt{-g}\left[R - 2\partial_\mu\phi\partial^\mu\phi - F[\phi]F_{\mu\nu}F^{\mu\nu}\right], \tag{5.1}$$

where units are set in such a way that $c = G = 4\pi\epsilon_0 = 1$, $g_{\mu\nu}$ is the metric tensor, R is the Ricci scalar and $F_{\mu\nu}$ is the usual Maxwell field strength tensor expressed in terms of the vector potential A_μ, as $F_{\mu\nu} = \partial_\mu A_\nu - \partial_\nu A_\mu$. The generic coupling function between the scalar field and the Maxwell invariant $F_{\mu\nu}F^{\mu\nu}$ is expressed by $F[\phi]$.

Such a theory is particularly motivated and appealing because the gravitational sector is described by GR, and hence we expect strong hyperbolicity for any reasonable choices of $F[\phi]$. Its hairy BH solutions have been studied in detail in [30, 31, 278], showing significant deviations from the Reissner–Nordström BHs. Binary BH mergers in this theory with $F[\phi] \propto e^{-2\alpha\phi}$, where α is a dimensionless coupling constant, have been studied in Ref. [282], motivated by computing the full merger signal in a theory that can be non-perturbatively different from GR. The QNM spectrum of weakly-charged BHs in this theory has been studied in [283]. In [35] we considered a different coupling function, giving rise to BH scalarization and more striking deviations from GR.

By varying the action (5.1) with respect to ϕ, A_μ and $g_{\mu\nu}$ we derive the following field equations

$$\Box\phi - \frac{1}{4}\frac{\delta F[\phi]}{\delta\phi}F_{\mu\nu}F^{\mu\nu} = 0 \,, \tag{5.2}$$

$$\nabla_\mu(F[\phi]F^{\mu\nu}) = 0 \,, \tag{5.3}$$

$$R_{\mu\nu} - \frac{1}{2}R\,g_{\mu\nu} = T^{\phi}_{\mu\nu} + T^{\rm EM}_{\mu\nu} \,, \tag{5.4}$$

where $T^{\phi}_{\mu\nu}$ and $T^{\rm EM}_{\mu\nu}$ are the stress-energy tensors of the scalar and electromagnetic fields, respectively given by

$$T^{\phi}_{\mu\nu} = 2\nabla_\mu\phi\nabla_\nu\phi - g_{\mu\nu}\nabla_\rho\phi\nabla^\rho\phi \,, \tag{5.5}$$

$$T^{\rm EM}_{\mu\nu} = (2F_{\mu\rho}F_\nu{}^\rho - \frac{1}{2}g_{\mu\nu}F_{\rho\sigma}F^{\rho\sigma})F[\phi] \,. \tag{5.6}$$

5.1.1 Spherically symmetric BH solutions

Following [30], in order to find static and spherically symmetric BH solutions to this theory we impose the following ansatz

$$ds^2 = -N(r)e^{-2\delta(r)}dt^2 + \frac{1}{N(r)}dr^2 + r^2(d\theta^2 + \sin^2\theta d\varphi^2) \,, \tag{5.7}$$

where, using the Misner-Sharp mass function $m(r)$, $N(r) = 1 - 2m(r)/r$ [284]. Spherical symmetry also implies that the electromagnetic field $A_\mu = (V(r), 0, 0, 0)$ and the scalar field $\phi(r)$ only depend on the radial coordinate r. Thanks to this simplification we can write the field equations as follows

$$\delta' + r\phi'^2 = 0 \,, \tag{5.8}$$

$$(e^\delta F[\phi]\, r^2 V')' = 0 \,, \tag{5.9}$$

$$r(r-2m)\phi'^2 + r^2V'^2e^{2\delta}F[\phi] - 2m' = 0 \,, \tag{5.10}$$

$$r(r-2m)\phi'' - [2(m + rm' - r) + (r^2 - 2mr)\delta']\phi' + \frac{r^2V'^2e^{2\delta}}{2}\frac{\delta F[\phi]}{\delta\phi} = 0 \,, \tag{5.11}$$

where the prime denotes a derivative with respect to r. Eq. (5.9) can be integrated with respect to r, giving

$$V' = -\frac{Q}{r^2 F[\phi]\, e^{\delta}} \,, \tag{5.12}$$

where the electric charge of the spacetime Q is precisely the integration constant.

To solve the set of ODEs of Eqs. (5.8)- (5.12) we need to implement suitable boundary conditions for the functions δ, V, m and ϕ and for their derivatives. Assuming the existence of a horizon located at $r = r_H > 0$, we consider the following expansion

$$m(r) = \frac{r_H}{2} + m_1(r - r_H) + \dots \,, \tag{5.13}$$

$$\delta(r) = \delta_0 + \delta_1(r - r_H) + \dots \,, \tag{5.14}$$

$$V(r) = V_1(r - r_H) + \dots \,, \tag{5.15}$$

$$\phi(r) = \phi_0 + \phi_1(r - r_H) + \dots \,, \tag{5.16}$$

where

$$m_1 = \frac{Q^2}{2\, r_H^2 F[\phi_0]} \,, \tag{5.17}$$

$$\delta_1 = -\phi_1^2 r_H \,, \tag{5.18}$$

$$\phi_1 = \frac{Q^2}{2\, r_H Q^2 F[\phi_0] - 2 r_H^3 F[\phi_0]^2} \frac{\delta F[\phi_0]}{\delta \phi} \,, \tag{5.19}$$

$$V_1 = -\frac{Q^2}{r_H^2 e^{\delta_0} F[\phi_0]} \,, \tag{5.20}$$

in terms of the two parameters δ_0 and ϕ_0. The latter are found with a shooting method, imposing that the solution is asymptotically flat and given by the following expansion

$$m(r) = M - \frac{Q^2 + Q_s^2}{2r} + \dots \,, \tag{5.21}$$

$$\delta(r) = \frac{Q_s^2}{2r^2} + \dots \,, \tag{5.22}$$

$$\phi(r) = \frac{Q_s}{r} + \frac{Q_s M}{r^2} + \dots \,, \tag{5.23}$$

$$V(r) = V_\infty + \frac{Q}{r} + \dots \,, \tag{5.24}$$

where M is the ADM mass, Q_s is the charge of the scalar field, and V_∞ is the electrostatic potential at infinity.

We now turn to a specific realization of EMS theory, characterized by the following coupling function

$$F[\phi] = e^{\alpha \phi^2} \,, \tag{5.25}$$

where $\alpha \geq 0$ is a dimensionless coupling constant. Since the coupling function of Eq. (5.25) fulfills the condition

$$\left. \frac{\delta F[\phi]}{\delta \phi} \right|_{\phi=0} = 0 \,, \tag{5.26}$$

the trivial scalar field solution $\phi = 0$ solves the field equations. Therefore, the model admits the scalar-free solution given by the Reissner–Nordström BH with mass M and electric charge Q, for any value of α. This solution corresponds to $m(r) = M - \frac{Q^2}{2r}$, $V(r) = V_\infty + Q/r$, and $\phi = \delta = 0$.

Moreover, for any $\alpha > 1/4$ the theory also admits scalarized BH solutions with a charge Q ranging from a minimum value (at which they connect to the Reissner–Nordström BHs) to a maximum critical value $Q_{\rm crit}$ marking the upper bound of the domain of existence [30] [1] . In [30] different scalarized solutions, where the scalar field profile $\phi(r)$ is characterized by more nodes, are presented. In what follows we will only consider the so-called fundamental modes of scalarized BHs, namely the configurations for which the scalar field $\phi(r)$ has zero nodes. As an example of scalarized solution, in Fig. 5.1 we display the metric functions and the scalar field for $\alpha = 20$ and $q = Q/M = 0.7$. The plot illustrates that the scalar

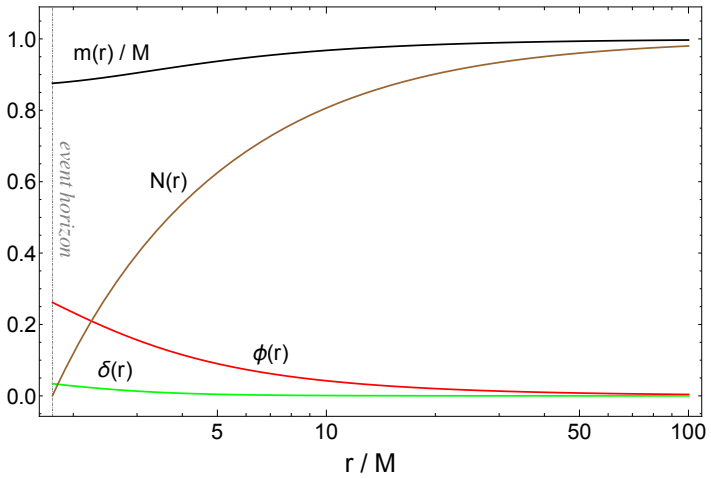

Figure 5.1. Metric functions $m(r)$, $N(r)$, $\delta(r)$ and scalar field $\phi(r)$ of the scalarized BH with $\alpha = 20$ and $q = Q/M = 0.7$.

field vanishes asymptotically, and the metric functions converge to those of a flat spacetime, ensuring asymptotic flatness.

5.1.2 Photon spheres

As shown in [285, 286], scalarized BH solutions can display a remarkably richer geodesic structure than their GR counterparts. In particular, within certain regions of the parameter space, they are not characterized solely by the usual unstable photon sphere, but also admit an additional stable one. The coexistence of unstable and stable photon spheres is a distinctive feature, with important consequences for the phenomenology.

In order to find the photon sphere(s) of these background solutions we study the geodesics described by massless particles in the spacetime of the scalarized BH. Solving the geodesic equation for a photon is equivalent to solving the Euler–Lagrange

[1] Note that in [30] the coupling function is defined as $F[\phi] = e^{-\alpha\phi^2}$, as a consequence, in order to trigger the scalarization mechanism, the dimensionless coupling constant α is negative definite.

equations

$$\frac{\partial \mathcal{L}}{\partial x^\rho} - \frac{d}{d\lambda}\frac{\partial \mathcal{L}}{\partial \dot{x}^\rho} = 0\,, \tag{5.27}$$

where the dot denotes derivative with respect to the affine parameter λ, and $\mathcal{L}$ is the Lagrangian of a massless particle in the metric of Eq. (5.7), given by

$$\mathcal{L} = \frac{1}{2}\left[-Ne^{-2\delta}\dot{t}^2 + \frac{1}{N}\dot{r}^2 + r^2\dot{\theta}^2 + r^2\sin^2\theta\dot{\varphi}^2\right]. \tag{5.28}$$

Since the spacetime is spherically symmetric, a natural simplification comes from restricting ourselves to the study of planar orbits, setting $\theta = \pi/2$ without loss of generality. From Eq. (5.27) we derive the equations for the t, φ and r components of the null geodesic

$$\dot{t} = \frac{E}{Ne^{-2\delta}}\,, \quad \dot{\varphi} = \frac{L}{r^2}\,, \quad \dot{r}^2 = e^{\delta}[E^2 - V_{\rm ph}(r)L^2]\,, \tag{5.29}$$

where E and L are the constants of motion associated to the two isometries of the spacetime, and the potential $V_{\rm ph}$ is given by

$$V_{\rm ph}(r) = \frac{Ne^{-2\delta}}{r^2}\,. \tag{5.30}$$

A photon sphere at radial distance $\bar{r}$ is identified by the conditions of vanishing radial velocity and acceleration ($\dot{r} = \ddot{r} = 0$), which correspond to the equations $E^2 = V_{\rm ph}(\bar{r})L^2$ and $dV_{\rm ph}(\bar{r})/dr = 0$. Local maxima (minima) of $V_{\rm ph}$ correspond to unstable (stable) photon orbits.

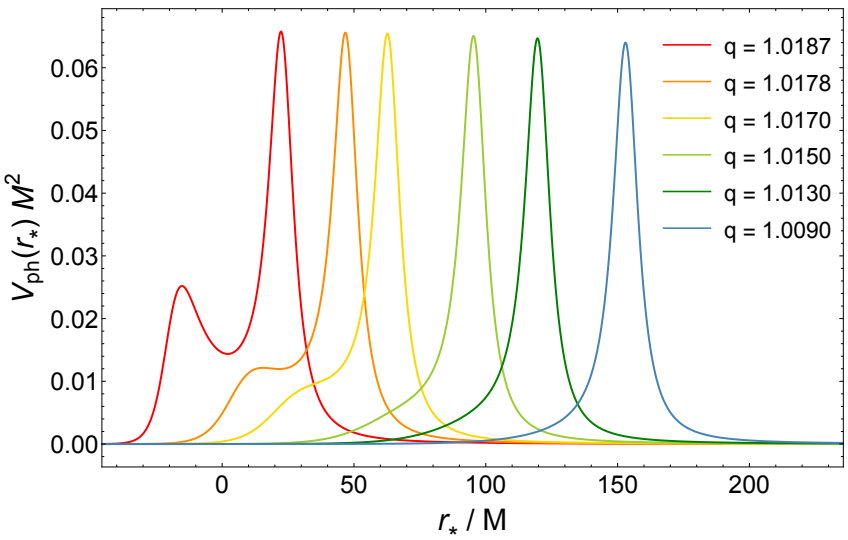

Figure 5.2. Null-geodesic potential $V_{\rm ph}$ in terms of the tortoise coordinate r_*, for different values of $q = Q/M$ in the case $\alpha = 0.6$. The potential for $q = 1.0187$ shows a well, signaling the presence of a stable photon sphere.

An analysis of the parameter space shows that scalarized BH solutions can develop a stable photon sphere in certain regions. They are present for small values of the coupling constant α and near the critical charge $Q_{\rm crit}$, above which the

solutions cease to exist [285, 286]. A representative example is shown in Fig. 5.2, where we display the profile of the potential in Eq. (5.30) as a function of the tortoise coordinate r_*, defined by $dr_*/dr = e^{\delta}/N$. We considered the case $\alpha = 0.6$, and different values of the charge-to-mass ratio q. As we can see, $V_{\rm ph}$ develops a stable photon sphere as $q \to q_{\rm crit} \approx 1.0187$.

5.2 Perturbed field equations

The presence of a richer geodesic structure, showing more than just the usual unstable photon sphere, suggests that the dynamics of perturbations on the background of these scalarized BHs may differ from the standard case. In the following we derive the linearized field equations governing perturbations of the background of Eq. (5.7).

5.2.1 Radial perturbations

We begin with the simplest case of radial perturbations, which, despite their relative simplicity, already capture the phenomenology we aim to highlight, before turning to the more general case of non-spherical modes. For the derivation we keep the coupling function $F[\phi]$ general.

Following [31] we consider spherically symmetric, linear perturbations of the metric, vector potential, and scalar field as follows

$$ds^2 = -\tilde{N}(t,r)\, e^{-2\tilde{\delta}(t,r)} dt^2 + \frac{dr^2}{\tilde{N}(t,r)} + r^2(d\theta^2 + \sin^2\theta d\varphi^2) \,, \tag{5.31}$$

$$A = \tilde{V}(t,r)dt \,, \tag{5.32}$$

$$\phi = \tilde{\phi}(t,r) \,, \tag{5.33}$$

where we defined

$$\tilde{N}(t,r) = N(r) + \epsilon\, N_1(t,r) \,, \tag{5.34}$$

$$\tilde{\delta}(t,r) = \delta(r) + \epsilon\, \delta_1(t,r) \,, \tag{5.35}$$

$$\tilde{\phi}(t,r) = \phi(r) + \epsilon\, \phi_1(t,r) \,, \tag{5.36}$$

$$\tilde{V}(t,r) = V(r) + \epsilon\, V_1(t,r) \,. \tag{5.37}$$

If we keep only the terms that are linear in ϵ it is possible to linearize the field equations

$$\dot{N}_1(t,r) = -2rN(r)\phi'(r)\dot{\phi}_1(t,r) \,, \tag{5.38}$$

$$\delta_1'(t,r) = -2r\phi'(r)\phi_1'(t,r) \,, \tag{5.39}$$

$$\dot{V}_1'(t,r) = -V'(r)\left(\dot{\delta}_1(t,r) + \frac{\dot{\phi}_1(t,r)}{F[\phi]}\frac{\delta F[\phi]}{\delta\phi}\right) \,, \tag{5.40}$$

where the prime and the dot denote partial derivatives with respect to r and t, respectively. Through t integration, the above equations provide the following

constraints

$$N_1(t,r) = -2rN(r)\phi'(r)\phi_1(t,r) + b(r) \,, \tag{5.41}$$

$$\delta_1'(t,r) = -2r\phi'(r)\phi_1'(t,r) \,, \tag{5.42}$$

$$V_1'(t,r) = -V'(r)\left(\delta_1(t,r) + \frac{\phi_1(t,r)}{F[\phi]}\frac{\delta F[\phi]}{\delta\phi}\right) + c(r) \,, \tag{5.43}$$

where $b(r)$ and $c(r)$ are free radial functions representing the integration constants with respect to time. In the late time, for a stable scalarized BH, we expect the perturbation functions $\{N_1, \delta_1, \phi_1, V_1\}$ to vanish, corresponding to the unperturbed solution; this automatically evaluates the integration constants as $b(r) = c(r) = 0$.

The perturbation equations can be reduced to the familiar form of the one-dimensional wave equation by performing a field redefinition $\Psi(t,r) = r\phi_1(t,r)$

$$\left(\frac{\partial^2}{\partial r_*^2} - \frac{\partial^2}{\partial t^2}\right)\Psi(t,r_*) = V_\phi \Psi(t,r_*) \,, \tag{5.44}$$

where the tortoise coordinate is defined by $dr_*/dr = e^\delta/N$, and the effective potential reads

$$V_\phi = \frac{e^{-2\delta}N}{r^2}\Bigg\{1 - N - 2r^2\phi'^2 - \frac{Q^2}{2r^2}\Bigg[\frac{2}{F[\phi]}(1-2r^2\phi'^2) - \frac{2}{F^3[\phi]}\left(\frac{\delta F[\phi]}{\delta\phi}\right)^2 + \frac{1}{F^2[\phi]}\left(\frac{\delta^2 F[\phi]}{\delta\phi^2} + 4r\phi'\frac{\delta F[\phi]}{\delta\phi}\right)\Bigg]\Bigg\} \,. \tag{5.45}$$

This expression is identical to the one in [31]. In the specific case given by Eq. (5.25) the potential V_ϕ becomes

$$V_\phi = \frac{Ne^{-2\delta}}{r^2}\left\{1 - N - 2r^2\phi'^2 - \frac{Q^2}{r^2 e^{\alpha\phi^2}}[1 + \alpha - 2(\alpha\phi - r\phi')^2]\right\} \,, \tag{5.46}$$

or, in terms of the Misner-Sharp mass function $m(r)$,

$$V_\phi = \frac{(r-2m)e^{-2\delta}}{r^3}\left\{\frac{2m}{r} - 2r^2\phi'^2 - \frac{Q^2}{r^2 e^{\alpha\phi^2}}[1 + \alpha - 2(\alpha\phi - r\phi')^2]\right\} \,. \tag{5.47}$$

It is straightforward to show that for $\alpha = \phi = \delta = 0$ and $m(r) = M - \frac{Q^2}{2r}$ the latter reduces to the effective potential of linear and radial perturbations of a test scalar field in the Reissner–Nordström background, i.e.

$$V_{\phi,RN} = \frac{2}{r^3}\left(1 - \frac{2M}{r} + \frac{Q^2}{r^2}\right)\left(M - \frac{Q^2}{r}\right) \,. \tag{5.48}$$

In order to study the QNM spectrum of the scalarized solution, we express the scalar field in terms of its Fourier transform, $\Psi(t,r) = \int d\omega e^{-i\omega t}\tilde{\Psi}(\omega,r)$ and, dropping the tilde notation, we rewrite Eq. (5.44) as

$$\left(\frac{d^2}{dr_*^2} + \omega^2\right)\Psi = V_\phi \Psi \,. \tag{5.49}$$

In the region of parameter space with a stable photon sphere, the hairy BH exhibits an effective potential V_ϕ that differs from that of a standard BH. Indeed, as illustrated in Fig. 5.3, it can form one or more cavities that influence the corresponding QNMs.

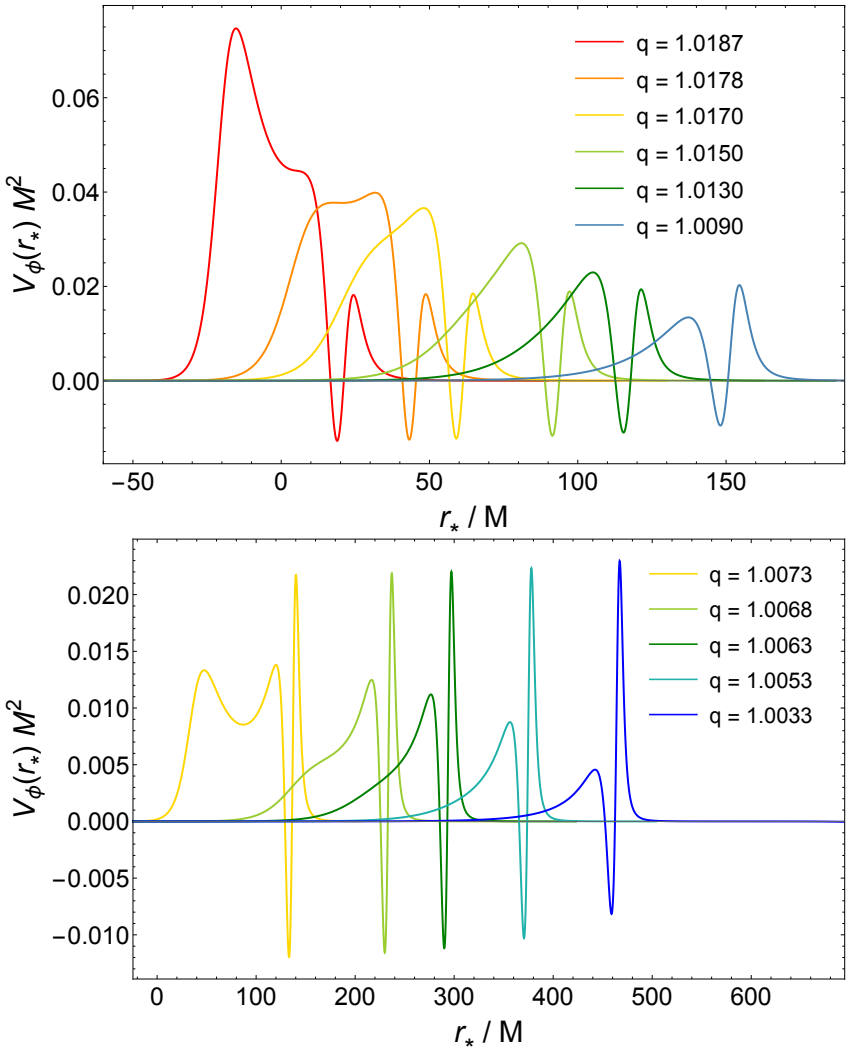

Figure 5.3. Effective potential V_ϕ for radial perturbations of scalarized BHs in terms of the tortoise coordinate r_*. We show the case $\alpha = 0.6$ in the top panel, and $\alpha = 0.5$ in the bottom panel. Different colors refer to different choices of $q = Q/M$.

A sufficient, but not necessary condition, for the perturbation to develop an instability is that $\int_{-\infty}^{\infty} dr_* V_{\rm eff}(r) \leq 0$. However, this is not the case for the potentials shown in Fig. 5.3, therefore, no obvious instabilities are present. Indeed, as will be discussed later, our analysis shows that the QNM spectrum remains stable, even in cases where the effective potential develops regions of negative sign. Nevertheless, a multi-peaked potential of this kind can sustain long-lived modes which, in the time domain, slowly tunnel through the potential barrier, producing a sequence of echoes in the ringdown signal.

5.2.2 Non-spherical perturbations

We now proceed to derive the linearized equations for non-spherical perturbations of the BH solution of Eq. (5.7). Let us consider the perturbed metric tensor $g_{\mu\nu} = \bar{g}_{\mu\nu} + h_{\mu\nu}$, where $\bar{g}_{\mu\nu}$ represents the background line element. In the same fashion we introduce the perturbed vector potential and scalar field as $A_\mu = \bar{A}_\mu + \delta A_\mu$ and $\phi = \bar{\phi} + \delta\phi$, respectively. Given the spherical symmetry of the background, it is natural to decompose the field perturbations into scalar, vector, and tensor spherical harmonics characterized by indices l and m. This procedure allows the splitting of the perturbations into axial (which acquire a factor $(-1)^{l+1}$ under parity inversion) and polar (which acquire a factor $(-1)^l$). Since we are interested in the gravitational perturbations, in the following we will focus on the $l \geq 2$ case [2] .

Let us expand the metric perturbations in tensor spherical harmonics using the Regge-Wheeler gauge [154]

$$h_{\mu\nu} = h^A_{\mu\nu} + h^P_{\mu\nu} \,, \tag{5.50}$$

$$h^A_{\mu\nu} = \sum_{l,m} \int d\omega \, e^{-i\omega t} \begin{bmatrix} 0 & 0 & -\frac{h_0(r)\partial_\varphi Y^m_l}{\sin\theta} & h_0(r)\sin\theta\partial_\theta Y^m_l \\ * & 0 & -\frac{h_1(r)\partial_\varphi Y^m_l}{\sin\theta} & h_1(r)\sin\theta\partial_\theta Y^m_l \\ * & * & 0 & 0 \\ * & * & * & 0 \end{bmatrix} \,, \tag{5.51}$$

$$h^P_{\mu\nu} = \sum_{l,m} \int d\omega \, e^{-i\omega t} Y^m_l \begin{bmatrix} e^{-2\delta(r)}N(r)H_0(r) & H_1(r) & 0 & 0 \\ * & \frac{H_2(r)}{N(r)} & 0 & 0 \\ * & * & r^2K(r) & 0 \\ * & * & * & r^2\sin^2\theta K(r) \end{bmatrix} \,, \tag{5.52}$$

where the asterisk "$*$" here denotes symmetrization, and A and P stand for axial and polar, respectively. The perturbation of the vector potential is decomposed similarly

$$\delta A_\mu = \delta A^A_\mu + \delta A^P_\mu \,, \tag{5.53}$$

$$\delta A^A_\mu = \sum_{l,m} \int d\omega \, e^{-i\omega t} \left(0, 0, -\frac{u_4(r)\partial_\varphi Y^m_l}{\sin\theta}, u_4(r)\sin\theta\partial_\theta Y^m_l\right) \,, \tag{5.54}$$

$$\delta A^P_\mu = \sum_{l,m} \int d\omega \, e^{-i\omega t} \left(\frac{u_1(r)Y^m_l}{r}, \frac{u_2(r)Y^m_l}{rN(r)}, 0, 0\right) \,, \tag{5.55}$$

where we have fixed the gauge by setting the angular components of δA^P_μ to zero. However, for the subsequent derivation, it is more convenient to treat the perturbations of the Maxwell tensor $F_{\mu\nu}$ as the dynamical variable, with the following

[2] Note that for $l = 1$ the only propagating degrees of freedom are the scalar and a polar electromagnetic mode.

decomposition

$$\delta F_{\mu\nu} = \delta F^A_{\mu\nu} + \delta F^B_{\mu\nu} \,, \tag{5.56}$$

$$\delta F^A_{\mu\nu} = \sum_{l,m} \int d\omega \, e^{-i\omega t} \begin{bmatrix} 0 & 0 & -\frac{i\omega u_4(r)\partial_\varphi Y_l^m}{\sin\theta} & i\omega u_4(r)\sin\theta\partial_\theta Y_l^m \\ \star & 0 & \frac{u_4'(r)\partial_\varphi Y_l^m}{\sin\theta} & -u_4'(r)\sin\theta\partial_\theta Y_l^m \\ \star & \star & 0 & l(l+1)u_4(r)\sin\theta Y_l^m \\ \star & \star & \star & 0 \end{bmatrix} , \tag{5.57}$$

$$\delta F^P_{\mu\nu} = \sum_{l,m} \int d\omega \, e^{-i\omega t} \begin{bmatrix} 0 & f_{01}(r)Y_l^m & f_{02}(r)\partial_\theta Y_l^m & f_{02}(r)\partial_\varphi Y_l^m \\ \star & 0 & f_{12}(r)\partial_\theta Y_l^m & f_{12}(r)\partial_\theta Y_l^m \\ \star & \star & 0 & 0 \\ \star & \star & \star & 0 \end{bmatrix} , \tag{5.58}$$

where the star "$\star$" denotes antisymmetrization. The functions f_{01}, f_{02} and f_{12} can be written in terms of u_1 and u_2 as follows

$$f_{01}(r) = \frac{i\omega r u_2(r) + N(r)(r u_1'(r) - u_1(r))}{r^2 N(r)} \,, \tag{5.59}$$

$$f_{02}(r) = \frac{u_1(r)}{r} \,, \tag{5.60}$$

$$f_{12}(r) = \frac{u_2(r)}{r N(r)} \,, \tag{5.61}$$

and are related by the following equation

$$f_{01}(r) = i\omega f_{12}(r) + f_{02}'(r) \,. \tag{5.62}$$

Finally, the scalar field perturbation is decomposed as

$$\delta\phi = \sum_{l,m} \int d\omega \, e^{-i\omega t} z(r) Y_l^m \,. \tag{5.63}$$

A detailed derivation of the linearized perturbation equations is presented in Appendix C, where all intermediate steps and technical details are provided.

Axial sector

The axial sector, which contains only perturbations of the Maxwell tensor and of the metric, can be written as a system of two coupled second order differential equations

$$\left(\frac{d^2}{dr_*^2} + \omega^2\right) U(r) = V_{UU} U(r) + V_{UH} H(r) \,, \tag{5.64}$$

$$\left(\frac{d^2}{dr_*^2} + \omega^2\right) H(r) = V_{HU} U(r) + V_{HH} H(r) \,, \tag{5.65}$$

where $U(r)$ and $H(r)$, defined in Eq. (C.18), are functions of $u_4(r)$ and $h_1(r)$, respectively. The potentials are given by

$$V_{UU} = \frac{r-2m}{r^3 e^{2\delta}}\Bigg\{\Lambda + 2 + \frac{Q^2}{4r^2F^3[\phi]}\left[16\,F^2[\phi] - \left(\frac{\delta F[\phi]}{\delta\phi}\right)^2\right] + \frac{(r-2m)\phi'}{4F[\phi]}\left[2r\phi'\frac{\delta^2 F[\phi]}{\delta\phi^2} - 4\frac{\delta F[\phi]}{\delta\phi} - \frac{r\phi'}{F[\phi]}\left(\frac{\delta F[\phi]}{\delta\phi}\right)^2\right]\Bigg\}, \tag{5.66}$$

$$V_{UH} = V_{HU} = \frac{r-2m}{r^3 e^{2\delta}}\left(\frac{2\sqrt{\Lambda}}{\sqrt{F[\phi]}}\frac{Q}{r}\right), \tag{5.67}$$

$$V_{HH} = \frac{r-2m}{r^3 e^{2\delta}}\left[\Lambda - \frac{2m}{r} + 2m' + 2\left(1-\frac{2m}{r}\right) + (r-2m)\delta'\right], \tag{5.68}$$

where we defined $\Lambda \equiv (l+2)(l-1)$. As shown in [287], a system of this type can be decoupled via an $r-$independent transformation if the potentials satisfy the following requirement

$$\frac{V_{UU} - V_{HH}}{V_{UH}} = const. \tag{5.69}$$

While this is the case in the Reissner–Nordström limit, as expected, we verified numerically that this requirement is not fulfilled in general for scalarized BHs. If we consider the EMS model in Eq. (5.25), the potentials simplify to

$$V_{UU} = \frac{r-2m}{r^3 e^{2\delta}}\left[\Lambda^2 + 2 - \frac{e^{-\alpha\phi^2}Q^2(\alpha^2\phi^2-4)}{r^2} + \alpha\phi'(r-2m)(r\phi' - 2\phi + r\alpha\phi'\phi^2)\right], \tag{5.70}$$

$$V_{UH} = V_{HU} = \frac{r-2m}{r^3 e^{2\delta}}\left(2\sqrt{\Lambda}e^{-\frac{1}{2}\alpha\phi^2}\frac{Q}{r}\right), \tag{5.71}$$

$$V_{HH} = \frac{r-2m}{r^3 e^{2\delta}}\left[\Lambda^2 - \frac{2m}{r} + 2m' + 2\left(1-\frac{2m}{r}\right) + (r-2m)\delta'\right]. \tag{5.72}$$

Polar sector

The polar sector (containing scalar, electromagnetic and metric perturbations) is described by a system of five first-order differential equations

$$f_{12}'(r) = \left(\delta' - \frac{N'}{N} - \frac{1}{F[\phi]}\frac{\delta F[\phi]}{\delta\phi}\phi'\right) f_{12}(r) - \frac{i\omega e^{2\delta}}{N^2} f_{02}(r) \,, \tag{5.73}$$

$$H_1'(r) = \left(\delta' - \frac{N'}{N}\right) H_1(r) - \frac{i\omega}{N}[H_0(r) + K(r)] - 4F[\phi]V' f_{12}(r) \,, \tag{5.74}$$

$$f_{02}'(r) = \left[\frac{l(l+1)Ne^{-2\delta}}{r^2\omega} - \omega\right] i f_{12}(r) - V'K(r) - \frac{V'}{F[\phi]}\frac{\delta F[\phi]}{\delta\phi}\, z(r) \,, \tag{5.75}$$

$$\begin{aligned} K'(r) = {} & \frac{H_0(r)}{r} - \left(\frac{1}{r} + \delta' - \frac{N'}{2N}\right) K(r) - 2\phi' z(r) \\ & + \frac{i}{2r^2\omega}[l(l+1) - 2 + 2rN' + 2e^{2\delta}r^2 V'^2 F[\phi] + 2N(1 + r^2\phi'^2)] H_1(r) \,, \end{aligned} \tag{5.76}$$

$$\begin{aligned} H_0'(r) = {} & -\frac{4V'e^{2\delta}F[\phi]}{N} f_{02}(r) + \left(\frac{N'}{2N} - \delta' - \frac{1}{r}\right) K(r) + \left(\frac{1}{r} + 2\delta' - \frac{N'}{N}\right) H_0(r) \\ & + 2\phi' z(r) - \left\{ \frac{i\omega e^{2\delta}}{N} - \frac{i}{2r^2\omega}\Big[l(l+1) - 2 + 2rN' \right. \\ & \left. + 2r^2 V'^2 e^{2\delta} F[\phi] + 2N + 2r^2 N\phi'^2 \Big] \right\} H_1(r) \,, \end{aligned} \tag{5.77}$$

and a second-order one,

$$\begin{aligned} z''(r) = {} & -\frac{i}{r^2\omega} l(l+1) V' \frac{\delta F[\phi]}{\delta\phi} f_{12}(r) + \frac{1}{N} V'^2 e^{2\delta} \frac{\delta F[\phi]}{\delta\phi} K(r) - \frac{4}{N}\phi' V' e^{2\delta} F[\phi] f_{02}(r) \\ & - \frac{1}{2N}[V'^2 e^{2\delta}\frac{\delta F[\phi]}{\delta\phi} + 2(N' - 2N\delta')\phi'] H_0(r) + \left(\delta' - \frac{2}{r} - \frac{N'}{N}\right) z'(r) \\ & + \left\{ 4\phi'^2 + \frac{1}{N}\left[\frac{l(l+1)}{r^2} - e^{2\delta}\omega^2 - \frac{e^{2\delta}V'^2}{2F[\phi]}\left(F[\phi]\frac{\delta^2 F[\phi]}{\delta\phi^2} - 2\left(\frac{\delta F[\phi]}{\delta\phi}\right)^2 \right) \right] \right\} z(r) \,. \end{aligned} \tag{5.78}$$

5.3 QNMs and time-domain response

In this section we present the QNM spectrum obtained by solving the perturbation equations. We compute the QNMs by solving the equations previously derived as an eigenvalue problem, imposing the usual purely outgoing boundary conditions at infinity and purely ingoing boundary conditions near the BH horizon. The frequencies of the modes are evaluated numerically using a direct integration shooting method as discussed in details in Sec. 2.4.1. The calculations are carried out using MATHEMATICA, employing high numerical precision and high-order series expansions near both boundaries for improved accuracy.

As discussed in [35], the perturbation equation (5.44) is then solved in the time-domain by collaborators to extract the ringdown signal of the perturbed scalarized BH under linear radial perturbations. The signal is then compared with the associated QNM spectrum.

5.3.1 QNM spectrum and ringdown of linear radial perturbations

The QNMs of linear radial perturbations of the scalarized BH are shown in Figs. 5.4 and 5.5 as functions of the charge-to-mass ratio of the background. We focus on the regime $Q/M \gtrsim 1$, which is the regime where the effective potential develops multiple peaks. Fig. 5.4 focuses on the fundamental mode for different values of the coupling constant α. It is worth noting that, while the real part is only weakly affected by α, the imaginary part depends more strongly on that, especially in the vicinity of $Q/M \approx 1$. As expected from the behavior of the effective potential, the quality factor $\omega_R/|\omega_I|$ increases for smaller values of α and when $Q/M \approx 1$ (see inset in the right panel). When $\alpha = 0.5$, the quality factor can reach values up to ≈ 15; by comparison, the corresponding value for a Schwarzschild BH is almost four times lower. The first few overtones for $\alpha = 0.6$ and $\alpha = 0.5$ are shown in Fig. 5.5, since they will be used to fit the time-domain evolution, as discussed in the present and in the next sections.

In [35], the linear radial perturbations have been also analyzed in the time-domain by collaborators. The steep potential wall reflects most of the initial wave, yet a small fraction tunnels through and triggers oscillations within the cavity. The cavity supports a quasi-long lived and quasi-periodic excitation that slowly decays via radiation being emitted from each side of the potential well. The signal emitted to large radius is then recorded at a fixed radius. The time-domain response of a wave scattered off the BH for specific values of q and α is shown in Fig. 5.6. As can

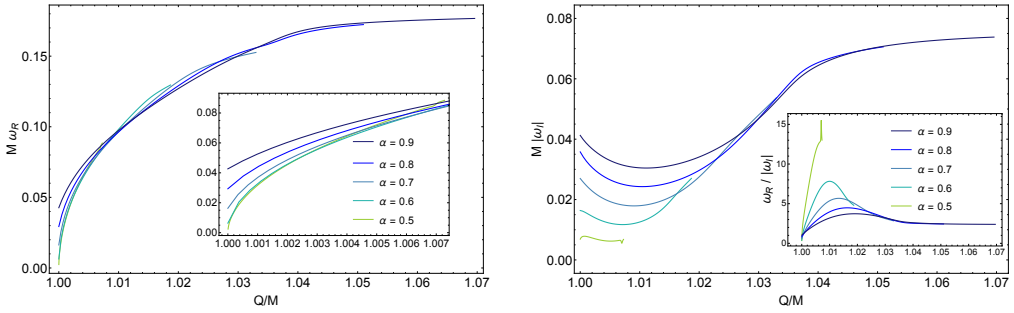

Figure 5.4. Fundamental QNMs for linear radial perturbations as a function of the charge-to-mass ratio $q = Q/M$ for different values of the coupling constant α. Note that we refer to the fundamental mode as the one with the least damping for $Q/M \approx 1$, but increasing Q/M this mode ceases to be the least damped due to a crossing in the imaginary part of the frequency with other modes. The peak present in the imaginary part of the mode for $\alpha = 0.5$ and shown in the inset of the right panel represents a genuine physical behavior, verified by increasing the resolution.

be seen in the insets, in these cases the potential presents multiple peaks, that are able to trap radiation and give rise to a complex ringdown signal. While the signal at late times is governed by the (relatively long-lived) fundamental QNM, initially one can clearly notice repeated modes that are reminiscent of echoes [28, 29, 234]. As anticipated in Sec. 2.5.2, these repeated modes are due to perturbations being trapped in the potential cavity. Because in this model the cavity lacks significant width and depth, the confinement of perturbations is weak. As a consequence, the successive echoes decay rapidly in time and become more evident only when the

signal is displayed on a logarithmic scale (see right panels of Fig. 5.6).

Despite the complex time-domain signal due to cavity effects, it is remarkable that a superposition of the first few QNMs fits the entire signal quite accurately. In Fig. 5.6 we compare the signal with a fit

$$\Psi \sim \sum_{n=0}^{3} A_n e^{i(\omega_R^{(n)} t+\phi_n)} e^{-t/\tau_n} \,, \tag{5.79}$$

where A_n and ϕ_n are the amplitude and phase of the n-th tone and $\tau_n = 1/|\omega_I^{(n)}|$ is the damping time. This superposition well reproduces also the nontrivial behavior at early times.

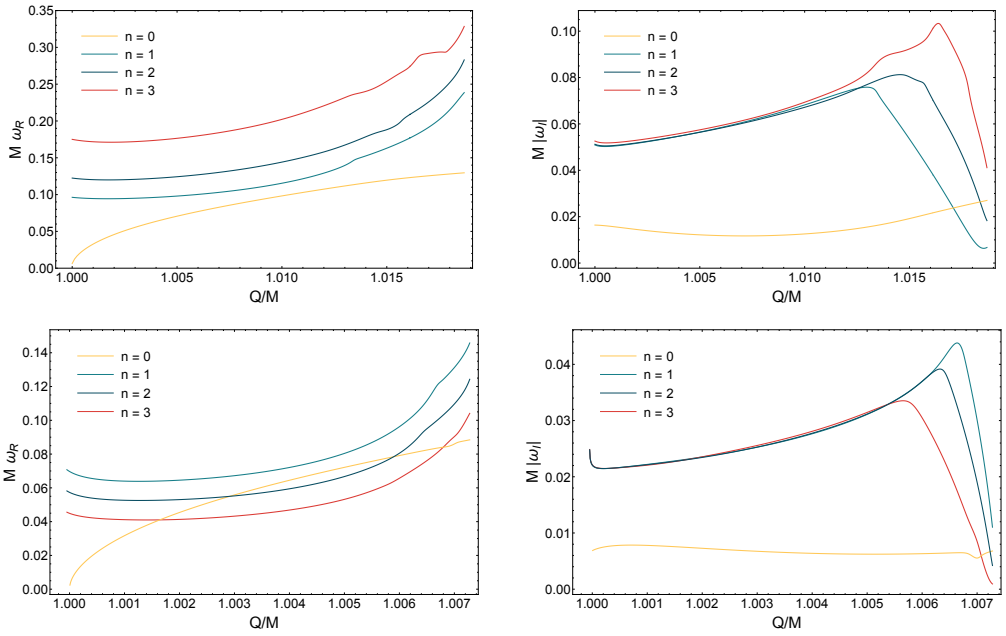

Figure 5.5. Fundamental QNM and first three overtones for linear and spherical perturbations as a function of the charge-to-mass ratio $q = Q/M$ for $\alpha = 0.6$ (top panels) and $\alpha = 0.5$ (bottom panels).

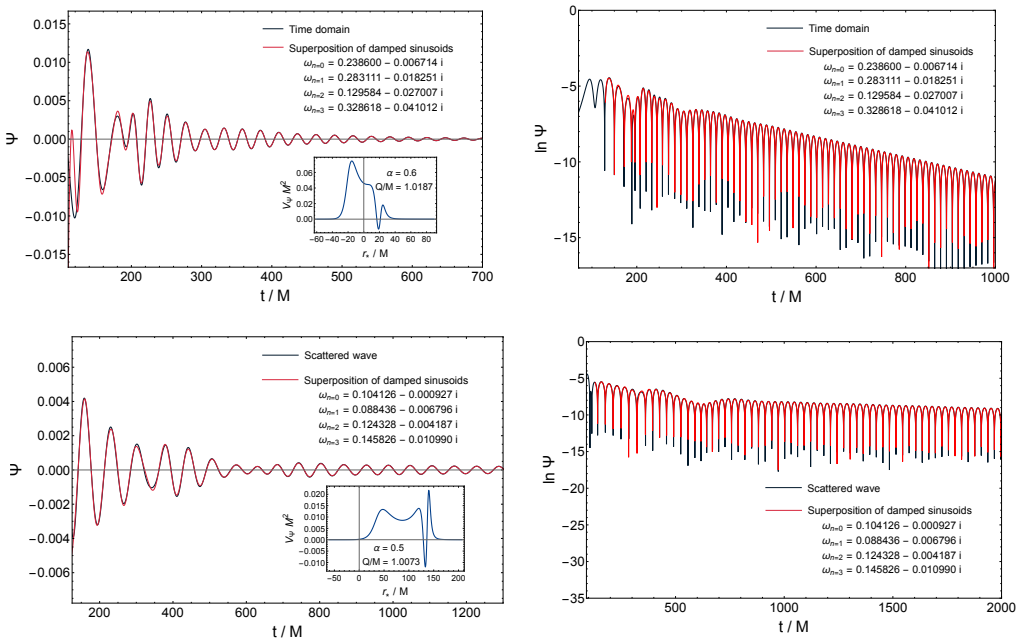

Figure 5.6. Comparison between the scattered wave in the time domain and a superposition of four damped sinusoids with the fundamental QNM and the first three overtones for $\alpha = 0.6$, $Q/M = 1.0187$ (top panels) and for $\alpha = 0.5$, $Q/M = 1.0073$ (bottom panels). The QNM used for the fit are the same as those shown in Fig. 5.5 and are provided in the plots. The inset shows the associated effective potential of the scalar perturbation equation. The right panel shows the signal in a logarithmic scale, to better appreciate the echoes.

5.3.2 QNMs of axial perturbations

The QNMs of the non-spherical perturbations are computed in the axial sector, since this is easier to solve numerically compared to the polar one. Fig. 5.7 presents the QNMs as a function of q for different values of α, compared with modes of the Reissner–Nordström BH, which is also a static solution of the theory. Here we restrict to higher values of α, since the numerical treatment of the small-α region proves difficult with the shooting method employed.

The QNM frequencies are computed across the full parameter space of the scalarized BHs, for different values of the coupling constant α. As shown in the insets of Fig. 5.7, for the minimum values of q, the QNMs of the BHs with scalar hair are continuously connected to the QNMs of the Reissner–Nordström BH. Since the Eqs. (5.64)-(5.65) are coupled, the QNMs are solutions to both equations and are not induced by a single perturbation. Nevertheless, we refer to modes as EM-led (or gravitational-led) if they reduce to those induced by electromagnetic (or gravitational) perturbations in the Reissner–Nordström case. Focusing on the real part of the frequencies, for moderately low values of q the differences with the Reissner–Nordström BH are small, particularly for the gravitational-led modes. The differences become more pronounced for larger values of q, especially for $q > 1$ where the Reissner–Nordström solutions ceases to exist. As already discussed for

the radial perturbations, the real part is only weakly dependent on α. The role of α is much more evident for the imaginary part, where notable differences arise not only compared to the Reissner–Nordström case but also among different values of the coupling constant.

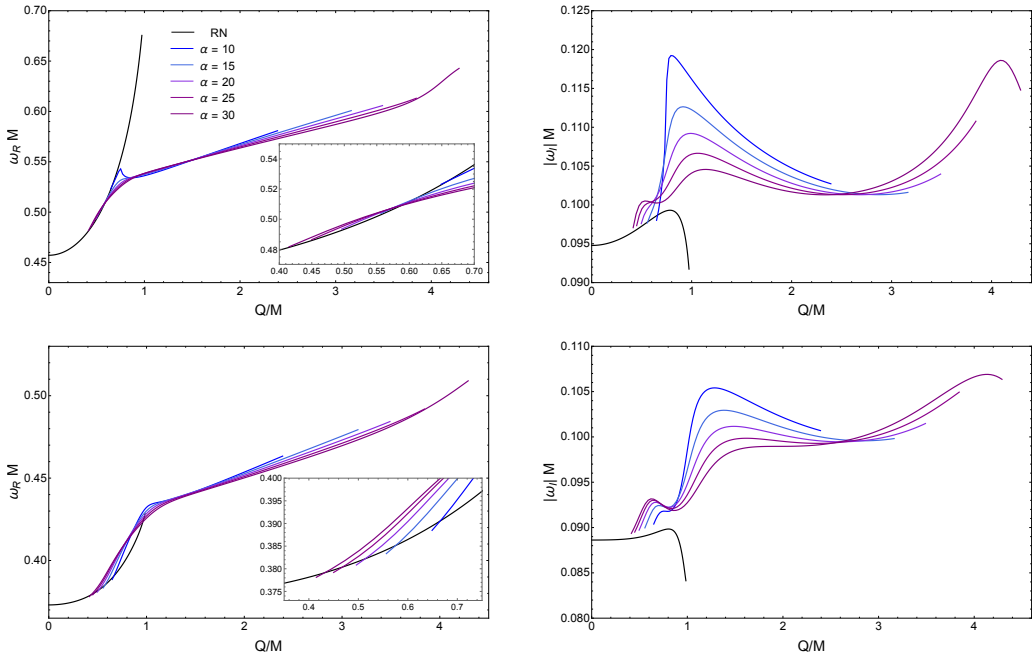

Figure 5.7. Real (left panels) and imaginary (right panels) frequencies of the $l = 2$ QNMs for EM-led (top panels) and gravitational-led (bottom panels) modes as a function of the charge-to-mass ratio $q = Q/M$ for different values of the coupling constant α. The limit of $\alpha = 0$ represents the Reissner–Nordström QNMs shown in black.

5.3.3 Non-linear radial dynamics

Although the analysis presented in this section was performed by collaborators as part of [35], we briefly summarize the results here, since they provide an important confirmation of the linear study. In particular, while the QNM spectrum and the linear time-domain response already indicate the presence of long-lived modes and echoes, it is crucial to assess whether these features survive once nonlinearities are taken into account.

Fully non-linear $1 + 1$ simulations of scalarized black holes evolving under radial perturbations show that echoes indeed persist beyond the linear regime. The qualitative features of the signal, namely the initial prompt ringdown dominated by the fundamental QNM and followed by a series of damped echoes associated with the trapping potential, remain present also at the non-linear level. This represents, to our knowledge, the first explicit example of echoes appearing in a consistent beyond-GR theory beyond linear perturbation theory. For details of the numerical framework (the initial data construction and the evolution scheme) we refer the reader to Ref. [35]. A representative example of the nonlinear evolution is displayed in Fig. 5.8, which shows the persistence of echoes in the time-domain signal.

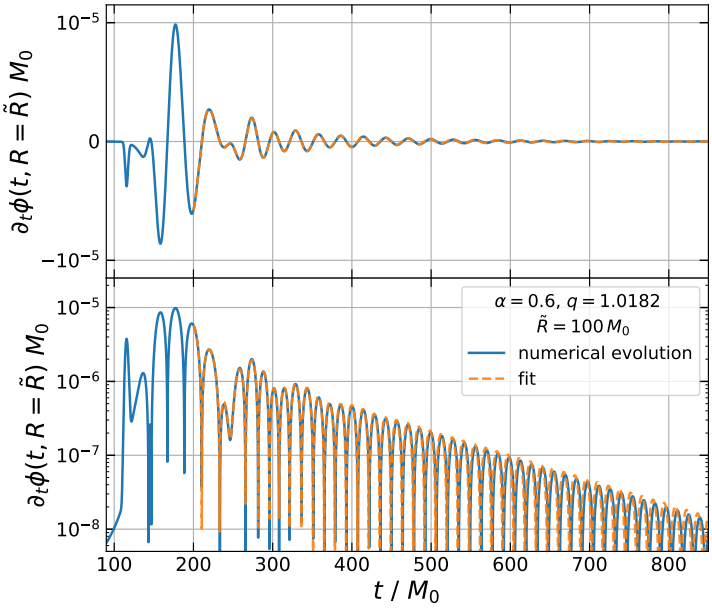

Figure 5.8. Asymptotic behavior of the time derivative of the scalar field at $\tilde{R} = 100\,M_0$ for the simulation in which the dynamics is in the nonlinear regime. As shown, echoes appear and the asymptotic behavior is well-approximated by a superposition of the first 4 QNMs of the final BH configuration. Credits to F. Corelli of Ref.[35].

Chapter 6

Topological stars and magnetized BHs

Among the various horizonless and regular spacetimes that have been proposed as ECOs, topological stars (TS) [26] have recently emerged as particularly compelling toy models to tackle the analysis of the more involved microstate geometries (see Chapter 1).

These solutions arise in the context of five-dimensional Einstein–Maxwell theory, where a magnetic flux supports a smooth soliton against gravitational collapse. TSs provide a rare example of analytically tractable, horizonless compact objects that are nonetheless derived from a well-defined theory, rather than introduced in a purely phenomenological fashion. In this regard, they capture some of the essential features of Fuzzball microstate geometries, such as their nontrivial topology and the role of the extra dimensions. However, in contrast to microstate geometries that lack spatial isometries, TSs maintain spherical symmetry and thus remain sufficiently simple for detailed dynamical studies.

Depending on their parameters, TSs can exhibit a rich geodesic structure, including the presence of both unstable and stable photon spheres. This makes them ultracompact objects with the ability to support long-lived QNMs [288–292], a hallmark feature typically associated with horizonless BH mimickers. From the phenomenological perspective, TSs offer an excellent laboratory to explore how the absence of an event horizon affects the late-time GW response of compact objects. Their linear perturbations display a prompt ringdown that closely resembles that of BHs, followed by a sequence of slowly decaying echoes at late times [290, 292]. Furthermore, in [290–292] it was confirmed that TSs are linearly stable under both radial and nonradial perturbations in the most relevant parameter range, reinforcing their role as robust models for horizonless compact objects.

The goal of this chapter is to present the TS solution and to study its dynamical response under perturbations, with emphasis on the quasinormal spectrum and time-domain signals. We will also highlight the photon spheres structure of these solutions, as a bridge to the discussion of EMRIs in Chapter 7.

The present chapter is based on the original work of Refs.[290, 292].

6.1 Framework and solutions: TSs and magnetized BHs

Let us consider the Einstein-Maxwell theory in five dimensions, whose action is given by

$$S_5 = \int d^5x\sqrt{-\mathbf{g}}\left(\frac{1}{2\kappa_5^2}\mathbf{R} - \frac{1}{4}\mathbf{F}_{AB}\mathbf{F}^{AB}\right), \tag{6.1}$$

where $\mathbf{g} = \det \mathbf{g}_{AB}$ is the determinant of the metric, $\mathbf{R}$ is the Ricci scalar and $\mathbf{F}_{AB}$ is the Maxwell field, all in the five-dimensional space. The coordinates of the latter are denoted with Latin letters. From the above action one can derive the following field equations

$$\mathbf{R}_{AB} - \frac{1}{2}\mathbf{g}_{AB}\mathbf{R} + \kappa_5^2\left(\mathbf{F}_{AC}\mathbf{F}^{C}{}_{B} + \frac{1}{4}\mathbf{g}_{AB}\mathbf{F}_{CD}\mathbf{F}^{CD}\right) = 0\,, \tag{6.2}$$

$$\nabla^B\mathbf{F}_{AB} = 0\,. \tag{6.3}$$

The theory admits two solutions [26]: a regular soliton dubbed topological star (TS) and a magnetized black string, both simultaneously described by the same line element and magnetic charge P as follows

$$ds^2 = -f_S dt^2 + f_B dy^2 + \frac{1}{h}dr^2 + r^2 d\Omega_2^2\,, \tag{6.4}$$

$$F = P\sin\theta\, d\theta \wedge d\phi\,, \tag{6.5}$$

where

$$f_S(r) = 1 - \frac{r_S}{r}\,, \quad f_B(r) = 1 - \frac{r_B}{r}\,, \quad h(r) = f_B f_S\,, \quad P = \pm\frac{1}{\kappa_5}\sqrt{\frac{3r_S r_B}{2}}\,. \tag{6.6}$$

The TS solution corresponds to the case in which $r_B > r_S$, while the magnetized black string corresponds to $r_B \leq r_S$, with r_S being its horizon. The fifth dimension is compact and described by the coordinate y, with period $2\pi R_y$, where R_y is its radius [1]. . The TS solution is everywhere regular and, together with the magnetized black string, they asymptote to four dimensional Minkowski times a circle, parametrized by the coordinate y.

6.1.1 Four-dimensional compactification

Both solutions can be studied, providing interesting insights, after a compactification to the four-dimensional spacetime. Following [290], we introduce a scalar field Φ and a gauge field $\mathcal{A}_\mu$ for the gravity sector, and a scalar field Ξ for the EM sector, as follows

$$ds_5^2 = e^{-\frac{\sqrt{3}}{3}\Phi}ds_4^2 + e^{2\frac{\sqrt{3}}{3}\Phi}(dy + \mathcal{A}_\mu dx^\mu)^2\,, \tag{6.7}$$

$$\mathbf{F}_{AB}dx^A dx^B = F_{\mu\nu}dx^\mu dx^\nu + (\partial_\mu \Xi dx^\mu) \wedge (dy + A_\mu dx^\mu)\,, \tag{6.8}$$

where the four-dimensional field strengths are defined as $\mathcal{F}_{\mu\nu} = \partial_\mu\mathcal{A}_\nu - \partial_\nu\mathcal{A}_\mu$ and $F_{\mu\nu} = \partial_\mu A_\nu - \partial_\nu A_\mu$. Let us assume that all variables are independent of the extra

[1] The radius R_y of the y-circle and the parameters r_B and r_S are related by an orbifold condition that also implies an upper bound $2r_B \leq nR_y$, where n is an integer [26]. See [293, 294] for more details about this relation.

dimension y. As shown from Eqs. (6.4)- (6.5), this is true for the background solution. Moreover, the translation symmetry along y of the latter implies that perturbations can be decomposed with a e^{iky} dependence, where $k = p_y/R_y$ is the quantized momentum along y and $p_y = 0, 1, 2, \ldots$. From a phenomenological perspective, one is interested in the case in which the extra dimension is small and the solution is macroscopic. This is equivalent to ask that $R_y \ll r_S$, so perturbations with $p_y \neq 0$ are hardly excited in classical processes if the object is macroscopic. Therefore we will assume $p_y = 0$, so there is no y dependence in the dynamical variables.

After the four-dimensional compactification, the theory is described by the following Einstein-Maxwell-Dilaton (EMD) action in four dimensions, with two scalars and two gauge fields

$$\mathcal{S} = \int d^4x\sqrt{-g}\left[\frac{1}{2\kappa_4^2}\left(R - \frac{1}{2}\partial_\mu\Phi\partial^\mu\Phi - \frac{1}{4}e^{\sqrt{3}\Phi}\mathcal{F}_{\mu\nu}\mathcal{F}^{\mu\nu}\right) + \frac{1}{e^2}\left(-\frac{1}{4}e^{\frac{\sqrt{3}}{3}\Phi}F_{\mu\nu}F^{\mu\nu} - \frac{1}{2}e^{-\frac{2\sqrt{3}}{3}\Phi}(\partial_\mu\Xi)^2\right)\right]. \quad (6.9)$$

By varying the action with respect to the fields of the theory we get the associated field equations

$$G_{\mu\nu} + \left[\frac{1}{2}e^{\sqrt{3}\Phi}\left(\mathcal{F}_{\mu\rho}\mathcal{F}^{\rho}{}_{\nu} + \frac{1}{4}g_{\mu\nu}\mathcal{F}_{\rho\sigma}\mathcal{F}^{\rho\sigma}\right) - \frac{1}{2}\left(\partial_\mu\Phi\partial_\nu\Phi - \frac{1}{2}g_{\mu\nu}\partial_\rho\Phi\partial^\rho\Phi\right)\right] + \frac{\kappa_4^2}{e^2}\left[e^{\frac{\Phi}{\sqrt{3}}}\left(F_{\mu\rho}F^{\rho}{}_{\nu} + \frac{1}{4}g_{\mu\nu}F_{\rho\sigma}F^{\rho\sigma}\right) - e^{-\frac{2\Phi}{\sqrt{3}}}\left(\partial_\mu\Xi\partial_\nu\Xi - \frac{1}{2}g_{\mu\nu}\partial^\rho\Xi\partial_\rho\Xi\right)\right] = 0\,, \quad (6.10)$$

$$\nabla^\rho\left(e^{\sqrt{3}\Phi}\mathcal{F}_{\mu\rho}\right) = 0\,, \quad (6.11)$$

$$\Box\Phi - \frac{\sqrt{3}}{4}e^{\sqrt{3}\Phi}\mathcal{F}_{\mu\nu}\mathcal{F}^{\mu\nu} + \frac{\kappa_4^2}{e^2}\left[\frac{2\sqrt{3}}{3}e^{-\frac{2\Phi}{\sqrt{3}}}(\partial_\mu\Xi)^2 - \frac{\sqrt{3}}{6}e^{\frac{\Phi}{\sqrt{3}}}F_{\mu\nu}F^{\mu\nu}\right] = 0\,, \quad (6.12)$$

$$\nabla^\rho\left(e^{\frac{\sqrt{3}}{3}\Phi}F_{\mu\rho}\right) = 0\,, \quad (6.13)$$

$$\nabla^\rho\left(e^{-\frac{2\sqrt{3}}{3}\Phi}\partial_\rho\Xi\right) = 0\,. \quad (6.14)$$

In the equations above we have defined $\kappa_4^2 := \kappa_5^2/(2\pi R_y)$ and $e^2 := 1/(2\pi R_y)$ [2]. The TS and the magnetized black string are described in four dimensions as follows

$$ds_4^2 = -f_S f_B^{1/2}dt^2 + \frac{1}{f_S f_B^{1/2}}dr^2 + r^2 f_B^{1/2}d\Omega_2^2\,, \quad (6.15)$$

$$\Phi = \frac{\sqrt{3}}{2}\log f_B\,, \quad (6.16)$$

$$F = \pm eQ_m\sin\theta\, d\theta\wedge d\phi = \pm\frac{e}{\kappa_4}\sqrt{\frac{3}{2}r_B r_S}\sin\theta\, d\theta\wedge d\phi\,, \quad (6.17)$$

$$\mathcal{F} = 0 = \Xi\,. \quad (6.18)$$

[2]We will keep these coupling constants explicit but, when presenting numerical results, we will use units such that $\kappa_4 = \sqrt{8\pi}$ and $e = \sqrt{4\pi}$.

The magnetized black string is now described by a magnetized BH in the four-dimensional space. It is worth noting that both the metric and the dilaton diverge at $r = r_B$. From the four-dimensional perspective, this corresponds to a curvature singularity. However, the five-dimensional uplift is everywhere smooth, and the full solution remains perfectly regular. From the four-dimensional perspective one can derive the ADM mass and magnetic charge of the background, that are respectively

$$M = \frac{2\pi}{\kappa_4^2}(2r_S + r_B)\,, \qquad Q_m = \frac{1}{\kappa_4}\sqrt{\frac{3}{2}r_S r_B}\,. \tag{6.19}$$

By using Eq. (6.19) it is possible to draw the parameter space of the TS and the magnetized BH, as depicted in Fig. 6.1. Magnetized BHs belong to the region of

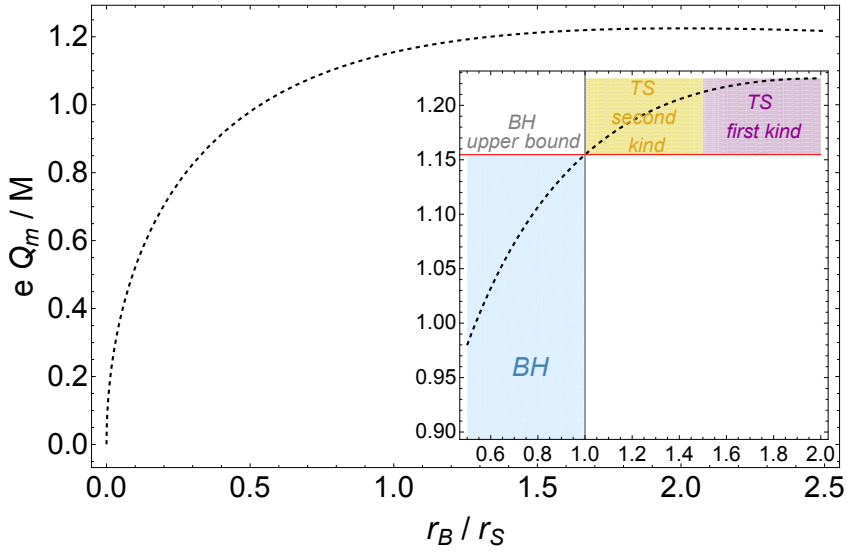

Figure 6.1. Parameter space of static magnetized BHs and TSs. Since the Gregory-Laflamme instability affects BHs with $0 < r_B/r_S < 1/2$ and TSs with $r_B > 2r_S$, in the inset we show the parameter space region free of such instabilities. TSs are classified in *first kind*, if they possess a single unstable photon sphere at $\frac{3}{2}r_S$, and *second kind* if they also acquire a stable one at r_B.

the parameter space with $r_B/r_S < 1$, which implies $\frac{eQ_m}{M} \leq \frac{e\kappa_4}{2\pi\sqrt{6}} \approx 1.1547$. When $0 < r_B/r_S < 1/2$, these solutions are linearly unstable against the Gregory-Laflamme mechanism [295, 296]. For TSs ($r_B/r_S > 1$) we have $\frac{e\kappa_4}{2\pi\sqrt{6}} \leq \frac{eQ_m}{M} \leq \frac{\sqrt{3}e\kappa_4}{8\pi}$. However, this parameter space region is not fully stable for TSs. Indeed, one can show that it is possible to map the magnetized BH to the TS by performing a double Wick rotation $(t, y, r_S, r_B) \to (iy, it, r_B, r_S)$ [297, 298]. Therefore, TSs with $r_B > 2r_S$ are unstable under radial perturbations with purely imaginary frequency (see Sec. 6.1.2 for the results on this instability for TSs). Consequently, the portion of the parameter space that is not affected by the Gregory–Laflamme instability of BHs, nor by its analogue in TSs, is displayed in the inset of Fig. 6.1.

One observes that both magnetized BHs and TSs can have $eQ_m/M > 1$, unlike the four-dimensional Reissner–Nordström BH, which is not a solution to this theory.

As discussed more in detail in Sec. 6.1.2, while the magnetized BH possesses a single unstable photon sphere at $r_{\rm ph} = \frac{3}{2}r_S$, the TS can feature both a stable and an

unstable photon sphere depending on the region of the parameter space. Depending on the compactness and number and features of the associated photon spheres, we can classify the TS in the following way

$$\textit{TS first kind}, \quad \frac{3}{2} < \frac{r_B}{r_S} \leq 2 : \quad r_{\rm ph}^{(1)} = r_B \,, \tag{6.20}$$

$$\textit{TS second kind}, \quad 1 \leq \frac{r_B}{r_S} \leq \frac{3}{2} : \quad r_{\rm ph}^{(1)} = \frac{3}{2} r_S \,, \quad r_{\rm ph}^{(2)} = r_B \,. \tag{6.21}$$

TSs of the second kind have an unstable photon sphere at $r_{\rm ph}^{(1)} = \frac{3}{2} r_S$, like the magnetized BH, but they also possess a *stable* one at $r_{\rm ph}^{(2)} = r_B$.

6.1.2 Geodesic equations: null and time-like circular orbits

Let us study the geodesic motion of null and time-like particles in the background of the TS and of the magnetized black string. In this section we present the main results related to the photon spheres structure and to time-like circular orbits. For a more detailed discussion see [299–301].

For simplicity we restrict the analysis only to circular geodesics on the equatorial plane, i.e. $\dot\theta = 0$ and $\theta = \pi/2$. The Lagrangian for a free particle is given by

$$\mathcal{L} = \frac{1}{2}\left[-f_S \dot t^2 + f_B \dot y^2 + \frac{\dot r^2}{f_B f_S} + r^2 \dot\varphi^2 \right] , \tag{6.22}$$

where the dot denotes the derivative with respect to an affine parameter λ. The five-momentum $P_\mu = \partial\mathcal{L}/\partial\dot x^\mu$ of the test particle reads

$$P_t = -f_S \dot t = -E \,, \qquad P_y = f_B \dot y = p \,, \qquad P_r = \frac{\dot r}{f_B f_S} \,, \qquad P_\varphi = r^2 \dot\varphi = L \,, \tag{6.23}$$

where E, L, and p are integrals of motion associated to isometries along the t, φ, and y directions, respectively. If we denote by μ the mass of the free particle, whose limit for null geodesics is zero, we can write the Hamiltonian below

$$H = \frac{1}{2} g_{\mu\nu} P^\mu P^\nu = -\frac{\mu^2}{2} \,. \tag{6.24}$$

By neglecting the momentum p along the compact dimension, the radial geodesic equation is the following

$$\dot r^2 = E^2 - V_{\rm eff} \,, \tag{6.25}$$

where the effective potential $V_{\rm eff}$ is

$$V_{\rm eff} = \frac{r_B}{r} E^2 + f_S f_B \left(\mu^2 + \frac{L^2}{r^2} \right) . \tag{6.26}$$

Circular geodesics are defined by vanishing radial velocity and acceleration, $\dot r = \ddot r = 0$, and can be parametrized in terms of the energy E and of the angular momentum L, given by

$$\frac{E}{\mu} = \sqrt{\frac{2(r - r_S)^2}{r(2r - 3r_S)}} \,, \qquad \frac{L}{\mu} = \sqrt{\frac{r_S\, r^2}{2r - 3r_S}} \,. \tag{6.27}$$

The roots of $\dot{r} = \ddot{r} = 0$ are

$$\mu = 0 : \qquad r_1 = r_B\,, \quad r_2 = \frac{3}{2} r_S\,, \tag{6.28}$$

$$\mu \neq 0 : \qquad r_1 = r_B\,, \quad r_{2\pm} = L^2 \frac{1 \pm \sqrt{L^2 - 3 r_S^2 \mu^2}}{r_S \mu^2}\,. \tag{6.29}$$

The case $\mu = 0$ corresponds to null circular orbits, in particular for TSs with $3/2 \leq r_B/r_S \leq 2$ (called TSs of the *first kind*, see Sec. 6.1.1 for the discussion on the parameter space) there is a single unstable photon sphere at r_2, while for TSs with $1 \leq r_B/r_S \leq 3/2$ (*second kind*) there is an unstable photon sphere at r_2 and a stable one at r_1. The case $\mu \neq 0$ describes circular orbits for massive probes. When the two roots coincide, $r_{2+} = r_{2-}$, we find the *innermost stable circular orbit* (ISCO)

$$r_{\rm ISCO} = 3 r_S\,. \tag{6.30}$$

The t-component of the four-velocity and the angular velocity are given by

$$u^t = \frac{dt}{d\tau} = \frac{E}{\mu f_S}\,, \qquad \Omega = \frac{d\varphi}{dt} = u^t \frac{L}{\mu}\,, \tag{6.31}$$

that in the case of circular orbits with $r = r_0$ read

$$u^t = \frac{1}{\sqrt{1 - \frac{r_S}{r_0} - r_0^2 \Omega^2}}\,, \qquad \Omega = \sqrt{\frac{r_S}{2 r_0^3}}\,. \tag{6.32}$$

6.2 Linearized perturbed equations

In this section we present the linearized perturbed equations that will be studied to compute the QNM spectrum of the two solutions and to analyze their ringdown signal.

Before [290–292], linear perturbations of magnetized BHs were partially studied in [302, 303]. Moreover, only linear perturbations of a test scalar field have been studied in the case of the TS [288, 289], finding the presence of long-lived QNMs for TSs of the second kind.

Because of the presence of a magnetic flux in the background solutions, it is not straightforward to separate polar (i.e. even-parity) from axial (i.e. odd-parity) perturbations, as described in Sec 2.2.2. Indeed, polar gravitational perturbations are coupled to axial EM perturbations, and viceversa. This introduces a major difficulty in the study of linear perturbations on the backgrounds of the two solutions. For this reason, it is useful to divide the perturbations into two distinct sectors: Type-I sector, containing axial gravitational perturbations coupled to polar EM; and Type-II sector, containing polar gravitational, and scalar, perturbations coupled to axial EM [3] .

Type-I and radial Type-II perturbation equations were derived and analyzed in [290], whereas the nonradial Type-II sector was investigated in [292]. The derivation

[3] One should note that it is possible to avoid coupling perturbations with opposite parity by means of the electromagnetic duality transformations, see [291, 304].

of the perturbation equations, that we outline in Appendix D, has been carried out in [290, 292] in different frameworks for practical reasons: Type-I sector and radial Type-II were obtained after dimensional reduction to four dimensions, while the nonradial Type-II sector was treated directly in the five-dimensional setup. This choice was made solely for convenience and the two frameworks are perfectly consistent. Moreover, for Type-I and radial Type-II perturbations it is possible to derive, in each case, a single master equation of the Schrödinger-like form. The corresponding effective potentials can then be analyzed to gain insight into the dynamics of the perturbations. On the contrary, the nonradial Type-II sector is considerably more involved: the perturbation equations remain coupled, preventing a direct study of the effective potentials.

The linearized perturbed equations of the two sectors (Type-I and Type-II) have been studied in the phenomenologically more interesting case of null momentum along the fifth extra dimension. Therefore, all the perturbations are independent of the coordinate y.

Since $\mathcal{F} = 0 = \Xi$ on the background, the perturbations of these fields decouple from the others. By using an appropriate field redefinition, one can show that, at the linear level, Eq. (6.11) and Eq. (6.14) respectively reduce to those for a test Maxwell and massless scalar field propagating on the fixed backgrounds of the two solutions. Test scalar perturbations of TSs and BHs have been studied in [288, 289] and Maxwell perturbations of a magnetized BH have been studied in [303], therefore, we will not present the equations here. The interested reader can find the equations in [290].

6.2.1 Type-I perturbations

The Type-I sector couples axial metric components with polar EM components and is decoupled from the scalar perturbations. For $l \geq 2$ perturbations, we obtain a system of two equations

$$\begin{aligned}
&\mathcal{D}[\mathcal{R}^-(r)] + \left(2f_S^2 f_B' + 3f_B f_S f_S'\right)\partial_r \mathcal{R}^-(r) \\
&- \left(\frac{2f_B f_S^2}{r^2} + \frac{(\Lambda-2)\,f_S}{r^2} + \frac{2f_S^2 f_B' + f_B f_S f_S'}{r} - 3f_S f_B' f_S' - f_B f_S'^2\right)\mathcal{R}^-(r) \\
&\qquad\qquad - \frac{2\kappa_4^2 Q_m}{e r^3}\mathcal{E}(r) = 0\,, \qquad (6.33)\\
&\mathcal{D}[\mathcal{E}(r)] + \left(2f_S^2 f_B' + f_B f_S f_S'\right)\partial_r \mathcal{E}(r) \\
&- \left(\frac{2\kappa_4^2 Q_m^2 f_S}{r^4} + \frac{\Lambda f_S}{r^2} + \frac{2f_S^2 f_B'}{r} - f_S f_B' f_S'\right)\mathcal{E}(r) - \frac{eQ_m\,(\Lambda-2)\,f_S^2}{r^3}\mathcal{R}^-(r) = 0\,, \qquad (6.34)
\end{aligned}$$

where we defined the second-order differential operator

$$\mathcal{D} = \left(f_B f_S^2\right)\partial_r^2 + \omega^2\,, \qquad (6.35)$$

and $\Lambda = l(l+1)$. The functions $\mathcal{R}^-$ and $\mathcal{E}$ represent the gravitational and EM degrees of freedom of the perturbations, respectively, and are defined by Eqs. (D.9)- (D.10).

Interestingly, the above equations can be decoupled. Let us introduce a generalized tortoise coordinate defined by

$$d\rho = \frac{dr}{f_B^{1/2} f_S}\,. \tag{6.36}$$

By making the field redefinition

$$\tilde{\mathcal{R}}^-(r) = f_B^{3/4} f_S \mathcal{R}^-(r)\,, \qquad \tilde{\mathcal{E}}(r) = f_B^{3/4}\frac{\kappa_4}{e}\sqrt{\frac{2}{\Lambda-2}}\mathcal{E}(r)\,, \tag{6.37}$$

we obtain

$$\left(\frac{d^2}{d\rho^2}+\omega^2\right)\begin{pmatrix}\tilde{\mathcal{R}}^-\\ \tilde{\mathcal{E}}\end{pmatrix} = \mathbf{B}\begin{pmatrix}\tilde{\mathcal{R}}^-\\ \tilde{\mathcal{E}}\end{pmatrix}\,, \tag{6.38}$$

where

$$\mathbf{B} = \frac{f_S}{r^3}\left[F(r)\begin{pmatrix}1 & 0\\ 0 & 1\end{pmatrix} + \begin{pmatrix}0 & P\\ P & 2r_B+3r_S\end{pmatrix}\right]\,, \tag{6.39}$$

with

$$F(r) = \Lambda r - \frac{3(13r_B^2 r_S + 8r^2(r_B+2r_S) - r r_B(9r_B+28r_S))}{16r(r-r_B)}\,, \tag{6.40}$$

$$P = \sqrt{3(\Lambda-2)r_B r_S}\,. \tag{6.41}$$

The system above can be decoupled by performing a linear, $r-$independent transformation

$$Z_1 = \mathcal{L}_1\tilde{\mathcal{R}}^- + \mathcal{L}_2\tilde{\mathcal{E}}\,, \tag{6.42}$$

$$Z_2 = \mathcal{L}_2\tilde{\mathcal{R}}^- - \mathcal{L}_1\tilde{\mathcal{E}}\,, \tag{6.43}$$

with

$$\mathcal{L}_1 = -(2r_B+3r_S) - \sqrt{(2r_B+3r_S)^2 + 12\Lambda r_S r_B}\,, \tag{6.44}$$

$$\mathcal{L}_2 = 2\sqrt{3(\Lambda-2)r_S r_B}\,. \tag{6.45}$$

The decoupled system is

$$\left(\frac{d^2}{d\rho^2}+\omega^2\right)Z_i = V^i_{\rm eff} Z_i \qquad i=1,2 \tag{6.46}$$

with the effective potentials

$$V^{1,2}_{\rm eff} = \frac{r-r_S}{16r^5(r-r_B)}[16r^3\Lambda - r^2(8r_B+24r_S+16\Lambda r_B) + r(11r_B^2+60r_B r_S) - 39r_B^2 r_S \\ \mp 8r(r-r_B)\sqrt{(2r_B-3r_S)^2+12r_B r_S\Lambda}] \tag{6.47}$$

where the minus and the plus signs correspond to $V^1_{\rm eff}$ and $V^2_{\rm eff}$, respectively.

For $l = 1$ the gravitational degree of freedom of the perturbations is non-dynamical, therefore we have a single master equation for the EM perturbation function $\mathcal{E}$

$$\mathcal{D}[\mathcal{E}(r)] + (2f_S^2 f'_B + f_B f_S f'_S)\partial_r \mathcal{E}(r) - V_{\text{eff}}^{l=1}\mathcal{E}(r) = 0\,, \tag{6.48}$$

where the effective potential is given by

$$V_{\text{eff}}^{l=1} = f_S\left(\frac{2\kappa_4^2 Q_m^2}{r^4} + \frac{2}{r^2} + \frac{2f_S f'_B}{r} - f'_B f'_S\right). \tag{6.49}$$

6.2.2 Radial Type-II perturbations

Radial perturbations belong to the Type-II sector, however, since for $l = 0$ gravitational and EM perturbations are non-dynamical, their analysis is considerably simplified. Indeed, it is possible to derive a single master equation for the dynamical scalar perturbation φ

$$\mathcal{D}[\varphi] + \left(f_S^2 f'_B + f_B f_S f'_S\right)\partial_r \varphi - V_{\text{eff}}^{l=0}\varphi = 0\,, \tag{6.50}$$

with effective potential given by

$$\begin{aligned} V_{\text{eff}}^{l=0}(r) = {} & \frac{f_S^2 f'_B + f_B f_S f'_S}{r} + \frac{Q_m^2\kappa_4^2 f_S}{3r^4} + \frac{Q_m^2\kappa_4^2 f_S f'_B}{2r^3(4f_B + r f'_B)} \\ & - \frac{6f_S^2 f_B'^2(f_B + r f'_B)}{(4f_B + r f'_B)^2} + \frac{3r f_S f_B'^2 f'_S}{4(4f_B + r f'_B)}\,. \end{aligned} \tag{6.51}$$

6.2.3 Comparison of effective potentials

As shown in the previous section, the equations for the radial ($l = 0$) perturbations, and for all ($l \geq 1$) Type-I perturbations can be written in the canonical form of the Schrödinger-like equation

$$\frac{d^2\Psi}{d\rho^2} + (\omega^2 - V_{\text{eff}})\Psi = 0\,, \tag{6.52}$$

using some suitable master variable Ψ, and the generalized tortoise coordinate ρ. The effective potentials are written below:

- $l = 0$, (Type-II)

$$\begin{aligned} V_{\text{eff}}^{l=0} = {} & \frac{r - r_S}{16r^5(4r - 3r_B)^2(r - r_B)}[189r_B^4 r_S + 128r^4(r_B + 2r_S) \\ & + 64r^2 r_B^2(6r_B + 19r_S) - 16r^3 r_B(27r_B + 52r_S) - 9r r_B^3(9r_B + 92r_S)] \end{aligned} \tag{6.53}$$

- $l = 1$, Type-I

$$V_{\text{eff}}^{l=1} = \frac{(r - r_S)\left(32r^3 - 24r^2 r_B - 39r_B^2 r_S + r r_B(36r_S - 5r_B)\right)}{16r^5(r - r_B)} \tag{6.54}$$

- $l \geq 2$, Type-I

$$V_{\rm eff}^{(1,2)} = \frac{(r-r_S)}{16r^5(r-r_B)}[16r^3\Lambda - r^2(8r_B+24r_S+16\Lambda r_B) \tag{6.55}$$
$$+ r(11r_B^2+60r_Br_S) - 39r_B^2r_S \mp 8r(r-r_B)\sqrt{(2r_B-3r_S)^2+12r_Br_S\Lambda}]$$

For $l \geq 2$, the decoupling of Type-I perturbations requires the explicit form of the background functions f_S and f_B, whereas the remaining potentials can be expressed for a generic spherically symmetric background.

In Fig. 6.2 we show the effective potentials for some representative values of the parameters: we display two magnetized BH solutions (with different values of the charge) and two TSs, of the first and second kind, respectively.

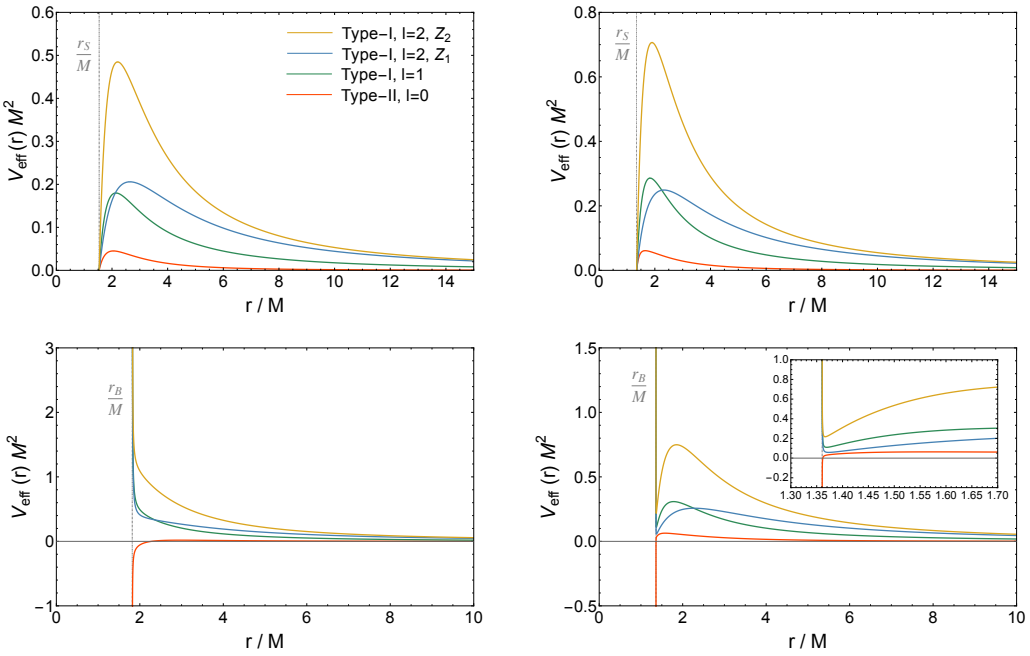

Figure 6.2. Effective potentials $V_{\rm eff}$ for perturbations of a magnetized BH: top left $eQ_m/M = 1.032$ (equivalently $r_B/r_S = 0.6$), top right $eQ_m/M = 1.149$ ($r_B/r_S = 0.97$); and a TS: bottom left $eQ_m/M = 1.220$ ($r_B/r_S = 1.67$), bottom right $eQ_m/M = 1.160$ ($r_B/r_S = 1.03$).

For the magnetized BHs, the effective potentials possess the standard shape: they go to zero at both boundaries (the horizon and asymptotic infinity) and present a single maximum that in the eikonal limit $l \gg 1$ corresponds to the unstable photon sphere. On the contrary, the effective potentials of TSs have a richer structure. In all cases the potential diverges for positive values at $r = r_B$, except for the radial case, where it diverges for *negative* values. Despite this fact, we have not found any unstable mode or signature of linear instability for $r_B < 2r_S$, as later discussed.

In addition, the form of the effective potentials for $l > 0$ Type-I perturbations is highly sensitive to the underlying background solution: only compact TSs of the second-kind have an unstable photon sphere at some $r > r_B$, so that they display a local maximum, a cavity, and finally a positively diverging potential at $r = r_B$. As

already anticipated, this shape of the potential naturally supports long-lived QNMs as we will explicitly show.

6.2.4 Nonradial Type-II perturbations

As anticipated, the perturbed equations for the nonradial Type-II sector are all coupled and it is not straightforward to derive a single master equation for each case.

The simplest Type-II mode, after the monopole $l = 0$ discussed above, is the dipole $l = 1$, that contains scalar and axial EM perturbations, since the gravitational perturbations are non-dynamical. The evolution equations for the two dynamical degrees of freedom corresponding to Type-II perturbations with $l = 1$ are given by

$$\mathcal{D}[\Upsilon_i] + \sum_{j=1,2} W_{ij}\partial_r \Upsilon_j - \sum_{j=1,2} V_{ij}\Upsilon_j = 0\,, \tag{6.56}$$

where $i\,, j = 1, 2$ and the differential operator is defined in Eq. (6.35). The dynamical fields, which correspond, respectively, to scalar-driven and electromagnetic-driven perturbations, are defined in Eqs. (D.43)- (D.44). The coefficients appearing in Eq. (6.56) are reported in Appendix D.

For $l \geq 2$, there are three dynamical degrees of freedom: a scalar, an axial EM, and a polar gravitational mode. They are described by the equations:

$$\mathcal{D}[\tilde{\Upsilon}_i] + \sum_{j=1,2,3} \tilde{W}_{ij}\partial_r \tilde{\Upsilon}_j - \sum_{j=1,2,3} \tilde{V}_{ij}\tilde{\Upsilon}_j + \sum_{j=1,2,3} \tilde{U}_{ij}\partial_r^2 \tilde{\Upsilon}_j = 0 \tag{6.57}$$

where $\{\tilde{\Upsilon}\}_{i=1,2,3} = \{\Phi, \mathcal{B}, \mathcal{R}^+\}$ are the scalar-driven, electromagnetic-driven and gravity-driven perturbation fields defined in Appendix D. Also in this case the explicit coefficients are reported in detail in Appendix D.

6.3 Boundary conditions

In order to solve the perturbed equations of Sec. 6.2, we need to impose the appropriate boundary conditions. Since both the solutions of magnetized BH and TS reduce to Minkowski spacetime at infinity, in that case we require purely outgoing waves. A different boundary condition prescription is instead applied at the inner boundary (at the horizon r_S for the BH, and at r_B for the TS), depending on the background spacetime. If the background solution is a BH, we impose radiative purely ingoing BCs at the horizon, $r = r_S$. On the contrary, if the background is a TS, we impose regularity of the perturbation at the boundary $r = r_B$. More in detail, for a generic array of perturbations Ψ, we impose the series expansion

$$\Psi = (r - r_B)^\lambda \sum_{i=0}^{\infty} c_i (r - r_B)^i\,. \tag{6.58}$$

By inserting the above expansion into the linearized perturbed equation, we obtain two independent solutions by solving the indicial equation for λ. In all cases under consideration, only one of the two solutions is regular at $r = r_B$. As usual, the

coefficients c_i with $i > 0$ can be derived in terms of c_0 by solving the field equations order by order close to the inner boundary. In order to improve numerical accuracy, we solve the field equations near both boundaries perturbatively to high order.

As a representative example, we consider the case of Type-I $l = 1$ perturbations, whose equation is

$$\mathcal{E}''(r) + \frac{1}{(r-r_B)}\left(\frac{r(2r_B+r_S)-3r_Br_S}{r(r-r_S)}\right)\mathcal{E}'(r) + \frac{1}{(r-r_B)}\left(\frac{\omega^2r^4-2r^2-2r(r_B-r_S)+2r_Br_S}{r(r-r_S)^2}\right)\mathcal{E}(r) = 0\,. \tag{6.59}$$

By using the series expansion of Eq. (6.58), we get the indicial equation $\lambda(1+\lambda) = 0$, therefore, the two linearly independent solutions are

$$\mathcal{E}_1(r) = \sum_{i=0}^{\infty} a_i (r-r_B)^i \tag{6.60}$$

$$\mathcal{E}_2(r) = (r-r_B)^{-1}\sum_{i=0}^{\infty} b_i (r-r_B)^i + \alpha \log(r-r_B)\mathcal{E}_1(r)\,. \tag{6.61}$$

The second solution is divergent at $r = r_B$. For the QNMs computation in the frequency domain it is enough to pick the solution with $\lambda = 0$. A general solution, instead, would be a linear combination of the two independent solutions, that after reabsorbing some coefficients, reads $\mathcal{E}(x) = (a_0+a_1x+...)+\frac{b_0}{x}+\alpha\log(x)(c_0+c_1x+...)$, with $x = r - r_B$. This suggests that the regularity condition $x\partial_x\mathcal{E}|_{x=0} = 0$ implies correctly $b_0 = 0 = \alpha c_0$.

As a second illustrative case, we consider the equation for Type-II radial perturbations, whose indicial equation gives $\lambda^2 = 0$. The most general solution in the asymptotic limit $r \to r_B$ can be written as

$$\varphi(r) = \sum_{i=0}^{\infty} a_i (r-r_B)^i + \log(r-r_B)\sum_{i=0}^{\infty} b_i (r-r_B)^i \tag{6.62}$$

As explained before, we can ask for regularity by imposing $x\partial_x\varphi|_{x=0} = 0$. A similar procedure applies to any kind of perturbations, including those in coupled systems.

It should be noted that regularity is not required in the four-dimensional compactification as long as it is guaranteed in the five-dimensional uplift. In the case discussed here, namely with zero momentum along the fifth compact dimension, regularity of the perturbations in four dimensions also implies regularity in five dimensions. Indeed, as discussed in [290, 292], perturbation equations derived in the five-dimensional uplift correctly reduced to those derived in the four-dimensional framework in the limit of vanishing y-momentum. As a consequence, it is possible to verify that the regularity boundary conditions required for five-dimensional perturbations with trivial y-momentum coincide with those we employ for the four-dimensional perturbations. Moreover, for what regards the Type-I and radial Type-II sectors, our results are perfectly consistent with the independent analysis of [291], performed in five dimensions.

6.4 Spectroscopy and ringdown analysis

Having presented the perturbation equations and boundary conditions, we now turn to the discussion of the numerical results concerning the QNM spectrum of magnetized BHs and TSs of the first and second kind. Each sector will be analyzed separately to identify their common features and main differences. The QNMs results will be then compared with the ringdown signal of the two solutions, obtained by solving the perturbation equations in the time domain.

6.4.1 Type-I QNMs of magnetized BHs and TSs

Let us start by considering the Type-I sector, since it is simpler than the Type-II case. Indeed, the Type-I sector couples axial gravitational perturbations with polar EM ones, while the scalar perturbation is polar and belongs to the Type-II sector. As a consequence the Type-I case features fewer degrees of freedom and does not possess the $l = 0$ mode.

$l = 1$ dipolar perturbations

In order to study $l = 1$ Type-I perturbations we need to solve the single master equation for the polar EM degree of freedom given by Eq. (6.48). The QNMs, computed with the direct integration method discussed in Sec. 2.4.1 and implementing the boundary conditions of Sec. 6.3, are reported in Table 6.1 for some representative examples of magnetized BHs and TSs. In particular, we consider a nearly-extremal magnetized BH with $eQ_m/M \approx 1.153$, a TS of the first kind with $eQ_m/M \approx 1.220$, and a TS of the second kind with $eQ_m/M \approx 1.157$, so with a charge-to-mass ratio very similar to that of the BH. The QNM frequencies obtained in the frequency domain via the direct integration method are compared to those computed by collaborators by means of the Fourier transform of the ringdown signal in the time domain (see [290] for more details on the method). The comparison shows a great agreement between the two methods, valid also for the perturbations discussed in the next sections and even for higher overtones. QNMs with a smaller quality factor, defined as $\omega_R/|\omega_I|$, are less accurate, because in this case the direct integration method is less efficient and the accuracy of the Fourier analysis of the ringdown is lost for short signals.

In the magnetized BH and first kind TS cases we only show the fundamental mode that is already quite damped. On the contrary, as expected from the effective potential analysis, for second-kind TSs we find long-lived modes QNMs. This allowed us to compute several overtones up to a point in which their imaginary part is comparable to that of an ordinary BH QNM.

In the top panel of Fig. 6.3 we show the fundamental QNM of magnetized BH as a function of Q_m/M up to the nearly-extremal case. As can be seen, the behavior of this mode is qualitatively similar to that of a Reissner-Nordström BH (see, e.g., [147]).

More interestingly, the top panels of Fig. 6.4 show the evolution of the fundamental mode and the first overtone of Type-I dipolar perturbations of the TS as a function of Q_m/M, highlighting the smooth transition between first- and second-kind

		Magnetized BH	TS, second kind	TS, first kind
0	ƒ	$0.530286 - i\,8.207 \times 10^{-2}$	$0.237163 - i\,1.326 \times 10^{-9}$	$0.752068 - i\,0.248$
	t	$0.530486 - i\,8.140 \times 10^{-2}$	$0.237247 - i\,1.412 \times 10^{-9}$	$0.759523 - i\,0.238$
1	ƒ	-	$0.30767 \quad - i\,1.24 \quad \times 10^{-7}$	-
	t	-	$0.307681 - i\,1.240 \times 10^{-7}$	-
2	ƒ	-	$0.376555 - i\,4.521 \times 10^{-6}$	-
	t	-	$0.376595 - i\,4.532 \times 10^{-6}$	-
3	ƒ	-	$0.443242 - i\,9.362 \times 10^{-5}$	-
	t	-	$0.44339 \quad - i\,9.34 \quad \times 10^{-5}$	-
4	ƒ	-	$0.506573 - i\,1.141 \times 10^{-3}$	-
	t	-	$0.50653 \quad - i\,1.41 \quad \times 10^{-3}$	-
5	ƒ	-	$0.566991 - i\,6.682 \times 10^{-3}$	-
	t	-	$0.56660 \quad - i\,6.950 \times 10^{-3}$	-
6	ƒ	-	$0.630407 - i\,1.955 \times 10^{-2}$	-
	t	-	$0.6269 \quad - i\,2.28 \quad \times 10^{-2}$	-

Table 6.1. Type-I QNMs, $l = 1$: magnetized BH with $eQ_m/M = 1.153$ (equivalently, $r_B/r_S = 0.99$), second kind TS with $eQ_m/M = 1.157$ ($r_B/r_S = 1.01$), and first kind TS with $eQ_m/M = 1.220$ ($r_B/r_S = 1.67$). For the magnetized BH and first-kind TS we computed only the fundamental mode ($n = 0$), while for the second-kind TS we computed also the first overtones ($n = 1, 2, 3, ...$). The QNMs computed in the frequency domain with the direct integration method are also compared to those those extracted from the Fourier transform of the time domain signal (see [290] for further details on the procedure carried out by other collaborators). Here and in subsequent tables, the QNMs are normalized by the mass, i.e. we show the complex quantity $M\omega$, and - means that the mode has not been computed. The notation ƒ and t indicates the modes computed in the frequency and time domain, respectively.

solutions. As expected, first-kind solutions exhibit BH-like modes, whose imaginary parts are only slightly smaller than the real ones, resembling the so-called w-modes of a neutron star [146]. On the contrary, when the charge-to-mass ratio decreases, the solution develops a stable photon sphere that is able to excite long-lived modes. By comparing the fundamental mode ($n = 0$) and the first overtone ($n = 1$), one can note that the damping time of the latter is longer than that of the former for any Q_m (i.e., the curves on the right panel do not cross each other), so the fundamental mode does not change during the tracking at different Q_m.

In the left panel of Fig. 6.5 we also reported the modes for different values of Q_m/M in the complex (ω_R, ω_I) plane. In this case the transition between first kind and second kind TSs is more clear.

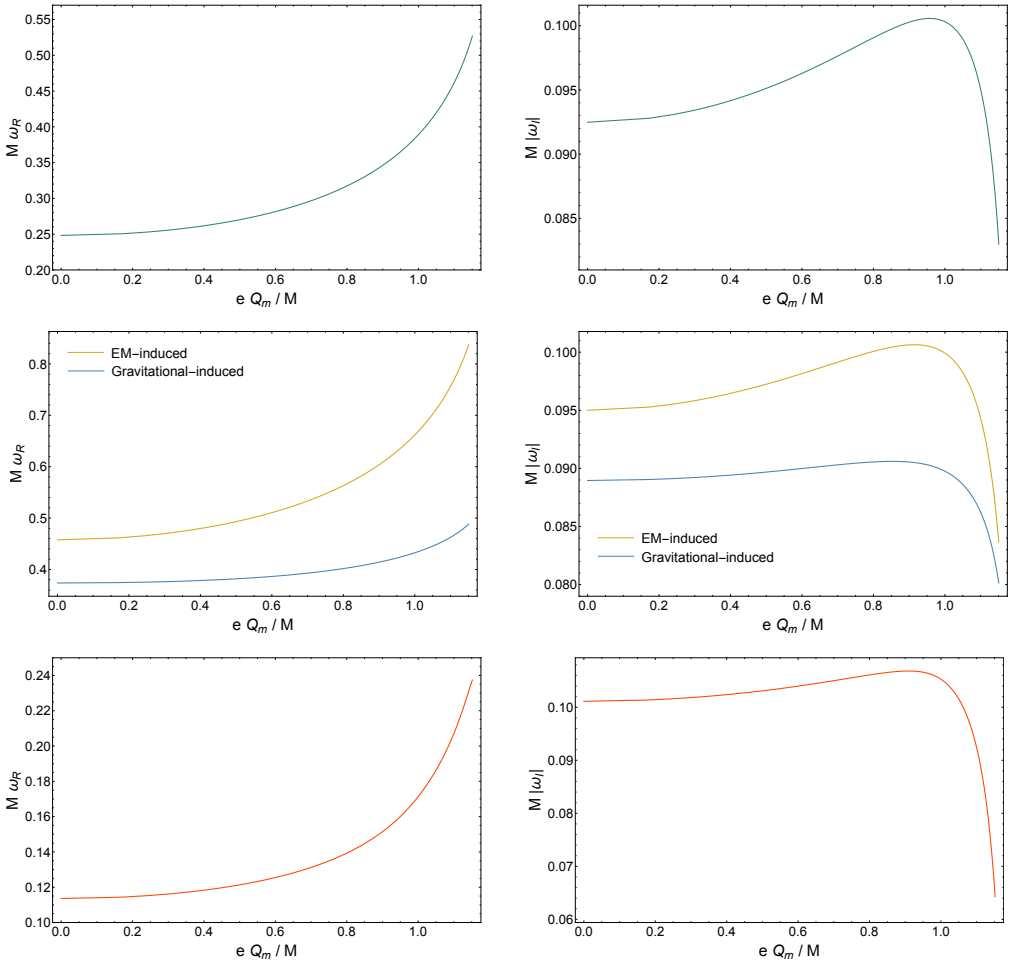

Figure 6.3. Fundamental QNMs of a magnetized BH as a function of the magnetic charge. The left (right) panels show the real (imaginary) part of the mode. Top panels: even EM perturbations (Type-I, $l = 1$). Middle panels: even EM and odd metric perturbations (Type-I, $l = 2$). Bottom panels: scalar perturbations (Type-II, $l = 0$).

$l \geq 2$ perturbations

The perturbations of the $l \geq 2$ Type-I sector are described by the two decoupled Eqs. (6.46). However, the gravitational and EM degrees of freedom are anyway mixed. Nevertheless, one can notice that, in the decoupling limit ($r_B \to 0$), the master variables Z_1 and Z_2 are associated to gravitational and EM perturbations of a Schwarzschild BH, respectively. Therefore, in what follows, we will refer to modes coming from the first and second equation in (6.46) as *gravitational-induced* and *EM-induced*, respectively, even for generic values of r_B/r_S. The frequencies of the QNMs are reported in Table 6.2 and Table 6.3, both for BHs and TSs, and for the gravitational-induced and EM-induced modes, respectively. Some modes of both families are tracked as function of Q_m/M in the middle panels of Fig. 6.3 and Fig. 6.4 for BHs and TSs, respectively. Beside the presence of an extra degree of freedom, we observe the same qualitative behavior as previously discussed for $l = 1$

Type-I modes.

		Magnetized BH	TS, second kind	TS, first kind
0	ʃ	$0.489568 - i\,7.972 \times 10^{-2}$	$0.183217 - i\,4.674 \times 10^{-10}$	$0.644348 - i\,0.1551$
	t	$0.489600 - i\,7.978 \times 10^{-2}$	$0.183219 - i\,3.349 \times 10^{-10}$	$0.643938 - i\,0.1665$
1	ʃ	-	$0.254071 - i\,6.001 \times 10^{-8}$	-
	t	-	$0.254084 - i\,6.008 \times 10^{-8}$	-
2	ʃ	-	$0.323219 - i\,2.615 \times 10^{-6}$	-
	t	-	$0.323263 - i\,2.622 \times 10^{-6}$	-
3	ʃ	-	$0.390169 - i\,6.116 \times 10^{-5}$	-
	t	-	$0.390256 - i\,6.142 \times 10^{-5}$	-
4	ʃ	-	$0.453786 - i\,8.348 \times 10^{-4}$	-
	t	-	$0.453832 - i\,8.340 \times 10^{-4}$	-
5	ʃ	-	$0.513765 - i\,5.463 \times 10^{-3}$	-
	t	-	$0.513375 - i\,2.754 \times 10^{-3}$	-
6	ʃ	-	$0.574947 - i\,1.658 \times 10^{-2}$	-
	t	-	$0.572869 - i\,1.140 \times 10^{-2}$	-

Table 6.2. Same as Table 6.1 but for $l = 2$, gravitational-induced Type-I perturbations.

		Magnetized BH	TS, second kind	TS, first kind
0	ʃ	$0.841470 - i\,8.294 \times 10^{-2}$	$0.315245 - i\,4.949 \times 10^{-15}$	$1.09087 - i\,0.1836$
	t	$0.841302 - i\,8.296 \times 10^{-2}$	$0.315258 - i\,(*)$	$1.09109 - i\,0.2110$
1	ʃ	-	$0.386772 - i\,1.074 \times 10^{-12}$	-
	t	-	$0.386809 - i\,(*)$	-
2	ʃ	-	$0.457413 - i\,8.441 \times 10^{-11}$	-
	t	-	$0.457631 - i\,(*)$	-
3	ʃ	-	$0.527134 - i\,3.691 \times 10^{-9}$	-
	t	-	$0.527232 - i\,3.697 \times 10^{-9}$	-
4	ʃ	-	$0.596474 - i\,1.133 \times 10^{-7}$	-
	t	-	$0.595908 - i\,1.077 \times 10^{-7}$	-
5	ʃ	-	$0.668166 - i\,3.204 \times 10^{-6}$	-
	t	-	$0.663237 - i\,2.284 \times 10^{-6}$	-

Table 6.3. Same as Table 6.2 but for EM-induced perturbations. The $(*)$ in the t-domain rows of the fundamental and first two overtones indicate that in these cases it was not possible to estimate the imaginary part of the frequency with sufficient accuracy.

6.4.2 Type-II QNMs of magnetized BHs and TSs

As anticipated in Sec. 6.2, the case of Type-II perturbations is more involved because of the larger number of degrees of freedom of perturbations. Moreover, only in the radial ($l = 0$) case it is possible to derive a single master equation for the perturbations, whereas in all other cases they remain mutually coupled.

Radial ($l = 0$) Type-II perturbations

Radial ($l = 0$) perturbations only exist in the Type-II sector since in this case only the (polar, i.e. even-parity) scalar perturbations are dynamical and described by Eq. (6.50). This sector is noteworthy since, as shown in Fig. 6.2, the TS effective potential diverges negatively as $r \to r_B$, which could correspond to an instability in the spectrum, namely QNMs with a positive imaginary part. Our search for unstable modes yielded no evidence of instabilities for $r_B < 2r_S$. This result is consistent with the time-domain evolution discussed in Sec. 6.5, where no growing modes are observed.

In Table 6.4 we present the fundamental QNMs and the first three overtones for radial Type-II perturbations of magnetized BHs and TSs. The fundamental mode of magnetized BHs and the $n = 0, 1$ modes of TSs as a function of the charge-to-mass ratio are presented in the bottom panels of Figs. 6.3 and 6.4, respectively.

As discussed in Sec. 6.1.1, magnetized black strings with $r_B \leq r_S/2$ suffer the well-known Gregory-Laflamme instability. Due to the duality $(t, y, r_S, r_B) \to (iy, it, r_B, r_S)$ that maps magnetized black strings to TSs and viceversa [298], also TSs with $r_B > 2r_S$ are unstable under radial perturbations with purely imaginary frequency. In agreement with the analysis in [298], for TSs with $r_B > 2r_S$ we found an unstable purely imaginary mode, i.e. $\omega = i\omega_I$ with $\omega_I > 0$, for radial perturbations with zero Kaluza-Klein momentum. As shown in Fig. 6.6, the frequency approaches zero in the $r_B = 2r_S$ limit, thus reaching the threshold of the Gregory-Laflamme zero mode of the corresponding black string.

		Magnetized BH	**TS, second kind**	**TS, first kind**
0	ƒ	$0.237009 - i\,6.249 \times 10^{-2}$	$0.143401 - i\,1.113 \times 10^{-5}$	$0.135919 - i\,5.716 \times 10^{-2}$
	t	$0.237393 - i\,5.953 \times 10^{-2}$	$0.143224 - i\,1.092 \times 10^{-5}$	$0.133896 - i\,2.986 \times 10^{-2}$
1	ƒ	-	$0.208064 - i\,6.541 \times 10^{-4}$	-
	t	-	$0.207059 - i\,6.065 \times 10^{-4}$	-
2	ƒ	-	$0.266300 - i\,7.071 \times 10^{-3}$	-
	t	-	$0.263869 - i\,6.273 \times 10^{-3}$	-
3	ƒ	-	$0.325630 - i\,2.225 \times 10^{-2}$	-
	t	-	$0.322313 - i\,2.612 \times 10^{-2}$	-

Table 6.4. Same as Table 6.1 but for radial (Type-II, $l = 0$) perturbations.

Nonradial Type-II perturbations

The QNM frequencies of the nonradial Type-II perturbations are computed by solving Eq. (6.56) and Eq. (6.57). In this case, both for $l = 1$ and $l \geq 2$ the equations are all coupled so the individual contribution of each perturbation to each mode cannot be isolated. However, similarly to the case of $l \geq 2$ Type-I perturbations, we can distinguish 3 different families of modes associated to the gravitational-, electromagnetic-, and scalar-driven perturbations in the neutral limit ($Q_m \to 0$). The QNMs are ordered accordingly to their imaginary part and labeled with an integer $p = 0, 1, 2, ..$, with $p = 0$ denoting the mode with the smallest imaginary part

(in absolute value). Note that this classification does not differentiate among modes belonging to different families (i.e., gravitational-, electromagnetic-, or scalar-driven).

The results for magnetized BHs are summarized in Fig. 6.7 for $l = 1$ (top panels) and $l = 2$ (bottom panels). For $l = 2$, we have all the gravitational-, electromagnetic-, and scalar-driven perturbations, while for $l = 1$, only the electromagnetic- and scalar-driven modes are present, since the gravitational ones do not propagate.

Also in this case there is a great agreement between the frequencies computed with the direction integration method and those extracted from the ringdown signal, as can be seen from Table 6.5 for selected cases and the first two tones.

$r_S/r_B =$			3/2	105/100
$l = 1$	$p = 0$	f-domain	$0.475099 - i\,9.839 \times 10^{-2}$	$0.560557 - i\,8.253 \times 10^{-2}$
		t-domain	$0.475190 - i\,9.838 \times 10^{-2}$	$0.560590 - i\,8.253 \times 10^{-2}$
	$p = 1$	f-domain	$0.354988 - i\,9.783 \times 10^{-2}$	$0.420558 - i\,8.874 \times 10^{-2}$
		t-domain	$0.354371 - i\,9.776 \times 10^{-2}$	$0.421263 - i\,8.647 \times 10^{-2}$

$r_S/r_B =$			3/2	105/100
$l = 2$	$p = 0$	f-domain	$0.746666 - i\,9.787 \times 10^{-2}$	$0.860856 - i\,8.465 \times 10^{-2}$
		t-domain	$0.746698 - i\,9.754 \times 10^{-2}$	$0.860790 - i\,8.451 \times 10^{-2}$
	$p = 1$	f-domain	$0.623768 - i\,9.629 \times 10^{-2}$	$0.706721 - i\,8.691 \times 10^{-2}$
		t-domain	$0.622475 - i\,9.716 \times 10^{-2}$	$0.706936 - i\,8.659 \times 10^{-2}$
	$p = 2$	f-domain	$0.441539 - i\,8.722 \times 10^{-2}$	$0.470346 - i\,8.122 \times 10^{-2}$
		t-domain	$0.441655 - i\,8.832 \times 10^{-2}$	$0.470706 - i\,8.112 \times 10^{-2}$

Table 6.5. Type-II QNMs of magnetized BH with $eQ_m/M \approx \{1.061\,, 1.116\,, 1.153\}$ for $l = 1$ (top table) and $l = 2$ (bottom table). Modes with $p = 0, 1$ correspond to scalar-driven and electromagnetic-driven perturbations, whereas $p = 2$ denotes gravitational-driven perturbations (which are not dynamical for $l = 1$).

The results for Type-II QNMs of TSs are plotted in Fig. 6.8 for the relevant cases of $l = 1, 2$. One can see that the mode hierarchy depends on the charge, since there are crossings in the imaginary part. Hints of a similar phenomenon can possibly be observed in other models [305], in which the modes of test-field perturbations of regular compact stars exhibit similar crossings.

We classify $p = 0, 1, 2, ...$ modes referring to the region near the BH transition (i.e., smallest value of eQ_m/M).

We again compare the QNMs computed in the frequency domain with those extracted from the time-domain response (see Table 6.6), observing excellent consistency between the two approaches.

As in the Type-I sector, the QNM spectrum of TSs continuously evolves from BH-like modes in first kind solutions to long-lived modes characteristic of second kind TSs.

$r_S/r_B =$			19/20	99/100
$l=1$	$p=0$	f-domain	$0.463193 - i\,2.163 \times 10^{-5}$	$0.221521 - i\,1.967 \times 10^{-11}$
		t-domain	$0.463183 - i\,2.160 \times 10^{-5}$	$0.221438 - i\,2.110 \times 10^{-11}$
	$p=1$	f-domain	$0.581303 - i\,4.013 \times 10^{-3}$	$0.293106 - i\,4.147 \times 10^{-9}$
		t-domain	$0.581265 - i\,4.006 \times 10^{-3}$	$0.292507 - i\,4.089 \times 10^{-9}$
	$p=2$	f-domain	$0.441270 - i\,3.926 \times 10^{-3}$	$0.220050 - i\,1.896 \times 10^{-7}$
		t-domain	$0.441245 - i\,3.910 \times 10^{-3}$	$0.220049 - i\,1.875 \times 10^{-7}$
	$p=3$	f-domain	$0.681979 - i\,3.779 \times 10^{-2}$	$0.362912 - i\,2.424 \times 10^{-7}$
		t-domain	$0.682161 - i\,3.173 \times 10^{-2}$	$0.362168 - i\,2.329 \times 10^{-7}$
$r_S/r_B =$			19/20	99/100
$l=2$	$p=0$	f-domain	$0.630961 - i\,2.895 \times 10^{-8}$	$0.368629 - i\,3.221 \times 10^{-14}$
		t-domain	$0.630844 - i\,3.245 \times 10^{-8}$	$0.368733 - i\,(*)$
	$p=1$	f-domain	$0.317783 - i\,5.510 \times 10^{-6}$	$0.295274 - i\,3.206 \times 10^{-12}$
		t-domain	$0.317827 - i\,5.551 \times 10^{-6}$	$0.295660 - i\,(*)$
	$p=2$	f-domain	$0.764893 - i\,2.534 \times 10^{-5}$	$0.439992 - i\,3.944 \times 10^{-12}$
		t-domain	$0.765489 - i\,3.821 \times 10^{-5}$	$0.440391 - i\,(*)$
	$p=3$	f-domain	$0.616095 - i\,4.239 \times 10^{-5}$	$0.148446 - i\,6.337 \times 10^{-11}$
		t-domain	$0.616099 - i\,4.103 \times 10^{-5}$	$0.148477 - i\,6.262 \times 10^{-11}$

Table 6.6. Same as in Table 6.5 but for TSs with $eQ_m/M \approx \{1.208\,, 1.174\,, 1.164\,, 1.157\}$ (equivalently, $r_S/r_B = \{0.70\,, 0.90\,, 0.95\,, 0.99\}$). The asterisk indicates QNMs with a characteristic damping time that is too large for the spectral analysis to retrieve an accurate fit thereof.

6.5 Ringdown signal and comparison between magnetized BHs and TSs

As anticipated from the comparison between the QNMs computed in the frequency domain using the direct integration method and those extracted via Fourier transform from the ringdown signal, the perturbation equations have also been integrated in the time domain by collaborators (see Refs. [290, 292] for a detailed discussion of the numerical methods and techniques employed). The ringdown signal is shown for some selected cases in Fig. 6.9. More in detail, three specific cases are reported: dipolar ($l = 1$) Type-I perturbations (polar EM), and radial ($l = 0$) Type-II perturbations (scalar) in the top panels; quadrupolar ($l = 2$) Type-I perturbations (axial metric and polar EM) in the middle panel; dipolar ($l = 1$) Type-II perturbations (scalar and axial EM) in the bottom panel. Each plot displays the comparison between the ringdown response of a nearly extremal magnetized BH and a second kind TS with a very similar charge to mass ratio. In other words, we consider a magnetized BH and a TS slightly below and above the $r_B/r_S = 1$ threshold, respectively. Since, as discussed, all the results are normalized by the mass of the solution, the BH and TS present the same mass and a very similar charge (as shown in the phase diagram 6.1, it is not possible to have TSs and BHs with exactly the same charge-to-mass ratio). Under these conditions, the effective potentials (when present) for BH and TS exhibit almost identical profiles at large radii and remain closely matched down to the inner region, as shown in Fig. 6.10 for dipolar Type-I perturbations; similar

behavior is found in the other sectors. As can be seen from Fig. 6.10, the potentials are very similar around the maximum, whose shape is responsible for the prompt ringdown in the time domain. Conversely, approaching the inner boundary, their behavior is completely different: the potential vanishes as $r \to r_S$ for the BH while it diverges to positive values as $r \to r_B$ for the TS. The effective potential for the TS, before diverging, develops a cavity supporting the long-lived modes discussed in the previous section, which dominate the signal at late times. This description is indeed consistent with all the signal comparisons shown in Fig. 6.9. The initial response is almost indistinguishable between the two cases, with differences due to the slightly different charge-to-mass ratio. On the contrary, at late time the signal is dominated by echoes associated with perturbations being reflected back and forth between the inner boundary and the unstable photon sphere.

The ringdown response does not possess the echo pattern in the case of first kind TS. As presented in the plots, due to the absence of unstable photon sphere, in this case the response does not show long-lived modes and the prompt ringdown is completely different from the BH case, even though the charge-to-mass ratio is only $\approx 6\%$ different.

TSs thus provide a robust and physically consistent realization of ultracompact objects, where the time domain response naturally evolves across different regimes and eventually produces distinct GW echoes. This extends earlier studies of ultracompact objects, which typically relied on simplified or phenomenological setups, or on test-field approximations (see [22] for an overview).

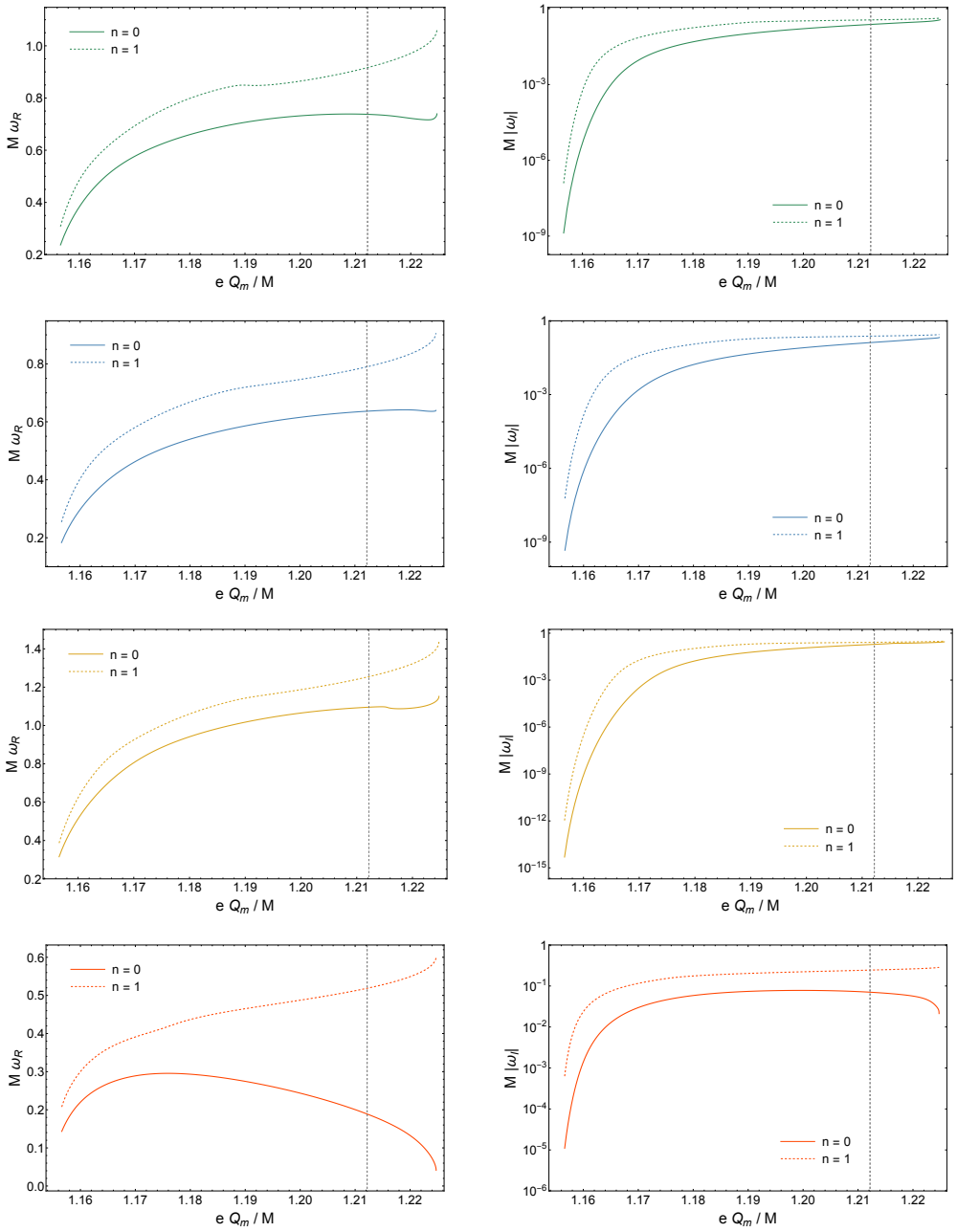

Figure 6.4. Same as Fig. 6.3 but for TSs. Note that in this case the modes smoothly interpolate between being long-lived for a TS of the second kind to BH-like modes for a TS of the first kind (the vertical dashed line denotes the transition between the two regimes). First panels: even EM perturbations (Type I, $l = 1$). Second and third panels: odd metric and even EM perturbations (Type I, $l = 2$) respectively. Fourth panels scalar perturbations (Type II, $l = 0$).

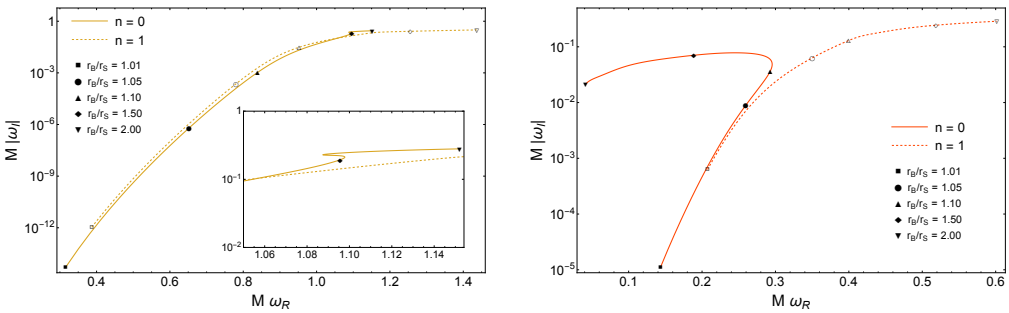

Figure 6.5. Fundamental QNMs for TSs of even EM perturbations (Type I, $l = 1$, left panel) and scalar perturbations (Type II, $l = 0$, right panel).

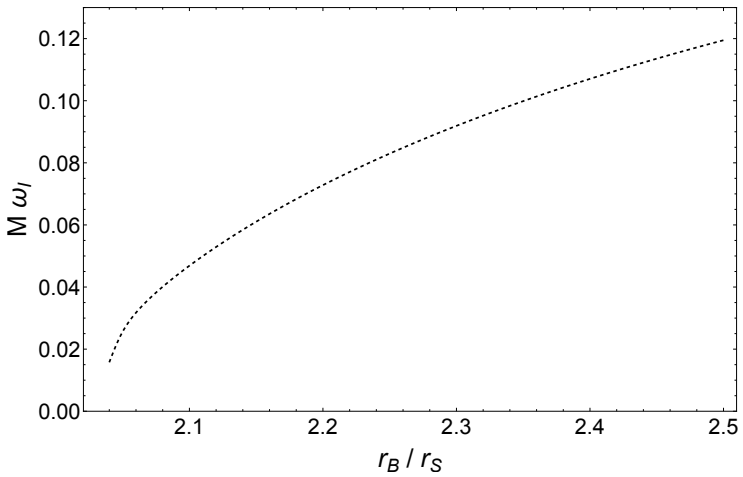

Figure 6.6. Purely imaginary frequency of the unstable mode of a TS as a function of r_B/r_S under scalar perturbations (Type II, $l = 0$). This instability exists only for $r_B > 2r_S$.

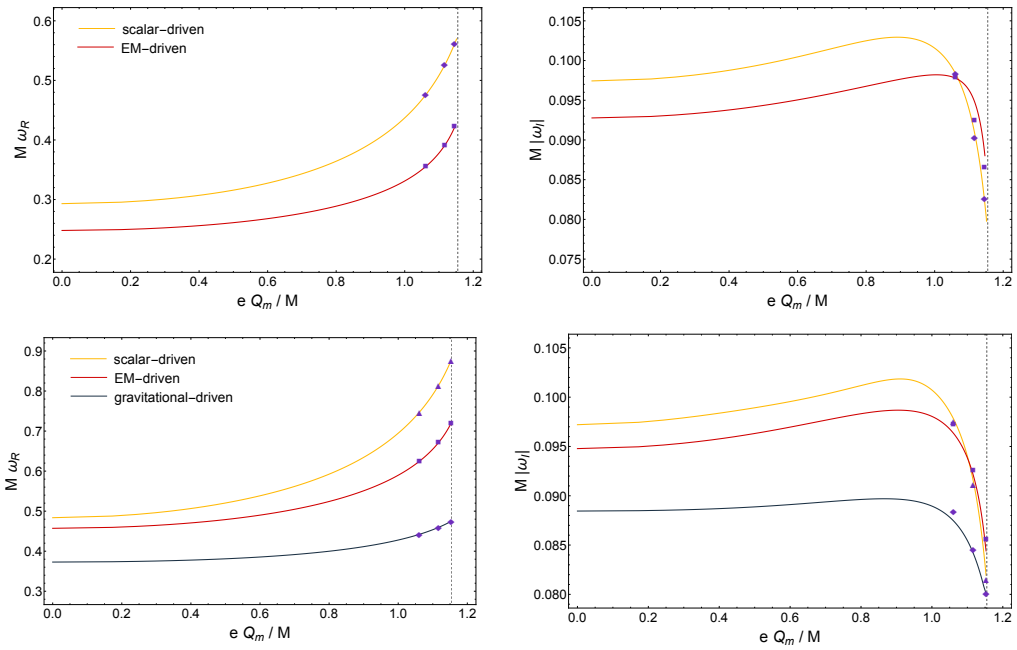

Figure 6.7. QNMs of a magnetized BH as a function of the magnetic charge for Type-II perturbations. Top panels refer to $l = 1$, electromagnetic and scalar perturbations, while bottom panels refer to $l = 2$ gravitational, electromagnetic, and scalar perturbations. The left (right) panels show the real (imaginary) part of the mode. In the limit $r_B \to 0$, i.e. $Q_m \to 0$, the frequencies are those of the fundamental QNMs for test scalar, vector and spin-2 tensor fields in the background of the Schwarzschild BH. The vertical dashed line denotes the extremal BH. The solid lines where obtained with the f-domain method, while the markers corresponds to the modes extracted from the Fourier transform of the time-domain signal (see [292]). We classify the modes based on the hierarchy also in terms of p: for $l = 1$, $p = 0, 1$ correspond to electromagnetic- and scalar-driven modes, respectively; whereas for $l = 2$, $p = 0, 1, 2$ correspond to gravitational-, electromagnetic- and scalar-driven modes, respectively.

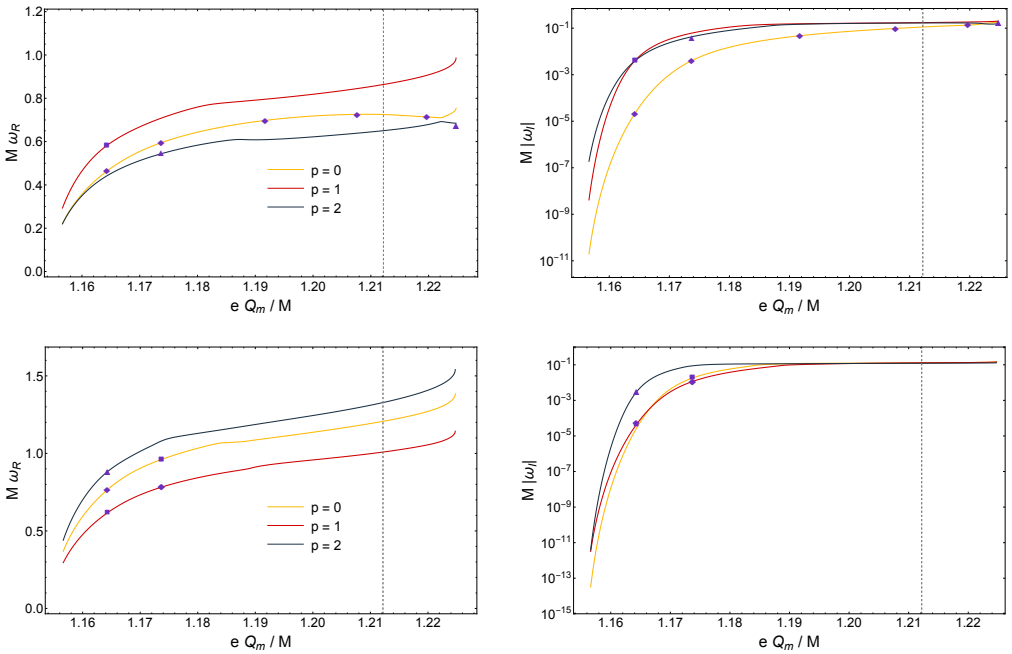

Figure 6.8. The first $p = 0, 1, 2$ QNMs of a TS as a function of the magnetic charge for Type-II, $l = 1$ (top panels) and $l = 2$ (bottom panels) perturbations. The left (right) panels show the real (imaginary) part of the mode. The vertical dashed line denotes the transition between second-kind and first-kind TS. The markers corresponds to the modes extracted from the Fourier transform of the time-domain signal. Note that the mode hierarchy (labeled by p) depends on the charge, since there are crossings in the imaginary part.

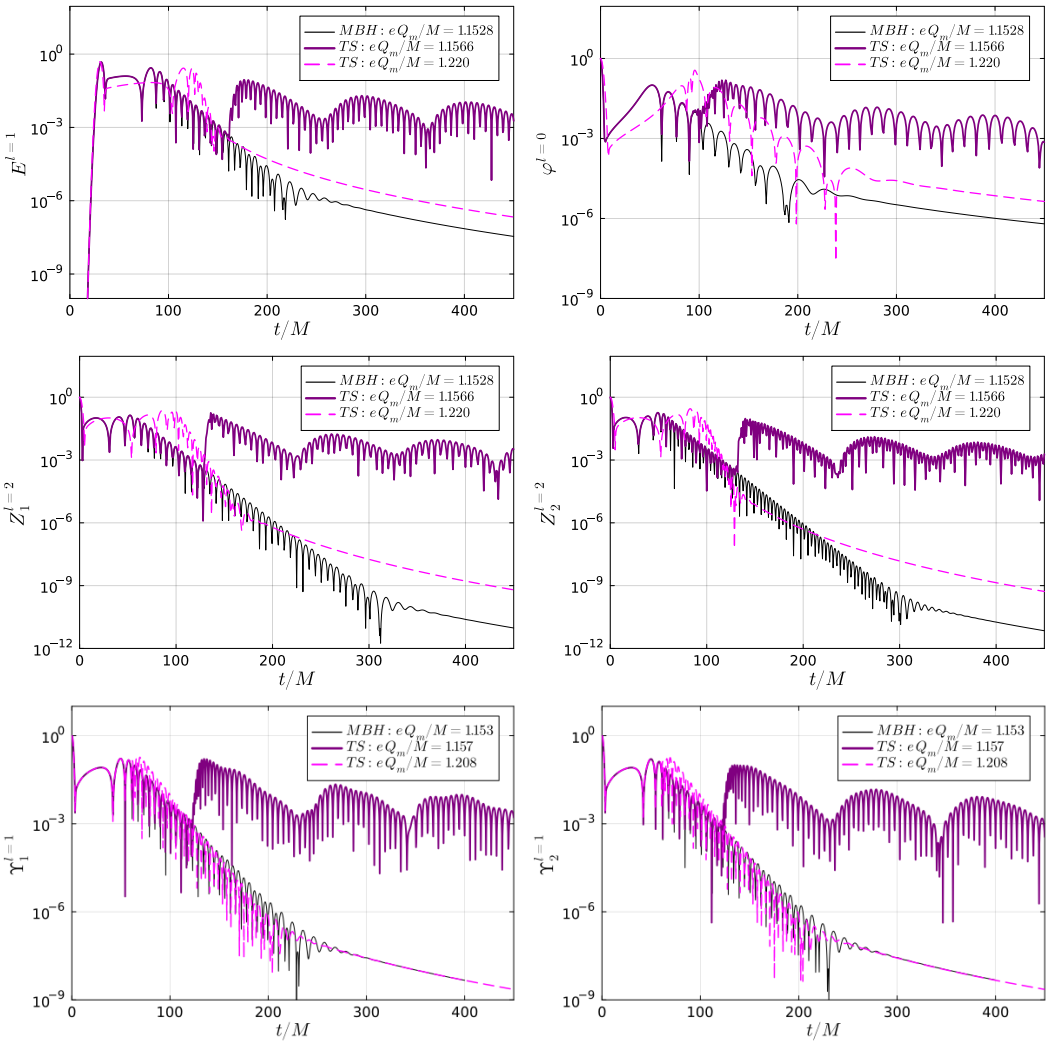

Figure 6.9. Comparison between the linear response of a nearly-extremal magnetized BH (black curve), a second-kind TS with same mass and similar charge-to-mass ratio (purple curve), and a first-kind TS (magenta curve). The top panels are for Type-I $l = 1$ perturbations (left panel) and Type-II $l = 0$ perturbations (right panel). Middle panels are for $l = 2$ Type-I perturbations: left and right panel referring to gravitational-driven and EM-driven perturbations, respectively. Finally, the bottom panels are for $l = 1$ Type-II perturbations: the left and right panels referring to scalar-driven and electromagnetic-driven perturbations, respectively. The plots shown were obtained by collaborators (credits to A. Dima); the numerical methods adopted to integrate the perturbation equations in the time domain are discussed in [290, 292].

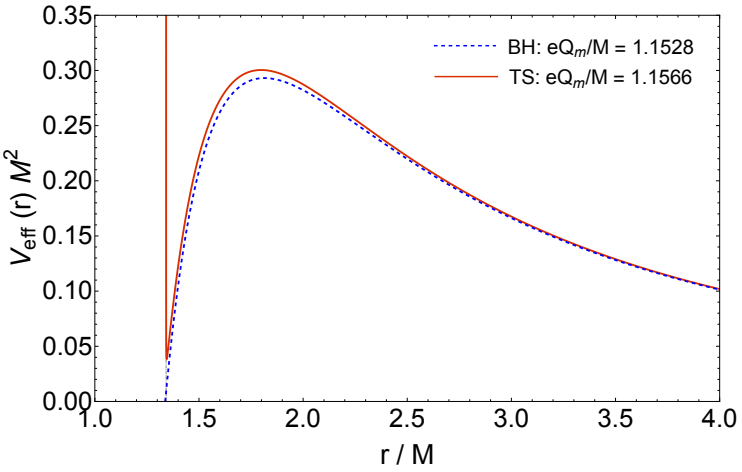

Figure 6.10. Comparison between the effective potentials for $l = 1$ Type-I perturbations of a magnetized BH with $eQ_m/M \approx 1.1528$ and a TS with $eQ_m/M \approx 1.1566$.

Chapter 7

EMRIs with TSs

In this chapter we investigate the dynamics of EMRIs when the central object is a TS rather than a classical BH. The purpose of this study, based on the original work of Ref. [306], is to highlight the phenomenological consequences arising in the absence of an event horizon in the specific case of the TS. We will focus, for convenience, on the scalar radiation emitted by a test scalar charge moving along circular orbits in the TS (and magnetized BH) background spacetime.

This analysis confirms what anticipated on EMRIs with ECOs in Sec. 3.3. After deriving the scalar field equation and the associated energy fluxes both at infinity and (for the BH case) through the horizon, we compute the total radiated power and analyze its dependence on the orbital radius. Particular attention is devoted to the appearance of resonances in the TS case, which are associated with the excitation of long-lived modes trapped within the potential well of the background spacetime. Finally, we evaluate the cumulative dephasing between inspirals around TSs and magnetized BHs, discussing the potential observational relevance of these effects for future space-based gravitational-wave detectors.

Recently, Refs. [307–309] studied the scalar emission by a point test scalar charge moving around a TS. The analysis presented in this chapter further studies the dynamics and emission of a point test charge in orbital motion around these geometries, as a proxy for EMRIs that can be used to test the absence of BH horizons. At variance with the analysis in [307], we solve the full numerical problem for generic circular orbits, also beyond the weak-field approximation.

7.1 Scalar field equation

Let us consider a test scalar charge moving along circular orbits with null momentum along the y direction ($P_y = 0 = p$, see Eq. (6.23)), in the background of TSs or magnetized BHs. Without loss of generality we can restrict ourselves to the study of planar circular orbits ($\theta = \pi/2$) of radial distance $r_0 \geq r_{\rm ISCO}$, thanks to the spherical symmetry of the background.

The scalar field Φ satisfies the inhomogeneous Klein-Gordon equation below

$$\Box\Phi = \rho_p \,, \tag{7.1}$$

where ρ_p is the scalar charge density defined by the integral over the affine parameter

τ along the worldline of the particle

$$\rho_p = \mu\, q \int d\tau \frac{1}{\sqrt{-g}} \delta^{(5)}(x^\rho - z^\rho(\tau))\,, \tag{7.2}$$

where μ is the mass of the scalar charge, and the coupling q has the dimensions of a length if Φ is taken to be dimensionless. The test particle follows time-like geodesics defined by circular orbits at r_0, therefore, the five-dimensional Dirac delta function can be decomposed in the following way

$$\delta^{(5)}(x^\rho - z^\rho(\tau)) = \delta(t - u^t\tau)\delta(r - r_0)\delta(y)\delta\left(\theta - \frac{\pi}{2}\right)\delta(\varphi - \Omega t)\,. \tag{7.3}$$

By using the closure relation of scalar spherical harmonics and that the determinant of the metric is $\sqrt{-g} = r^2 \sin\theta$, after performing the integral we get

$$\rho_p = \frac{\mu q}{u^t r^2}\delta(r - r_0) \sum_n \frac{e^{in\frac{y}{R_y}}}{2\pi R_y} \sum_{lm} Y_{lm}(\theta,\varphi) Y^*_{lm}\left(\frac{\pi}{2}, 0\right) e^{-im\Omega t}\,, \tag{7.4}$$

where we have used the relation

$$\delta(y) = \sum_n \frac{e^{in\frac{y}{R_y}}}{2\pi R_y}\,. \tag{7.5}$$

If we apply the Fourier transform and we use the following identity

$$\delta(\omega - m\Omega) = \int \frac{dt}{2\pi} e^{i(\omega - m\Omega)t}\,, \tag{7.6}$$

we can write the source ρ_p in a more convenient way as follows

$$\rho_p = \sum_{nlm} \int \frac{d\omega}{2\pi} e^{i\omega t} \tilde{S}_{mln}(\omega, r) e^{in\frac{y}{R_y}} Y_{lm}(\theta,\varphi)\,, \tag{7.7}$$

where we defined

$$\tilde{S}_{mln}(\omega, r) \equiv \frac{\mu q}{u^t r^2 R_y}\delta(\omega - m\Omega)\delta(r - r_0) Y^*_{lm}\left(\frac{\pi}{2}, 0\right)\,. \tag{7.8}$$

The scalar field Φ can be expanded in spherical harmonics and Fourier transformed

$$\Phi = \sum_{nlm} \int \frac{d\omega}{2\pi} e^{-i\omega t} e^{in\frac{y}{R_y}} \psi_{nlm}(r) Y_{lm}(\theta,\varphi)\,, \tag{7.9}$$

in order to isolate the radial part of the Klein-Gordon equation

$$\left[f_S f_B \partial_r^2 + \frac{f_S + f_B}{r}\partial_r + \frac{\omega^2}{f_S} - \frac{n^2}{f_B R_y^2} - \frac{l(l+1)}{r^2}\right]\psi_{nlm}(r) = \tilde{S}_{nlm}(\omega, r)\,. \tag{7.10}$$

By introducing the tortoise coordinate $d\rho/dr = f_S^{-1} f_B^{-1/2}$ and performing the following field redefinition

$$\Psi_{nlm} = r f_B^{1/4} \psi_{nlm}\,, \tag{7.11}$$

we get a single Schrödinger-like equation,

$$\left[\partial_\rho^2 + (\omega^2 - V_{\rm eff})\right]\Psi_{nlm} = \mathcal{S}_{nlm}(\omega,\rho)\,, \tag{7.12}$$

where the effective potential is given by

$$V_{\rm eff} = \frac{r-r_S}{r-r_B}\left\{\frac{n^2}{R_y^2} + \frac{1}{16r^5}\Big[16r^3 l(l+1) + 21r_B^2 r_S + 8r^2(r_B - 2lr_B - 2l^2 r_B + 2r_S) - 9rr_B(r_B+4r_S)\Big]\right\}, \tag{7.13}$$

and the source is

$$\mathcal{S}_{nlm}(\omega,\rho) \equiv \frac{\mu q}{u^t R_y}\frac{f_S f_B^{1/4}}{r}\delta(\omega - m\Omega)\delta(r-r_0)Y^*_{lm}\left(\frac{\pi}{2},0\right). \tag{7.14}$$

From now on we will drop the nlm indices for notation convenience.

From Eq. (7.10) one can see that perturbations have a mass proportional to n/R_y and only the $n=0$ mode is massless and propagates to infinity as a free wave. In the phenomenologically interesting case $R_y \ll r_S$, the $n\neq 0$ modes have a large mass and are therefore exponentially suppressed on a length scale $R_y \ll r_S$. Thus, from now on we will focus on the massless $n=0$ modes only.

7.2 Energy flux

We now proceed with the derivation of the equations describing the scalar energy flux emitted at infinity and absorbed at the horizon r_S in the BH case.

The general solution of Eq. (7.12) can be written by means of the Green function solution of the equation sourced by a Dirac delta source $\delta(\rho-\rho')$

$$\Psi(\rho) = \frac{\Psi_+}{W}\int_{\rho_{\rm in}}^{\rho}\mathcal{S}(\omega,\rho')\Psi_- d\rho' + \frac{\Psi_-}{W}\int_{\rho}^{+\infty}\mathcal{S}(\omega,\rho')\Psi_+ d\rho'\,, \tag{7.15}$$

where $\rho_{\rm in}$ is the inner-boundary value of the tortoise coordinate, i.e. $\rho_{\rm in} = \{-\infty, \rho(r_B)\}$ for the magnetized BH and TS, respectively. Ψ_- and Ψ_+ are two independent solutions of the homogeneous equation, satisfying the boundary conditions presented below. Their corresponding Wronskian reads

$$W = \Psi_-\frac{d\Psi_+}{dr} - \Psi_+\frac{d\Psi_-}{dr}\,, \tag{7.16}$$

and does not depend on r by construction, as can be easily verified by means of Eq. (7.12) without the source term.

Asymptotically at spatial infinity ($r\to+\infty$), the two independent solutions Ψ_- and Ψ_+ behave as

$$\Psi_- \sim A_{\rm out}e^{i\omega\rho} + A_{\rm in}e^{-i\omega\rho} \tag{7.17}$$

$$\Psi_+ \sim e^{i\omega\rho}\,, \tag{7.18}$$

while their asymptotic behavior close to the inner boundary is sensitive to the specific background spacetime. For a magnetized BH, the boundary condition at $r \to r_S$ is

$$\Psi_- \sim (r - r_S)^{-ik_S\omega} \tag{7.19}$$

$$\Psi_+ \sim B_{\rm out}(r - r_S)^{ik_S\omega} + B_{\rm in}(r - r_S)^{-ik_S\omega}\,, \tag{7.20}$$

where $k_S \equiv r_S^{3/2}/\sqrt{r_S - r_B}$, and we used the radial coordinate r for convenience. In the case of a TS, the boundary condition at $r \to r_B$ reads

$$\Psi_- \sim (r - r_B)^{1/4} \tag{7.21}$$

$$\Psi_+ \sim C\,(r - r_B)^{1/4} + D(r - r_B)^{1/4}\log(r - r_B)\,. \tag{7.22}$$

Since $dW/dr = 0$, we can use the behavior of the two independent solutions at infinity to get $W = 2i\omega A_{\rm in}$. The final solution at asymptotic infinity is given by

$$\begin{aligned}\Psi_\infty &= \frac{e^{i\omega\rho}}{2i\omega A_{\rm in}}\int_{\rho_{\rm in}}^{+\infty}\mathcal{S}(\omega,\rho')\Psi_-(\rho')d\rho' = \frac{e^{i\omega\rho}}{2i\omega A_{\rm in}}\int_{r_{\rm in}}^{+\infty}\frac{dr'}{f_S f_B^{1/2}}\mathcal{S}(\omega,r')\Psi_-(r') \\ &= \frac{e^{i\omega\rho}}{2i\omega A_{\rm in}}\frac{\mu q}{u^t|_{r_0}R_y}\frac{\Psi_-(r_0)}{r_0 f_B^{1/4}(r_0)}\delta(\omega - m\Omega)Y^*_{lm}\left(\frac{\pi}{2},0\right)\,,\end{aligned} \tag{7.23}$$

where $r_{\rm in} = \{r_S, r_B\}$ for magnetized BH or TS, respectively. Similarly, the final solution near the horizon of the magnetized BH is

$$\begin{aligned}\Psi_{r_S} &= \frac{e^{-i\omega\rho}}{2i\omega A_{\rm in}}\int_{-\infty}^{+\infty}\mathcal{S}(\omega,\rho')\Psi_+(\rho')d\rho' \\ &= \frac{e^{-i\omega\rho}}{2i\omega A_{\rm in}}\frac{\mu q}{u^t|_{r_0}R_y}\frac{\Psi_+(r_0)}{r_0 f_B^{1/4}(r_0)}\delta(\omega - m\Omega)Y^*_{lm}\left(\frac{\pi}{2},0\right)\,.\end{aligned} \tag{7.24}$$

The scalar energy flux at infinity and at r_S is defined by

$$\dot{E}_{\infty,r_S} = \lim_{r\to+\infty,r_S}\int d\theta d\varphi\sqrt{-g}T^r_t\,, \tag{7.25}$$

where the stress-energy tensor of the scalar field is

$$T_{\mu\nu} = \partial_\mu\Phi\partial_\nu\Phi - \frac{1}{2}g_{\mu\nu}\partial_\rho\Phi\partial^\rho\Phi\,. \tag{7.26}$$

Finally, by using the decomposition (7.9) with $n = 0$ and using Eq. (7.23) we get

$$\dot{E}_{\infty,r_S} = \sum_{lm}(m\Omega)^2|\Psi_{\infty,r_S}|^2 \equiv \sum_{lm}\dot{E}^{lm}_{\infty,r_S}\,. \tag{7.27}$$

As anticipated, the energy flux at the horizon, $\dot{E}_{r_S}$, is present only in the BH case. However, in the cases of horizonless compact objects (like the TS), efficient trapping of radiation within the object could effectively produce an effect similar to the energy loss at the horizon [48, 49, 310]. This happens when the radiation trapping time near the object, $T_{\rm trap}$, becomes longer than the typical radiation–reaction timescale

of the binary [49]. In the Newtonian limit, taking the gravitational case as a proxy, the latter is given by

$$T_{\rm RR} \sim \frac{5}{64}\left(\frac{r_0}{M}\right)^4 \frac{M^2}{\mu}\,, \tag{7.28}$$

where M is the four-dimensional ADM mass given in Eq. (6.19) and we shall use units such as $\kappa_4^2 = 8\pi$.

The trapping time can be estimated as follows. Let us compute the time that radiation in radial infall takes to reach the boundary of the TS. Setting $\mu = 0 = L$ we can compute

$$\Delta T = \int_{r_i}^{r_B} dr \frac{\dot{t}}{\dot{r}}\,, \tag{7.29}$$

where r_i is the initial radial distance. The integral can be expressed in closed form for all r_B, with a notably simpler expression in the BH limit, $r_B \to r_S$:

$$\Delta T \sim \frac{\pi r_S^{3/2}}{\sqrt{r_B - r_S}}\,. \tag{7.30}$$

As expected this quantity diverges as $r_B \to r_S$, namely as the TS approaches the extremal BH solution. Therefore, the trapping time in the most relevant regime $r_B \to r_S$ (where it diverges) is

$$T_{\rm trap} \sim \frac{\pi r_S^{3/2}}{\sqrt{r_B - r_S}}\,. \tag{7.31}$$

By comparing $T_{\rm trap}$ with $T_{\rm RR}$, we find that trapping is inefficient when

$$\frac{r_B}{r_S} - 1 \gg \frac{4096\pi^2}{25}\frac{r_S^2}{M^2}\left(\frac{M}{r_0}\right)^8 \frac{\mu^2}{M^2} \approx 10^{-15}\left(\frac{\mu}{10^{-6}M}\right)^2\,, \tag{7.32}$$

where in the last estimate we considered $r_S \approx M$ and $r_0 \approx 6M$. Thus, except when r_B is within one part in 10^{15} of r_S, effective trapping does not occur, and the flux at infinity remains the only relevant source of energy loss for a TS.

7.3 Orbital evolution

As explained in Chapter 3, the first level of approximation of the EMRI dynamics is when the system evolves adiabatically under radiation reaction. This is true as long as the radiation reaction time scale is much longer than the orbital period of the secondary around the primary compact object. Under this assumption, to leading order, the evolution of the parameters describing the system is governed by the balance equation

$$\dot{E}_b = \dot{r}\frac{dE_b}{dr} = -\dot{E}^s_{\rm tot}\,, \tag{7.33}$$

where E_b is the binding energy of Eq. (6.27), and $\dot{E}^s_{\rm tot}$ is the total emitted scalar energy flux

$$\begin{aligned} \dot{E}^s_{\rm tot} &= \dot{E}^s_\infty && \text{for the TS,} \\ \dot{E}^s_{\rm tot} &= \dot{E}^s_{r_S} + \dot{E}^s_\infty && \text{for the BH,} \end{aligned} \tag{7.34}$$

where for the TS we assumed that effective trapping is negligible, i.e. Eq. (7.32). The above balance equation can be used to estimate the time necessary for the test scalar charge to reach the ISCO

$$t_{\rm ISCO} = \int_{r_{\rm ini}}^{r_{\rm ISCO}} dr \left(-\frac{dE_b}{dr}\right) \frac{1}{\dot{E}^s_{\rm tot}} \,. \tag{7.35}$$

The phase of the scalar wave emitted by the test charge can be computed as

$$\phi_s = \int_{r_{\rm ini}}^{r_{\rm fin}} dr \, \frac{\Omega(r)}{\dot{r}} \,. \tag{7.36}$$

7.4 Analytical solution at large orbital distance

Eq. (7.12) can be solved numerically, however, in the regime where the orbital frequency remains low, namely for large orbital separation, it is possible to get an analytical solution (see [311–316] for similar analyses in other contexts). The procedure we follow is the standard matching asymptotics technique: we match the solution near the inner boundary to the one valid asymptotically at infinity; such matching is possible only in the low-frequency approximation, $r_S\Omega \ll 1$. This allows us to compute the amplitude of the solution at $r_0 \gg r_S$ and the corresponding scalar flux analytically. Since the procedure varies depending on the background spacetime, we shall treat the two cases separately in what follows.

7.4.1 Magnetized BH

By defining $\Delta \equiv r^2 f_B f_S$, the homogeneous version of Eq. (7.10) with $n = 0$ can be written in the following convenient way

$$\frac{d}{dr}\left(\Delta \frac{d\psi}{dr}\right) + \frac{r^3\omega^2 - l(l+1)(r-r_S)}{r-r_S}\psi = 0 \,. \tag{7.37}$$

Let us first focus on the magnetized BH. We consider the change of variable of the radial coordinate r, introducing a new coordinate h

$$h \equiv \frac{r-r_S}{r-r_B} \,, \tag{7.38}$$

that approaches zero at the horizon. In the $h \ll 1$ limit, Eq. (7.37) can be written as

$$h(1-h)\frac{d^2\psi}{dh^2} + (1-h)\frac{d\psi}{dh} + \left[\frac{r_S^3\omega^2}{(r_S-r_B)h(1-h)} - \frac{l(l+1)}{1-h}\right]\psi = 0 \,. \tag{7.39}$$

By making use of the field redefinition $\psi(h) \equiv h^\alpha (1-h)^\beta F(h)$, the above equation can be recast as a hypergeometric differential equation

$$h(1-h)\frac{d^2F}{dh^2} + [c - (a+b+1)h]\frac{dF}{dh} - abF = 0 \,, \tag{7.40}$$

where $a = b = \alpha + \beta$, $c = 1 + 2\alpha$, whereas α and β satisfy the following algebraic equations

$$\alpha^2 + \frac{r_S^3 \omega^2}{r_S - r_B} = 0 \tag{7.41}$$

$$\beta^2 - \beta - \alpha^2 - l(l+1) = 0 \tag{7.42}$$

with solutions

$$\alpha_\pm = \pm i \sqrt{\frac{r_S^3}{r_S - r_B}}\, \omega = \pm i k_S\, \omega \tag{7.43}$$

$$\beta_\pm = \frac{1}{2}[1 \pm \sqrt{(1+2l)^2 + 4\alpha^2}]\,. \tag{7.44}$$

From the general solution of the hypergeometric differential equation we get

$$\begin{aligned}\psi(h) &= A_1 h^{\alpha}(1-h)^{\beta} F(a,b,c;h) \\ &+ B_1 h^{-\alpha}(1-h)^{\beta} F(a-c+1, b-c+1, 2-c; h)\,,\end{aligned} \tag{7.45}$$

where $F(a,b,c;h)$ is the hypergeometric function. To ensure convergence of the hypergeometric functions for $|h| \leq 1$, i.e. $\mathrm{Re}[c-a-b] > 0$, we select the solutions $\beta = \beta_-$ and $\alpha = \alpha_-$. If we expand the solution near the horizon r_S we get

$$\psi(h) = A_1 h^{-i k_S \omega} + B_1 h^{i k_S \omega}\,, \tag{7.46}$$

and imposing only ingoing waves we require $B_1 = 0$. We aim to match the near-horizon and far-field solutions in an intermediate region that exists in the low-frequency regime. In order to do so, using the properties of the hypergeometric function [317], we change the argument of the hypergeometric function from h to $1-h$ to get

$$\begin{aligned}\psi(h) =& A_1 h^{\alpha}(1-h)^{\beta}\Bigg[\frac{\Gamma(1+2\alpha)\Gamma(1-2\beta)}{\Gamma(1+\alpha-\beta)^2} F(a,b,a+b-c+1;1-h) \\ &+ (1-h)^{1-2\beta}\frac{\Gamma(1+2\alpha)\Gamma(2\beta-1)}{\Gamma(\alpha+\beta)^2} F(c-a,c-b,c-a-b+1;1-h)\Bigg]\,.\end{aligned} \tag{7.47}$$

Since we are interested in the low-frequency approximation, i.e. $r_S\,\Omega = r_S\,\omega/m \ll 1$, as long as the $\omega r_S \ll 1$ condition is fulfilled, $\beta \leq 0$. Expanding the solutions for $1 - h \ll 1$, namely $r \gg r_S$, we get

$$\Psi(r) = r f_B^{1/4} \psi(r) \sim \frac{r^{l+1}}{r_S^{3/4}(r_S - r_B)^{l+1/4}} \frac{\Gamma(1+2\alpha)\Gamma(1-2\beta)}{\Gamma(1+\alpha-\beta)^2}\,, \tag{7.48}$$

where we obtained $A_1 = r_S^{-3/4}(r_S - r_B)^{-1/4}$ by comparing Eq. (7.46) with the boundary condition in Eq. (7.19).

The far-field limit solution of Eq. (7.12) can be studied following the procedure in [311]. By expanding the equation for $r \to +\infty$, defining $\epsilon_{S,B} = \omega r_{S,B}$ and performing

a change of variable $z = \omega r$, we get

$$\left[1 - \frac{\epsilon_B + 2\epsilon_B}{z} + \frac{2\epsilon_S\epsilon_B + \epsilon_S^2}{z^2} - \frac{\epsilon_B\epsilon_S^2}{z^3} + \mathcal{O}\left(\frac{1}{z^4}\right)\right]\frac{d^2\Psi(z)}{dz^2} + \left[\frac{\epsilon_S + \epsilon_B/2}{z^2} - \frac{2\epsilon_S\epsilon_B + \epsilon_S^2}{z^3} + \mathcal{O}\left(\frac{1}{z^4}\right)\right]\frac{d\Psi(z)}{dz} \left[1 - \frac{l(l+1)}{z^2} + \frac{\epsilon_S(l^2+l-1) - \epsilon_B/2}{z^3} + \mathcal{O}\left(\frac{1}{z^4}\right)\right]\Psi(z) = 0\,, \tag{7.49}$$

that in the limit $\{\epsilon_S, \epsilon_B\} \ll 1$ simply becomes

$$\frac{d^2\Psi(z)}{dz^2} + \left[1 - \frac{l(l+1)}{z^2}\right]\Psi(z) = 0\,. \tag{7.50}$$

The general solution of the above equation is a linear combination of Riccati-Bessel functions $\sqrt{z}J_{l+\frac{1}{2}}(z)$ and $\sqrt{z}N_{l+\frac{1}{2}}(z)$. Since the solution Ψ_- must be regular at the inner boundary, we can choose just Bessel functions of the first kind, i.e.

$$\Psi_-(z) = B\sqrt{z}J_{l+\frac{1}{2}}(z)\,, \tag{7.51}$$

where B is a constant. By taking the small z expansion of the Bessel function we find

$$\begin{aligned}\Psi_-(z \ll 1) &= \frac{B}{2^{l+1/2}\Gamma(l+3/2)}z^{l+1} + \mathcal{O}(z^2) \\ &= \frac{B\sqrt{2}\,\epsilon_S^{l+1}}{(2r_S)^{l+1}\Gamma(l+\frac{3}{2})}r^{l+1} + \mathcal{O}(r^2)\,.\end{aligned} \tag{7.52}$$

In order to determine the constant B, we match the two solutions: the near–inner boundary solution and the asymptotic one, extended to large and small values of r, respectively:

$$B = \frac{(2r_S)^{l+1}\Gamma(l+3/2)\Gamma(1+2\alpha)\Gamma(1-2\beta)}{\sqrt{2}\epsilon_S^{l+1}r_S^{3/4}\,(r_S - r_B)^{l+1/4}\,\Gamma(1+\alpha-\beta)^2}\,. \tag{7.53}$$

The amplitude $A_{\rm in}$, entering the Wronskian, can be computed by comparing the far-field solution with the asymptotic behavior of Eq. (7.17)

$$A_{\rm in} = \frac{i^{l+1}(2r_S)^{l+1}\Gamma(l+3/2)\Gamma(1+2\alpha)\Gamma(1-2\beta)}{2\sqrt{\pi}\epsilon_S^{l+1}r_S^{3/4}\,(r_S - r_B)^{l+1/4}\,\Gamma(1+\alpha-\beta)^2}\,. \tag{7.54}$$

Using Eqs. (7.52), (7.23) and (7.27) we get the $lm-$component of the energy flux at infinity

$$\dot{E}_\infty^{lm} = \left(\frac{\mu\,q}{R_y}\right)^2\left|\frac{\sqrt{\pi}\,Y_{lm}^*\left(\frac{\pi}{2},0\right)}{2^{l+1}\Gamma(l+\frac{3}{2})}\right|^2 m^{2l+2}\left(\frac{r_S}{2}\right)^{l+1} r_0^{-(l+3)}\,, \tag{7.55}$$

where we used $\omega = m\Omega$ and the fact that at large distances $f_B \to 1$ and $u^t \to 1$. One can note that, in the Schwarzschild limit, the energy flux correctly reduces to the one of a scalar particle in circular orbit around the Schwarzschild BH [316], after identifying q/R_y with the scalar charge.

By applying an analogous procedure, one can compute the analytical approximation of the scalar energy flux at r_S. In this case, the solution to Eq. (7.50) with the appropriate boundary conditions is given by

$$\Psi_+(z) = C\sqrt{z}\, H^{(1)}_{l+1/2}(z)\,, \tag{7.56}$$

where $H^{(1)}_{l+1/2}(z) = J_{l+1/2}(z) + iN_{l+1/2}(z)$ is the Hankel function of the first kind. By matching this asymptotic solution with the correct boundary condition at infinity

$$\Psi_+(z \to +\infty) \sim e^{iz}\,, \tag{7.57}$$

and using the expression of the Hankel function for large argument

$$C\,\sqrt{z}\, H^{(1)}_{l+1/2}(z \to +\infty) \sim C\sqrt{\frac{2}{\pi}} e^{iz}(-i)^{l+1}\,, \tag{7.58}$$

we get $C = i^{l+1}\sqrt{\frac{\pi}{2}}$. At this stage one can note that the function $J_{l+1/2}$ is subdominant by considering the small-argument behavior of the Riccati-Bessel functions

$$\begin{aligned} J_{l+1/2}(z \ll 1) &\sim \frac{z^{l+1/2}}{2^{l+1/2}\,\Gamma(l+3/2)}[1+\mathcal{O}(z^2)]\,, \\ N_{l+1/2}(z \ll 1) &\sim -\frac{2^{l+1/2}}{\pi}\frac{\Gamma(l+1/2)}{z^{l+1/2}}[1+\mathcal{O}(z^2)]\,, \end{aligned} \tag{7.59}$$

to get

$$\Psi_+(z \ll 1) \sim i^l \frac{2^l}{\sqrt{\pi}}\Gamma(l+1/2) z^{-l}\,. \tag{7.60}$$

Finally, using Eqs. (7.24) and (7.27) we can compute the lm-component of the flux at the horizon

$$\dot{E}^{lm}_{r_S} = \left(\frac{\mu q}{R_y}\right)^2 \left|Y^*_{lm}\left(\frac{\pi}{2}, 0\right)\right|^2 \bar{\Gamma}^2 \frac{m^2 r_S^{5/2}(r_S - r_B)^{2l+1/2}}{2} r_0^{-2l-5}\,, \tag{7.61}$$

where we defined

$$\bar{\Gamma} \equiv \frac{\Gamma(l+1/2)\Gamma(1+\alpha-\beta)^2}{2\,\Gamma(l+3/2)\Gamma(1+2\alpha)\Gamma(1-2\beta)}\,. \tag{7.62}$$

7.4.2 Topological star

In the case of the TS, the analytical solution is derived through a procedure analogous to that used in the previous section, though with important differences since the inner boundary is located at r_B. For this purpose, let us define the variable h as follows

$$h \equiv \frac{r - r_B}{r - r_S}\,. \tag{7.63}$$

In the limit $h \ll 1$, the radial equation becomes

$$h(1-h)^2\frac{d^2\psi}{dh^2} + (1-h)\frac{d\psi}{dh} + \left[\frac{r_B^3\omega^2}{(1-h)(r_B - r_S)} - \frac{l(l+1)}{1-h}\right]\psi = 0\,. \tag{7.64}$$

Using the field redefinition $\psi(h) \equiv h^\alpha(1-h)^\beta F(h)$ we get the hypergeometric equation (7.40), where again $a = b = \alpha + \beta$ and $c = 1 + 2\alpha$, but this time α and β are solutions to

$$\alpha^2 = 0\,, \qquad \beta^2 - \beta + \frac{r_B^3\omega^2}{r_B - r_S} - l(l+1) = 0\,, \tag{7.65}$$

namely,

$$\alpha = 0\,, \qquad \beta_\pm = \frac{1}{2}\left[1 \pm \sqrt{(1+2l)^2 + 4\frac{r_B^3\omega^2}{r_B - r_S}}\right]\,. \tag{7.66}$$

Since in this case $c = 1$, the general solution of the hypergeometric equation is [317]

$$\begin{aligned}\psi(h) =& A_1(1-h)^\beta F(a,b,1;h) + B_1(1-h)^\beta\Bigg\{\ln|h|F(a,b,1;h) + \sum_{n=1}^{\infty}\frac{(a)_n(b)_c}{(n!)^2}h^n \\ &\times\left[\chi(a+n) - \chi(a) + \chi(b+n) - \chi(b) - 2\chi(n+1) + 2\chi(1)\right]\Bigg\}\,,\end{aligned} \tag{7.67}$$

where χ is the digamma function, i.e. the logarithmic derivative of the Gamma function. Since we consider the approximation $h \ll 1$ we can neglect the $\mathcal{O}(h)$ terms within the curly brackets. Furthermore, to ensure that the boundary condition of the TS near the inner boundary are satisfied, we require $B_1 = 0$. Using the properties of the hypergeometric functions, we get

$$\begin{aligned}\psi(h) = A_1(1-h)^\beta\Bigg[&\frac{\Gamma(-2\beta)}{\Gamma(\beta)^2}F(a,b,a+b;1-h) \\ &+ (1-h)^{-2\beta}\frac{\Gamma(2\beta)}{\Gamma(\beta)^2}F(-a,-b,-a-b,1-h)\Bigg]\,.\end{aligned} \tag{7.68}$$

In the limit $1 - h \ll 1$ and within the low-frequency approximation, the above solution becomes

$$\Psi(r) = r f_B^{1/4}\psi(r) \sim \frac{r^{l+1}}{r_B^{3/4}(r_B - r_S)^l}\frac{\Gamma(-2\beta)}{\Gamma(1-\beta)^2}\,, \tag{7.69}$$

where we derived $A_1 = r_B^{3/4}$ from the comparison between Eq. (7.67) with $B_1 = 0$ and the boundary condition of Eq. (7.21). The far-field solution is identical to the one of the magnetized BH, see Eq. (7.50), that for small z becomes Eq. (7.51) with

$$B = \frac{(2r_S)^{l+1}\Gamma(l+3/2)\Gamma(-2\beta)}{\sqrt{2}\epsilon_S^{l+1}r_B^{3/4}\,(r_B - r_S)^l\Gamma(1-\beta)^2}\,. \tag{7.70}$$

The amplitude $A_{\rm in}$ is instead given by

$$A_{\rm in} = \frac{i^{l+1}(2r_S)^{l+1}\Gamma(l+3/2)\Gamma(-2\beta)}{2\sqrt{\pi}\epsilon_S^{l+1}r_B^{3/4}\,(r_B - r_S)^l\Gamma(1-\beta)^2}\,. \tag{7.71}$$

It turns out that the $lm-$component of the energy flux at infinity is given again by Eq. (7.55). The fact that the analytical expression for the flux at infinity is the same for both BH and TS is a consequence of the fact that the two solutions coincide asymptotically and their different inner boundaries are negligible in the small-frequency regime. Since the low frequency approximation holds for large orbital radii, the analytical flux at infinity is expected to be the same.

7.5 Numerical results

We now turn to the numerical computation of the energy flux and its comparison with the low-frequency analytical approximation in the cases of magnetized BHs and TSs. The emitted power is computed for different values of the ratio r_B/r_S and varying the radial distance of the stable circular orbit $r_0 > r_{\rm ISCO}$.

While for magnetized BHs, and to some extent for first kind TSs, the general behavior of the flux at infinity is overall quite similar to the one of a Schwarzschild BH, the case of second kind TSs is particularly interesting: for ultracompact solutions (i.e. when $r_B/r_S \to 1$) the orbiting scalar particle can excite long-lived QNMs with a low real frequency, leading to sharp resonances in the emitted energy flux that are not present in standard BHs within GR.

Finally, we also compute the dephasing between the magnetized BH and the TS, accumulated within one year of evolution of the test scalar charge up to the ISCO of the BH.

7.5.1 Energy flux of magnetized BHs and TSs

The scalar energy fluxes are computed from Eq. (7.27), with Ψ_- obtained by numerically solving the source free version of Eq. (7.12) under the appropriate boundary conditions. The fluxes are compared to the analytical result which is valid at large orbital separation. Fig. 7.1 presents the results for both magnetized BHs and

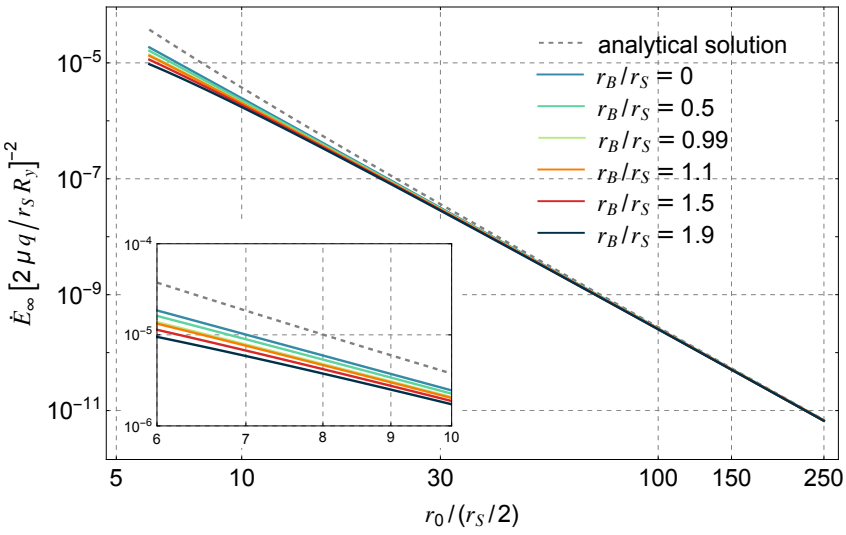

Figure 7.1. Scalar energy flux at infinity as a function of the orbital radial distance r_0, starting from $r_{\rm ISCO}$, for different values of the ratio r_B/r_S of the magnetized BH and the TS. The flux is computed truncating the summation at $l_{\rm max} = 3$. The dashed gray line represents the flux computed using the analytical solution. The inset shows a zoom of the region close to the ISCO, where the differences in the flux are larger.

TSs and different values of the parameters ratio r_B/r_S. As can be seen, the numerical results for $r_0 \gg r_S$ are in good agreement with the analytical approximation. This match gradually loses validity as the orbit approaches the ISCO, as evident from

the inset. As expected, and partially confirmed by the analytical expression, the maximum power emitted at infinity occurs when the particle orbits along the ISCO and monotonically decreases for circular orbits farther from the compact object. We compute the total flux by truncating the lm summation at $l_{\max} = 3$, since higher-order contributions are subleading and have no significant impact on the results presented. Indeed, as can be seen from the analytical expression in Eq. (7.55) and Fig. 7.2 for a TS with $r_B/r_S = 1.5$, the leading term is given by the dipolar ($l = 1$) mode and each subsequent contribution decreases monotonically as l increases. The agreement with the analytical approximation at large separation is present also for each lm-component of the flux, as shown in Fig. 7.2 for a TS.

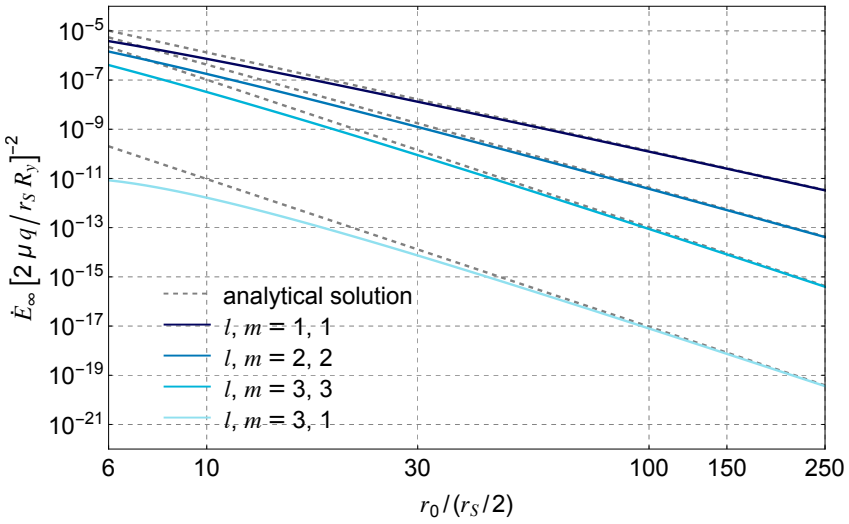

Figure 7.2. lm-component of the scalar energy flux emitted at infinity as a function of the radial distance r_0 of the circular orbit, starting from $r_{\rm ISCO}$, for a TS with $r_B/r_S = 1.5$. The dashed gray lines represent the flux computed using the low-frequency analytical approximation. Note that the cases $l, m = 2, 1$ and $l, m = 3, 2$ are not present because the spherical harmonics $Y_{21}(\pi/2, 0) = Y_{32}(\pi/2, 0) = 0$.

Due to the presence of the horizon at r_S in the magnetized BH case, we also computed the scalar flux absorbed by the BH, as shown in Fig. 7.3. Also in this case, the comparison between the numerical results and the analytical solution of Eq. (7.61) provides an excellent agreement for large orbital separation. As can be seen from the plot, the contribution of the flux at the horizon is subleading compared to the flux at infinity and the value of the first decreases as the BH approaches extremality at $r_B/r_S = 1$, since this is the point in parameter space where the BH and the TS are continuously connected. As opposed to the flux at infinity, the fluxes at the horizon for the different r_B/r_S values considered do not asymptotically tend to the same value for large orbital radii.

7.5.2 Resonances

As discussed in Chapter 6, TSs of the *second kind* behave like BH mimickers but exhibit key differences from BHs that can serve as signatures of the absence of the

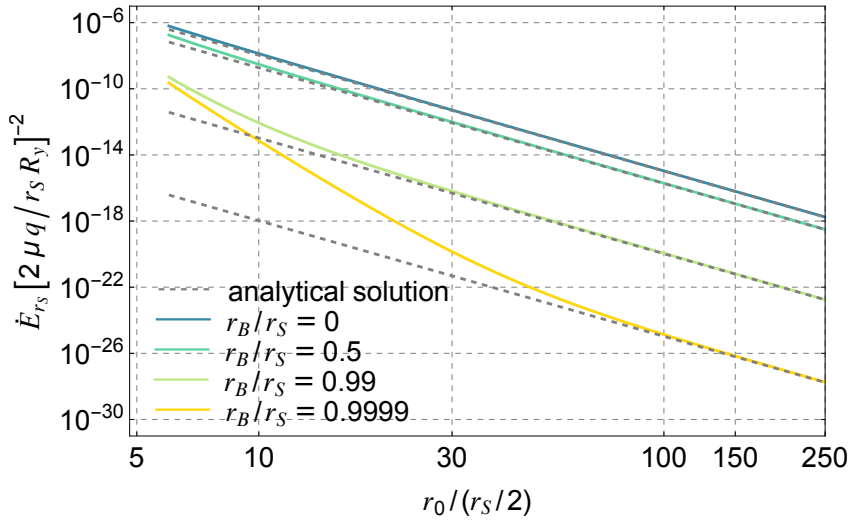

Figure 7.3. Scalar energy flux at the horizon as a function of the orbital distance r_0, starting from $r_{\rm ISCO}$, for different values of the ratio r_B/r_S of the magnetized BH. The flux is computed truncating the summation at $l_{\rm max} = 3$.

horizon [22]. In Sec. 3.3 we anticipated that EMRIs with ECOs are able to excite the long-lived QNMs of the primary. This is precisely the phenomenon that takes place here. As can be seen from the expression of the source in Eq. (7.14), the point particle following a stable circular orbit around the primary object can excite the QNMs of the compact object as long as $m\Omega$ matches the real part of the QNMs frequency

$$\omega_R = m\Omega\,, \tag{7.72}$$

where we defined $\omega_R = {\rm Re}[\omega_{\rm QNM}]$ and $\omega_I = {\rm Im}[\omega_{\rm QNM}]$. When the resonant condition above is fulfilled, the energy flux develops sharp peaks for values of r_0 that satisfy Eq. (7.72). This is clear also from the denominator of Eq. (7.23) that involves the Wronskian, which vanishes when the considered frequency corresponds to the one of a QNM. If the modes are long-lived ($|\omega_I| \ll \omega_R$, as it happens for ultracompact TSs [289–292]) then the Wronskian is almost zero on the real axis when the resonant condition (7.72) is satisfied.

The QNMs of a test scalar field in the background of a TS in the full parameter space are shown in Fig 7.4. As can be seen in Fig. 7.4, as the $r_B/r_S = 1$ limit is approached, the fundamental mode becomes increasingly long-lived, and its real part tends to zero, thus making the scalar energy flux at infinity more prone to develop a resonance. Moreover, as shown in the zoom of Fig. 7.5, the second kind TS presents long-lived modes with a sufficiently small real part of the frequency. Indeed, as long as the QNM real frequency remains below the horizontal lines (which represent multiples of the ISCO orbital frequency, $m\Omega_{\rm ISCO}$) the point particle can excite the corresponding QNM.

By exploring the relevant parameter space, guided by the information of Fig. 7.5, we found several resonances in the energy flux of the TS, for different values of r_B/r_S. In Fig. 7.6 we show the scalar energy flux at infinity for several TSs with

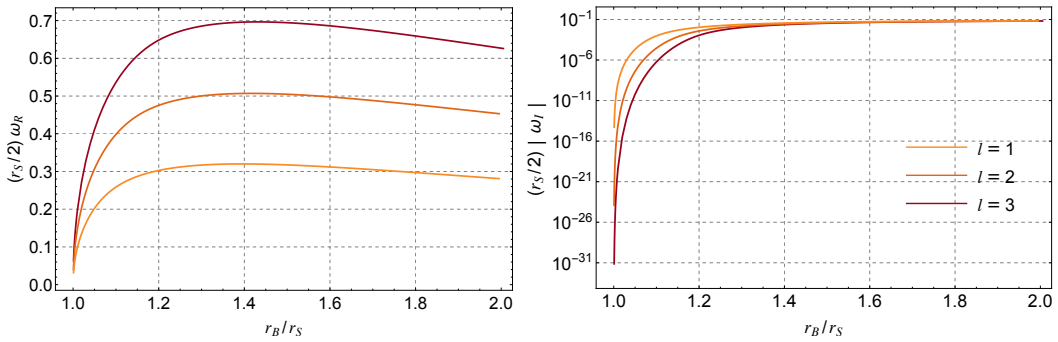

Figure 7.4. Real part (left panel) and imaginary part (right panel) of the fundamental QNMs frequencies for test scalar perturbations in the background of the TS varying the ratio r_B/r_S for different values of $l = 1, 2, 3$.

different r_B/r_S, along with their characteristic resonances, compared to that of a nearly-extremal magnetized BH. A clearer view at some specific resonances is present in Fig. 7.7 where, zooming-in near a resonance, we show the typical structure of the peaks for three distinct TSs. One can note that in all cases the resonances are extremely narrow, indeed we needed to employ high resolution in scanning the orbital distance to identify them. This is due to the rather small value of the imaginary part of the excited QNM frequency, that can range from $(r_S/2)|\omega_I| \sim 10^{-11}$ for the $l = 1$ mode of the TS with $r_B/r_S = 1.004$, to $(r_S/2)|\omega_I| \sim 10^{-19}$ for the $l = 2$ mode of the TS with $r_B/r_S = 1.003$. The other QNMs with $(l, m) = (2, 2), (3, 3), (3, 1)$ that, according to Fig. 7.5, are prone to be excited were not identified because of their extremely small imaginary part ($(r_S/2)|\omega_I| \lesssim 10^{-20}$, as shown in Fig. 7.4).

The minimum shown in the plots of Fig. 7.7 is commonly dubbed anti-resonance. The latter is common and can be easily explained by a simple toy model where the perturbations of the compact object are described by a forced harmonic oscillator, sourced by the secondary object (see [44, 48, 318] for more details). This allows us to model the energy flux across a single resonance as

$$\frac{\dot{E}^{\rm res}_{\infty}}{\dot{E}_{\infty}} = \frac{[(1-b)(m\Omega)^2 - \omega_R^2 - \omega_I^2]^2 + (2m\Omega\omega_I)^2}{[(m\Omega)^2 - \omega_R^2 - \omega_I^2]^2 + (2m\Omega\omega_I)^2}\,, \tag{7.73}$$

where $\dot{E}^{\rm res}_{\infty}$ and $\dot{E}_{\infty}$ are the energy flux at infinity with and without the resonance, respectively, $b = 1 - (\Omega_{\rm max}/\Omega_{\rm min})^2$, with $\Omega_{\rm max}$ and $\Omega_{\rm min}$ denoting the frequencies corresponding to the maximum and the minimum of the resonance. In the bottom-right panel of Fig. 7.7 we show the resonance for a TS with $r_B/r_S = 1.001$, associated to the $l = m = 1$ mode, together with the best fit obtained using Eq. (7.73).

7.5.3 Dephasing

In the final part of this section, we compute the phase of the scalar wave emitted by a test charge in orbit around a TS or a magnetized BH, focusing on the resulting differences in dephasing. Let us define

$$\delta\phi_s(t) = |\phi_s^{\rm BH}(t) - \phi_s^{\rm TS}(t)|\,, \tag{7.74}$$

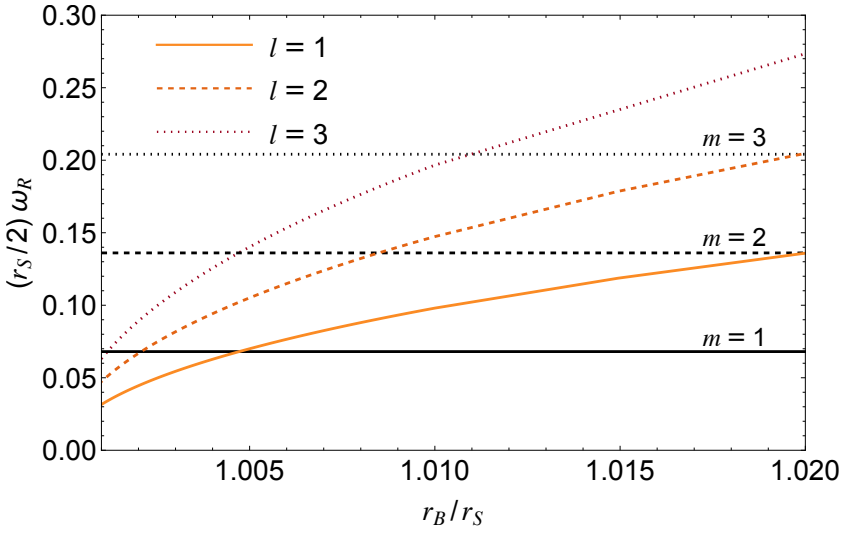

Figure 7.5. Real part of the QNM frequencies for test scalar field perturbations in the background of a TS, for different values of $l = 1, 2, 3$. The solid, dashed and dotted horizontal lines represent multiples of the orbital frequency at the ISCO, $m\,\Omega_{\rm ISCO}\,(r_S/2)$ for $m = 1, 2, 3$, respectively.

where $\phi_s^{\rm BH}(t)$ and $\phi_s^{\rm TS}(t)$ are the phase at time t for the BH and TS, respectively. Without loss of generality we can choose $\phi_s^{\rm BH}(t = 0) = \phi_s^{\rm TS}(t = 0) = 0$. To evaluate the impact of resonances on the inspiral evolution, we computed the dephasing between two scenarios: a TS including the resonance and a TS in which the resonance was artificially removed by adopting a numerical resolution larger than its width. This analysis was performed for the case $r_B/r_S = 1.001$, corresponding to the bottom-right panel of Fig. 7.7. In order to do so, let us introduce the dephasing accumulated during the inspiral evolution from an initial radius $r_{\rm ini}$ at $t_{\rm ini} = 0$ to a final radius $r_{\rm fin}$, between the two TS cases with and without the resonance

$$\Delta\phi_s = |\phi^{TS}_{s,\,\rm res}(r_{\rm fin}) - \phi^{TS}_{s,\,\rm no\,res}(r_{\rm fin})|\,, \tag{7.75}$$

where again $\phi^{TS}_{s,\,\rm res}(r_{\rm ini}) = \phi^{TS}_{s,\,\rm no\,res}(r_{\rm ini}) = 0$. Considering the evolution centered on the resonance with a width of $(r_{\rm fin} - r_{\rm ini})/(r_S/2) \approx 3 \times 10^{-8}$, we computed the dephasing $\Delta\phi_s \lesssim \mathcal{O}(10^{-1})$ rads. The specific case we considered represents the widest resonance among all those studied and shown in Fig. 7.6. Therefore, we conclude that all the resonances are too narrow to produce a detectable dephasing. Indeed, as a rough rule of thumb, a dephasing greater than 1 rad would substantially impact a matched-filter search, leading to a significant loss of detected events [319]. Nevertheless, such a rule should be confirmed through more detailed, model-dependent analysis; for instance, correlations might still enable detection using incorrect models, though this would introduce systematic errors in the estimated parameters.

We therefore omit the resonances and evaluate the dephasing between magnetized BHs and TSs via Eq. (7.74). In the left panel of Fig. 7.8 we show the results for the parameters $q/R_y = 1$, $r_S/2 = 10^6 M_\odot$ and $\mu = 30 M_\odot$. As we will discuss later on in Sec. 7.5.3, the choice of the q and R_y parameters such that $q/R_y = 1$ is made to match the gravitational case. In the latter, indeed, the source is only proportional to

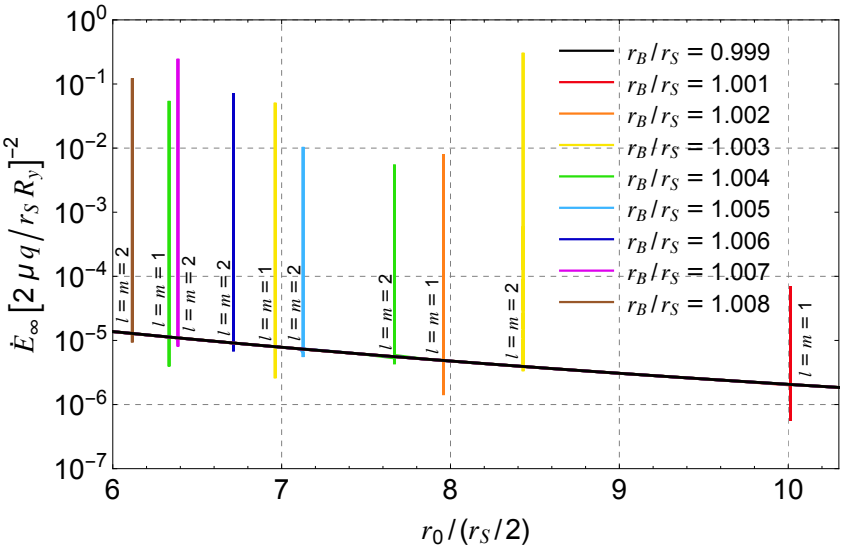

Figure 7.6. Resonances of the scalar energy flux at infinity for different values of r_B/r_S in the parameter space of ultracompact TSs. The black curve represents the scalar energy flux at infinity for a nearly-extremal magnetized BH, providing a comparison with the considered TS solutions. For each resonance, we indicate the angular momentum and azimuthal numbers of the excited QNM that generates the peak in the flux.

μ and independent of R_y. Clearly the fluxes can be easily rescaled for different values of q/R_y. In each case the starting point is chosen such that the test scalar charge completes the orbital evolution up to the ISCO of the BH in one year. In the right panel of Fig. 7.8 we show the evolution of the orbital radius r_0 of circular orbits as a function of time, for both magnetized BHs and TSs, varying r_B/r_S. As can be seen, the test charge reaches the ISCO in the BH case faster than in the TS case due to the additional flux at the horizon and the larger flux at infinity, as shown in Fig. 7.1. Moreover, the further away the BH and the TS are in the parameter space, the larger is the accumulated dephasing, arriving up to $\mathcal{O}(10^4)$ rads in the comparison between the Schwarzschild limit and a TS with $r_B/r_S = 1.9$. On the other hand, we estimate that the minimum ϵ difference, defined as $r_B/r_S = 1 \pm \epsilon$, to develop a dephasing of around 1 radiant between a nearly extremal magnetized BH and an ultra-compact TS, is $\epsilon \approx 10^{-4}$, that corresponds to $\Delta Q/M \approx 4 \times 10^{-5}$ between the two solutions. In other words, the dephasing between a TS with $r_B = r_S(1+\epsilon)$ and a BH with $r_S = r_B(1-\epsilon)$ is negligible when $\epsilon \lesssim 10^{-4}$. Therefore, the regime in which effective trapping can occur is likely beyond the observational accuracy.

As already discussed, the scalar flux captured by the BH horizon is subdominant when compared to the flux carried away to infinity. However, it is only near the extremal BH limit at $r_B/r_S = 1$ that it becomes completely negligible, as shown in Fig. 7.8, which illustrates the dephasing after 1 year of evolution between a BH with $r_B/r_S = 0.9999$ and a TS with $r_B/r_S = 1.0001$. The much larger dephasing observed in all other comparisons is due to the different fluxes, both at the horizon and at infinity.

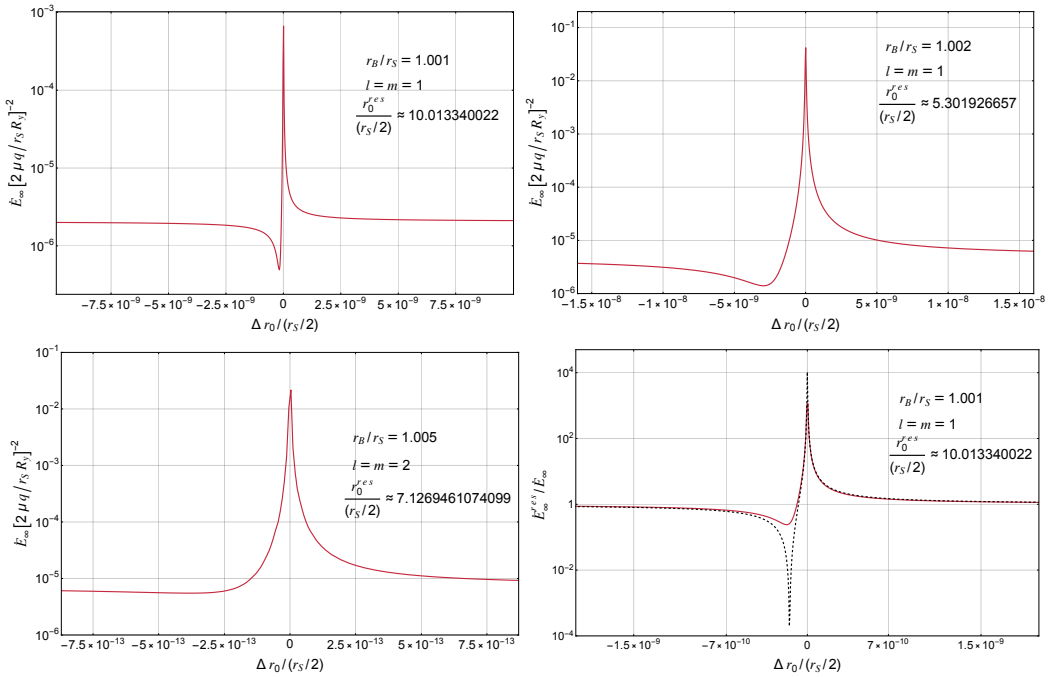

Figure 7.7. Resonances of the scalar energy flux at infinity for TSs of the *second kind* with $r_B/r_S = 1.001$ (top-left panel), $r_B/r_S = 1.002$ (top-right panel) and $r_B/r_S = 1.005$ (bottom-left panel). The peaks are associated to QNMs with $l = m = 1$ (top and middle panels) and $l = m = 2$ (bottom panel). The origin of the axis is chosen to coincide with the radial distance $r_0^{\rm res}$, where the peak of the resonance occurs. The bottom-right panel shows the comparison between the energy flux at infinity $\dot{E}_\infty^{\rm res}$, normalized by the flux ignoring the resonance $\dot{E}_\infty$, computed with the exact numerical results (red solid line) and with the best fit of a forced-oscillator model described by Eq. (7.73) (dashed black line).

Extension to the gravitational case

In the present chapter, we focused on the scalar radiation emitted by a test charge moving along circular orbits in the background of a TS (or a magnetized BH). A particularly interesting extension of this work would be to study gravitational radiation by incorporating a source into the analysis of Chapter 6. Although this case should, in principle, be tractable with standard techniques, it remains technically challenging because, as discussed, gravitational, scalar, and electromagnetic perturbations are all mutually coupled.

However, in preparation of this work it is useful to estimate the scaling of the source with the model parameters. In the case of a point mass, the relevant action reads

$$S = \int d^5x\sqrt{-g}\left(\frac{R}{2\kappa_5^2} - \frac{1}{4}F_{\mu\nu}F^{\mu\nu}\right) - \mu\int_\gamma d\tau\sqrt{g_{\mu\nu}u^\mu u^\nu}\,, \tag{7.76}$$

where γ is the particle worldline. This gives Einstein-Maxwell equations in five dimensions,

$$G_{\mu\nu} = \kappa_5^2(T_{\mu\nu}^{\rm EM} + T_{\mu\nu}^{\rm particle})\,, \tag{7.77}$$

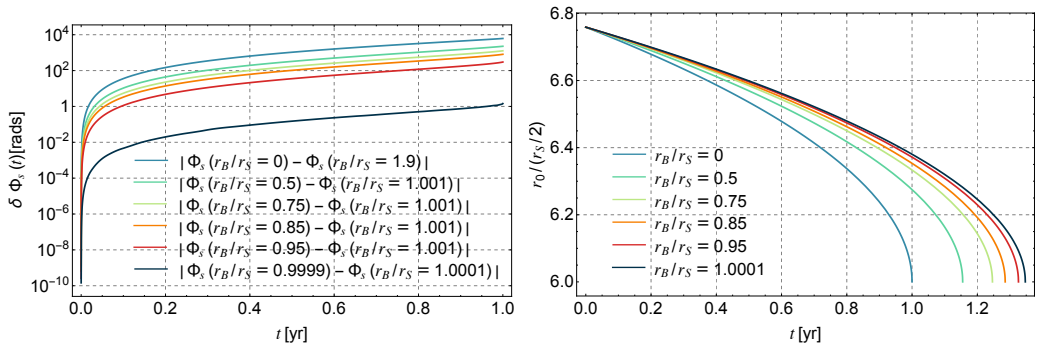

Figure 7.8. The left panel shows the scalar wave dephasing between magnetized BH and the TS as a function of time for $q/R_y = 1$, $r_S/2 = 10^6 M_\odot$ and $\mu = 30 M_\odot$. For each curve the starting point at $t_{\rm ini} = 0$ is set to guarantee 1 year of evolution up to the ISCO for the scalar charge orbiting around the BH. The right panel presents the evolution of the orbital radius of the point particle under radiation reaction for $q/R_y = 1$, $r_S/2 = 10^6 M_\odot$ and $\mu = 30 M_\odot$. The evolution begins at a radial distance $r_0 \approx 6.759\, r_S/2$ at $t_{\rm ini} = 0$, to guarantee 1 year of evolution for the magnetized BH case with $r_B/r_S = 0$, and stops as the particle reaches $r_{\rm ISCO}$ at $t_{\rm ISCO}$.

where $T^{\rm EM}_{\mu\nu}$ is the electromagnetic stress-energy tensor and, for a particle in equatorial motion as described above,

$$T^{\rm particle}_{\mu\nu} = \mu \frac{u_\mu u_\nu}{\sqrt{-g} u^t} \delta(r - r_0)\delta(\theta - \pi/2)\delta(\phi - \Omega t)\delta(y)\,. \tag{7.78}$$

Following the same procedure done for the test scalar charge, one would obtain

$$T^{\rm particle}_{\mu\nu} = \mu \frac{u_\mu u_\nu}{r^2 u^t} \delta(r - r_0) \sum_n \frac{e^{in\frac{y}{R_y}}}{2\pi R_y} \sum_{lm} Y_{lm}(\theta, \varphi) Y^*_{lm}\left(\frac{\pi}{2}, 0\right) e^{-im\Omega t}\,. \tag{7.79}$$

Notably, since $\kappa_5^2 = \kappa_4^2 R_y$ and $T^{\rm particle}_{\mu\nu} \sim 1/R_y$, it is easy to see that R_y disappears from the source of the massless ($n = 0$) modes, which depends on $\kappa_5^2 T^{\rm particle}_{\mu\nu}$. This corresponds to the case $R_y = q$ previously discussed for scalar radiation.

Chapter 8

$\mathcal{W}$-soliton and the corresponding BH

Over the past few years considerable progress has been made in the construction of smooth, horizonless and non-extremal geometries from five–dimensional supergravity, providing analytically tractable toy models of BH microstates. In particular, topological stars (TSs), discussed in Chapter 6, represent a remarkable example in which some intriguing phenomenological properties of ECOs, and more specifically of microstate geometries, are effectively captured.

More recently, a new class of solutions, dubbed $\mathcal{W}$-solitons, has been discovered within five–dimensional minimal supergravity [27]. These novel solutions asymptotically are four-dimensional Minkowski spacetime times a compact circle and carry the same mass and charges as Reissner–Nordström-like BHs of four-dimensional supergravity [320], including the neutral case that is particularly relevant in astrophysics. A topological bubble with electromagnetic flux supports their smooth caps, thus preventing the collapse. Like TSs, the novel $\mathcal{W}$-solitons remain analytically tractable but overcome their main limitations (see Sec. 8.1), thereby providing excellent prototypes of non-extremal BH microstates. In the neutral limit, the solution reduces to a new smooth horizonless configuration that can be directly compared with the Schwarzschild BH, and in a four-dimensional description is sustained by a massless axion and the dilaton field emerging from compactification.

Compared to typical ECOs, the $\mathcal{W}$-soliton more closely resembles a standard BH, featuring a single unstable photon sphere and exhibiting only short-lived QNMs without late-time echoes. However, measurable deviations persist, offering potential observational signatures in both GW and electromagnetic signals.

In the present thesis we will focus on the GW analysis conducted in [321], presenting the QNM spectrum of the solution, compared to the BH case, and summarizing the results of the ringdown signal. Other results, like the gravitational lensing and imaging through ray-tracing simulations, or more details on the structure of null geodesics and the associated photon sphere, can be found in [321].

8.1 $\mathcal{W}$-solitons and BHs

Recently in [27] static non-extremal black string solutions and novel smooth horizonless topological solitons have been derived through a new solution-generating technique in $\mathcal{N}=2$ five-dimensional supergravity coupled to two vector multiplets. The two solutions, asymptotically Minkowski times a compact extra dimension, are particularly intriguing since they can coexist with the same mass and charge. Among these solutions, the $\mathcal{W}$-soliton and its corresponding black string counterpart are particularly noteworthy.

Let us consider a truncation to five-dimensional minimal supergravity, corresponding to the Einstein–Maxwell theory with a $U(1)$ gauge field and a Chern–Simons term

$$\mathcal{S}=\frac{1}{16\pi G_5}\int\left(R_5\star_5 1-\frac{3}{2}F\wedge\star_5 F-F\wedge F\wedge A\right), \tag{8.1}$$

where G_5 is the five-dimensional Newton constant, $F=dA$ is the field strength of the gauge field A, and R_5 is the Ricci scalar in five dimensions.

The five-dimensional spacetime can be decomposed into a four-dimensional space parametrized in terms of the spherical coordinates (t,r,θ,ϕ), and a compact fifth dimension ψ. The periodicity of the compact direction is given by

$$(\psi,\phi)=(\psi,\phi)+(0,2\pi),\qquad (\psi,\phi)=(\psi,\phi)+(2\pi R_\psi,0), \tag{8.2}$$

where R_ψ is the radius of the compact circle.

In the following we present two solutions of this theory: the $\mathcal{W}$-soliton and its corresponding black string. Note that, since the extra dimension is compact, the black-object solutions can be referred to either as a black hole or as a black string, depending on whether the system is viewed from a four- or five-dimensional perspective.

8.1.1 The $\mathcal{W}$-soliton

The $\mathcal{W}$-solitons are a class of static, non-extremal, smooth and horizonless geometries with the same mass and charges as four-dimensional black holes but removing the horizon in five dimensions through a smooth Kaluza-Klein bubble supported by electromagnetic flux. Such solutions carry electric and magnetic charges under the $U(1)$ gauge field and electric and magnetic Kaluza–Klein charges along the compact fifth dimension [27]. If we consider the case in which all charges are the same, the line element of the five-dimensional solution is given by

$$\begin{aligned} ds^2_{\mathcal{W}} &= \frac{f_Q(2f_M-f_Q)}{f_M^2}\left(d\psi+\frac{Q\,f_M}{r\,f_Q}dt+Q(\cos\theta+1)\,d\phi\right)^2-\frac{f_M}{f_Q}\,dt^2 \\ &\quad + f_M\left[\frac{dr^2}{2f_M-f_Q}+r^2\left(d\theta^2+\sin^2\theta\,d\phi^2\right)\right], \\ A &= \frac{Q}{r}\,dt+\frac{f_Q-f_M}{f_M}\left(d\psi+Q(\cos\theta+1)\,d\phi\right)-Q(\cos\theta+1)\,d\phi\,, \end{aligned} \tag{8.3}$$

with

$$f_M\equiv 1-\frac{2M}{r},\qquad f_Q\equiv 1-\frac{2Q^2}{r^2}, \tag{8.4}$$

where M and Q denote the mass and the magnitude of the charge, respectively (in units with $G_4 = 1$). For a more detailed discussion on the charge content see [27].

One can notice that r is not the standard radial coordinate because the radius of the two-sphere is $r\sqrt{f_M}$ rather than r. However, the following study is performed keeping r for convenience and simplicity in the analysis.

The $\mathcal{W}$-soliton possesses a spacetime geometry that terminates at the coordinate degeneracy of the ψ direction, namely at r_+, the largest of the two roots of $2f_M - f_Q = 0$:

$$r_\pm \equiv 2M \pm \sqrt{2(2M^2 - Q^2)}. \tag{8.5}$$

From Eq. (8.5) one can derive that the domain of existence of the soliton requires

$$|Q| \leq \sqrt{2}M\,, \tag{8.6}$$

with the equality corresponding to the extremal and supersymmetric limit [27]. By requiring regularity at the coordinate degeneracy [27] we derive the following conditions

$$kR_\psi = \frac{r_+}{\sqrt{2}}, \qquad Q = \frac{N}{2}R_\psi\,, \tag{8.7}$$

where N and k are integers, with $k \geq 1$. These conditions can be inverted if and only if $2k \geq |N|$, yielding a family of smooth solitons with quantized mass and charge as follows

$$M = \frac{4k^2 + N^2}{8\sqrt{2}k}\,R_\psi, \qquad Q = \frac{N}{2}\,R_\psi\,, \qquad 2k \geq |N|. \tag{8.8}$$

The radius of the two-sphere, that also provides the real size of the $\mathcal{W}$-soliton is given by

$$R_{\mathcal{W}} = r\sqrt{f_M}|_{r=r_+} = \sqrt{r_+(r_+ - 2M)} = \frac{\sqrt{4k^2 - N^2}}{2}\,R_\psi\,, \tag{8.9}$$

reducing to $2\sqrt{2}M$ in the neutral limit and vanishing in the extremal limit, where the whole sphere smoothly shrinks.

As already anticipated, the $\mathcal{W}$-soliton shares many features with the TS. They are static, non-extremal, smooth and horizonless solutions in a five-dimensional theory of gravity coupled to a Maxwell field. However, the $\mathcal{W}$-soliton possesses some interesting advantages. In particular, the extremal limit of the TS is singular, since it corresponds to a singular extremal black string. Conversely, the extremal limit of the $\mathcal{W}$-soliton remains smooth and horizonless. Moreover, the metric component along the fifth dimension in the TS behaves as $1 + \mathcal{O}(r^{-1})$ at large distances, leading to a mismatch between the five-dimensional and four-dimensional mass. On the other hand, for the $\mathcal{W}$-soliton the expansion at large r of the metric component along the fifth dimension is $g_{\psi\psi} \sim 1 - \frac{4M^2}{r^2} + \ldots$, without $1/r$ terms. This property ensures that the five- and four-dimensional masses coincide.

As stated above, the neutral $N = Q = 0$ limit of the $\mathcal{W}$-soliton is astrophysically relevant. Instead of reducing to the so-called bubble-of-nothing [322], it yields a new smooth horizonless solution with the same redshift factor as the Schwarzschild BH and a single free parameter (the mass). The spacetime smoothly ends at $r = 4M$

and it possesses a nontrivial axion profile as follows

$$\begin{aligned} ds^2_{\mathcal{W}}|_{Q=0} &= -\left(1-\frac{2M}{r}\right)dt^2+\frac{r-2M}{r-4M}dr^2+\frac{r(r-4M)}{(r-2M)^2}d\psi^2 \\ &\quad + r(r-2M)(d\theta^2+\sin^2\theta\, d\phi^2), \\ A &= \frac{2M}{r-2M}d\psi\,. \end{aligned} \tag{8.10}$$

8.1.2 The black hole

The $\mathcal{W}$-soliton shares the same parameter space of mass and electromagnetic charges as the non-extremal black string constructed in [27], which, after Kaluza–Klein reduction along the fifth dimension, corresponds to a static charged black hole. Its line element in the five-dimensional spacetime is given by

$$\begin{aligned} ds^2_{\rm BH} &= f_+f_-\left(d\psi+\frac{Q}{r\,f_+}dt+Q(\cos\theta+1)\,d\phi\right)^2-\frac{f_M}{f_+f_-}\,dt^2 \\ &\quad + f_-\left[\frac{dr^2}{f_-f_M}+r^2(d\theta^2+\sin^2\theta\,d\phi^2)\right], \\ A &= \frac{Q}{r}dt+\frac{f_+-f_-}{2}\left(d\psi+Q(\cos\theta+1)\,d\phi\right)-Q(\cos\theta+1)\,d\phi\,. \end{aligned} \tag{8.11}$$

where we have defined

$$f_\pm \equiv 1\pm\frac{\sqrt{M^2+4Q^2}-M}{r}. \tag{8.12}$$

Also in this case the coordinate r is not the standard spherical radial coordinate. Regularity at the poles of the two-sphere requires the same quantization of the Kaluza–Klein monopole charge $Q = NR_\psi/2$ as for the $\mathcal{W}$-soliton (8.8). The extremal bound of Eq. (8.6), valid for the $\mathcal{W}$-soliton, is present also in this case, as a consequence of requiring that the horizon appears before the singularities at the zero of f_-. In the extremal limit $M = |Q|/\sqrt{2}$, the black string and the $\mathcal{W}$-soliton coincide, reducing to the same smooth, horizonless and supersymmetric center.

The neutral limit $Q = 0$ yields the trivial embedding of the Schwarzschild black hole in five dimensions:

$$\begin{aligned} ds^2_{\rm BH}|_{Q=0} &= -\left(1-\frac{2M}{r}\right)dt^2+\left(1-\frac{2M}{r}\right)^{-1}dr^2+d\psi^2+r^2(d\theta^2+\sin^2\theta\,d\phi^2)\,, \\ A &= 0. \end{aligned} \tag{8.13}$$

8.1.3 Four-dimensional effective description

Similarly to the TS case and the corresponding BH counterpart, also in the $\mathcal{W}$-soliton case it is possible to provide a four-dimensional description through dimensional reduction along the compact circle S^1. Following [27], the dimensional reduction of $\mathcal{N} = 2$ five-dimensional supergravity coupled to two vector multiplets yields

four-dimensional supergravity, consisting of three complex scalars, z^I, and four U(1) gauge fields, $(\mathcal{A}, A^I)$. However, in minimal supergravity three of the gauge fields and the two scalars coincide. Under these conditions the line element of the $\mathcal{W}$-soliton after the dimensional reduction reads

$$\begin{aligned} ds^2_{\mathcal{W}} &= \sqrt{f_Q(2f_M - f_Q)}\left[-\frac{dt^2}{f_Q} + \frac{dr^2}{2f_M - f_Q} + r^2\left(d\theta^2 + \sin^2\theta\, d\phi^2\right)\right], \\ A &= \frac{Q}{r}\frac{f_M}{f_Q}\,dt - Q(\cos\theta + 1)\,d\phi\,, \quad \mathcal{A} = -\frac{Q\,f_M}{r\,f_Q}dt - Q(\cos\theta+1)\,d\phi, \\ z &= \frac{f_Q - f_M}{f_M} + i\,\frac{\sqrt{f_Q(2f_M - f_Q)}}{f_M}\,, \end{aligned} \tag{8.14}$$

In the neutral $Q = 0$ the two gauge fields vanish and one is left with a nontrivial complex scalar, whose real and imaginary parts correspond to the axion and dilaton fields, respectively. Again, similarly to the TS case, the dimensionally reduced solution possesses a singularity at the bubble locus where $2f_M - f_Q = 0$. This feature is a common outcome of reducing geometries along a smoothly degenerating compact direction: although the higher-dimensional geometry remains completely regular, this degeneration appears as a naked singularity when viewed from the lower dimensional viewpoint.

The black string reduces to a regular dyonic and dilatonic black hole in four dimensions:

$$\begin{aligned} ds^2_{\rm BH} &= -\frac{f_M}{\sqrt{f_+ f_-}}\,dt^2 + \sqrt{f_+ f_-}\left[\frac{dr^2}{f_M} + r^2 f_-(d\theta^2 + \sin^2\theta\, d\phi^2)\right], \\ A &= \frac{Q}{r\,f_+}dt - Q(\cos\theta+1)\,d\phi\,, \qquad \mathcal{A} = -\frac{Q}{r\,f_+}dt - Q(\cos\theta+1)\,d\phi, \\ z &= \frac{f_+ - f_-}{2} + i\,\sqrt{f_+ f_-}. \end{aligned} \tag{8.15}$$

8.2 Geodesic structure and photon sphere

Let us now discuss the motion along null geodesics in the background of the $\mathcal{W}$-soliton and the corresponding BH. If we define with τ the affine parameter, we can introduce the conjugate momenta p_μ as

$$p_\mu \equiv g_{\mu\nu}\,\dot{x}^\nu\,, \tag{8.16}$$

where $\dot{x}^\nu = dx^\nu/d\tau$. Since the two spacetimes are characterized by three isometries along the t, ϕ and ψ directions, they possess three conserved quantities: the momenta associated to the Killing vectors, given by $p_t = -E$, p_ϕ, and p_ψ. Moreover, a fourth conserved quantity comes from the Hamiltonian $H = \frac{1}{2}g^{\mu\nu}p_\mu p_\nu = 0$. Additionally, the spacetimes are also characterized by a Carter-like constant given by

$$C = p_\theta^2 + \frac{1}{\sin^2\theta}\left[(p_\phi - 2p_\psi Q)^2\cos^2\frac{\theta}{2} + p_\phi^2\sin^2\frac{\theta}{2}\right]. \tag{8.17}$$

that allows for separation of variables. We now turn our attention to closed null geodesics, focusing on effectively massless four-dimensional probes that correspond to the lowest Kaluza–Klein excitation with $p_\psi = 0$.

By using the Hamiltonian equation

$$\dot{p}_\mu = -\frac{dH}{dx^\mu}\,. \tag{8.18}$$

one can derive the following first order equations for the $\mathcal{W}$-soliton

$$\begin{aligned}
\dot{t} &= \frac{f_Q}{f_M}\,E + \frac{Q\,p_\psi}{r}, \qquad \dot{\phi} = \frac{p_\phi - Q\,p_\psi(1+\cos\theta)}{r^2 f_M \sin^2\theta}, \\
\dot{\psi} &= \frac{f_M^2}{f_Q(2f_M - f_Q)}\,p_\psi - \frac{Q f_M}{r f_Q}\,\dot{t} - Q(1+\cos\theta)\,\dot{\phi}, \\
\dot{\theta} &= \pm\frac{\sqrt{\Theta(\theta)}}{r^2 f_M}, \qquad \dot{r} = \pm\sqrt{R(r)},
\end{aligned} \tag{8.19}$$

where we have defined

$$\begin{aligned}
\Theta(\theta) &\equiv C - \frac{1}{\sin^2\theta}\left[(p_\phi - 2p_\psi Q)^2\cos^2\frac{\theta}{2} + p_\phi^2\sin^2\frac{\theta}{2}\right], \\
R(r) &\equiv \frac{2f_M - f_Q}{r^2 f_M^2 f_Q}\left[(rEf_Q + Qp_\psi f_M)^2 + \left(Q^2 f_Q - \frac{r^2 f_M(f_M - f_Q)^2}{2f_M - f_Q}\right)p_\psi^2 - C f_Q\right]
\end{aligned} \tag{8.20}$$

Similarly, for the BH case we find that the null geodesics obey the following first order equations

$$\begin{aligned}
\dot{t} &= \frac{f_-}{f_M}\left(f_+\,E + \frac{Q}{r}\,p_\psi\right), \qquad \dot{\phi} = \frac{p_\phi - Q\,p_\psi(1+\cos\theta)}{r^2 f_- \sin^2\theta}, \\
\dot{\psi} &= \frac{p_\psi^2}{f_- f_+}\,p_\psi - \frac{Q}{r f_+}\,\dot{t} - Q(1+\cos\theta)\,\dot{\phi}, \\
\dot{\theta} &= \pm\frac{\sqrt{\Theta(\theta)}}{r^2 f_-}, \qquad \dot{r} = \pm\sqrt{\widetilde{R}(r)},
\end{aligned} \tag{8.21}$$

where Θ is still defined in Eq. (8.20) and $\widetilde{R}$ is given by

$$\widetilde{R}(r) \equiv \frac{f_M}{r^2 f_-}\left[\frac{r^2 f_+ f_-^2}{f_M}\left(E + \frac{Q}{r f_+}p_\psi\right)^2 - \frac{r^2 - Q^2 f_+}{f_+}p_\psi^2 - C\right]. \tag{8.22}$$

We are free to choose $E = 1$, which corresponds to taking the affine parameter τ as the proper time of the probe.

8.2.1 Photon sphere of the $\mathcal{W}$-soliton

For null geodesics with $p_\psi = 0$ the probe experiences no motion along the compact fifth dimension and can, without loss of generality, be restricted to the equatorial plane $\theta = \pi/2$. In the equatorial plane the Carter-like constant of Eq. (8.17) is simply given by $C = p_\phi^2$.

In order to find the photon spheres of the $\mathcal{W}$-soliton we impose the usual conditions $\dot{r} = \ddot{r} = 0$. The equation $\dot{r} = 0$ yields two possible radii beyond the bubble locus r_+, one of which lies at it, whereas the additional condition $\ddot{r} = 0$ fixes

p_ϕ and merges the two solutions. Hence, the $\mathcal{W}$-soliton possesses a single photon orbit, located precisely at the bubble locus $R_o = r_+$. The corresponding angular velocity $\Omega_{\mathcal{W}} = \dot{\phi}/\dot{t}$ is given by

$$p_\phi = \Omega_{\mathcal{W}}^{-1} = \sqrt{2}\,\lambda_{\mathcal{W}}^{-1} = \sqrt{2r_+(r_+ - 2M)}, \tag{8.23}$$

where $\lambda_{\mathcal{W}}$ is the Lyapunov exponent measuring the average rate of expansion or contraction of adjacent geodesics at the photon sphere given by, for spherically symmetric spacetimes [323, 324],

$$\lambda = \sqrt{\frac{1}{2\dot{t}^2}\,\frac{d^2R(r)}{dr^2}}\,\Big|_{r=R_o}. \tag{8.24}$$

A real Lyapunov exponent λ corresponds to an unstable photon sphere. Since the coordinate r is not the usual radial spherical coordinate, $R_o = r_+$ does not represent the physical size of the photon sphere. Indeed the correct physical radius of the two-sphere located at the photon sphere is given by

$$R_{\mathcal{W}} = \sqrt{r_+(r_+ - 2M)} = \frac{1}{\lambda_{\mathcal{W}}}. \tag{8.25}$$

In the case of the neutral $\mathcal{W}$-soliton, the characteristics of the photon sphere are

$$R_o = 4M, \qquad p_\phi = \Omega_{\mathcal{W}}^{-1} = 4M, \qquad \lambda_{\mathcal{W}} = {R_{\mathcal{W}}}^{-1} = \frac{1}{2\sqrt{2}\,M}\,, \tag{8.26}$$

similar to the corresponding values of the Schwarzschild case.

If compared to the structure of the photon spheres of the TS (discussed in Sec. 6.1), one can notice that the $\mathcal{W}$-soliton behaves as a first-kind TS, featuring a single unstable photon sphere. As discussed for the TS, the absence of a stable photon sphere does not allow formation of long-lived QNMs or echoes. Consequently, the $\mathcal{W}$-soliton is expected to display only short-lived QNMs and to lack late-time echoes, resembling the behavior of an ordinary BH.

8.2.2 Photon sphere of the BH

Also in the BH case the spherical symmetry of the spacetime allows us to consider motion in the equatorial plane ($\theta = \pi/2$) once we focused on effectively massless probes ($p_\psi = 0$). Proceeding similarly, we find that the black string admits a unique photon sphere outside its horizon, with the following characteristics

$$\begin{aligned}
R_o &= \frac{\left(\sqrt{m_+} + \sqrt{9m_+ - 16m_-}\right)\left(3\sqrt{m_+} + \sqrt{9m_+ - 16m_-}\right)}{8}, \\
p_\phi = \Omega_{\rm BH}^{-1} &= \frac{\left(\sqrt{9m_+ - 16m_-} - \sqrt{m_+}\right)^{\frac{1}{2}}\left(3\sqrt{m_+} + \sqrt{9m_+ - 16m_-}\right)^{\frac{3}{2}}}{4}, \\
\lambda_{\rm BH} &= \frac{4\sqrt{2}\,(9m_+ - 16m_-)^{\frac{1}{4}}}{\left(\sqrt{9m_+ - 16m_-} - \sqrt{m_+}\right)^{\frac{1}{2}}\left(3\sqrt{m_+} + \sqrt{9m_+ - 16m_-}\right)^{2}},
\end{aligned} \tag{8.27}$$

where

$$m_\pm \equiv \frac{\sqrt{M^2 + 4Q^2} \pm M}{2}\,. \tag{8.28}$$

The physical radius of the photon sphere is given by

$$R_{\rm BH} = r\sqrt{f_-}|_{r=R_o} = \sqrt{R_o(R_o - m_-)}. \tag{8.29}$$

In the neutral limit $Q = 0$, we recover the standard Schwarzschild values

$$R_o = 3M, \qquad p_\phi = \Omega_{\rm BH}^{-1} = 3\sqrt{3}M, \qquad \lambda_{\rm BH} = \frac{1}{3\sqrt{3}M}\,, \tag{8.30}$$

as expected from Eq. (8.13). For all M and Q within the allowed range (8.6), the Lyapunov exponent $\lambda_{\rm BH}$ is real, which proves that the photon sphere is always unstable.

Comparison between the $\mathcal{W}$-soliton and the BH

In both the $\mathcal{W}$-soliton and its BH counterpart, null rays define a single unstable circular orbit, showing a similar qualitative behavior. However, the detailed properties of the photon spheres show clear quantitative differences. As shown in Fig. 8.1, one can notice order-one differences in the dependence on the charge to mass ratio of the angular momentum, Lyapunov exponent and angular velocity.

As anticipated, the Lyapunov exponent measures the instability of null geodesics at the photon sphere. Since the exponent for the $\mathcal{W}$-soliton is in general twice that of the BH, across all the parameter space, we expect a stronger instability of null geodesics. As a consequence, we also expect the ringdown signal of the $\mathcal{W}$-soliton to exhibit a faster damping rate than that of the corresponding BH, due to its connection with the Lyapunov exponent (see [236, 289, 324]). As the two solutions approach extremality, the Lyapunov exponents diverge, indicating that their photon sphere shrinks to a point.

The angular velocity of photons at the photon sphere is given by the inverse of their angular momentum, $\Omega = p_\phi^{-1}$. Moreover, the angular velocity is approximately proportional to the real part of the QNM frequencies.

8.3 The scalar perturbations

Let us now present the dynamics of a minimally coupled massless scalar field in the $\mathcal{W}$-soliton and its corresponding BH. In the following we will derive the master equation for massless test scalar field perturbations on the background of both solutions. The QNM spectrum is then derived using both WKB approximation and numerical methods (direct integration and continued fraction, see Appendix E). Finally, we present selected results for the ringdown signal obtained by integrating the perturbation equation in the time domain.

8.3.1 The scalar wave perturbation equation

A test massless scalar field, minimally coupled to the background, obeys the Klein–Gordon equation

$$\frac{1}{\sqrt{-g}}\partial_\mu(g^{\mu\nu}\sqrt{-g}\,\partial_\nu\Phi) = 0\,, \tag{8.31}$$

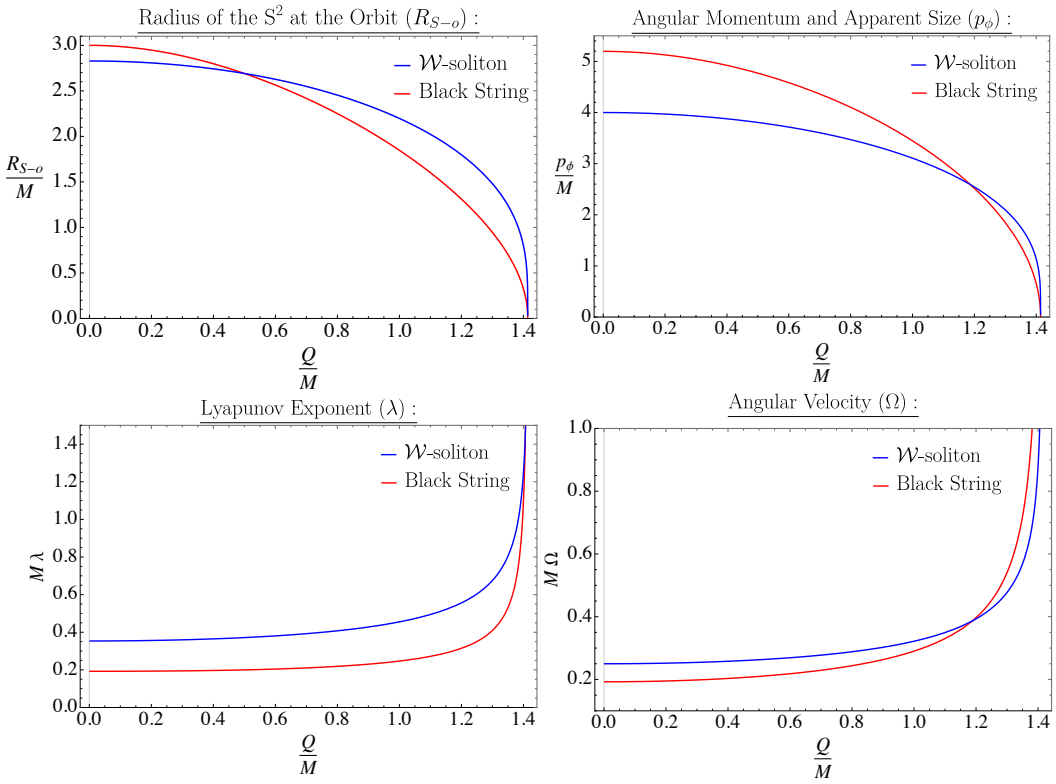

Figure 8.1. Properties of the photon sphere for the $\mathcal{W}$-soliton and the BH as functions of the charge-to-mass ratio. The top left panel shows the radius of the round two-sphere at the location of the photon orbit. The top right panel presents the angular momentum of photons on the orbit, which also determines the apparent size of the photon sphere as seen by an asymptotic observer. The bottom left panel displays the Lyapunov exponent characterizing the instability of the photon sphere. Finally, the bottom right panel shows the angular velocity of photons at the photon sphere, related to the QNM frequencies. These plots and the associated analysis of the geodesic structure of the $\mathcal{W}$-soliton and the corresponding BH were performed by other collaborators of Ref.[321]

where $\Phi = \Phi(t, r, \psi, \theta, \phi)$ is the scalar field. Thanks to the isometries of the background spacetime we can consider to following ansatz for the perturbation

$$\Phi_{\omega pm} = \Psi(r)\, S(\theta)\, e^{i\left(\frac{p}{R_\psi}\psi + m\phi - \omega t\right)}\,, \tag{8.32}$$

where m and p are integers due to the periodicity of ϕ and ψ given by 2π and $2\pi R_\psi$, respectively.

If we plug the scalar profile of Eq. (8.32) into the Klein-Gordon equation for the $\mathcal{W}$-soliton background we can separate the variables and isolate the radial part

$$\partial_r\left(r^2(2f_M - f_Q)\,\partial_r\Psi\right) - \left[\frac{r^2 f_M^3}{f_Q(2f_M - f_Q)}\frac{p^2}{R_\psi^2} - r^2 f_Q\left(\omega + \frac{f_M}{2r f_Q}Np\right)^2 + \lambda\right]\Psi = 0\,, \tag{8.33}$$

where λ is the separation constant and we used Eq. (8.8) for the charge Q. The

angular equation is given by

$$\frac{1}{\sin\theta}\partial_\theta\left(\sin\theta\,\partial_\theta S\right) - \left[\frac{1}{\sin^2\theta}\left(m - \frac{pN}{2}(1+\cos\theta)\right)^2 - \lambda\right] S = 0\,, \tag{8.34}$$

Similarly, for the BH case we get a radial equation given by

$$\partial_r\left(r^2 f_- f_M\,\partial_r\Psi\right) - \left[\frac{r^2}{f_+}\frac{p^2}{R_\psi^2} - \frac{r^2 f_-^2 f_+}{f_M}\left(\omega + \frac{1}{2rf_+}Np\right)^2 + \lambda\right]\Psi = 0\,, \tag{8.35}$$

while the angular equation is the same as (8.34).

The quantity $p_\psi = p/R_\psi$ labels the Kaluza–Klein modes and induces an effective mass in the analysis. Since the modes with $|p| \geq 1$ correspond to scalar fields with large effective mass when R_ψ is small compared to the object's size, in the following analysis we will focus on the phenomenologically relevant massless Kaluza–Klein mode with $p = 0$.

The solutions of the angular equation (8.34) are the spin-weighted spherical harmonics with half-integer spin $s = -\frac{pN}{2} \in \frac{1}{2}\mathbb{Z}$ (see [325–329]). By requiring regularity of the waveform at $\theta = 0$ and π we find that the separation constant must be positive and quantized as follows

$$\begin{gathered}\lambda = l(l+1) + s(1+2l) = l(l+1) - \frac{pN}{2}(1+2l), \\ l \in \mathbb{N}, \qquad l \geq \frac{|pN| + pN}{2}, \qquad l \geq |m|\,.\end{gathered} \tag{8.36}$$

For the explicit expression of the regular angular waveforms, together with a broader discussion, see [321].

Schrödinger-like form and boundary conditions

The master equations (8.33) and (8.35) for the massless test scalar field perturbation on the background of the $\mathcal{W}$-soliton and corresponding BH, respectively, can be recast into a Schrödinger-like form by rescaling the field and introducing a tortoise-like coordinate as follows

$$\mathcal{W}\text{-soliton:} \qquad \Psi = \frac{\overline{\Psi}}{r\sqrt{f_M}}, \qquad \frac{dr_*}{dr} = \frac{f_M}{2f_M - f_Q}, \tag{8.37}$$

$$\text{BH:} \qquad \Psi = \frac{\overline{\Psi}}{r\sqrt{f_-}}, \qquad \frac{dr_*}{dr} = \frac{1}{f_M}\,. \tag{8.38}$$

The tortoise-like coordinates can be integrated to obtain a closed form

$$\mathcal{W}\text{-soliton:} \qquad r_* = r - r_+ + \frac{r_+}{2}\log\left(\frac{r}{r_+} - 1\right) + \frac{r_-}{2}\log\left(\frac{r}{r_+} - 1\right), \tag{8.39}$$

$$\text{BH:} \qquad r_* = r - 2M + 2M\log\left(\frac{r}{2M} - 1\right), \tag{8.40}$$

where for $r \to \infty$ we have $r_* \to \infty$, while for the inner boundary (the smooth cap for the soliton and the horizon for the BH) the tortoise behaves as $r_* \to -\infty$. The two Schrödinger-like equations can be written as follows

$$\frac{d^2\overline{\Psi}}{{dr_*}^2} - V\,\overline{\Psi} = 0, \tag{8.41}$$

where the effective potential V is given below

$$V_{\mathcal{W}} = \frac{2f_M - f_Q}{f_M^2}\left[\frac{f_M^3}{f_Q(2f_M - f_Q)}\frac{p^2}{R_\psi^2} - f_Q\left(\omega + \frac{f_M}{2rf_Q}Np\right)^2 + \frac{\lambda}{r^2} + \frac{3f_Q(1+f_M^2) - 2f_M(f_M^2 - f_Q + 3)}{4r^2 f_M^2}\right], \tag{8.42}$$

$$V_{\rm BH} = \frac{f_M}{f_- f_+}\frac{p^2}{R_\psi^2} - f_- f_+\left(\omega + \frac{1}{2rf_+}Np\right)^2 + \frac{\lambda\, f_M}{r^2 f_-} + f_M\,\frac{2f_-(1+f_-) - f_M(1+3f_-^2)}{4r^2 f_-^2}, \tag{8.43}$$

with $V_{\mathcal{W}}$ and $V_{\rm BH}$ denoting the scalar potentials for the $\mathcal{W}$-soliton and the BH, respectively.

Asymptotically, at spatial infinity, the two potentials behave as $V \sim \frac{p^2}{R_\psi^2} - \omega^2$. In the background spacetime of the $\mathcal{W}$-soliton, due to the absence of the horizon, regular modes of the probe scalar field can be dissipative (i.e. QNMs) when $\frac{p}{R_\psi} < |\omega|$, or trapped normal modes when $\frac{p}{R_\psi} > |\omega|$. Since the term $\frac{p}{R_\psi}$ behaves as an effective mass, the trapped modes correspond to massive excitations confined by the spacetime. The boundary condition at infinity reads

$$\Psi(r)e^{-i\omega t} \underset{r_*\to\infty}{\propto} \frac{1}{r_*}e^{i\left(\sqrt{\omega^2 - \frac{p^2}{R_\psi^2}}\, r_* - \omega t\right)}. \tag{8.44}$$

corresponding to outgoing waves for the QNMs and decaying waves for normal modes, depending on the previous inequalities.

At the BH horizon ($r_* \to -\infty$), the potential tends to a finite negative value $-\omega'^2$, with,

$$\omega' = \frac{\sqrt{3M - \sqrt{M^2+4Q^2}}\left((M + \sqrt{M^2+4Q^2})\,\omega + \frac{pN}{2}\right)}{2M\sqrt{M + \sqrt{M^2+4Q^2}}}, \tag{8.45}$$

and regular solutions correspond to ingoing modes

$$\Psi(r)e^{-i\omega t} \underset{r_*\to-\infty}{\propto} e^{-i(\omega' r_* + \omega t)}. \tag{8.46}$$

In the case of the $\mathcal{W}$-soliton the potential at the inner boundary (the smooth cap of the soliton) behaves differently depending on the value of p: for $p = 0$ it vanishes; while for $p \neq 0$ it approaches a finite positive value. Regularity requires Neumann boundary conditions in terms of the local radial coordinate $\rho^2 = 4(r - r_+) \sim 4r_+ e^{\frac{r_*}{r_+}}$, leading to:

$$e^{-\frac{r_*}{2r_+}}\,\partial_{r_*}\Psi \underset{r_*\to-\infty}{=} 0, \tag{8.47}$$

which implies that Ψ must converge to a constant faster than $e^{\frac{r_*}{2r_+}}$ at $r_* \to -\infty$.

A preliminary test of stability of the two spacetimes under test scalar perturbations can be performed by searching for critical static modes with $\omega = 0$. One

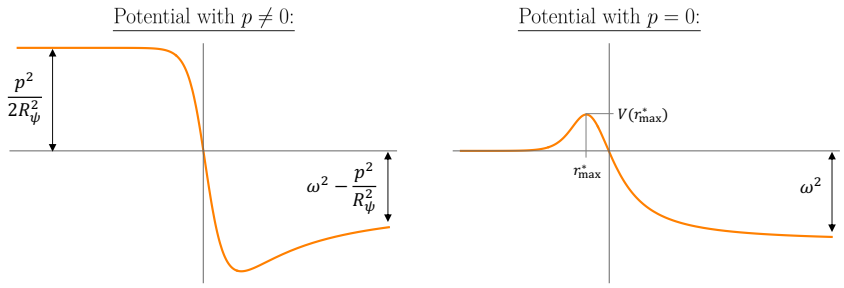

Figure 8.2. Scalar potential of the $\mathcal{W}$-soliton for $p = 0$ and $p \neq 0$, in regimes where the potential changes sign. The plots show $V_{\mathcal{W}}(r_*)$ from (8.42) for $k = 100$, $N = 30$, $l = 10$, and $(\omega R_\psi, p) = (1.03, 1)$ or $(1/3, 0)$.

can check that for $\omega = 0$ the two potentials of Eqs.(8.42)-(8.43) are positive definite everywhere across the full parameter space, respecting the condition of Eq. (8.6). As a result, regularity cannot be achieved simultaneously at the two boundaries, since any mode inevitably diverges at one of them. Hence, $\mathcal{W}$-solitons do not admit critical static modes.

The stability analysis will be confirmed and extended in the next section with the numerical derivation of the QNMs and the study of the time domain signal.

8.3.2 QNMs from WKB approximation

In this section we review the computation of the QNM spectrum of the $\mathcal{W}$-soliton and of the corresponding BH using the WKB approximation. This analytical approach provides an accurate estimate of the QNM frequencies in the eikonal ($l \gg 1$) regime, with a close connection to the photon sphere discussed in Sec. 8.2. The results presented in this section, based on the analysis performed by other collaborators of Ref. [321], highlight the correspondence between the $\mathcal{W}$-soliton and BH QNMs, revealing also some quantitative deviations, consequence of the absence of the horizon in the solitonic spacetime.

More in detail, the WKB approximation is valid when the potential of the perturbation equation varies slowly and the imaginary part of the QNM frequencies is negligible compared to the real part (namely, slowly damped modes). In our case, these conditions hold when

$$l \gg 1, \qquad \omega_R \gg \omega_I, \qquad \omega \equiv \omega_R + i\,\omega_I\,. \tag{8.48}$$

Slowly-damped QNMs of the $\mathcal{W}$-soliton

After an analysis of the potential of Eq. (8.42), one can check that, across the full domain $-\infty < r_* < \infty$, at most one root is present. Moreover, the potential can be entirely negative, or can become negative at large values of r_*. In the first case, the WKB approximation fails to produce any regular wave solutions that satisfy both boundary conditions. In the second case, two different types of potentials arise, as shown in Fig. 8.2. For $p \neq 0$, left panel of Fig. 8.2, the potential presents a centrifugal barrier close to the smooth cap of the soliton; while for $p = 0$, right panel, the barrier is not present. As discussed more in details in [321], no slowly damped

QNMs are captured by the WKB approximation when $p \neq 0$. As a consequence, the modes with $p \neq 0$ must have a non-negligible imaginary component of the frequency, implying they are rapidly damped. For $p = 0$, the same conclusion applies when the maximum of the potential is large. However, when the maximum is small (right panel of Fig. 8.2), as shown in [289], regular, slowly damped QNMs exist in this regime if the following quantization condition is satisfied for an overtone number $n \geq 0$

$$i\,\frac{\sqrt{2}\,V_{\mathcal{W}}(r_{*\max})}{\sqrt{|V''_{\mathcal{W}}(r_{*\max})|}} = -n - \frac{1}{2}, \qquad n \in \mathbb{Z}, \quad n \geq 0. \tag{8.49}$$

For large l and $\omega = \mathcal{O}(l)$, the potential becomes $V_{\mathcal{W}} \approx -R(r)$ with $E = -\omega$ and $C = \lambda$, where $R(r)$ is the geodesic potential (8.20), such that the properties of the potential around the maximum are intimately connected to the properties of the photon sphere. The QNM frequencies are given by by [236, 289, 324]:

$$\omega_{\mathcal{W};l,n} = \Omega_{\mathcal{W}} \left(l + \frac{1}{2}\right) - i\,\lambda_{\mathcal{W}} \left(n + \frac{1}{2}\right), \qquad n \in \mathbb{Z}, \quad n \geq 0, \tag{8.50}$$

where $\Omega_{\mathcal{W}}$ is the angular velocity at the photon sphere, and $\lambda_{\mathcal{W}}$ is the Lyapunov exponent defined in (8.23). The WKB approximation holds as long as $\omega_R \gg \omega_I$, which means $\frac{2l+1}{2n+1} \gg \sqrt{2}$ since for the $\mathcal{W}$-soliton, $\lambda_{\mathcal{W}}/\Omega_{\mathcal{W}} = \sqrt{2}$.

Slowly-damped QNMs of the BH

The potential for the BH case, given by Eq. (8.43), behaves as $\sim -\omega'^2$, with ω' defined in Eq. (8.45), for $r_* \to -\infty$, and as $\sim -\omega^2 + \frac{p^2}{R_\psi^2}$ for $r_* \to +\infty$. Between these two asymptotic regions, the potential may develop a positive "bump," a characteristic feature of static BH spacetimes, as extensively studied in the Schwarzschild case [330, 331]. If the region with positive potential is narrow enough and can be approximated with a parabola, the WKB approximation is able to capture the slowly-damped QNMs. Requiring the QNMs to be regular at the horizon and at infinity gives the quantization condition [331]

$$i\,\frac{V_{\rm BH}(r_{*\max})}{\sqrt{2|V''_{\rm BH}(r_{*\max})|}} = -n - \frac{1}{2}, \qquad n \in \mathbb{Z}, \quad n \geq 0\,, \tag{8.51}$$

where $r_{*\max}$ denotes the location of the potential maximum.

In the special case of $p = 0$, assuming large l with $\omega = \mathcal{O}(l)$, we find that $V_{\rm BH} \approx -\widetilde{R}(r)$ with $E = -\omega$ and $C = \lambda$, where $\widetilde{R}(r)$ is the geodesic potential (8.22). Therefore, similarly to the $\mathcal{W}$-soliton case, we get the well known QNM spectrum from the WKB approximation [324], expressed in terms of the photon sphere characteristics

$$\omega_{{\rm BH};l,n} = \Omega_{\rm BH} \left(l + \frac{1}{2}\right) - i\,\lambda_{\rm BH} \left(n + \frac{1}{2}\right), \qquad n \in \mathbb{Z}, \quad n \geq 0, \tag{8.52}$$

where $\Omega_{\rm BH}$ is the angular velocity of photons at the photon sphere, and $\lambda_{\rm BH}$ is the Lyapunov exponent defined in Eq. (8.27). In this case the WKB approximation is valid in the regime $\omega_R \gg \omega_I$, which corresponds to $\frac{2l+1}{2n+1} \gg 1$, since for the BH the ratio $\lambda_{\rm BH}/\Omega_{\rm BH}$ lies in the range $\frac{1}{\sqrt{2}} \leq \lambda_{\rm BH}/\Omega_{\rm BH} \leq 1$.

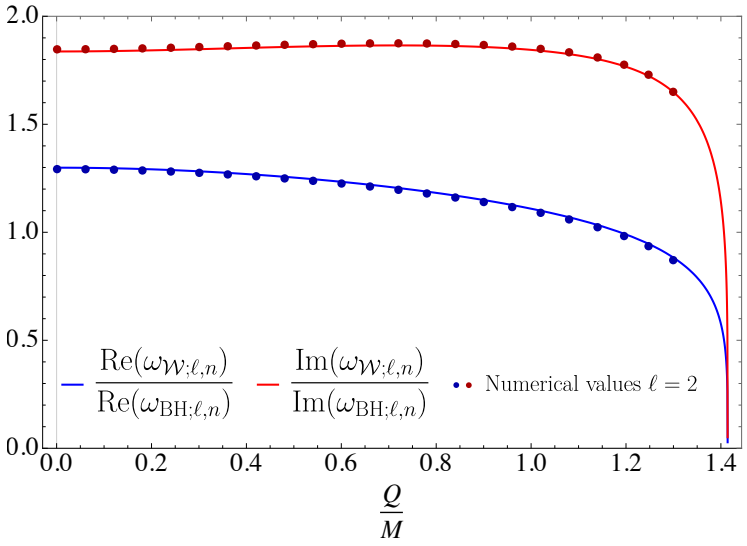

Figure 8.3. Ratios of the QNM frequencies for the $\mathcal{W}$-soliton and the black string. In the WKB approximation (solid lines), these ratios depend only on Q/M and are independent of (M, l, n). The dots are the numerical values from the direct-integration method at $l = 2$ (up to $Q/M = 1.3$), indicating an excellent agreement with WKB values, even for small l.

Comparison

As shown in the sections before, slowly-damped modes, effectively captured by the WKB approximation, are defined in terms of the angular velocities and Lyapunov exponents associated to the photon sphere of the two spacetimes. Therefore, due to the order-one differences in the properties of the photon spheres of $\mathcal{W}$-soliton and BH, these differences will appear also in the QNM spectrum. Fig. 8.3 shows the ratios of the real and imaginary parts of the QNM frequencies as functions of the charge-to-mass ratio across the full parameter space. As can be seen, for $|Q|/M \leq 1.19$, the $\mathcal{W}$-soliton features QNMs with a larger real frequency and a greater damping rate compared to the BH, indicating a faster and more strongly attenuated ringdown signal. Moreover, the WKB results (solid lines of Fig. 8.3) are in excellent agreement with the full QNM spectrum (dots in Fig. 8.3), computed numerically as discussed in Sec. 8.3.3.

8.3.3 Numerical QNM spectrum

In this section we compute the complete QNM spectrum of an effectively massless scalar field ($p = 0$) for both the neutral $\mathcal{W}$-soliton and the corresponding BH backgrounds. The associated frequencies are computed numerically by using both the continued fraction method [145] (see Appendix E for the complete procedure) and the direct integration shooting method [153, 183–185], finding excellent agreement. In Table 8.1 we present the results for the fundamental ($n = 0$) QNM, normalized by the mass M, for several values of the harmonic index l, compared to the corresponding WKB values. Notably, the WKB approximation yields an error below 1% already at $l = 1$ for both the soliton and the BH, highlighting its remarkable accuracy

in reproducing the slowly damped modes of the spectrum, even for small l. As illustrated in Fig. 8.3, with the QNM frequencies obtained from the direct integration method plotted on top of the WKB values, this remarkable agreement persists also for the charged solutions. For practical reasons, the numerical data terminate around $Q/M \sim 1.3$, rather than extending to extremality, because the numerical cost increases substantially as extremality is approached, with the QNM frequencies becoming progressively larger.

l	Neutral $\mathcal{W}$-soliton		Schwarzschild BH	
	continued fraction	WKB	continued fraction	WKB
0	$0.13669 - i\,0.20545$	$0.125 - i\,0.17678$	$0.11046 - i\,0.10490$	$0.09623 - i\,0.09623$
1	$0.37542 - i\,0.18194$	$0.375 - i\,0.17678$	$0.29294 - i\,0.09766$	$0.28868 - i\,0.09623$
2	$0.62508 - i\,0.17872$	$0.625 - i\,0.17678$	$0.48364 - i\,0.09676$	$0.48113 - i\,0.09623$
3	$0.87503 - i\,0.17778$	$0.875 - i\,0.17678$	$0.67537 - i\,0.09650$	$0.67358 - i\,0.09623$
5	$1.37501 - i\,0.17719$	$1.375 - i\,0.17678$	$1.05961 - i\,0.09634$	$1.05848 - i\,0.09623$
10	$2.62500 - i\,0.17689$	$2.625 - i\,0.17678$	$2.02132 - i\,0.09626$	$2.0207 - i\,0.09623$
30	$7.62500 - i\,0.17679$	$7.625 - i\,0.17678$	$5.86993 - i\,0.09623$	$5.8697 - i\,0.09623$

Table 8.1. Fundamental ($n = 0$) QNM of an effectively massless scalar field ($p = 0$) in the neutral ($Q = 0$) $\mathcal{W}$-soliton and Schwarzschild BH background spacetimes, for various harmonic numbers l. We report both the dimensionless frequencies ωM computed with the continued fraction method and the WKB approximation.

While the WKB approximation is quite effective in capturing the short-lived QNM frequencies, where the condition $\omega_R \gg \omega_I$ is satisfied, even for low values of the harmonic index l, it fails to accurately describe the highly damped modes, for which the imaginary part is comparable to the real frequency. These modes are captured by the continued fraction method, and reported in Table 8.2 for $l = 1$ and $l = 5$ in both the Schwarzschild BH and the neutral $\mathcal{W}$-soliton backgrounds. By comparing

n	Neutral $\mathcal{W}$-soliton		Schwarzschild BH	
	$l = 1$	$l = 5$	$l = 1$	$l = 5$
0	$0.37542 - i\,0.18194$	$1.37501 - i\,0.17719$	$0.29294 - i\,0.09766$	$1.05961 - i\,0.09634$
1	$0.28371 - i\,0.60411$	$1.34139 - i\,0.53626$	$0.26445 - i\,0.30626$	$1.05004 - i\,0.29015$
2	$0.20907 - i\,1.10779$	$1.27631 - i\,0.90978$	$0.22954 - i\,0.54013$	$1.03150 - i\,0.48735$
3	$0.17171 - i\,1.62472$	$1.18556 - i\,1.30773$	$0.20326 - i\,0.78830$	$1.00520 - i\,0.68993$
4	$0.15050 - i\,2.13882$	$1.08008 - i\,1.73772$	$0.18511 - i\,1.04076$	$0.97297 - i\,0.89948$

Table 8.2. Overtone QNMs of an effectively massless scalar field ($p = 0$) in the neutral ($Q = 0$) $\mathcal{W}$-soliton and Schwarzschild BH background spacetimes, for different overtones n, and for $l = 1$ and $l = 5$.

the behavior of the modes, for the two background spacetimes, as the overtone index n increases, one can notice that they display a broadly similar behavior: the imaginary part grows and the real part decays with n. If the fundamental mode differs significantly, the higher overtones display very similar characteristics in both cases. This suggests that the time domain ringdown signals of the soliton and the Schwarzschild BH possess a comparable overall structure, differing mainly in

their fundamental oscillation frequency and damping rate (see Sec. 8.3.4 for a more detailed discussion).

8.3.4 Time-domain ringdown

In this section we report the main results concerning the study of the ringdown signal of both $\mathcal{W}$-soliton and corresponding BH spacetimes, obtained by integrating the corresponding master equations in the time domain. The results shown here were produced by collaborators of Ref. [321]. For a more detailed discussion of the numerical methods used to solve the perturbation equations see [321].

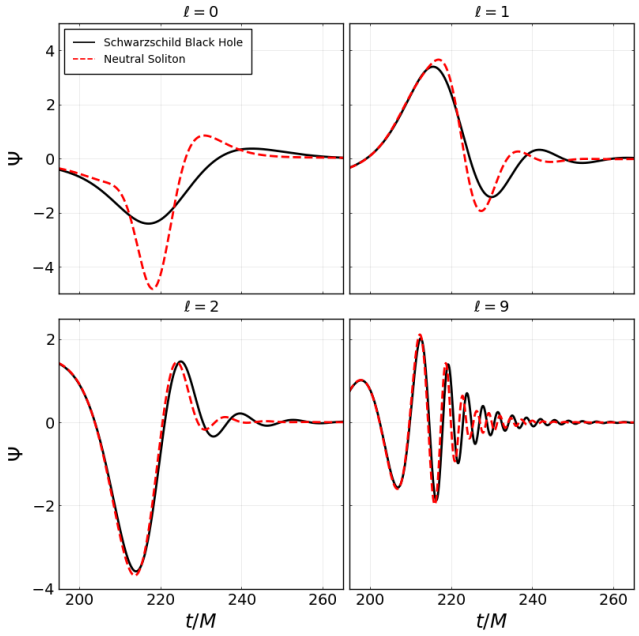

Figure 8.4. Ringdown signals of an effectively massless test scalar perturbation Ψ as a function of time and evaluated at $R_{\rm ext} = 100M$ for the Schwarzschild BH and the neutral $\mathcal{W}$-soliton, for different harmonic index $l = 0\,, 1\,, 2\,, 9$. Credits to A. Dima of Ref. [321].

In Fig. 8.4 we report the waveforms corresponding to the linear scalar ringdown of the neutral $\mathcal{W}$-soliton and the Schwarzschild BH for different values of the harmonic index l. The cases with $l = 1, 2, 9$ feature common properties in the overall behavior, that are in agreement with the QNMs derived in the previous sections. Because of the absence of long-lived modes in the spectrum of the $\mathcal{W}$-soliton spacetime, no echoes appear in the ringdown response, a direct consequence of the absence of a stable photon sphere, discussed in Sec. 8.2. While the prompt response is quite similar between the two spacetimes, as expected by the similar spectrum of highly damped and low-frequency modes, in the intermediate region the $\mathcal{W}$-soliton waveform displays a higher oscillation frequency and a faster damping rate. The latter behavior is explained again in terms of the QNMs by noticing that the fundamental frequency of the $\mathcal{W}$-soliton has a real and an imaginary part slightly larger than those associated to the fundamental mode of the BH.

The waveform for $l = 0$ is different, showing a soliton response much stronger than that of Schwarzschild BH.

The $\mathcal{W}$-soliton and corresponding BH response for $Q \neq 0$ is plotted in Fig. 8.5 for $l = 0, 1, 2$.

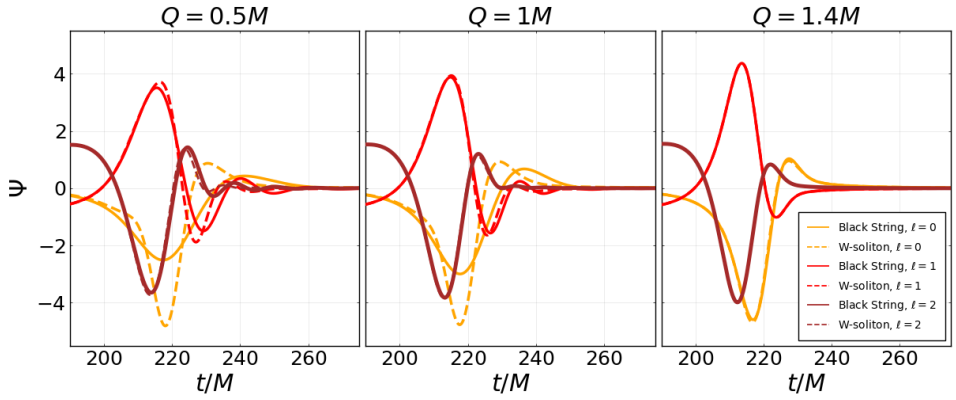

Figure 8.5. Ringdown responses of a test scalar perturbation Ψ as a function of time and evaluated at $R_{\rm ext} = 100M$ for BH and $\mathcal{W}$-soliton with charge $Q = \{0.5\,, 1\,, 1.4\}M$ (respectively, left, middle and right panels). We considered three harmonics $l = \{0\,, 1\,, 2\}$ (respectively, orange, red and brown curves). Credits to A. Dima of Ref. [321].

As can be seen in the right panel of the plot, when approaching the extremal limit, the two spacetimes, and consequently their ringdown waveforms, become nearly identical. On the other hand, far from extremality, the behavior is similar to the already discussed neutral case. It is worth noting that even for extremality the WKB short-lived spectrum indicates significant differences between the QNM frequencies of the two solutions. Indeed, for $Q = 1.4M$ the fundamental QNM of the BH is expected to oscillate about 1.7 times faster and be 1.1 times less damped than that of the soliton, in contrast to what observed in Fig. 8.5. Close to extremality, the fundamental frequencies are different but very high (see Fig. 8.1); therefore, a very narrow initial Gaussian perturbation is required to excite these modes. In other words, when $Q \simeq \sqrt{2}M$, both solutions approach a point-like geometry, so only perturbations with very short wavelengths (i.e. large frequency) can probe the spacetime. When the initial Gaussian perturbation is not narrow enough, the response is determined by the prompt signal which depends on the initial data, as shown in Fig.8.5.

In Fig. 8.6 we show how well the fundamental QNM is able to describe the ringdown signal of the $\mathcal{W}$-soliton, for $Q = \{0, 1.2\}M$ with harmonic index $l = 2$.

The ringdown waveform, plotted in a logarithmic scale, is compared to a damped sinusoid obtained from the fundamental QNM of the $\mathcal{W}$-soliton. Although the prompt response is highly sensitive to the initial conditions and involves contributions from strongly damped modes, the intermediate phase of the signal is accurately captured by the fundamental mode. During this second phase of the waveform, the contribution from highly damped modes has already decayed and no longer affects the overall signal.

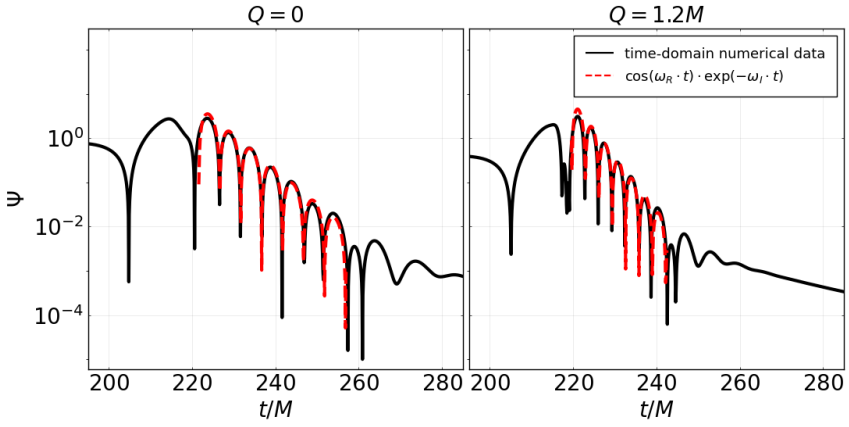

Figure 8.6. Comparison of the time-domain response with a single-mode damped sinusoid using the QNM estimate, for $\mathcal{W}$-solitons with $Q = 0$ (left) and $Q = 1.2M$ (right) for test scalar perturbations with $l = 2$. Credits to A. Dima of Ref. [321].

Chapter 9

Conclusions and future prospects

In the vast landscape of compact objects in the universe, BHs stand out for their remarkable simplicity. Nonetheless, their conceptually simple nature masks profound foundational problems that continue to puzzle the gravity community. Despite the large number of exotic compact objects (ECOs) proposed to mimic BH behavior while addressing their conceptual problems, only the Fuzzball paradigm represents a genuine top-down approach rather than a purely phenomenological model. The specific realization of this program, the microstate geometries, however, while resolving the challenges of BH physics, lack the usual isometries of BH, making their dynamical analysis a challenging task.

In this thesis, we explored several simplified, yet physically motivated, models that capture some of the essential features of Fuzzball microstates while remaining analytically and numerically tractable. These models provide an effective framework to investigate the phenomenology of horizonless and regular geometries that can mimic or rather deviate from classical BHs in their observational signatures. We focused on several representative families of solutions arising in gravity theories coupled to additional fields or formulated in higher dimensions. In most cases, we highlighted how certain characteristic features of these spacetimes, such as the presence of an unstable photon sphere, can lead to significant deviations in the GW signals produced by these compact objects.

Scalarized BHs in EMS theory

We first analyzed charged BHs with scalar hair in Einstein–Maxwell–scalar theory, a model that admits spontaneous scalarization through the non-minimal coupling between the scalar and the electromagnetic sectors. The effective potential of such configurations feature multiple extrema, with a rich QNM spectrum and the emergence of long-lived modes trapped within the potential cavities. The appearance of these weakly damped QNMs, that is a direct consequence of the rich structure of circular null geodesics in the spacetimes of these scalarized BHs, is able to trigger echoes in the ringdown signal. The presence of the echo pattern was confirmed both in the linear approximation and in the fully nonlinear regime for radial perturbations.

This work sets the stage for exploring the post-merger GW emission from BHs collisions in Einstein–Maxwell–scalar theory. Future studies should clarify whether the linear and nonlinear echoes reported here persist during the dynamics of a coalescence.

Another possible direction of study is to include the polar (nonradial) sector in the perturbation analysis, in order to verify whether the long-lived QNMs and the echo pattern are also features of this sector.

TSs and magnetized BHs: QNMs and ringdown properties

We then turned to five-dimensional Einstein–Maxwell theory, which provides a natural framework for constructing smooth horizonless geometries. In this theory we first focused on the analysis of a recently discovered smooth horizonless solution, called topological star (TS) and its magnetized BH counterpart. A full perturbative analysis in the frequency and time domains demonstrated the linear stability of TSs and their magnetized BH counterparts, revealing a rich oscillation spectrum. For sufficiently compact configurations (second kind TSs) with an additional stable photon orbit, the effective potential develops a cavity , supporting long-lived modes that manifest as echoes in the late-time response. Less compact configurations, instead, display a standard exponentially damped ringdown.

Phenomenological features of EMRIs with TSs

The phenomenological relevance of TSs was further explored by studying extreme mass-ratio inspirals (EMRIs) in their background. We computed the scalar energy flux emitted by a point particle in circular orbit around a TS, identifying two key effects: sharp resonances when the orbital frequency matches the long-lived modes of the TS; and a cumulative dephasing of the emitted signal relative to the BH case due to the absence of the event horizon. Although the resonances are extremely narrow to produce a change in the phase of the scalar wave, the overall dephasing accumulated during a year-long inspiral, due to the lack of the horizon, could be measurable by future space-based detectors such as LISA.

The $\mathcal{W}$-soliton and the corresponding BH solutions

We finally studied a novel class of smooth, non-extremal solutions of minimal five-dimensional supergravity, dubbed $\mathcal{W}$-solitons, that share the same mass and charge as the four-dimensional charged BHs, where the horizon has been replaced by a smooth topological cap supported by electromagnetic fluxes. These objects represent prototypical examples of BH microstates in a top-down setting. We have derived the response of $\mathcal{W}$-solitons to classical probes by studying test scalar perturbations in this spacetime. Differently to usual ECOs, $\mathcal{W}$-solitons closely resemble classical BHs. The presence of a single unstable photon sphere, coinciding with the bubble locus, and the absence of a stable one, prevents the formation of long-lived modes, allowing only short-lived oscillations in their QNM spectrum. These results were confirmed

by a complementary analysis in the time domain, that showed how the $\mathcal{W}$-soliton ringdown is qualitatively similar to that of the corresponding BH, while displaying some quantitative differences in the oscillation frequency and in the damping rate. Our analysis also confirmed the linear stability of these objects under effectively massless test scalar field perturbations.

While our study was limited to test scalar fields, a natural extension would be to investigate gravitational and electromagnetic perturbations, which remains technically challenging but would complete the discussion on the linear stability of these geometries.

Moreover, even if modes with a non vanishing momentum along the fifth compact dimension (i.e. with $p \neq 0$) are not phenomenologically motivated when R_ψ is small, a preliminary study has found some evidence for the existence of bound states in the $\mathcal{W}$-soliton spacetime. A comprehensive analysis of their normal modes constitutes an important avenue for future work.

Recent developments in the inclusion of rotation for this kind of solutions appeared in the literature [332, 333]. Since most of the astrophysical BHs carry significant angular momentum, a perturbative analysis of these new spinning solutions is phenomenologically relevant and crucial to fully understand their stability and dynamics.

Appendix A

Tensorial Spherical Harmonics decomposition

Any spherically symmetric manifold $\mathbf{M}$, such as the Schwarzschild spacetime, can be written as the product of two submanifolds $\mathbf{M} = \mathbf{M_2} \times \mathbf{S}^2$, where $\mathbf{M_2}$ is a two-dimensional manifold with coordinates $x^A = (t, r)$ and $\mathbf{S}^2$ is the two-sphere, whose angular coordinates are $x^a = (\theta, \phi)$, with $A = 0, 1$ and $a = 2, 3$. As a consequence, any tensor living on this manifold can be similarly decomposed into a tensor of $\mathbf{M_2}$ and a tensor of $\mathbf{S}^2$, such that a general vector V^μ can be written as

$$V^\mu = (V^A, V^a)\,, \tag{A.1}$$

and a symmetric rank-two tensor $T^{\mu\nu}$ as

$$T_{\mu\nu} = \begin{pmatrix} T_{AB} & T_{Aa} \\ T_{aA} & T_{ab} \end{pmatrix}. \tag{A.2}$$

If we define the metric of the two-sphere $\mathbf{S}^2$ as

$$\gamma_{ab} = \begin{pmatrix} 1 & 0 \\ 0 & \sin^2\theta \end{pmatrix}, \tag{A.3}$$

we can write the Laplacian operator in polar coordinates acting on the scalar spherical harmonics

$$\nabla_b \nabla_a \gamma^{ab} Y_{lm}\,(\theta, \phi) = -l(l+1) Y_{lm}(\theta, \phi)\,, \tag{A.4}$$

where ∇_a indicates the covariant derivative with respect to the metric γ_{ab}. We can define the Levi-Civita tensor on the two-sphere $\mathbf{S}^2$ as

$$\varepsilon_{ab} \equiv \sqrt{\det \gamma_{ab}}\, \epsilon_{ab}\,, \tag{A.5}$$

with $\det \gamma_{ab} = \sin^2\theta$, and where ϵ_{ab} denotes the two-dimensional Levi-Civita symbol, such that $\epsilon_{ab} = -\epsilon_{ba}$ and $\epsilon_{12} = 1$. Let us introduce the so-called *vector* spherical harmonics

$$S_a^{lm}(\theta, \phi) \equiv -\varepsilon_a{}^b\, \nabla_b Y^{lm} = \left(-\frac{\partial_\phi Y^{lm}}{\sin\theta}\,, \sin\theta\, \partial_\theta Y^{lm} \right), \tag{A.6}$$

$$Y_a^{lm}(\theta, \phi) \equiv \nabla_a Y^{lm} = (\partial_\theta Y^{lm}, \partial_\phi Y^{lm})\,, \tag{A.7}$$

and *tensor* spherical harmonics

$$S^{lm}_{ab}(\theta,\phi) \equiv \frac{1}{2}(\nabla_b S^{lm}_a + \nabla_a S^{lm}_b) = \frac{1}{2}\begin{pmatrix} -\frac{X^{lm}}{\sin\theta} & \sin\theta\, W^{lm} \\ \sin\theta\, W^{lm} & \sin\theta X^{lm} \end{pmatrix}, \tag{A.8}$$

$$Z^{lm}_{ab}(\theta,\phi) \equiv \nabla_b\nabla_a Y^{lm} + \frac{l(l+1)}{2}\gamma_{ab}Y^{lm} = \frac{1}{2}\begin{pmatrix} W^{lm} & X^{lm} \\ X^{lm} & -\sin^2\theta\, W^{lm} \end{pmatrix}, \tag{A.9}$$

where we defined the following scalar functions

$$\begin{aligned} X^{lm}(\theta,\phi) &\equiv 2(\partial_\phi\partial_\theta Y^{lm} - \cot\theta\partial_\phi Y^{lm})\,, \\ W^{lm}(\theta,\phi) &\equiv \partial^2_\theta Y^{lm} - \cot\theta\,\partial_\theta Y^{lm} - \frac{\partial^2_\phi Y^{lm}}{\sin^2\theta}\,. \end{aligned} \tag{A.10}$$

The action of parity inversion ($\theta \to \pi - \theta$, $\phi \to \phi + \pi$) on scalar spherical harmonics is given by

$$Y^{lm}(\pi-\theta,\phi+\pi) = (-1)^l Y^{lm}(\theta,\phi)\,. \tag{A.11}$$

The *vector* spherical harmonics Y^{lm}_a and the *tensor* spherical harmonics Z^{lm}_{ab} transform as in Eq. (A.11), and for this reason they are called *polar* (or *even*) spherical harmonics. On the other hand, the *vector* harmonics S^{lm}_a transform as

$$S^{lm}_a(\pi-\theta,\phi+\pi) = (-1)^{l+1} S^{lm}_a(\theta,\phi)\,, \tag{A.12}$$

together with the *tensor* harmonics S^{lm}_{ab}, and they are called *axial* (or *odd*) spherical harmonics.

As anticipated we can expand the rank-two tensor of the metric perturbations $h_{\mu\nu}$ using scalar, vector and tensor spherical harmonics as written below

$$\begin{aligned} h_{AB}(t,r,\theta,\phi) &= \sum_{lm} \bar{h}_{AB\,lm}(r)\, Y^{lm}(\theta,\phi)\, e^{-i\omega t}\,, \\ h_{aA}(t,r,\theta,\phi) &= \sum_{lm} \left[\bar{h}^{\rm pol}_{A\,lm}(r)\, Y^{lm}_a(\theta,\phi) + \bar{h}^{\rm ax}_{A\,lm}(r)\, S^{lm}_a(\theta,\phi)\right] e^{-i\omega t}\,, \\ h_{ab}(t,r,\theta,\phi) &= \sum_{lm}\{r^2\left[K_{lm}(r)\,\gamma_{ab}\,Y^{lm}(\theta,\phi) + G_{lm}(r)\, Z^{lm}_{ab}(\theta,\phi)\right] \\ &\quad + 2\bar{h}_{lm}(r) S^{lm}_{ab}(\theta,\phi)\}\, e^{-i\omega t}\,. \end{aligned} \tag{A.13}$$

where we factorized the time dependence with $e^{-i\omega t}$ since we will focus on static background spacetimes. The functions $\bar{h}_{AB\,lm}(r)$, $\bar{h}^{\rm pol}_{A\,lm}(r)$, $K_{lm}(r)$ and $G_{lm}(r)$ are called *polar perturbations*, since they multiply the *polar* spherical harmonics. Conversely, $\bar{h}^{\rm ax}_{A\,lm}(r)$ and $\bar{h}_{lm}(r)$ are called *axial perturbations* because they multiply the *axial* harmonics.

Appendix B

Derivation of the Regge–Wheeler and Zerilli equations on the Schwarzschild background

In this Appendix we present the derivation of the Regge–Wheeler and Zerilli equations, which describe axial (odd-parity) and polar (even-parity) gravitational perturbations, respectively, on the Schwarzschild BH background.

We now consider the linearized Einstein equations in vacuum, which can be expressed in the following convenient form

$$2\delta R_{\mu\nu} = \nabla_\rho \nabla_\mu h^\rho{}_\nu + \nabla_\rho \nabla_\nu h^\rho{}_\mu - \nabla_\nu \nabla_\mu h^\rho{}_\rho - \nabla_\rho \nabla^\rho h_{\mu\nu} = 0\,. \tag{B.1}$$

As described in Appendix A, since the linearized perturbed Ricci tensor $\delta R_{\mu\nu}$ is a symmetric rank-two tensor field on the Schwarzschild background $\mathbf{M} = \mathbf{M_2} \times \mathbf{S}^2$, it can be decomposed as in Eq. (A.2)

$$\delta R_{\mu\nu} = \begin{pmatrix} \delta R_{AB} & \delta R_{Aa} \\ \delta R_{aA} & \delta R_{ab} \end{pmatrix}. \tag{B.2}$$

Each component can be expanded in scalar, vector and tensor spherical harmonics after using the Regge-Wheeler gauge of Eqs. (2.22)- (2.24)

$$2\delta R_{AB}(t,r,\theta,\phi) = \begin{pmatrix} A^{(0)}_{lm}(\omega,r) & A^{(1)}_{lm}(\omega,r) \\ A^{(1)}_{lm}(\omega,r) & A^{(2)}_{lm}(\omega,r) \end{pmatrix} Y^{lm}(\theta,\phi)\, e^{-i\omega t} = 0\,, \tag{B.3}$$

$$2\delta R_{Aa}(t,r,\theta,\phi) = \left(\alpha^{(A)}_{lm}(\omega,r) Y^{lm}_a(\theta,\phi) + \beta^{(A)}_{lm}(\omega,r) S^{lm}_a(\theta,\phi)\right) e^{-i\omega t} = 0\,, \tag{B.4}$$

$$\begin{aligned} 2\delta R_{ab}(t,r,\theta,\phi) = [&A^{(3)}_{lm}(\omega,r) r^2 \gamma_{ab} Y^{lm}(\theta,\phi) + s_{lm}(\omega,r) Z^{lm}_{ab}(\theta,\phi) \\ &+ t_{lm}(\omega,r) S^{lm}_{ab}(\theta,\phi)] e^{-i\omega t} = 0\,. \end{aligned} \tag{B.5}$$

The functions $\beta^{(A)}_{lm}$ (for $A = 0, 1$) and t_{lm} are combinations of the axial perturbations

$h_{0\,lm}(\omega, r)$, $h_{1\,lm}(\omega, r)$, and of their derivatives

$$\beta^{(0)}(\omega, r) = -\frac{2i\omega f\, h_1}{r} - i\omega f\, h_1' + \left(f'' + \frac{2rf' + 2f + l(l+1) - 2}{r^2}\right) h_0 - f\, h_0'' \,, \tag{B.6}$$

$$\beta^{(1)}(\omega, r) = -\frac{2i\omega h_0}{rf} + \frac{i\omega h_0'}{f} + \left(-\frac{\omega^2}{f} + \frac{2rf' + l(l+1) - 2}{r^2}\right) h_1 \,, \tag{B.7}$$

$$t(\omega, r) = \frac{i\omega h_0}{f} + h_1 f' + f h_1' \,, \tag{B.8}$$

where we omitted the indices lm for notation convenience, the prime denotes derivatives with respect to the radial coordinate r, and $f(r) = 1 - 2M/r$. On the other hand, the functions $A^{(I)}_{lm}$ and $\alpha^{(A)}_{lm}$ (for $I = 0, \ldots, 3$ and $A = 0, 1$) are given in terms of the polar perturbations $H_{0\,lm}(\omega, r)$, $H_{1\,lm}(\omega, r)$, $H_{2\,lm}(\omega, r)$ and $K_{lm}(\omega, r)$ and of their radial derivatives

$$\begin{aligned} A^{(0)}(\omega, r) = {} & \frac{(l(l+1) - 2) f\, K}{r^2} + \frac{2f(rf' + f - 1) H_0}{r^2} + \frac{(l(l+1) + 2f + 2rf') f H_2}{r^2} \\ & + \frac{2f^2 H_2'}{r} - \frac{f(6f + rf') K'}{r} - 2f^2 K'' \,, \end{aligned} \tag{B.9}$$

$$\begin{aligned} A^{(1)}(\omega, r) = {} & -\frac{2i\omega H_2}{r} + \frac{(l(l+1) - 2 + 2f + 2rf') H_1}{r^2} + i\omega \left(\frac{2}{r} - \frac{f'}{f}\right) K \\ & + 2i\omega K' \,, \end{aligned} \tag{B.10}$$

$$\begin{aligned} A^{(2)}(\omega, r) = {} & \frac{l(l+1) H_0}{r^2 f} - \frac{4i\omega H_1}{rf} - \frac{2H_2}{r^2 f} + \left[\frac{2\omega^2}{f^2} - \frac{l(l+1) - 2}{r^2 f}\right] K \\ & - \frac{2H_0'}{r} + \left(\frac{2}{r} + \frac{f'}{f}\right) K' \,, \end{aligned} \tag{B.11}$$

$$\begin{aligned} A^{(3)}(\omega, r) = {} & \frac{l(l+1) H_0}{2r^2} - i\omega \left(\frac{2}{r} + \frac{f'}{f}\right) H_1 - \left(\frac{f}{r} + \frac{3f'}{2}\right) H_0' - 2i\omega H_1' - \left(\frac{f}{r} + \frac{f'}{2}\right) H_2' \\ & + \left(\frac{2f}{r} + f'\right) K' + \left(\frac{\omega^2}{f} - \frac{l(l+1) + 4rf'}{2r^2} - f''\right) H_2 \\ & + \left(\frac{\omega^2}{f} + \frac{2f'}{r} + f''\right) K - f(H_0'' - K'') \,, \end{aligned} \tag{B.12}$$

$$\alpha^{(0)}(\omega, r) = i\omega(H_2 + K) + f' H_1 + f H_1' \,, \tag{B.13}$$

$$\alpha^{(1)}(\omega, r) = \frac{i\omega H_1}{f} + \left(\frac{f'}{2f} - \frac{1}{r}\right) H_0 + \left(\frac{f'}{2f} + \frac{1}{r}\right) H_2 + H_0' - K' \,, \tag{B.14}$$

$$s(\omega, r) = \frac{1}{2}(H_0 - H_2) \,. \tag{B.15}$$

By using the orthogonality properties of the spherical harmonics it is possible to separate the angular from the radial part, to get a system of ten coupled ODEs. In

addition, axial and polar perturbations turn out to decouple entirely, allowing each sector to be analyzed separately. For the axial sector we have the following three differential equations

$$\beta^{(J)}(\omega, r) = 0\,, \tag{B.16}$$
$$t(\omega, r) = 0\,, \tag{B.17}$$

for $J = 0, 1$. For the polar sector we have a system of seven differential equations

$$A^{(I)}(\omega, r) = 0\,, \tag{B.18}$$
$$\alpha^{(J)}(\omega, r) = 0\,, \tag{B.19}$$
$$s(\omega, r) = 0\,, \tag{B.20}$$

for $I = 0, \ldots, 3$ and $J = 0, 1$.

Axial sector: Regge-Wheeler equation

In order to find a single master equation for the axial sector, let us define the so-called Regge-Wheeler function $Q_{lm}(\omega, r)$ as follows

$$Q_{lm}(\omega, r) \equiv \frac{f}{r} h_{1\,lm}(\omega, r)\,. \tag{B.21}$$

By using this definition in the equation $t(\omega, r) = 0$ we get

$$h_{0\,lm} = \frac{if}{\omega}(Q_{lm} r)'\,. \tag{B.22}$$

Finally by using Eq. (B.22) and the expression of $h_{1\,lm}$ in terms of the new Regge-Wheeler function, we find the single Schrödinger-like master equation of Regge-Wheeler for the axial perturbations

$$\frac{d^2 Q_l}{dr_*^2} + [\omega^2 - V_l^{\text{axial}}(r)] Q_l = 0\,, \tag{B.23}$$

whose gravitational potential is

$$V_l^{\text{axial}}(r) = \left(1 - \frac{2M}{r}\right)\left[\frac{l(l+1)}{r^2} - \frac{6M}{r^3}\right]\,. \tag{B.24}$$

Polar sector: Zerilli equation

The analysis of the polar sector is slightly more intricate than that of the axial sector. From equation $s_{lm}(\omega, r) = 0$ we can express H_2 in terms of H_0, i.e.

$$H_{2\,lm} = H_{0\,lm}\,. \tag{B.25}$$

By using Eq. (B.25) to eliminate the H_2 dependence from the Eqs. (B.18)- (B.19), we can recast the latter into three first order ODEs

$$H_1' + \frac{f'}{f}H_1 + \frac{i\omega}{f}(K + H_0) = 0\,, \tag{B.26}$$

$$\begin{aligned} H_0' + \left(\frac{f'}{f} - \frac{1}{r}\right)H_0 - \left(\frac{f'}{2f} - \frac{1}{r}\right)K \\ + \left[\frac{i\omega}{f} - \frac{i(l(l+1) - 2 + 2f + 2rf')}{2r^2\omega}\right]H_1 = 0\,, \end{aligned} \tag{B.27}$$

$$K' + \left(\frac{1}{r} - \frac{f'}{2f}\right)K - \frac{H_0}{r} - \frac{i(l(l+1) - 2 + 2f + 2rf')}{2r^2\omega}H_1 = 0\,, \tag{B.28}$$

plus an algebraic equation

$$\begin{aligned} &(l(l+1) - 2 - 3rf')H_0 + \left[2ir\omega - \frac{if'}{2\omega}(l(l+1) - 2 + 2f + 2rf')\right]H_1 \\ &+ \left[l(l+1) - 2 + rf' - \frac{r^2(4\omega^2 + f'^2)}{2f}\right]K = 0\,. \end{aligned} \tag{B.29}$$

One can isolate H_0 from Eq. (B.29) and replace it in the other ODEs to get a system of two coupled linear ODEs for H_1 and K

$$\begin{aligned} &K' + \frac{4r\omega^2 - f'(l(l+1) - 2 - 4f + 2rf')}{2f(l(l+1) - 2 + 3rf')}K \\ &- i\frac{[(l(l+1) - 2)^2 + 4r^2\omega^2 + 4rf'(l(l+1) - 2 + rf') + 2f(l(l+1) - 2) + 2rf']}{2r^2\omega(l(l+1) - 2 + 3rf')}H_1 = 0\,, \end{aligned} \tag{B.30}$$

$$\begin{aligned} H_1' + \frac{f'(-6 + 3l(l+1) + 2f + 8rf') - 4r\omega^2}{2f(l(l+1) - 2 + 3rf')}H_1 \\ - i\omega\frac{r^2(4\omega^2 + f'^2) - 4f(l(l+1) - 2 + 2rf')}{2f^2(l(l+1) - 2 + 3rf')}K = 0 \end{aligned} \tag{B.31}$$

Defining the Zerilli function $Z_{lm}(\omega, r)$ as follows

$$K = W_{11}Z + W_{12}\frac{dZ}{dr_*}\,, \tag{B.32}$$

$$H_1 = W_{21}Z + W_{22}\frac{dZ}{dr_*}\,, \tag{B.33}$$

with

$$\begin{aligned} W_{11} &= \frac{\lambda(\lambda+1)r^2 + 3\lambda Mr + 6M^2}{r^2(\lambda r + 3M)}\,, \\ W_{12} &= 1\,, \\ W_{21} &= \frac{i\omega(3M^2 + 3\lambda Mr - \lambda r^2)}{(r - 2M)(\lambda r + 3M)}\,, \\ W_{22} &= -\frac{i\omega r^2}{r - 2M}\,, \end{aligned} \tag{B.34}$$

where $\lambda \equiv (l-1)(l-2)/2$, we can derive the Zerilli equation

$$\frac{d^2 Z_l}{dr_*^2} + [\omega^2 - V_l^{\rm polar}(r)] Z_l = 0\,, \tag{B.35}$$

where the effective potential is

$$V_l^{\rm polar}(r) = \left(1 - \frac{2M}{r}\right)\left[\frac{(l-1)(l+2)}{3}\left(\frac{1}{r^2} + \frac{2(l-1)(l+2)(l^2+l+1)}{(6M + r(l-1)(l+2))^2}\right)\right]. \tag{B.36}$$

Appendix C

Derivation of the perturbation equations in EMS theory

In this Appendix we outline the main steps to derive the perturbed field equations (5.64)-(5.65) and (5.73)-(5.78). The linearized Einstein, Maxwell and scalar equations can be divided into three distinct groups ("scalar", "vector" and "tensor") as described in [334] (see also [283]). By denoting the linearized Einstein, Maxwell and scalar equations respectively as $\delta\mathcal{E}_{\mu\nu}=0$, $\delta J_\mu=0$ and $\delta S=0$, the "scalar" group is given by the equations

$$\delta\mathcal{E}_{(I)}=\sum_{l,m}A^{(I)}_{lm}(r)\,Y^m_l\,, \qquad (I=0,\dots,3) \tag{C.1}$$

$$\delta J_{(I)}=\sum_{l,m}A^{(I)}_{lm}(r)\,Y^m_l\,, \qquad (I=4,5) \tag{C.2}$$

$$\delta S=\sum_{l,m}A^{(6)}_{lm}(r)\,Y^m_l\,, \tag{C.3}$$

where $I=0,1,2$ stand for the (tt), (tr) and (rr) components of the Einstein equations, $I=4$ represents the following combination

$$\delta\mathcal{E}_{\theta\theta}+\frac{\delta\mathcal{E}_{\varphi\varphi}}{\sin^2\theta}=0\,, \tag{C.4}$$

and $I=4,5$ indicate the (t) and (r) components of the Maxwell equations. The "vector" group is represented by the following Einstein equations

$$\delta\mathcal{E}_{(L\theta)}=\alpha^{(L)}_l(r)\,\partial_\theta Y^m_l-\beta^{(L)}_l(r)\,\frac{\partial_\varphi Y^m_l}{\sin\theta}=0\,, \tag{C.5}$$

$$\frac{\delta\mathcal{E}_{(L\varphi)}}{\sin\theta}=\beta^{(L)}_l(r)\,\partial_\theta Y^m_l+\alpha^{(L)}_l(r)\,\frac{\partial_\varphi}{\sin\theta}=0\,, \tag{C.6}$$

where $L=0,1$ stand for (t) and (r), and by the remaining Maxwell equations

$$\delta J_\theta=\alpha^{(2)}_l(r)\,\partial_\theta Y^m_l-\beta^{(2)}_l(r)\,\frac{\partial_\varphi Y^m_l}{\sin\theta}=0\,, \tag{C.7}$$

$$\frac{\delta J_\varphi}{\sin\theta}=\beta^{(2)}_l(r)\,\partial_\theta Y^m_l+\alpha^{(2)}_l(r)\,\frac{\partial_\varphi Y^m_l}{\sin\theta}=0\,. \tag{C.8}$$

The "tensor" group consists of the remaining Einstein equations

$$\frac{\delta\mathcal{E}_{\theta\varphi}}{\sin\theta} = s_l(r)\frac{X^l}{\sin\theta} + t_l(r)W^l = 0 \,, \tag{C.9}$$

$$\delta\mathcal{E}_{\theta\theta} + \frac{\delta\mathcal{E}_{\varphi\varphi}}{\sin^2\theta} = -t_l(r)\frac{X^l}{\sin\theta} + s_l(r)W^l = 0 \,, \tag{C.10}$$

where X^l and W^l are so defined

$$X^l = 2\partial_\varphi(\partial_\theta Y_l^m - \cot\theta Y_l^m) \,, \tag{C.11}$$

$$W^l = \partial_\theta^2 Y_l^m - \cot\theta\partial_\theta Y_l^m - \frac{\partial_\varphi^2 Y_l^m}{\sin^2\theta}. \tag{C.12}$$

The coefficients $A_l^{(I)}$, $\alpha_l^{(L)}$, $\beta_l^{(L)}$, s_l and t_l are linear functions of the perturbations and purely radial. By using the orthogonality of the spherical harmonics it is possible to separate the radial from the angular part, to get the following equations that naturally divide into the axial sector

$$\begin{cases} \beta_l^{(L)} = 0 \quad L = 0,1,2 \\ t_l = 0 \end{cases} \tag{C.13}$$

with perturbation fields $u_4(r)$, $h_0(r)$ and $h_1(r)$, and polar sector

$$\begin{cases} A_l^{(L)} = 0 \quad I = 0,\dots,6 \\ \alpha_l^{(L)} = 0 \quad L = 0,1,2 \\ s_l = 0 \,, \end{cases} \tag{C.14}$$

with perturbation fields $H_0(r)$, $H_1(r)$, $H_2(r)$, $K(r)$, $f_{01}(r)$, $f_{02}(r)$, $f_{12}(r)$ and $z(r)$.

In order to obtain the final form of the axial equations (5.64)-(5.65), we first consider the definitions

$$h_1(r) = \frac{Q_1(r)}{N(r)} \,, \qquad u_4(r) = \frac{iU_4(r)}{\omega} \,. \tag{C.15}$$

From the equation $t_l = 0$ we obtain the following relation

$$h_0(r) = \frac{iN(r)}{\omega e^{2\delta(r)}}[Q_1'(r) - Q_1(r)\delta'(r)] \tag{C.16}$$

that removes $h_0(r)$ from the system. It is easy to prove that equation $\beta_l^{(0)} = 0$ is redundant because it can be derived from $\beta_l^{(1)} = 0$ and $\beta_l^{(2)} = 0$. We are left with a system of two differential equations $\beta_l^{(1)} = 0$ and $\beta_l^{(2)} = 0$, where for convenience we replace the latter with the following linear combination

$$\beta_l^{(2)} + \frac{2N(r)V'(r)\,e^{\alpha\phi^2(r)}}{\omega}\beta_l^{(1)} = 0 \,. \tag{C.17}$$

Finally, using a further redefinition given by

$$U_4(r) = r\,e^{-\frac{1}{2}\alpha\phi^2(r)}\,U(r) \,, \qquad Q_1(r) = r\,e^{\delta(r)}H(r) \,, \tag{C.18}$$

we obtain the desired form of the axial perturbed equations.

The polar equations (C.14), after eliminating $f_{01}(r)$ with Eq. (5.62) and deriving $H_2(r) = H_0(r)$ from $s_l = 0$, directly give the Eqs. (5.73)-(5.78).

Appendix D

Derivation of perturbed equations for magnetized BHs and TSs

In this Appendix we outline the main steps for the derivations of the linear perturbed equations (6.33)- (6.34), (6.48), (6.50), (6.56) and (6.57) of magnetized BHs and TSs presented in Sec. 6.2.

D.1 Type-I and Type-II radial perturbed equations

As stated before, the derivation of the Type-I and radial Type-II sector has been carried out after the compactification in the four-dimensional framework, whose field equations are Eqs. (6.10)- (6.14).

D.1.1 Regge-Wheeler-Zerilli gauge for perturbations in four dimensions

Let us consider a Regge-Wheeler-Zerilli [154, 155] spherical-harmonic decomposition of the metric, EM, and scalar perturbations of the background. The axial (odd-parity) and polar (even-parity) metric perturbations are given by

$$h^{\rm even}_{\mu\nu} = \sum_{l,m} \begin{pmatrix} f_S f_B^{1/2} H_0(t,r) & H_1(t,r) & 0 & 0 \\ H_1(t,r) & f_S^{-1} f_B^{-1/2} H_2(t,r) & 0 & 0 \\ 0 & 0 & r^2 f_B^{1/2} K(t,r) & 0 \\ 0 & 0 & 0 & r^2 f_B^{1/2} \sin\theta^2 K(t,r) \end{pmatrix} Y_{lm}(\theta,\phi)\,, \tag{D.1}$$

$$h^{\rm odd}_{\mu\nu} = \sum_{l,m} \begin{pmatrix} 0 & 0 & -h_0(t,r)/\sin\theta\partial_\phi & h_0(t,r)\sin\theta\partial_\theta \\ 0 & 0 & -h_1(t,r)/\sin\theta\partial_\phi & h_1(t,r)\sin\theta\partial_\theta \\ -h_0(t,r)/\sin\theta\partial_\phi & -h_1(t,r)/\sin\theta\partial_\phi & 0 & 0 \\ h_0(t,r)\sin\theta\partial_\theta & h_1(t,r)\sin\theta\partial_\theta & 0 & 0 \end{pmatrix} Y_{lm}(\theta,\phi)\,. \tag{D.2}$$

The polar (even-parity) EM perturbations (for either $F_{\mu\nu}$ or $\mathcal{F}_{\mu\nu}$) read

$$f^{\rm even}_{\mu\nu} = \sum_{l,m} \begin{pmatrix} 0 & f^+_{01}(t,r) & f^+_{02}(t,r)\partial_\theta & f^+_{02}(t,r)\partial_\phi \\ -f^+_{01}(t,r) & 0 & f^+_{12}(t,r)\partial_\theta & f^+_{12}(t,r)\partial_\phi \\ -f^+_{02}(t,r)\partial_\theta & -f^+_{12}(t,r)\partial_\theta & 0 & 0 \\ -f^+_{02}(t,r)\partial_\phi & -f^+_{12}(t,r)\partial_\phi & 0 & 0 \end{pmatrix} Y_{lm}(\theta,\phi)\,, \tag{D.3}$$

$$g^{\rm even}_{\mu\nu} = \sum_{l,m} \begin{pmatrix} 0 & g^+_{01}(t,r) & g^+_{02}(t,r)\partial_\theta & g^+_{02}(t,r)\partial_\phi \\ -g^+_{01}(t,r) & 0 & g^+_{12}(t,r)\partial_\theta & g^+_{12}(t,r)\partial_\phi \\ -g^+_{02}(t,r)\partial_\theta & -g^+_{12}(t,r)\partial_\theta & 0 & 0 \\ -g^+_{02}(t,r)\partial_\phi & -g^+_{12}(t,r)\partial_\phi & 0 & 0 \end{pmatrix} Y_{lm}(\theta,\phi)\,, \tag{D.4}$$

while the axial (odd-parity) EM perturbations are

$$f^{\rm odd}_{\mu\nu} = \sum_{l,m} \begin{pmatrix} 0 & 0 & f^-_{02}(t,r)/\sin\theta\partial_\phi & -f^-_{02}(t,r)\sin\theta\partial_\theta \\ 0 & 0 & f^-_{12}(t,r)/\sin\theta\partial_\phi & -f^-_{12}(t,r)\sin\theta\partial_\theta \\ -f^-_{02}(t,r)/\sin\theta\partial_\phi & -f^-_{12}(t,r)/\sin\theta\partial_\phi & 0 & f^-_{23}(t,r)\sin\theta \\ f^-_{02}(t,r)\sin\theta\partial_\theta & f^-_{12}(t,r)\sin\theta\partial_\theta & -f^-_{23}(t,r)\sin\theta & 0 \end{pmatrix} \times Y_{lm}(\theta,\phi)\,, \tag{D.5}$$

$$g^{\rm odd}_{\mu\nu} = \sum_{l,m} \begin{pmatrix} 0 & 0 & g^-_{02}(t,r)/\sin\theta\partial_\phi & -g^-_{02}(t,r)\sin\theta\partial_\theta \\ 0 & 0 & g^-_{12}(t,r)/\sin\theta\partial_\phi & -g^-_{12}(t,r)\sin\theta\partial_\theta \\ -g^-_{02}(t,r)/\sin\theta\partial_\phi & -g^-_{12}(t,r)/\sin\theta\partial_\phi & 0 & g^-_{23}(t,r)\sin\theta \\ g^-_{02}(t,r)\sin\theta\partial_\theta & g^-_{12}(t,r)\sin\theta\partial_\theta & -g^-_{23}(t,r)\sin\theta & 0 \end{pmatrix} \times Y_{lm}(\theta,\phi)\,. \tag{D.6}$$

The scalar perturbations are decomposed as

$$\delta\Phi = \sum_{l,m} \frac{\varphi(t,r)}{r} Y_{lm}(\theta,\phi)\,, \tag{D.7}$$

$$\delta\Xi = \sum_{l,m} \frac{\xi(t,r)}{r} Y_{lm}(\theta,\phi)\,. \tag{D.8}$$

D.1.2 Derivation

The system of Eqs. (6.33)- (6.34) is obtained by combining the $r\phi-$ and $\theta\phi-$components of the perturbed Einstein equation (6.10) and the radial component of the perturbed Maxwell equation (6.13) to get a second-order equation for h_1 sourced by f^+_{01}. The Maxwell constraint $f^+_{01} - i\,\omega f^+_{12} - \partial_r f^+_{02} = 0$, together with the $t-$ and $r-$components of the Maxwell equations provide a second-order equation for f^+_{01}. Finally the field perturbations $\mathcal{R}^-$ and $\mathcal{E}$ are so defined

$$h_1(r) = -i\,\omega r\sqrt{f_B}\mathcal{R}^-(r)\,, \tag{D.9}$$

$$f^+_{01}(r) = \frac{\Lambda}{r^2}\mathcal{E}(r)\,. \tag{D.10}$$

For Type-I $l = 1$ it is possible to show that the metric perturbation h_0 can be eliminated via a gauge transformation, and the perturbation h_1 is non-dynamical. Indeed, one can show that h_1 can be fixed in terms of f_{01}^{+} as follows

$$h_1 = \frac{Q_m \kappa_4^2 f_B^{1/2}}{i\,\omega e} f_{01}^{+}\,. \tag{D.11}$$

Finally Eq. (6.48) is recovered.

In the case of the radial ($l = 0$) Type-II sector, by means of a coordinate choice, the metric perturbations K and H_1 can be eliminated and one is left with H_0 and H_2. By using the Einstein's equations one can find a relation between the latter. Moreover, the radial mode of EM perturbations is polar, therefore it does not belong to the Type-II sector.

D.2 Type-II nonradial perturbed equations

Contrary to Type-I and radial ($l = 0$) Type-II, the nonradial Type-II sector equations are derived in the five-dimensional framework for practical reasons.

D.2.1 Regge-Wheeler-Zerilli gauge for perturbations in five dimensions

Let us consider an extended Regge-Wheeler ansatz for perturbations in five dimensions (see [304] for a discussion on how to fix the gauge starting from the most general ansatz). The perturbations h_{AB} of the metric in the five-dimensional spacetime are decomposed into polar (eve-parity) and axial (odd-parity) as follows

$$h_{AB}^{\text{even}} = \sum_{l,m} \begin{pmatrix} f_S H_0(t,y,r) & H_4(t,y,r) & H_1(t,y,r) & 0 & 0 \\ * & f_B H_3(t,y,r) & H_5(t,y,r) & 0 & 0 \\ * & * & (f_S f_B)^{-1} H_2(t,y,r) & 0 & 0 \\ 0 & 0 & 0 & r^2 K(t,y,r) & 0 \\ 0 & 0 & 0 & 0 & r^2 \sin\theta^2 K(t,y,r) \end{pmatrix} \times \\ \times\, Y_{lm}(\theta,\phi)\,, \tag{D.12}$$

$$h_{AB}^{\text{odd}} = \sum_{l,m} \begin{pmatrix} 0 & 0 & 0 & -h_0(t,y,r)/\sin\theta\partial_\phi & h_0(t,y,r)\sin\theta\partial_\theta \\ 0 & 0 & 0 & -h_2(t,y,r)/\sin\theta\partial_\phi & h_2(t,y,r)\sin\theta\partial_\theta \\ 0 & 0 & 0 & -h_1(t,y,r)/\sin\theta\partial_\phi & h_1(t,y,r)\sin\theta\partial_\theta \\ * & * & * & 0 & 0 \\ * & * & * & 0 & 0 \end{pmatrix} Y_{lm}(\theta,\phi)\,. \tag{D.13}$$

Similarly, the perturbations of the EM field in five dimensions are decomposed in axial and polar as follows

$$f^{\rm even}_{AB} = \sum_{l,m} \begin{pmatrix} 0 & f^{+}_{ty}(t,y,r) & f^{+}_{tr}(t,y,r) & f^{+}_{t\theta}(t,y,r)\partial_\theta & f^{+}_{t\theta}(t,y,r)\partial_\phi \\ \cdot & 0 & f^{+}_{yr}(t,y,r) & f^{+}_{y\theta}(t,y,r)\partial_\theta & f^{+}_{y\theta}(t,y,r)\partial_\phi \\ \cdot & \cdot & 0 & f^{+}_{r\theta}(t,y,r)\partial_\theta & f^{+}_{r\theta}(t,y,r)\partial_\phi \\ \cdot & \cdot & \cdot & 0 & 0 \\ \cdot & \cdot & \cdot & 0 & 0 \end{pmatrix} Y_{lm}(\theta,\phi)\,, \tag{D.14}$$

$$f^{\rm odd}_{AB} = \sum_{l,m} \begin{pmatrix} 0 & 0 & 0 & f^{-}_{t\theta}(t,y,r)/\sin\theta\partial_\phi & -f^{-}_{t\theta}(t,y,r)\sin\theta\partial_\theta \\ 0 & 0 & 0 & f^{-}_{y\theta}(t,y,r)/\sin\theta\partial_\phi & -f^{-}_{y\theta}(t,y,r)\sin\theta\partial_\theta \\ 0 & 0 & 0 & f^{-}_{r\theta}(t,y,r)/\sin\theta\partial_\phi & -f^{-}_{r\theta}(t,y,r)\sin\theta\partial_\theta \\ \cdot & \cdot & \cdot & 0 & l(l+1)f^{-}_{\theta\phi}(t,y,r)\sin\theta \\ \cdot & \cdot & \cdot & \cdot & 0 \end{pmatrix} Y_{lm}(\theta,\phi)\,. \tag{D.15}$$

The uppercase Latin indices span the coordinates $A\,,B\,=\,\{t\,,y\,,r\,,\theta\,,\phi\}$. The asterisks, $*$, (respectively, dots, $\cdot$) indicate symmetry (respectively, antisymmetry) with respect to the corresponding upper-half matrix elements.

Thanks to the isometries of the background spacetimes, we can factorize the t and y dependence as follows

$$A(t,y,r) = e^{-i\,\omega t}e^{i\,ky}a(r)\,, \tag{D.16}$$

where A is the generic perturbation field. Similarly to the other sector, we restrict to consider the scenario in which the fifth dimension is compactified, our compact objects are macroscopic and effectively four-dimensional and, thus, excitations in the fifth dimension are negligible, $k = 0$.

D.2.2 Derivation

Type-II, $l \geq 2$

In order to derive the system of equations (6.57), we can first eliminate H_2 by using the $\phi\theta-$component of the Einstein's equations. By combining the $rt-$, $\phi r-$ and $rr-$components we can relate H_0 to H_1, K, $f^{-}_{\theta\phi}$, H_3 and first derivatives. This relation can be inverted to eliminate H_0. From the θ-component of the linearized Maxwell equation we get a second-order equation for $f^{-}_{\theta\phi}$. Moreover, by a linear combination of $yy-$, $\theta\theta-$components of the linearized Einstein equations, we can construct a second-order equation for H_3. In addition, the linearized Einstein equations are reduced to a system of two first-order equations for H_1 and K. It is possible to generalize Zerilli's procedure to reduce the system of two fist-order equations to a single second-order equation for an auxiliary variable that encodes the gravitational degree of freedom.

We introduce two auxiliary variables $\hat{\Psi} = \left(\hat{K}\,,\hat{H}\right)$ linked to $\Psi = (K\,,H_1)$ via $\Psi = \mathbf{F}\hat{\Psi}$, and such that the original system of first-order equations

$$\frac{d\Psi}{dr} = \mathbf{A}\cdot\Psi + \mathcal{S} \tag{D.17}$$

reduces to

$$\frac{d\hat{\Psi}}{dr_*} = \mathbf{B}\cdot\hat{\Psi} + \hat{\mathcal{S}}\,, \tag{D.18}$$

where we introduced the generic coordinate $dr_* = n(r)^{-1}dr$. The elements of $\mathbf{F}$ are unknown, while the matrix elements of $\mathbf{A}$ are known and we fix the form of $\mathbf{B}$ to be

$$\mathbf{B} = \begin{pmatrix} q(r) & 1 \\ V_0(r) - \omega^2 & p(r) \end{pmatrix} \tag{D.19}$$

with $p(r)$, $q(r)$ and $V_0(r)$ free to be fixed. The equations above imply the following system

$$n(r)\mathbf{F}^{-1}\left(\mathbf{A}\mathbf{F} - \frac{d\mathbf{F}}{dr}\right) - \mathbf{B} = 0 \tag{D.20}$$

which can be solved to fix $\mathbf{F}$ and $\mathbf{B}$. We first fix $n(r) := (\sqrt{f_B}f_S)^{-1}$, in such a way that the coordinate r_* is the appropriate tortoise one for our background. As a consequence we get

$$\begin{aligned} K =& -\frac{(1+3f_B)}{8rf_B\zeta_B}\partial_r\hat{K} - \frac{3+4\lambda+3f_B(f_S-1)-3f_S}{8r^2f_Bf_S\zeta_B}\hat{K} - \frac{P\kappa_5^2(1+3f_B)^2f_S}{4r^2f_B\zeta_B}f^-_{\theta\phi} \\ &+ \frac{r(1+3f_B)f_S}{4\zeta_B}\partial_r H_3 + \frac{(1+3f_B)(2f_S+f_B(3f_S-1))}{8f_B\zeta_B}H_3\,, \end{aligned} \tag{D.21}$$

$$H_1 = -\frac{4r}{f_S(1+3f_B)}K - \frac{1}{rf_Bf_S^2(1+3f_B)}\hat{K}\,, \tag{D.22}$$

where $2\lambda = (l-1)(l+2)$ and $8f_B\zeta_B = f_B^2(6-15f_S) + 2f_B(9+8\lambda-6f_S) + 3f_S$. Finally, we introduce $\mathcal{R}^+ := \hat{K} - 2r^2f_Bf_SH_3$, $\Phi := H_3/f_B$ and $\mathcal{B} := f^-_{\theta\phi}/\kappa_5$, to obtain the final system (6.57), with coefficients defined as

$$\tilde{U}_{ij} = -\delta_{i1}\delta_{j3}\frac{(1-f_B)^2f_S^3}{4\zeta_B}\,, \tag{D.23}$$

$$\begin{aligned} \tilde{W}_{11} =& -\frac{f_S}{8r\zeta_B}\Big((15+16\lambda-9f_S)f_S - 2f_B(9+8\lambda+(9+16\lambda)f_S) \\ &+3f_B^2(-2+f_S+11f_S^2)\Big)\,, \end{aligned} \tag{D.24}$$

$$\tilde{W}_{12} = -\frac{P\kappa_5(1-f_B)f_S^2}{4r^3\zeta_B}\Big(-2f_B(9+8\lambda-8f_S) - f_S + f_B^2(-6+9f_S)\Big)\,, \tag{D.25}$$

$$\begin{aligned} \tilde{W}_{13} =& -\frac{(1-f_B)f_Bf_S^2}{64rf_B^2\zeta_B^2}\Big(f_S(-33-32\lambda+39f_S) + f_B(6(9+8\lambda) \\ &+(111+112\lambda)f_S - 87f_S^2) + f_B^2(108+80\lambda-(267+208\lambda)f_S - 15f_S^2) \\ &+15f_B^3(2-13f_S+17f_S^2)\Big)\,, \end{aligned} \tag{D.26}$$

$$\tilde{V}_{11} = \frac{f_S}{64r^2 f_B^2 \zeta_B^2} \Big(9(7+6\lambda-3f_S)f_S^2 \\ +f_B f_S(189+312\lambda+128\lambda^2-15(21+16\lambda)f_S+72f_S^2) \\ -3f_B^4(66+72\lambda-6(31+28\lambda)f_S+7(27+2\lambda)f_S^2-201f_S^3)+ \\ 2f_B^2((7+4\lambda)(9+8\lambda)^2-(927+1404\lambda+512\lambda^2)f_S+6(96+71\lambda)f_S^2-72f_S^3)+ \\ 9f_B^5(-6+31f_S-41f_S^2+10f_S^3)-2f_B^3(-15(9+8\lambda)+(738+924\lambda+320\lambda^2)f_S \\ -66(9+4\lambda)f_S^2+297f_S^3) \Big) , \tag{D.27}$$

$$\tilde{V}_{12} = \frac{P\kappa_5 f_B f_S}{96r^4 f_B^2 \zeta_B^2} \Big(3(45+44\lambda-51f_S)f_S^2+27f_B^5 f_S(10-41f_S+25f_S^2)+ \\ 3f_B f_S(-6(9+8\lambda)-5(33+32\lambda)f_S+189f_S^2)+6f_B^3(-16(9+17\lambda+8\lambda^2) \\ +(438+856\lambda+384\lambda^2)f_S-(189+400\lambda)f_S^2-63f_S^3)-9f_B^4(16(1+\lambda) \\ -8(23+22\lambda)f_S+3(71+52\lambda)f_S^2-51f_S^3)-2f_B^2(8(1+\lambda)(9+8\lambda)^2 \\ -12(9+46\lambda+32\lambda^2)f_S-3(369+308\lambda)f_S^2+585f_S^3) \Big) , \tag{D.28}$$

$$\tilde{V}_{13} = -\frac{(1-f_B)f_S}{32r^2 f_B^2 \zeta_B^2} \Big(9(1+\lambda)f_S^2-f_B f_S(2(9+17\lambda+8\lambda^2)+(12+13\lambda)f_S+9f_S^2) \\ +3f_B^4 f_S(10-53f_S+55f_S^2)+f_B^2(8(9+17\lambda+8\lambda^2)-6(15+22\lambda+8\lambda^2)f_S \\ +(78+63\lambda)f_S^2+27f_S^3)-f_B^3(-24(1+\lambda)+2(9+13\lambda)f_S+3(4+9\lambda)f_S^2+87f_S^3) \Big) , \tag{D.29}$$

$$\tilde{W}_{21} = 0 \tag{D.30}$$

$$\tilde{W}_{22} = \frac{f_S}{r} \Big(f_B+f_S-2f_B f_S \Big) \tag{D.31}$$

$$\tilde{W}_{23} = -\frac{P\kappa_5(1+3f_B)f_S^2}{8r f_B \zeta_B} \tag{D.32}$$

$$\tilde{V}_{21} = -\frac{P\kappa_5 f_S}{8r^2 f_B \zeta_B} \Big(9+8\lambda+3f_B(1-f_S)-9f_S \Big) \tag{D.33}$$

$$\tilde{V}_{22} = \frac{f_S}{8r^2} \left(16(1+\lambda)+\frac{3(1-f_B)(1-f_S)(1+3f_B)^2 f_S}{f_B \zeta_B} \right) \tag{D.34}$$

$$\tilde{V}_{23} = -\frac{P\kappa_5 f_S}{4r^2 f_B \zeta_B} \Big(2(1+\lambda)-(1-3f_B)f_S \Big) \tag{D.35}$$

$$\tilde{W}_{31} = 0\,, \tag{D.36}$$

$$\tilde{W}_{32} = 0\,, \tag{D.37}$$

$$\begin{aligned}\tilde{W}_{33} = -\frac{f_B f_S}{8r f_B \zeta_B}\Big(&(21+16\lambda-27f_S)f_S - 2f_B(9+8\lambda-3f_S)(1+2f_S) \\ &+f_B^2(-6-39f_S+87f_S^2)\Big)\,,\end{aligned} \tag{D.38}$$

$$\begin{aligned}\tilde{V}_{31} = -\frac{3(1-f_B)f_S}{8r^2 f_B \zeta_B}\Big(&f_S(-9-8\lambda+3f_S) + f_B^2(6-9f_S+9f_S^2) \\ &+2f_B(9+8\lambda-(27+20\lambda)f_S+18f_S^2)\Big)\,,\end{aligned} \tag{D.39}$$

$$\begin{aligned}\tilde{V}_{32} = \frac{P\kappa_5 f_B f_S}{4r^4 f_B \zeta_B}\Big(&f_S(-5(9+8\lambda)+33f_S) + 9f_B^3(2+f_S+f_S^2) \\ &-f_B(2(63+128\lambda+64\lambda^2)-(99+112\lambda)f_S+9f_S^2) \\ &+3f_B^2(4-3(7+8\lambda)f_S+21f_S^2)\Big)\,,\end{aligned} \tag{D.40}$$

$$\begin{aligned}\tilde{V}_{33} = \frac{f_S}{4r^2 f_B \zeta_B}\Big(&-3(1+\lambda)f_S + f_B^2(-36-38\lambda+(57+39\lambda)f_S-42f_S^2) \\ &+f_B(30+46\lambda+16\lambda^2-(33+28\lambda)f_S+12f_S^2)+3f_B^3(-2-7f_S+14f_S^2)\Big)\end{aligned} \tag{D.41}$$

Type-II, $l = 1$

For $l = 1$, the Type-II perturbation fields are $\{H_0, H_1, H_2, H_3, H_4, H_5,$ $f^-_{t\theta}, f^-_{r\theta}, f^-_{\theta\phi}\}$, while K is not defined for $l < 2$. Moreover, one can notice that $H_4\,, H_5\,, f^-_{y\theta}$ decouple from the rest and can be neglected. Since f_{AB} are perturbations of a Maxwell tensor derived from a vector potential, one can verify that $\{f^-_{t\theta}\,, f^-_{r\theta}\,, f^-_{\theta\phi}\}$ are related via $f^-_{t\theta} = -i\,\omega f^-_{\theta\phi}$ and $f^-_{r\theta} = \partial_r f^-_{\theta\phi}$. By using the $rr-$ and the $tr-$components of the linearized Einstein's equations, one can show that H_0 and H_2 can be recast as functions of the remaining perturbation fields.

What remains is the group of variables $\{H_1\,, H_3\,, f^-_{\theta\phi}\}$: H_1 satisfies a first order equation in r given by the $t\phi-$component of the Einstein equations; H_3 satisfies a second order equation constructed with a combination of the $tt-$, $yy-$ and $\theta\theta-$components; and a second order equation for $f^-_{\theta\phi}$ is obtained from the perturbed Maxwell equations.

Let us introduce the two dynamical variables, Υ_i with $i = 1\,, 2$, and the con-

strained variable Λ as follows

$$H_1 = \Lambda - \frac{2r}{f_S(1+3f_B)} H_3 \,, \tag{D.42}$$

$$H_3 = \left[\left(1 - \frac{4P^2\kappa_5^2}{(3-f_S)(9r^2 - 2P^2\kappa_5^2 - 3r^2 f_S)} \right) \frac{1}{r f_B^2} \Upsilon_1 + \frac{2P\kappa_5}{f_B(9r^2 - 2P^2\kappa_5^2 - 3r^2 f_S)} \Upsilon_2 - \frac{(1-f_B)(1+3f_B) f_S}{3r f_B (3 - f_S + f_B(1-3f_S))} \Lambda \right] , \tag{D.43}$$

$$f^-_{\theta\phi} = \kappa_5^{-1} \left[\Upsilon_2 - \left(\frac{2P\kappa_5}{r f_B (3-f_S)} \right) \Upsilon_1 + \frac{P\kappa_5 f_S (1+3f_B)}{3r(3 - f_S + f_B(1-3f_S))} \Lambda \right] . \tag{D.44}$$

By using these definitions one can recast the second order equations for $\{H_3 \,, f^-_{\theta\phi}\}$, containing source terms proportional to $\{H_1, H_3 \,, f^-_{\theta\phi}\}$ and their derivatives, into the system of coupled equations second order equations (6.56) that only contain $\{\Upsilon_i \,, \partial_r \Upsilon_i \,, \partial_r^2 \Upsilon_i\}$. Moreover, Λ is related to the two variables Υ_i with $i = 1\,, 2$ in terms of

$$\partial_r \Lambda + \mu_0 \Lambda + \mu_1 \Upsilon_1 + \mu_2 \Upsilon_2 = 0 \,, \tag{D.45}$$

where the coefficients μ_0, μ_1 and μ_2 are defined below

$$\mu_0 = \Bigg(\frac{1}{r f_B f_S (1+3f_B)(-3 + f_S + f_B(-1+3f_S))} \times \times \Big(-3 + 3f_B^3(-1+f_S) + 4f_S - f_S^2 + f_B^2(-13 + 30 f_S - 9 f_S^2) + f_B(-13 + 11 f_S - 6 f_S^2) \Big) \Bigg) \,, \tag{D.46}$$

$$\mu_1 = \frac{1}{r^3 f_B f_S^2} \left(\frac{4P^2\kappa_5^2 f_S}{3 - f_S} - \frac{3r^2(3+f_B)(1-f_S)}{(1+3f_B)^2} \cdot \cdot \left(1 + \frac{2}{3-f_S} - \frac{6r^2}{9r^2 - 2P^2\kappa_5^2 - 3r^2 f_S} \right) \right) \,, \tag{D.47}$$

$$\mu_2 = -\frac{2P\kappa_5}{f_S^2} \left(\frac{f_S}{r^2} + \frac{3(3+f_B)(1-f_S)}{(1+3f_B)^2 (9r^2 - 2P^2\kappa_5^2 - 3r^2 f_S)} \right) . \tag{D.48}$$

Finally, the coefficients of Eqs. (6.56) are reported below

$$
\begin{aligned}
W_{11} = & \frac{f_S}{r(1+3f_B)(3-f_S)(2+f_B(1-f_S))^2}\times \\
& \times \Big(-12(-3+f_S)f_S + 3f_B^4(-1+f_S)^2(3+f_S+2f_S^2) \\
& +4f_B(3+14f_S-21f_S^2+4f_S^3) + f_B^2(48-119f_S+23f_S^2+27f_S^3-3f_S^4) \\
& +f_B^3(39-174f_S+208f_S^2-74f_S^3+f_S^4)\Big) \,,
\end{aligned}
\tag{D.49}
$$

$$
\begin{aligned}
V_{11} = & \frac{f_S}{r^2(1+3f_B)^2(3-f_S)^2(2+f_B(1-f_S))^3(3-f_S+f_B(1-3f_S))^2}\times \\
& \times \Big(12(-3+f_S)^3 f_S(-21+f_S^2) + 54f_B^9(-1+f_S)^4(-3-2f_S+f_S^2) \\
& -4f_B(-3+f_S)^2(-63-876f_S+1315f_S^2-273f_S^3+f_S^5) \\
& +9f_B^8(-1+f_S)^3(87+96f_S+124f_S^2-250f_S^3-27f_S^4+18f_S^5) \\
& +3f_B^7(-1+f_S)^2(921-5782f_S+7581f_S^2-7268f_S^3+6123f_S^4-1446f_S^5+63f_S^6) \\
& +f_B^5(60060-306980f_S+685662f_S^2-771836f_S^3+423070f_S^4-95500f_S^5+3178f_S^6 \\
& +1260f_S^7-66f_S^8) + f_B^6(25230-141257f_S+348325f_S^2-501473f_S^3 \\
& +427073f_S^4-194707f_S^5+39335f_S^6-2499f_S^7-27f_S^8) + f_B^4(59529-283361f_S \\
& +456189f_S^2-253885f_S^3-15645f_S^4+54653f_S^5-15265f_S^6+1249f_S^7-8f_S^8) \\
& +f_B^2(11016+40185f_S-177621f_S^2+197161f_S^3-87965f_S^4+17235f_S^5 \\
& -1303f_S^6+11f_S^7+f_S^8) + f_B^3(26703-71064f_S-52318f_S^2+230692f_S^3 \\
& -189036f_S^4+61632f_S^5-8202f_S^6+308f_S^7+5f_S^8)\Big) \,,
\end{aligned}
\tag{D.50}
$$

$$
W_{12} = -\frac{4P\kappa_5 f_S^2}{3r^2(1+3f_B)(2+f_B(1-f_S))^2}\Big(9-f_S+5f_B(1-f_S)-6f_B^2(1-f_S)\Big) \,,
\tag{D.51}
$$

$$
\begin{aligned}
V_{12} = & \frac{-2P\kappa_5 f_S}{3r^3(1+3f_B)^2(2+f_B(1-f_S))^3(3-f_S+f_B(1-3f_S))^2}\times \\
& \times \Big(27f_B^7(-1+f_S)^3(1+f_S) - 2(-3+f_S)^2(-54+180f_S-23f_S^2+f_S^3) \\
& +9f_B^6(-1+f_S)^2(-19-15f_S-21f_S^2+15f_S^3) + f_B^3(9709-29512f_S \\
& +37424f_S^2-23938f_S^3+6915f_S^4-598f_S^5) + f_B^2(11733-33209f_S+38666f_S^2 \\
& -19922f_S^3+3857f_S^4-229f_S^5) + f_B(5868-17997f_S+18076f_S^2-6238f_S^3 \\
& +840f_S^4-37f_S^5) + 3f_B^5(38-587f_S+700f_S^2+146f_S^3-306f_S^4+9f_S^5) \\
& -2f_B^4(-1645+6227f_S-7659f_S^2+4957f_S^3-1880f_S^4 \\
& +288f_S^5)\Big)
\end{aligned}
\tag{D.52}
$$

$$W_{22} = \frac{f_S}{r(3-f_S)(1+3f_B)(2+f_B(1-f_S))^2}\times$$
$$\times\Big(-4(-3+f_S)f_S+3f_B^4(-1+f_S)^2(3-15f_S+2f_S^2)+4f_B(3-4f_S+5f_S^2)$$
$$+f_B^3(39-80f_S+18f_S^2+24f_S^3-f_S^4)-f_B^2(-48+69f_S-5f_S^2+7f_S^3+f_S^4)\Big)\,, \tag{D.53}$$

$$V_{22} = \frac{f_S}{r^2(1+3f_B)^2(3-f_S)(2+f_B(1-f_S))^3(3-f_S+f_B(1-3f_S))^2}\times$$
$$\times\Big(\,54f_B^9(-1+f_S)^4(1+f_S)+4(-3+f_S)^3(-12+7f_S+f_S^2)$$
$$-9f_B^8(-1+f_S)^3(41+9f_S+117f_S^2-105f_S^3+18f_S^4)$$
$$-4f_B(-2457+5616f_S-4716f_S^2+1666f_S^3-251f_S^4+14f_S^5)$$
$$-3f_B^7(-1+f_S)^2(1-339f_S-1954f_S^2+2718f_S^3-615f_S^4+45f_S^5)$$
$$+f_B^2(25236-67251f_S+71006f_S^2-37009f_S^3+8512f_S^4-765f_S^5+14f_S^6+f_S^7)$$
$$+f_B^3(22989-77809f_S+94013f_S^2-58169f_S^3+19751f_S^4-2275f_S^5-49f_S^6+13f_S^7)$$
$$+f_B^4(-1195-15084f_S+29469f_S^2-13224f_S^3+1015f_S^4+724f_S^5-617f_S^6+64f_S^7)$$
$$+2f_B^5(-5978+14642f_S-14269f_S^2+13497f_S^3-11896f_S^4+4688f_S^5$$
$$-753f_S^6+69f_S^7)+f_B^6(-5146+17301f_S-12032f_S^2-5489f_S^3+4038f_S^4$$
$$+2123f_S^5-876f_S^6+81f_S^7)\Big)\,, \tag{D.54}$$

$$W_{21} = -\frac{4P\kappa_5 f_B^2 f_S^2}{r^2(1+3f_B)(3-f_S)^2(2+f_B(1-f_S))^2}\times$$
$$\times\Big(\,10+3f_B^3(-9+f_S)(-1+f_S)^2+8f_S-2f_S^2+4f_B(-6-7f_S+f_S^2)$$
$$+f_B^2(-31+11f_S+23f_S^2-3f_S^3)\Big)\,, \tag{D.55}$$

$$
\begin{aligned}
V_{21} = &-\frac{2P\kappa_5 f_B f_S}{r^3(1+3f_B)^2(2+f_B(1-f_S))^3(3-f_S)^3(3-f_S+f_B(1-3f_S))^2}\times \\
&\times\Big(\,16(-3+f_S)^3 f_S(-5-4f_S+f_S^2)+54f_B^9(-1+f_S)^4(-3-2f_S+f_S^2) \\
&-4f_B(-3+f_S)^2(60-11f_S+187f_S^2+117f_S^3-43f_S^4+2f_S^5) \\
&-9f_B^8(-1+f_S)^3(-129+142f_S-976f_S^2+1430f_S^3-423f_S^4+36f_S^5) \\
&+3f_B^7(-1+f_S)^2(-189+2248f_S-18617f_S^2+25716f_S^3-7091f_S^4+420f_S^5+9f_S^6) \\
&+2f_B^2(-4968+174f_S+7727f_S^2-1370f_S^3+1843f_S^4-2014f_S^5+581f_S^6-54f_S^7+f_S^8) \\
&+4f_B^3(-867-5167f_S+31793f_S^2-33910f_S^3+14014f_S^4-3911f_S^5+1005f_S^6-148f_S^7+7f_S^8) \\
&+f_B^4(32142-102941f_S+246597f_S^2-377773f_S^3+249201f_S^4-79311f_S^5+14551f_S^6 \\
&-1767f_S^7+101f_S^8)+f_B^5(38937-106226f_S+152024f_S^2-270874f_S^3+320770f_S^4 \\
&-158742f_S^5+35856f_S^6-3870f_S^7+189f_S^8)+f_B^6(13767-29608f_S-53102f_S^2 \\
&+142280f_S^3-45248f_S^4-53128f_S^5+29758f_S^6-5016f_S^7+297f_S^8)\,\Big)\,.
\end{aligned}
\tag{D.56}
$$

Appendix E

Numerical techniques for $\mathcal{W}$-soliton and corresponding BH QNMs

In this Appendix we present the numerical method of continued fraction (Leaver's method) employed for the computation of the QNMs of the $\mathcal{W}$-soliton and the corresponding BH discussed in Chapter 8.

E.1 Continued fraction method

The continued fraction method has been applied to the two objects in the neutral case, namely when $Q = 0$, i.e. for $N = 0$, and with zero KK momentum along the fifth dimension ($p_\psi = 0$).

E.1.1 Neutral BH: Schwarzschild BH

As discussed in Chapter 8, the BH with $Q = 0$ reduces to the trivial embedding of the Schwarzschild black hole in five dimensions, and the master equation (8.35), together with the condition $p_\psi = 0$, reduces to the perturbation equation of a test scalar field on the background of the Schwarzschild geometry, given by Eq. (2.8). Let us rewrite the latter equation in the following more convenient form

$$r(r-2M)\frac{d^2\psi}{dr^2} + 2M\frac{d\psi}{dr} + \left[\frac{\omega^2 r^3}{r-2M} - \frac{2M}{r} - l(l+1)\right]\psi = 0\,. \tag{E.1}$$

The above ODE is subject to the following boundary conditions at the horizon ($r = 2M$) and at spatial infinity

$$\psi(r) \to (r-2M)^{-2i\omega M} \qquad (r \to 2M)\,, \tag{E.2}$$

$$\psi(r) \to r^{2i\omega M} e^{i\omega r} \qquad (r \to +\infty)\,. \tag{E.3}$$

Therefore a good ansatz that represents the desired solution of the ODE simultaneously at the two boundaries is given by

$$\psi(r) = \left(\frac{r-2M}{r}\right)^{-2i\omega M} r^{2i\omega M} e^{i\omega(r-2M)} \sum_{n=0}^{N_{\rm CF}} a_n \left(\frac{r-2M}{r}\right)^n\,. \tag{E.4}$$

By using the guess of Eq. (E.4) in the ODE, we can derive the following three-term recurrence relation that can be solved with the method described in Sec. 2.4.2

$$\alpha_0 a_1 + \beta_0 a_0 = 0 \qquad (n = 0)\,, \tag{E.5}$$

$$\alpha_n a_{n+1} + \beta_n a_n + \gamma_n a_{n-1} = 0 \qquad (n > 0)\,, \tag{E.6}$$

where the coefficients are given by

$$\alpha_n = n^2 + (2 - 4i\omega M)n + 1 - 4i\omega M\,, \tag{E.7}$$

$$\beta_n = -2n^2 + (16i\omega M - 2)n + 32\omega^2 M^2 + 8i\omega M - 1 - l(l+1)\,, \tag{E.8}$$

$$\gamma_n = (n - 4i\omega M)^2\,. \tag{E.9}$$

E.1.2 Neutral $\mathcal{W}$-soliton

The procedure for the neutral $\mathcal{W}$-soliton is similar to the one discussed in the previous section for the BH, with the difference that now the horizon at $r = 2M$ is replaced by an inner boundary at $r = 4M$. As a consequence, the inner boundary conditions will be different.

The scalar perturbation equation (8.33) for the neutral $\mathcal{W}$-soliton, with zero KK momentum ($p_\psi = 0$), reduces to

$$2(4M-1)\frac{d^2\Psi}{dr^2} - 4\left(1 - \frac{2M}{r}\right)\frac{d\Psi}{dr} - 2\left[\omega^2 r - \frac{l(l+1)}{r}\right]\Psi = 0\,, \tag{E.10}$$

with the following boundary conditions

$$\Psi(r) \to (r - 4M)^\rho \qquad (r \to 4M)\,, \tag{E.11}$$

$$\Psi(r) \to r^{-1+2i\omega M} e^{i\omega r} \qquad (r \to +\infty)\,, \tag{E.12}$$

with $\rho = 0$. Let us consider the following ansatz for the solution

$$\Psi(r) = \left(\frac{r-4M}{r}\right)^\rho r^{-1+2i\omega M} e^{i\omega(r-4M)} \sum_{n=0}^{N_{\rm CF}} a_n \left(\frac{r-4M}{r}\right)^n\,. \tag{E.13}$$

Finally, inserting the above guess in the ODE we find a three-term recurrence relation of the same form of Eqs. (E.5)- (E.6), with coefficients

$$\alpha_n = -(n+1)^2\,, \tag{E.14}$$

$$\beta_n = 2n^2 + 2n(1 - 6i\omega M) - 2M\omega(3i + 8M\omega) + 1 + l(l+1)\,, \tag{E.15}$$

$$\gamma_n = -(n - 2i\omega M)^2\,. \tag{E.16}$$

Acknowledgments

Il percorso di dottorato che ha portato al completamento di questa tesi non sarebbe stato possibile senza l'insegnamento, il sostegno, la compagnia e l'affetto delle persone che seguono.

In primo luogo vorrei ringraziare infinitamente il mio relatore, Prof. Paolo Pani, per la sua costaste guida durante questi tre anni. Il suo modo di studiare la fisica e approcciarsi alla ricerca rappresenta un bagaglio unico che porterò con me nei prossimi anni.

Un ringraziamento va a tutti i compagni del gruppo di gravità della Sapienza con cui ho incrociato il mio percorso in questi anni, in particolare a: Francesco Crescimbeni, Claudio Gambino, Loris Del Grosso, Alex Dima, Fabrizio Corelli, Robin Croft ed Enrico Cannizzaro.

Un pensiero va a tutti i colleghi dell'ufficio 301, per il quale, forse, son passati più pandori e panettoni che equazioni.

Ringrazio inoltre Prof. Richard Brito per avermi ospitato nel gruppo di ricerca CENTRA all'IST di Lisbona, e per la sua preziosa collaborazione. I sei mesi passati in Portogallo hanno rappresentato una delle esperienze più stimolanti che riesca a ricordare. Ringrazio tutto il gruppo di ricerca GRIT per l'immediata ospitalità che ho ricevuto al mio arrivo e per avermi fatto sentire parte del gruppo fin dal primo momento.

Un pensiero speciale ed imprescindibile va ai miei genitori, senza i quali ogni granello del mio percorso formativo e personale non sarebbe stato in alcun modo possibile. Ringrazio mia madre per la continua comprensione, presenza e dedizione che ha sempre mostrato nei miei confronti. Ringrazio mio padre per il suo inestimabile sostegno, il suo affetto, e l'immancabile volontà di dedicarsi a me.

Un pensiero d'affetto va a tutti i miei amici d'infanzia, che nonostante la distanza, grazie alla loro confidenza, complicità e compagnia hanno sempre mantenuto solido il legame: Riccardo, Francesco, Alessandro, Luca ed Enrico.

Infine ringrazio Melissa, per il tempo che ho passato, e per il tempo che passerò.

Bibliography

[1] B. P. Abbott et al. Observation of Gravitational Waves from a Binary Black Hole Merger. *Phys. Rev. Lett.*, 116(6):061102, 2016. doi: 10.1103/PhysRevLett.116.061102.

[2] B. P. Abbott et al. GWTC-1: A Gravitational-Wave Transient Catalog of Compact Binary Mergers Observed by LIGO and Virgo during the First and Second Observing Runs. *Phys. Rev. X*, 9(3):031040, 2019. doi: 10.1103/PhysRevX.9.031040.

[3] R. Abbott et al. GWTC-2: Compact Binary Coalescences Observed by LIGO and Virgo During the First Half of the Third Observing Run. *Phys. Rev. X*, 11:021053, 2021. doi: 10.1103/PhysRevX.11.021053.

[4] R. Abbott et al. GWTC-2.1: Deep extended catalog of compact binary coalescences observed by LIGO and Virgo during the first half of the third observing run. *Phys. Rev. D*, 109(2):022001, 2024. doi: 10.1103/PhysRevD.109.022001.

[5] R. Abbott et al. GWTC-3: Compact Binary Coalescences Observed by LIGO and Virgo during the Second Part of the Third Observing Run. *Phys. Rev. X*, 13(4):041039, 2023. doi: 10.1103/PhysRevX.13.041039.

[6] GWTC-4.0: Updating the Gravitational-Wave Transient Catalog with Observations from the First Part of the Fourth LIGO-Virgo-KAGRA Observing Run. 8 2025.

[7] B. P. Abbott et al. GW170817: Observation of Gravitational Waves from a Binary Neutron Star Inspiral. *Phys. Rev. Lett.*, 119(16):161101, 2017. doi: 10.1103/PhysRevLett.119.161101.

[8] B. P. Abbott et al. Multi-messenger Observations of a Binary Neutron Star Merger. *Astrophys. J. Lett.*, 848(2):L12, 2017. doi: 10.3847/2041-8213/aa91c9.

[9] Kazunori Akiyama et al. First M87 Event Horizon Telescope Results. I. The Shadow of the Supermassive Black Hole. *Astrophys. J. Lett.*, 875:L1, 2019. doi: 10.3847/2041-8213/ab0ec7.

[10] Kazunori Akiyama et al. First Sagittarius A* Event Horizon Telescope Results. I. The Shadow of the Supermassive Black Hole in the Center of the Milky Way. *Astrophys. J. Lett.*, 930(2):L12, 2022. doi: 10.3847/2041-8213/ac6674.

[11] R. Penrose. Gravitational collapse: The role of general relativity. *Riv. Nuovo Cim.*, 1:252–276, 1969. doi: 10.1023/A:1016578408204.

[12] Robert M. Wald. Gravitational collapse and cosmic censorship. pages 69–85, 10 1997. doi: 10.1007/978-94-017-0934-7_5.

[13] Werner Israel. Event horizons in static vacuum space-times. *Phys. Rev.*, 164: 1776–1779, 1967. doi: 10.1103/PhysRev.164.1776.

[14] Werner Israel. Event horizons in static electrovac space-times. *Commun. Math. Phys.*, 8:245–260, 1968. doi: 10.1007/BF01645859.

[15] B. Carter. Axisymmetric Black Hole Has Only Two Degrees of Freedom. *Phys. Rev. Lett.*, 26:331–333, 1971. doi: 10.1103/PhysRevLett.26.331.

[16] D. C. Robinson. Uniqueness of the Kerr black hole. *Phys. Rev. Lett.*, 34: 905–906, 1975. doi: 10.1103/PhysRevLett.34.905.

[17] Robert M. Wald. *General Relativity*. Chicago Univ. Pr., Chicago, USA, 1984. doi: 10.7208/chicago/9780226870373.001.0001.

[18] S. W. Hawking. Particle Creation by Black Holes. *Commun. Math. Phys.*, 43: 199–220, 1975. doi: 10.1007/BF02345020. [Erratum: Commun.Math.Phys. 46, 206 (1976)].

[19] S. W. Hawking. Breakdown of Predictability in Gravitational Collapse. *Phys. Rev. D*, 14:2460–2473, 1976. doi: 10.1103/PhysRevD.14.2460.

[20] Jacob D. Bekenstein. Black holes and entropy. *Phys. Rev. D*, 7:2333–2346, 1973. doi: 10.1103/PhysRevD.7.2333.

[21] Emanuele Berti et al. Testing General Relativity with Present and Future Astrophysical Observations. *Class. Quant. Grav.*, 32:243001, 2015. doi: 10.1088/0264-9381/32/24/243001.

[22] Vitor Cardoso and Paolo Pani. Testing the nature of dark compact objects: a status report. *Living Rev. Rel.*, 22(1):4, 2019. doi: 10.1007/s41114-019-0020-4.

[23] Daniel R. Mayerson. Fuzzballs and Observations. *Gen. Rel. Grav.*, 52(12):115, 2020. doi: 10.1007/s10714-020-02769-w.

[24] Iosif Bena, Emil J. Martinec, Samir D. Mathur, and Nicholas P. Warner. Snowmass White Paper: Micro- and Macro-Structure of Black Holes. 3 2022.

[25] Iosif Bena, Emil J. Martinec, Samir D. Mathur, and Nicholas P. Warner. Fuzzballs and Microstate Geometries: Black-Hole Structure in String Theory. 4 2022.

[26] Ibrahima Bah and Pierre Heidmann. Topological Stars and Black Holes. *Phys. Rev. Lett.*, 126(15):151101, 2021. doi: 10.1103/PhysRevLett.126.151101.

[27] Soumangsu Chakraborty and Pierre Heidmann. Microstates of non-extremal black holes: a new hope. *JHEP*, 07:101, 2025. doi: 10.1007/JHEP07(2025)101.

[28] Vitor Cardoso, Edgardo Franzin, and Paolo Pani. Is the gravitational-wave ringdown a probe of the event horizon? *Phys. Rev. Lett.*, 116(17):171101, 2016. doi: 10.1103/PhysRevLett.116.171101. [Erratum: Phys.Rev.Lett. 117, 089902 (2016)].

[29] Vitor Cardoso and Paolo Pani. Tests for the existence of black holes through gravitational wave echoes. *Nature Astron.*, 1(9):586–591, 2017. doi: 10.1038/s41550-017-0225-y.

[30] Carlos A. R. Herdeiro, Eugen Radu, Nicolas Sanchis-Gual, and José A. Font. Spontaneous Scalarization of Charged Black Holes. *Phys. Rev. Lett.*, 121(10): 101102, 2018. doi: 10.1103/PhysRevLett.121.101102.

[31] Pedro G. S. Fernandes, Carlos A. R. Herdeiro, Alexandre M. Pombo, Eugen Radu, and Nicolas Sanchis-Gual. Spontaneous Scalarisation of Charged Black Holes: Coupling Dependence and Dynamical Features. *Class. Quant. Grav.*, 36(13):134002, 2019. doi: 10.1088/1361-6382/ab23a1. [Erratum: Class.Quant.Grav. 37, 049501 (2020)].

[32] Daniela D. Doneva, Fethi M. Ramazanoğlu, Hector O. Silva, Thomas P. Sotiriou, and Stoytcho S. Yazadjiev. Spontaneous scalarization. *Rev. Mod. Phys.*, 96(1):015004, 2024. doi: 10.1103/RevModPhys.96.015004.

[33] Guangzhou Guo, Peng Wang, Houwen Wu, and Haitang Yang. Echoes from hairy black holes. *JHEP*, 06:073, 2022. doi: 10.1007/JHEP06(2022)073.

[34] Guangzhou Guo, Peng Wang, and Yu-Peng Zhang. Nonlinear stability of black holes with a stable light ring. *Phys. Rev. D*, 112(8):084023, 2025. doi: 10.1103/xlsl-8dtq.

[35] Marco Melis, Fabrizio Corelli, Robin Croft, and Paolo Pani. Black hole spectroscopy and nonlinear echoes in Einstein-Maxwell-scalar theory. *Phys. Rev. D*, 111(6):064072, 2025. doi: 10.1103/PhysRevD.111.064072.

[36] Jahed Abedi, Hannah Dykaar, and Niayesh Afshordi. Echoes from the Abyss: Tentative evidence for Planck-scale structure at black hole horizons. *Phys. Rev. D*, 96(8):082004, 2017. doi: 10.1103/PhysRevD.96.082004.

[37] Randy S. Conklin, Bob Holdom, and Jing Ren. Gravitational wave echoes through new windows. *Phys. Rev. D*, 98(4):044021, 2018. doi: 10.1103/PhysRevD.98.044021.

[38] Jahed Abedi, Hannah Dykaar, and Niayesh Afshordi. Echoes from the Abyss: The Holiday Edition! 1 2017.

[39] Gregory Ashton, Ofek Birnholtz, Miriam Cabero, Collin Capano, Thomas Dent, Badri Krishnan, Grant David Meadors, Alex B. Nielsen, Alex Nitz, and Julian Westerweck. Comments on: "Echoes from the abyss: Evidence for Planck-scale structure at black hole horizons". 12 2016.

[40] Julian Westerweck, Alex Nielsen, Ofek Fischer-Birnholtz, Miriam Cabero, Collin Capano, Thomas Dent, Badri Krishnan, Grant Meadors, and Alexander H. Nitz. Low significance of evidence for black hole echoes in gravitational wave data. *Phys. Rev. D*, 97(12):124037, 2018. doi: 10.1103/PhysRevD.97.124037.

[41] Alex B. Nielsen, Collin D. Capano, Ofek Birnholtz, and Julian Westerweck. Parameter estimation and statistical significance of echoes following black hole signals in the first Advanced LIGO observing run. *Phys. Rev. D*, 99(10):104012, 2019. doi: 10.1103/PhysRevD.99.104012.

[42] R. Abbott et al. Tests of general relativity with binary black holes from the second LIGO-Virgo gravitational-wave transient catalog. *Phys. Rev. D*, 103 (12):122002, 2021. doi: 10.1103/PhysRevD.103.122002.

[43] R. Abbott et al. Tests of General Relativity with GWTC-3. 12 2021.

[44] Paolo Pani, Emanuele Berti, Vitor Cardoso, Yanbei Chen, and Richard Norte. Gravitational-wave signatures of the absence of an event horizon. II. Extreme mass ratio inspirals in the spacetime of a thin-shell gravastar. *Phys. Rev. D*, 81:084011, 2010. doi: 10.1103/PhysRevD.81.084011.

[45] Caio F. B. Macedo, Paolo Pani, Vitor Cardoso, and Luís C. B. Crispino. Astrophysical signatures of boson stars: quasinormal modes and inspiral resonances. *Phys. Rev. D*, 88(6):064046, 2013. doi: 10.1103/PhysRevD.88.064046.

[46] Vitor Cardoso, Adrian del Rio, and Masashi Kimura. Distinguishing black holes from horizonless objects through the excitation of resonances during inspiral. *Phys. Rev. D*, 100:084046, 2019. doi: 10.1103/PhysRevD.100.084046. [Erratum: Phys.Rev.D 101, 069902 (2020)].

[47] Kwinten Fransen, Gideon Koekoek, Rob Tielemans, and Bert Vercnocke. Modeling and detecting resonant tides of exotic compact objects. *Phys. Rev. D*, 104(4):044044, 2021. doi: 10.1103/PhysRevD.104.044044.

[48] Elisa Maggio, Maarten van de Meent, and Paolo Pani. Extreme mass-ratio inspirals around a spinning horizonless compact object. *Phys. Rev. D*, 104(10):104026, 2021. doi: 10.1103/PhysRevD.104.104026.

[49] Sayak Datta, Richard Brito, Sukanta Bose, Paolo Pani, and Scott A. Hughes. Tidal heating as a discriminator for horizons in extreme mass ratio inspirals. *Phys. Rev. D*, 101(4):044004, 2020. doi: 10.1103/PhysRevD.101.044004.

[50] M. Punturo et al. The Einstein Telescope: A third-generation gravitational wave observatory. *Class. Quant. Grav.*, 27:194002, 2010. doi: 10.1088/0264-9381/27/19/194002.

[51] David Reitze et al. Cosmic Explorer: The U.S. Contribution to Gravitational-Wave Astronomy beyond LIGO. *Bull. Am. Astron. Soc.*, 51(7):035, 2019.

[52] Pau Amaro-Seoane et al. Laser Interferometer Space Antenna. 2 2017.

[53] Jonathan R. Gair, Stanislav Babak, Alberto Sesana, Pau Amaro-Seoane, Enrico Barausse, Christopher P. L. Berry, Emanuele Berti, and Carlos Sopuerta. Prospects for observing extreme-mass-ratio inspirals with LISA. *J. Phys. Conf. Ser.*, 840(1):012021, 2017. doi: 10.1088/1742-6596/840/1/012021.

[54] Karl Schwarzschild. On the gravitational field of a mass point according to Einstein's theory. *Sitzungsber. Preuss. Akad. Wiss. Berlin (Math. Phys.)*, 1916:189–196, 1916.

[55] H. Reissner. Über die Eigengravitation des elektrischen Feldes nach der Einsteinschen Theorie. *Annalen Phys.*, 355(9):106–120, 1916. doi: 10.1002/andp.19163550905.

[56] G. Nordström. On the energy of the gravitational field in einstein's theory. *Proc. Kon. Ned. Akad. Wet.*, 20:1238–1245, 1918.

[57] Roy P. Kerr. Gravitational field of a spinning mass as an example of algebraically special metrics. *Phys. Rev. Lett.*, 11:237–238, 1963. doi: 10.1103/PhysRevLett.11.237.

[58] E T. Newman, E. Couch, K. Chinnapared, A. Exton, A. Prakash, and R. Torrence. Metric of a Rotating, Charged Mass. *J. Math. Phys.*, 6:918–919, 1965. doi: 10.1063/1.1704351.

[59] Albert Einstein. On a stationary system with spherical symmetry consisting of many gravitating masses. *Annals Math.*, 40:922–936, 1939. doi: 10.2307/1968902.

[60] C. T. Bolton. Identification of cygnus x-1 with hde 226868. *Nature*, 235: 271–273, 1972. doi: 10.1038/235271b0.

[61] B. L. Webster and P. Murdin. Cygnus x-1 – a spectroscopic binary with a heavy companion? *Nature*, 235:37–38, 1972. doi: 10.1038/235037a0.

[62] A. M. Ghez et al. Measuring Distance and Properties of the Milky Way's Central Supermassive Black Hole with Stellar Orbits. *Astrophys. J.*, 689: 1044–1062, 2008. doi: 10.1086/592738.

[63] S. Gillessen, F. Eisenhauer, S. Trippe, T. Alexander, R. Genzel, F. Martins, and T. Ott. Monitoring stellar orbits around the Massive Black Hole in the Galactic Center. *Astrophys. J.*, 692:1075–1109, 2009. doi: 10.1088/0004-637X/692/2/1075.

[64] Samir D. Mathur and Madhur Mehta. The Fuzzball Paradigm. 12 2024.

[65] Samir D. Mathur. Resolving the black hole causality paradox. *Gen. Rel. Grav.*, 51(2):24, 2019. doi: 10.1007/s10714-019-2505-6.

[66] Samir D. Mathur. The Information paradox: A Pedagogical introduction. *Class. Quant. Grav.*, 26:224001, 2009. doi: 10.1088/0264-9381/26/22/224001.

[67] Borun D. Chowdhury and Samir D. Mathur. Radiation from the non-extremal fuzzball. *Class. Quant. Grav.*, 25:135005, 2008. doi: 10.1088/0264-9381/25/13/135005.

[68] Iosif Bena and Nicholas P. Warner. Resolving the Structure of Black Holes: Philosophizing with a Hammer. 11 2013.

[69] Fang Chen, Ben Michel, Joseph Polchinski, and Andrea Puhm. Journey to the Center of the Fuzzball. *JHEP*, 02:081, 2015. doi: 10.1007/JHEP02(2015)081.

[70] Suvrat Raju and Pushkal Shrivastava. Critique of the fuzzball program. *Phys. Rev. D*, 99(6):066009, 2019. doi: 10.1103/PhysRevD.99.066009.

[71] Iosif Bena and Nicholas P. Warner. Black holes, black rings and their microstates. *Lect. Notes Phys.*, 755:1–92, 2008. doi: 10.1007/978-3-540-79523-0_1.

[72] J. C. Breckenridge, Robert C. Myers, A. W. Peet, and C. Vafa. D-branes and spinning black holes. *Phys. Lett. B*, 391:93–98, 1997. doi: 10.1016/S0370-2693(96)01460-8.

[73] Stefano Giusto and Samir D. Mathur. Geometry of D1-D5-P bound states. *Nucl. Phys. B*, 729:203–220, 2005. doi: 10.1016/j.nuclphysb.2005.09.037.

[74] Iosif Bena and Nicholas P. Warner. Bubbling supertubes and foaming black holes. *Phys. Rev. D*, 74:066001, 2006. doi: 10.1103/PhysRevD.74.066001.

[75] Per Berglund, Eric G. Gimon, and Thomas S. Levi. Supergravity microstates for BPS black holes and black rings. *JHEP*, 06:007, 2006. doi: 10.1088/1126-6708/2006/06/007.

[76] Iosif Bena, Chih-Wei Wang, and Nicholas P. Warner. The Foaming three-charge black hole. *Phys. Rev. D*, 75:124026, 2007. doi: 10.1103/PhysRevD.75.124026.

[77] Iosif Bena, Chih-Wei Wang, and Nicholas P. Warner. Mergers and typical black hole microstates. *JHEP*, 11:042, 2006. doi: 10.1088/1126-6708/2006/11/042.

[78] Iosif Bena, Chih-Wei Wang, and Nicholas P. Warner. Plumbing the Abyss: Black ring microstates. *JHEP*, 07:019, 2008. doi: 10.1088/1126-6708/2008/07/019.

[79] Iosif Bena, Nikolay Bobev, and Nicholas P. Warner. Spectral Flow, and the Spectrum of Multi-Center Solutions. *Phys. Rev. D*, 77:125025, 2008. doi: 10.1103/PhysRevD.77.125025.

[80] Iosif Bena, Nikolay Bobev, Stefano Giusto, Clement Ruef, and Nicholas P. Warner. An Infinite-Dimensional Family of Black-Hole Microstate Geometries. *JHEP*, 03:022, 2011. doi: 10.1007/JHEP03(2011)022. [Erratum: JHEP 04, 059 (2011)].

[81] Iosif Bena, Stefano Giusto, Masaki Shigemori, and Nicholas P. Warner. Supersymmetric Solutions in Six Dimensions: A Linear Structure. *JHEP*, 03:084, 2012. doi: 10.1007/JHEP03(2012)084.

[82] Massimo Bianchi, Josè Francisco Morales, and Lorenzo Pieri. Stringy origin of 4d black hole microstates. *JHEP*, 06:003, 2016. doi: 10.1007/JHEP06(2016)003.

[83] Massimo Bianchi, Jose Francisco Morales, Lorenzo Pieri, and Natale Zinnato. More on microstate geometries of 4d black holes. *JHEP*, 05:147, 2017. doi: 10.1007/JHEP05(2017)147.

[84] Pierre Heidmann. Four-center bubbled BPS solutions with a Gibbons-Hawking base. *JHEP*, 10:009, 2017. doi: 10.1007/JHEP10(2017)009.

[85] Iosif Bena, Pierre Heidmann, and Pedro F. Ramirez. A systematic construction of microstate geometries with low angular momentum. *JHEP*, 10:217, 2017. doi: 10.1007/JHEP10(2017)217.

[86] Jesus Avila, Pedro F. Ramirez, and Alejandro Ruiperez. One Thousand and One Bubbles. *JHEP*, 01:041, 2018. doi: 10.1007/JHEP01(2018)041.

[87] Alexander Tyukov, Robert Walker, and Nicholas P. Warner. The Structure of BPS Equations for Ambi-polar Microstate Geometries. *Class. Quant. Grav.*, 36(1):015021, 2019. doi: 10.1088/1361-6382/aaf133.

[88] Nicholas P. Warner. Lectures on Microstate Geometries. 12 2019.

[89] Iosif Bena, Masaki Shigemori, and Nicholas P. Warner. Black-Hole Entropy from Supergravity Superstrata States. *JHEP*, 10:140, 2014. doi: 10.1007/JHEP10(2014)140.

[90] Masaki Shigemori. Counting Superstrata. *JHEP*, 10:017, 2019. doi: 10.1007/JHEP10(2019)017.

[91] Andrew Strominger and Cumrun Vafa. Microscopic origin of the Bekenstein-Hawking entropy. *Phys. Lett. B*, 379:99–104, 1996. doi: 10.1016/0370-2693(96)00345-0.

[92] Daniel R. Mayerson and Masaki Shigemori. Counting D1-D5-P microstates in supergravity. *SciPost Phys.*, 10(1):018, 2021. doi: 10.21468/SciPostPhys.10.1.018.

[93] Masaki Shigemori. Superstrata. *Gen. Rel. Grav.*, 52(5):51, 2020. doi: 10.1007/s10714-020-02698-8.

[94] Paul de Lange, Daniel R. Mayerson, and Bert Vercnocke. Structure of Six-Dimensional Microstate Geometries. *JHEP*, 09:075, 2015. doi: 10.1007/JHEP09(2015)075.

[95] Iosif Bena, Stefano Giusto, Rodolfo Russo, Masaki Shigemori, and Nicholas P. Warner. Habemus Superstratum! A constructive proof of the existence of superstrata. *JHEP*, 05:110, 2015. doi: 10.1007/JHEP05(2015)110.

[96] Iosif Bena, Emil Martinec, David Turton, and Nicholas P. Warner. Momentum Fractionation on Superstrata. *JHEP*, 05:064, 2016. doi: 10.1007/JHEP05(2016)064.

[97] Iosif Bena, Stefano Giusto, Emil J. Martinec, Rodolfo Russo, Masaki Shigemori, David Turton, and Nicholas P. Warner. Smooth horizonless geometries deep inside the black-hole regime. *Phys. Rev. Lett.*, 117(20):201601, 2016. doi: 10.1103/PhysRevLett.117.201601.

[98] Iosif Bena, Stefano Giusto, Emil J. Martinec, Rodolfo Russo, Masaki Shigemori, David Turton, and Nicholas P. Warner. Asymptotically-flat supergravity solutions deep inside the black-hole regime. *JHEP*, 02:014, 2018. doi: 10.1007/JHEP02(2018)014.

[99] Elaheh Bakhshaei and Alessandro Bombini. Three-charge superstrata with internal excitations. *Class. Quant. Grav.*, 36(5):055001, 2019. doi: 10.1088/1361-6382/ab01bc.

[100] Nejc Čeplak, Rodolfo Russo, and Masaki Shigemori. Supercharging Superstrata. *JHEP*, 03:095, 2019. doi: 10.1007/JHEP03(2019)095.

[101] Pierre Heidmann and Nicholas P. Warner. Superstratum Symbiosis. *JHEP*, 09:059, 2019. doi: 10.1007/JHEP09(2019)059.

[102] Daniel R. Mayerson, Robert A. Walker, and Nicholas P. Warner. Microstate Geometries from Gauged Supergravity in Three Dimensions. *JHEP*, 10:030, 2020. doi: 10.1007/JHEP10(2020)030.

[103] Bogdan Ganchev, Anthony Houppe, and Nicholas P. Warner. New superstrata from three-dimensional supergravity. *JHEP*, 04:065, 2022. doi: 10.1007/JHEP04(2022)065.

[104] Vishnu Jejjala, Owen Madden, Simon F. Ross, and Georgina Titchener. Non-supersymmetric smooth geometries and D1-D5-P bound states. *Phys. Rev. D*, 71:124030, 2005. doi: 10.1103/PhysRevD.71.124030.

[105] Iosif Bena, Stefano Giusto, Clement Ruef, and Nicholas P. Warner. Multi-Center non-BPS Black Holes: the Solution. *JHEP*, 11:032, 2009. doi: 10.1088/1126-6708/2009/11/032.

[106] Iosif Bena, Stefano Giusto, Clement Ruef, and Nicholas P. Warner. A (Running) Bolt for New Reasons. *JHEP*, 11:089, 2009. doi: 10.1088/1126-6708/2009/11/089.

[107] Gianguido Dall'Agata, Stefano Giusto, and Clement Ruef. U-duality and non-BPS solutions. *JHEP*, 02:074, 2011. doi: 10.1007/JHEP02(2011)074.

[108] Orestis Vasilakis and Nicholas P. Warner. Mind the Gap: Supersymmetry Breaking in Scaling, Microstate Geometries. *JHEP*, 10:006, 2011. doi: 10.1007/JHEP10(2011)006.

[109] Iosif Bena, Andrea Puhm, and Bert Vercnocke. Metastable Supertubes and non-extremal Black Hole Microstates. *JHEP*, 04:100, 2012. doi: 10.1007/JHEP04(2012)100.

[110] Iosif Bena, Andrea Puhm, and Bert Vercnocke. Non-extremal Black Hole Microstates: Fuzzballs of Fire or Fuzzballs of Fuzz ? *JHEP*, 12:014, 2012. doi: 10.1007/JHEP12(2012)014.

[111] Samir D. Mathur and David Turton. Oscillating supertubes and neutral rotating black hole microstates. *JHEP*, 04:072, 2014. doi: 10.1007/JHEP04(2014)072.

[112] Iosif Bena, Guillaume Bossard, Stefanos Katmadas, and David Turton. Non-BPS multi-bubble microstate geometries. *JHEP*, 02:073, 2016. doi: 10.1007/JHEP02(2016)073.

[113] Iosif Bena, Guillaume Bossard, Stefanos Katmadas, and David Turton. Bolting Multicenter Solutions. *JHEP*, 01:127, 2017. doi: 10.1007/JHEP01(2017)127.

[114] Guillaume Bossard, Stefanos Katmadas, and David Turton. Two Kissing Bolts. *JHEP*, 02:008, 2018. doi: 10.1007/JHEP02(2018)008.

[115] Samir D. Mathur. Tunneling into fuzzball states. *Gen. Rel. Grav.*, 42:113–118, 2010. doi: 10.1007/s10714-009-0837-3.

[116] Per Kraus and Samir D. Mathur. Nature abhors a horizon. *Int. J. Mod. Phys. D*, 24(12):1543003, 2015. doi: 10.1142/S0218271815430038.

[117] Samir D. Mathur. The VECRO hypothesis. 1 2020. doi: 10.1142/S0218271820300098.

[118] Jan de Boer, Sheer El-Showk, Ilies Messamah, and Dieter Van den Bleeken. A Bound on the entropy of supergravity? *JHEP*, 02:062, 2010. doi: 10.1007/JHEP02(2010)062.

[119] Jan de Boer, Sheer El-Showk, Ilies Messamah, and Dieter Van den Bleeken. Quantizing N=2 Multicenter Solutions. *JHEP*, 05:002, 2009. doi: 10.1088/1126-6708/2009/05/002.

[120] Alexander Tyukov, Robert Walker, and Nicholas P. Warner. Tidal Stresses and Energy Gaps in Microstate Geometries. *JHEP*, 02:122, 2018. doi: 10.1007/JHEP02(2018)122.

[121] Iosif Bena, Pierre Heidmann, Ruben Monten, and Nicholas P. Warner. Thermal Decay without Information Loss in Horizonless Microstate Geometries. *SciPost Phys.*, 7(5):063, 2019. doi: 10.21468/SciPostPhys.7.5.063.

[122] Daniel R. Mayerson. Modave Lectures on Horizon-Size Microstructure, Fuzzballs and Observations. 2 2022.

[123] Taishi Ikeda, Massimo Bianchi, Dario Consoli, Alfredo Grillo, Josè Francisco Morales, Paolo Pani, and Guilherme Raposo. Black-hole microstate spectroscopy: Ringdown, quasinormal modes, and echoes. *Phys. Rev. D*, 104(6):066021, 2021. doi: 10.1103/PhysRevD.104.066021.

[124] Robert P. Geroch. Multipole moments. II. Curved space. *J. Math. Phys.*, 11: 2580–2588, 1970. doi: 10.1063/1.1665427.

[125] R. O. Hansen. Multipole moments of stationary space-times. *J. Math. Phys.*, 15:46–52, 1974. doi: 10.1063/1.1666501.

[126] K. S. Thorne. Multipole Expansions of Gravitational Radiation. *Rev. Mod. Phys.*, 52:299–339, 1980. doi: 10.1103/RevModPhys.52.299.

[127] Vitor Cardoso and Leonardo Gualtieri. Testing the black hole 'no-hair' hypothesis. *Class. Quant. Grav.*, 33(17):174001, 2016. doi: 10.1088/0264-9381/33/17/174001.

[128] Thomas P. Sotiriou and Theocharis A. Apostolatos. Corrected multipole moments of axisymmetric electrovacuum spacetimes. *Class. Quant. Grav.*, 21: 5727–5733, 2004. doi: 10.1088/0264-9381/21/24/003.

[129] Iosif Bena and Daniel R. Mayerson. Multipole Ratios: A New Window into Black Holes. *Phys. Rev. Lett.*, 125(22):221602, 2020. doi: 10.1103/PhysRevLett.125.221602.

[130] Iosif Bena and Daniel R. Mayerson. Black Holes Lessons from Multipole Ratios. *JHEP*, 03:114, 2021. doi: 10.1007/JHEP03(2021)114.

[131] Massimo Bianchi, Dario Consoli, Alfredo Grillo, Josè Francisco Morales, Paolo Pani, and Guilherme Raposo. Distinguishing fuzzballs from black holes through their multipolar structure. *Phys. Rev. Lett.*, 125(22):221601, 2020. doi: 10.1103/PhysRevLett.125.221601.

[132] Massimo Bianchi, Dario Consoli, Alfredo Grillo, Jose Francisco Morales, Paolo Pani, and Guilherme Raposo. The multipolar structure of fuzzballs. *JHEP*, 01:003, 2021. doi: 10.1007/JHEP01(2021)003.

[133] Ibrahima Bah, Iosif Bena, Pierre Heidmann, Yixuan Li, and Daniel R. Mayerson. Gravitational footprints of black holes and their microstate geometries. *JHEP*, 10:138, 2021. doi: 10.1007/JHEP10(2021)138.

[134] Eric Poisson and Clifford M. Will. *Gravity: Newtonian, Post-Newtonian, Relativistic*. Cambridge University Press, 2014.

[135] Vitor Cardoso, Edgardo Franzin, Andrea Maselli, Paolo Pani, and Guilherme Raposo. Testing strong-field gravity with tidal Love numbers. *Phys. Rev. D*, 95 (8):084014, 2017. doi: 10.1103/PhysRevD.95.084014. [Addendum: Phys.Rev.D 95, 089901 (2017)].

[136] B. P. Abbott et al. Tests of general relativity with GW150914. *Phys. Rev. Lett.*, 116(22):221101, 2016. doi: 10.1103/PhysRevLett.116.221101. [Erratum: Phys.Rev.Lett. 121, 129902 (2018)].

[137] Luc Blanchet. Post-Newtonian Theory for Gravitational Waves. *Living Rev. Rel.*, 17:2, 2014. doi: 10.12942/lrr-2014-2.

[138] Luc Blanchet, Thibault Damour, Bala R. Iyer, Clifford M. Will, and Alan G. Wiseman. Gravitational radiation damping of compact binary systems to second postNewtonian order. *Phys. Rev. Lett.*, 74:3515–3518, 1995. doi: 10.1103/PhysRevLett.74.3515.

[139] Lawrence E. Kidder. Coalescing binary systems of compact objects to post-Newtonian 5/2 order. 5. Spin effects. *Phys. Rev. D*, 52:821–847, 1995. doi: 10.1103/PhysRevD.52.821.

[140] Thibault Damour, Piotr Jaranowski, and Gerhard Schaefer. Dimensional regularization of the gravitational interaction of point masses. *Phys. Lett. B*, 513:147–155, 2001. doi: 10.1016/S0370-2693(01)00642-6.

[141] K. G. Arun, Alessandra Buonanno, Guillaume Faye, and Evan Ochsner. Higher-order spin effects in the amplitude and phase of gravitational waveforms emitted by inspiraling compact binaries: Ready-to-use gravitational waveforms. *Phys. Rev. D*, 79:104023, 2009. doi: 10.1103/PhysRevD.79.104023. [Erratum: Phys.Rev.D 84, 049901 (2011)].

[142] Saul A. Teukolsky. Perturbations of a rotating black hole. 1. Fundamental equations for gravitational electromagnetic and neutrino field perturbations. *Astrophys. J.*, 185:635–647, 1973. doi: 10.1086/152444.

[143] William H. Press and Saul A. Teukolsky. Perturbations of a Rotating Black Hole. II. Dynamical Stability of the Kerr Metric. *Astrophys. J.*, 185:649–674, 1973. doi: 10.1086/152445.

[144] S. Chandrasekhar and Steven L. Detweiler. The quasi-normal modes of the Schwarzschild black hole. *Proc. Roy. Soc. Lond. A*, 344:441–452, 1975. doi: 10.1098/rspa.1975.0112.

[145] E. W. Leaver. An Analytic representation for the quasi normal modes of Kerr black holes. *Proc. Roy. Soc. Lond. A*, 402:285–298, 1985. doi: 10.1098/rspa.1985.0119.

[146] Kostas D. Kokkotas and Bernd G. Schmidt. Quasinormal modes of stars and black holes. *Living Rev. Rel.*, 2:2, 1999. doi: 10.12942/lrr-1999-2.

[147] Emanuele Berti, Vitor Cardoso, and Andrei O. Starinets. Quasinormal modes of black holes and black branes. *Class. Quant. Grav.*, 26:163001, 2009. doi: 10.1088/0264-9381/26/16/163001.

[148] Emanuele Berti et al. Black hole spectroscopy: from theory to experiment. 5 2025.

[149] Hans-Peter Nollert. TOPICAL REVIEW: Quasinormal modes: the characteristic 'sound' of black holes and neutron stars. *Class. Quant. Grav.*, 16: R159–R216, 1999. doi: 10.1088/0264-9381/16/12/201.

[150] Valeria Ferrari and Leonardo Gualtieri. Quasi-Normal Modes and Gravitational Wave Astronomy. *Gen. Rel. Grav.*, 40:945–970, 2008. doi: 10.1007/s10714-007-0585-1.

[151] R. A. Konoplya and A. Zhidenko. Quasinormal modes of black holes: From astrophysics to string theory. *Rev. Mod. Phys.*, 83:793–836, 2011. doi: 10.1103/RevModPhys.83.793.

[152] Vitor Cardoso et al. NR/HEP: roadmap for the future. *Class. Quant. Grav.*, 29:244001, 2012. doi: 10.1088/0264-9381/29/24/244001.

[153] Paolo Pani. Advanced Methods in Black-Hole Perturbation Theory. *Int. J. Mod. Phys. A*, 28:1340018, 2013. doi: 10.1142/S0217751X13400186.

[154] Tullio Regge and John A. Wheeler. Stability of a Schwarzschild singularity. *Phys. Rev.*, 108:1063–1069, 1957. doi: 10.1103/PhysRev.108.1063.

[155] Frank J. Zerilli. Effective potential for even parity Regge-Wheeler gravitational perturbation equations. *Phys. Rev. Lett.*, 24:737–738, 1970. doi: 10.1103/PhysRevLett.24.737.

[156] Ezra Newman and Roger Penrose. An Approach to gravitational radiation by a method of spin coefficients. *J. Math. Phys.*, 3:566–578, 1962. doi: 10.1063/1.1724257.

[157] S. A. Teukolsky. Rotating black holes - separable wave equations for gravitational and electromagnetic perturbations. *Phys. Rev. Lett.*, 29:1114–1118, 1972. doi: 10.1103/PhysRevLett.29.1114.

[158] S Chandrasekhar. *The mathematical theory of black holes*. Oxford classic texts in the physical sciences. Oxford Univ. Press, Oxford, 2002. URL `https://cds.cern.ch/record/579245`.

[159] Subrahmanyan Chandrasekhar. On algebraically special perturbations of black holes. *Proc. Roy. Soc. Lond. A*, 392(1802):1–13, 1984. doi: 10.1098/rspa.1984.0021.

[160] Fred Cooper, Avinash Khare, and Uday Sukhatme. Supersymmetry and quantum mechanics. *Phys. Rept.*, 251:267–385, 1995. doi: 10.1016/0370-1573(94)00080-M.

[161] Vitor Cardoso and Jose P. S. Lemos. Quasinormal modes of Schwarzschild anti-de Sitter black holes: Electromagnetic and gravitational perturbations. *Phys. Rev. D*, 64:084017, 2001. doi: 10.1103/PhysRevD.64.084017.

[162] Edward W. Leaver. Spectral decomposition of the perturbation response of the Schwarzschild geometry. *Phys. Rev. D*, 34:384–408, 1986. doi: 10.1103/PhysRevD.34.384.

[163] Hans-Peter Nollert. Quasinormal modes of Schwarzschild black holes: The determination of quasinormal frequencies with very large imaginary parts. *Phys. Rev. D*, 47:5253–5258, 1993. doi: 10.1103/PhysRevD.47.5253.

[164] N. Andersson. Excitation of Schwarzschild black hole quasinormal modes. *Phys. Rev. D*, 51:353–363, 1995. doi: 10.1103/PhysRevD.51.353.

[165] Nils Andersson. Evolving test fields in a black hole geometry. *Phys. Rev. D*, 55:468–479, 1997. doi: 10.1103/PhysRevD.55.468.

[166] Michele Maggiore. *Gravitational Waves. Vol. 2: Astrophysics and Cosmology*. Oxford University Press, 3 2018. ISBN 978-0-19-857089-9.

[167] E. S. C. Ching, P. T. Leung, W. M. Suen, and K. Young. Wave propagation in gravitational systems: Late time behavior. *Phys. Rev. D*, 52:2118–2132, 1995. doi: 10.1103/PhysRevD.52.2118.

[168] Emanuele Berti and Vitor Cardoso. Quasinormal ringing of Kerr black holes. I. The Excitation factors. *Phys. Rev. D*, 74:104020, 2006. doi: 10.1103/PhysRevD.74.104020.

[169] Richard H. Price. Nonspherical perturbations of relativistic gravitational collapse. 1. Scalar and gravitational perturbations. *Phys. Rev. D*, 5:2419–2438, 1972. doi: 10.1103/PhysRevD.5.2419.

[170] Matthew Giesler, Maximiliano Isi, Mark A. Scheel, and Saul Teukolsky. Black Hole Ringdown: The Importance of Overtones. *Phys. Rev. X*, 9(4):041060, 2019. doi: 10.1103/PhysRevX.9.041060.

[171] Vishal Baibhav, Mark Ho-Yeuk Cheung, Emanuele Berti, Vitor Cardoso, Gregorio Carullo, Roberto Cotesta, Walter Del Pozzo, and Francisco Duque. Agnostic black hole spectroscopy: Quasinormal mode content of numerical relativity waveforms and limits of validity of linear perturbation theory. *Phys. Rev. D*, 108(10):104020, 2023. doi: 10.1103/PhysRevD.108.104020.

[172] Reinaldo J. Gleiser, Carlos O. Nicasio, Richard H. Price, and Jorge Pullin. Second order perturbations of a Schwarzschild black hole. *Class. Quant. Grav.*, 13:L117–L124, 1996. doi: 10.1088/0264-9381/13/10/001.

[173] David Brizuela, Jose M. Martin-Garcia, and Manuel Tiglio. A Complete gauge-invariant formalism for arbitrary second-order perturbations of a Schwarzschild black hole. *Phys. Rev. D*, 80:024021, 2009. doi: 10.1103/PhysRevD.80.024021.

[174] Kunihito Ioka and Hiroyuki Nakano. Second and higher-order quasi-normal modes in binary black hole mergers. *Phys. Rev. D*, 76:061503, 2007. doi: 10.1103/PhysRevD.76.061503.

[175] Hiroyuki Nakano and Kunihito Ioka. Second Order Quasi-Normal Mode of the Schwarzschild Black Hole. *Phys. Rev. D*, 76:084007, 2007. doi: 10.1103/PhysRevD.76.084007.

[176] Nicholas Loutrel, Justin L. Ripley, Elena Giorgi, and Frans Pretorius. Second Order Perturbations of Kerr Black Holes: Reconstruction of the Metric. *Phys. Rev. D*, 103(10):104017, 2021. doi: 10.1103/PhysRevD.103.104017.

[177] Justin L. Ripley, Nicholas Loutrel, Elena Giorgi, and Frans Pretorius. Numerical computation of second order vacuum perturbations of Kerr black holes. *Phys. Rev. D*, 103:104018, 2021. doi: 10.1103/PhysRevD.103.104018.

[178] Mark Ho-Yeuk Cheung, Emanuele Berti, Vishal Baibhav, and Roberto Cotesta. Extracting linear and nonlinear quasinormal modes from black hole merger simulations. *Phys. Rev. D*, 109(4):044069, 2024. doi: 10.1103/PhysRevD.109.044069. [Erratum: Phys.Rev.D 110, 049902 (2024)].

[179] Mark Ho-Yeuk Cheung et al. Nonlinear Effects in Black Hole Ringdown. *Phys. Rev. Lett.*, 130(8):081401, 2023. doi: 10.1103/PhysRevLett.130.081401.

[180] Keefe Mitman et al. Nonlinearities in Black Hole Ringdowns. *Phys. Rev. Lett.*, 130(8):081402, 2023. doi: 10.1103/PhysRevLett.130.081402.

[181] Sizheng Ma, Keefe Mitman, Ling Sun, Nils Deppe, François Hébert, Lawrence E. Kidder, Jordan Moxon, William Throwe, Nils L. Vu, and Yanbei Chen. Quasinormal-mode filters: A new approach to analyze the gravitational-wave ringdown of binary black-hole mergers. *Phys. Rev. D*, 106(8):084036, 2022. doi: 10.1103/PhysRevD.106.084036.

[182] Emanuele Berti and Kostas D. Kokkotas. Quasinormal modes of Kerr-Newman black holes: Coupling of electromagnetic and gravitational perturbations. *Phys. Rev. D*, 71:124008, 2005. doi: 10.1103/PhysRevD.71.124008.

[183] Valeria. Ferrari, Leonardo Gualtieri, and Stefania Marassi. A New approach to the study of quasi-normal modes of rotating stars. *Phys. Rev. D*, 76:104033, 2007. doi: 10.1103/PhysRevD.76.104033.

[184] Joao G. Rosa and Sam R. Dolan. Massive vector fields on the Schwarzschild spacetime: quasi-normal modes and bound states. *Phys. Rev. D*, 85:044043, 2012. doi: 10.1103/PhysRevD.85.044043.

[185] Paolo Pani, Vitor Cardoso, Leonardo Gualtieri, Emanuele Berti, and Akihiro Ishibashi. Perturbations of slowly rotating black holes: massive vector fields in the Kerr metric. *Phys. Rev. D*, 86:104017, 2012. doi: 10.1103/PhysRevD.86.104017.

[186] Sam R. Dolan. Instability of the massive Klein-Gordon field on the Kerr spacetime. *Phys. Rev. D*, 76:084001, 2007. doi: 10.1103/PhysRevD.76.084001.

[187] C. Simmendinger, A. Wunderlin, and A. Pelster. Analytical approach for the floquet theory of delay differential equations. *Phys. Rev. E*, 59:5344–5353, May 1999. doi: 10.1103/PhysRevE.59.5344.

[188] A. G. Abac et al. GW250114: Testing Hawking's Area Law and the Kerr Nature of Black Holes. *Phys. Rev. Lett.*, 135(11):111403, 2025. doi: 10.1103/kw5g-d732.

[189] Black Hole Spectroscopy and Tests of General Relativity with GW250114. 9 2025.

[190] Piero Nicolini, Anais Smailagic, and Euro Spallucci. Noncommutative geometry inspired Schwarzschild black hole. *Phys. Lett. B*, 632:547–551, 2006. doi: 10.1016/j.physletb.2005.11.004.

[191] Steven B. Giddings. Possible observational windows for quantum effects from black holes. *Phys. Rev. D*, 90(12):124033, 2014. doi: 10.1103/PhysRevD.90.124033.

[192] Alexey S. Koshelev and Anupam Mazumdar. Do massive compact objects without event horizon exist in infinite derivative gravity? *Phys. Rev. D*, 96(8):084069, 2017. doi: 10.1103/PhysRevD.96.084069.

[193] Jahed Abedi, Niayesh Afshordi, Naritaka Oshita, and Qingwen Wang. Quantum Black Holes in the Sky. *Universe*, 6(3):43, 2020. doi: 10.3390/universe6030043.

[194] Steven L. Liebling and Carlos Palenzuela. Dynamical boson stars. *Living Rev. Rel.*, 26(1):1, 2023. doi: 10.1007/s41114-023-00043-4.

[195] Richard Brito, Vitor Cardoso, Carlos A. R. Herdeiro, and Eugen Radu. Proca stars: Gravitating Bose–Einstein condensates of massive spin 1 particles. *Phys. Lett. B*, 752:291–295, 2016. doi: 10.1016/j.physletb.2015.11.051.

[196] Gian F. Giudice, Matthew McCullough, and Alfredo Urbano. Hunting for Dark Particles with Gravitational Waves. *JCAP*, 10:001, 2016. doi: 10.1088/1475-7516/2016/10/001.

[197] Pawel O. Mazur and Emil Mottola. Gravitational Condensate Stars: An Alternative to Black Holes. *Universe*, 9(2):88, 2023. doi: 10.3390/universe9020088.

[198] Pawel O. Mazur and Emil Mottola. Gravitational vacuum condensate stars. *Proc. Nat. Acad. Sci.*, 101:9545–9550, 2004. doi: 10.1073/pnas.0402717101.

[199] David A. Feinblum and William A. McKinley. Stable States of a Scalar Particle in Its Own Gravational Field. *Phys. Rev.*, 168(5):1445, 1968. doi: 10.1103/PhysRev.168.1445.

[200] David J. Kaup. Klein-Gordon Geon. *Phys. Rev.*, 172:1331–1342, 1968. doi: 10.1103/PhysRev.172.1331.

[201] Remo Ruffini and Silvano Bonazzola. Systems of selfgravitating particles in general relativity and the concept of an equation of state. *Phys. Rev.*, 187:1767–1783, 1969. doi: 10.1103/PhysRev.187.1767.

[202] E. Seidel and W. M. Suen. Oscillating soliton stars. *Phys. Rev. Lett.*, 66:1659–1662, 1991. doi: 10.1103/PhysRevLett.66.1659.

[203] Albert Einstein and N. Rosen. The Particle Problem in the General Theory of Relativity. *Phys. Rev.*, 48:73–77, 1935. doi: 10.1103/PhysRev.48.73.

[204] M. S. Morris and K. S. Thorne. Wormholes in space-time and their use for interstellar travel: A tool for teaching general relativity. *Am. J. Phys.*, 56:395–412, 1988. doi: 10.1119/1.15620.

[205] Thibault Damour and Sergey N. Solodukhin. Wormholes as black hole foils. *Phys. Rev. D*, 76:024016, 2007. doi: 10.1103/PhysRevD.76.024016.

[206] Richard L. Bowers and E. P. T. Liang. Anisotropic Spheres in General Relativity. *Astrophys. J.*, 188:657–665, 1974. doi: 10.1086/152760.

[207] Eric G. Gimon and Petr Horava. Astrophysical violations of the Kerr bound as a possible signature of string theory. *Phys. Lett. B*, 672:299–302, 2009. doi: 10.1016/j.physletb.2009.01.026.

[208] Ram Brustein and A. J. M. Medved. Black holes as collapsed polymers. *Fortsch. Phys.*, 65(1):1600114, 2017. doi: 10.1002/prop.201600114.

[209] Bob Holdom and Jing Ren. Not quite a black hole. *Phys. Rev. D*, 95(8):084034, 2017. doi: 10.1103/PhysRevD.95.084034.

[210] Matt Visser and David L. Wiltshire. Stable gravastars: An Alternative to black holes? *Class. Quant. Grav.*, 21:1135–1152, 2004. doi: 10.1088/0264-9381/21/4/027.

[211] Pawel O. Mazur and Emil Mottola. Surface tension and negative pressure interior of a non-singular 'black hole'. *Class. Quant. Grav.*, 32(21):215024, 2015. doi: 10.1088/0264-9381/32/21/215024.

[212] Celine Cattoen, Tristan Faber, and Matt Visser. Gravastars must have anisotropic pressures. *Class. Quant. Grav.*, 22:4189–4202, 2005. doi: 10.1088/0264-9381/22/20/002.

[213] Hans A. Buchdahl. General Relativistic Fluid Spheres. *Phys. Rev.*, 116:1027, 1959. doi: 10.1103/PhysRev.116.1027.

[214] Philippe Jetzer. Boson stars. *Phys. Rept.*, 220:163–227, 1992. doi: 10.1016/0370-1573(92)90123-H.

[215] Franz E. Schunck and Eckehard W. Mielke. General relativistic boson stars. *Class. Quant. Grav.*, 20:R301–R356, 2003. doi: 10.1088/0264-9381/20/20/201.

[216] Edward Seidel and Wai-Mo Suen. Formation of solitonic stars through gravitational cooling. *Phys. Rev. Lett.*, 72:2516–2519, 1994. doi: 10.1103/PhysRevLett.72.2516.

[217] Hirotada Okawa, Vitor Cardoso, and Paolo Pani. Collapse of self-interacting fields in asymptotically flat spacetimes: do self-interactions render Minkowski spacetime unstable? *Phys. Rev. D*, 89(4):041502, 2014. doi: 10.1103/PhysRevD.89.041502.

[218] C. Palenzuela, L. Lehner, and Steven L. Liebling. Orbital Dynamics of Binary Boson Star Systems. *Phys. Rev. D*, 77:044036, 2008. doi: 10.1103/PhysRevD.77.044036.

[219] Carlos Palenzuela, Paolo Pani, Miguel Bezares, Vitor Cardoso, Luis Lehner, and Steven Liebling. Gravitational Wave Signatures of Highly Compact Boson Star Binaries. *Phys. Rev. D*, 96(10):104058, 2017. doi: 10.1103/PhysRevD.96.104058.

[220] Nicolas Sanchis-Gual, Carlos Herdeiro, José A. Font, Eugen Radu, and Fabrizio Di Giovanni. Head-on collisions and orbital mergers of Proca stars. *Phys. Rev. D*, 99(2):024017, 2019. doi: 10.1103/PhysRevD.99.024017.

[221] Matt. Visser. *Lorentzian wormholes : from Einstein to Hawking / Matt Visser.* AIP series in computational and applied mathematical physics. American Institute of Physics, Woodbury, N.Y, 1995. ISBN 1563963949.

[222] Panagiota Kanti, Burkhard Kleihaus, and Jutta Kunz. Wormholes in Dilatonic Einstein-Gauss-Bonnet Theory. *Phys. Rev. Lett.*, 107:271101, 2011. doi: 10.1103/PhysRevLett.107.271101.

[223] Jose' P. S. Lemos, Francisco S. N. Lobo, and Sergio Quinet de Oliveira. Morris-Thorne wormholes with a cosmological constant. *Phys. Rev. D*, 68:064004, 2003. doi: 10.1103/PhysRevD.68.064004.

[224] Juan Maldacena, Alexey Milekhin, and Fedor Popov. Traversable wormholes in four dimensions. *Class. Quant. Grav.*, 40(15):155016, 2023. doi: 10.1088/1361-6382/acde30.

[225] J. A. Gonzalez, F. S. Guzman, and O. Sarbach. Instability of wormholes supported by a ghost scalar field. I. Linear stability analysis. *Class. Quant. Grav.*, 26:015010, 2009. doi: 10.1088/0264-9381/26/1/015010.

[226] J. A. Gonzalez, F. S. Guzman, and O. Sarbach. Instability of wormholes supported by a ghost scalar field. II. Nonlinear evolution. *Class. Quant. Grav.*, 26:015011, 2009. doi: 10.1088/0264-9381/26/1/015011.

[227] K. A. Bronnikov, R. A. Konoplya, and A. Zhidenko. Instabilities of wormholes and regular black holes supported by a phantom scalar field. *Phys. Rev. D*, 86:024028, 2012. doi: 10.1103/PhysRevD.86.024028.

[228] M. A. Cuyubamba, R. A. Konoplya, and A. Zhidenko. No stable wormholes in Einstein-dilaton-Gauss-Bonnet theory. *Phys. Rev. D*, 98(4):044040, 2018. doi: 10.1103/PhysRevD.98.044040.

[229] A. Vilenkin. Exponential Amplification of Waves in the Gravitational Field of Ultrarelativistic Rotating Body. *Phys. Lett. B*, 78:301–303, 1978. doi: 10.1016/0370-2693(78)90027-8.

[230] Elisa Maggio, Paolo Pani, and Valeria Ferrari. Exotic Compact Objects and How to Quench their Ergoregion Instability. *Phys. Rev. D*, 96(10):104047, 2017. doi: 10.1103/PhysRevD.96.104047.

[231] Elisa Maggio, Vitor Cardoso, Sam R. Dolan, and Paolo Pani. Ergoregion instability of exotic compact objects: electromagnetic and gravitational perturbations and the role of absorption. *Phys. Rev. D*, 99(6):064007, 2019. doi: 10.1103/PhysRevD.99.064007.

[232] Alexei A. Starobinskil and S. M. Churilov. Amplification of electromagnetic and gravitational waves scattered by a rotating "black hole". *Sov. Phys. JETP*, 65(1):1–5, 1974.

[233] Sebastian H. Völkel and Kostas D. Kokkotas. A Semi-analytic Study of Axial Perturbations of Ultra Compact Stars. *Class. Quant. Grav.*, 34(12):125006, 2017. doi: 10.1088/1361-6382/aa68cc.

[234] Vitor Cardoso, Seth Hopper, Caio F. B. Macedo, Carlos Palenzuela, and Paolo Pani. Gravitational-wave signatures of exotic compact objects and of quantum corrections at the horizon scale. *Phys. Rev. D*, 94(8):084031, 2016. doi: 10.1103/PhysRevD.94.084031.

[235] Zachary Mark, Aaron Zimmerman, Song Ming Du, and Yanbei Chen. A recipe for echoes from exotic compact objects. *Phys. Rev. D*, 96(8):084002, 2017. doi: 10.1103/PhysRevD.96.084002.

[236] Valeria Ferrari and Bahram Mashhoon. New approach to the quasinormal modes of a black hole. *Phys. Rev. D*, 30:295–304, 1984. doi: 10.1103/PhysRevD.30.295.

[237] M. Davis, R. Ruffini, W. H. Press, and R. H. Price. Gravitational radiation from a particle falling radially into a schwarzschild black hole. *Phys. Rev. Lett.*, 27:1466–1469, 1971. doi: 10.1103/PhysRevLett.27.1466.

[238] M. Davis, R. Ruffini, and J. Tiomno. Pulses of gravitational radiation of a particle falling radially into a schwarzschild black hole. *Phys. Rev. D*, 5: 2932–2935, 1972. doi: 10.1103/PhysRevD.5.2932.

[239] Pau Amaro-Seoane. Relativistic dynamics and extreme mass ratio inspirals. *Living Rev. Rel.*, 21(1):4, 2018. doi: 10.1007/s41114-018-0013-8.

[240] Pau Amaro-Seoane, Carlos F. Sopuerta, and Marc Dewi Freitag. The role of the supermassive black hole spin in the estimation of the EMRI event rate. *Mon. Not. Roy. Astron. Soc.*, 429(4):3155–3165, 2013. doi: 10.1093/mnras/sts572.

[241] M. Coleman Miller, Marc Freitag, Douglas P. Hamilton, and Vanessa M. Lauburg. Binary encounters with supermassive black holes: Zero-eccentricity LISA events. *Astrophys. J. Lett.*, 631:L117–L120, 2005. doi: 10.1086/497335.

[242] Pau Amaro Seoane et al. The Gravitational Universe. 5 2013.

[243] Christopher P. L. Berry, Scott A. Hughes, Carlos F. Sopuerta, Alvin J. K. Chua, Anna Heffernan, Kelly Holley-Bockelmann, Deyan P. Mihaylov, M. Coleman Miller, and Alberto Sesana. The unique potential of extreme mass-ratio inspirals for gravitational-wave astronomy. *Bull. Am. Astron. Soc.*, 51:42, 2019.

[244] Stanislav Babak, Jonathan Gair, Alberto Sesana, Enrico Barausse, Carlos F. Sopuerta, Christopher P. L. Berry, Emanuele Berti, Pau Amaro-Seoane, Antoine Petiteau, and Antoine Klein. Science with the space-based interferometer LISA. V: Extreme mass-ratio inspirals. *Phys. Rev. D*, 95(10):103012, 2017. doi: 10.1103/PhysRevD.95.103012.

[245] Jun Luo et al. TianQin: a space-borne gravitational wave detector. *Class. Quant. Grav.*, 33(3):035010, 2016. doi: 10.1088/0264-9381/33/3/035010.

[246] Wen-Rui Hu and Yue-Liang Wu. The taiji program in space for gravitational wave physics and the nature of gravity. *National Science Review*, 4(5):685–686, 10 2017. ISSN 2095-5138. doi: 10.1093/nsr/nwx116. URL `https://doi.org/10.1093/nsr/nwx116`.

[247] Leor Barack and Adam Pound. Self-force and radiation reaction in general relativity. *Rept. Prog. Phys.*, 82(1):016904, 2019. doi: 10.1088/1361-6633/aae552.

[248] Yasushi Mino, Misao Sasaki, and Takahiro Tanaka. Gravitational radiation reaction to a particle motion. *Phys. Rev. D*, 55:3457–3476, 1997. doi: 10.1103/PhysRevD.55.3457.

[249] Leor Barack. Gravitational self force in extreme mass-ratio inspirals. *Class. Quant. Grav.*, 26:213001, 2009. doi: 10.1088/0264-9381/26/21/213001.

[250] Eric Poisson, Adam Pound, and Ian Vega. The Motion of point particles in curved spacetime. *Living Rev. Rel.*, 14:7, 2011. doi: 10.12942/lrr-2011-7.

[251] Adam Pound. Motion of small objects in curved spacetimes: An introduction to gravitational self-force. *Fund. Theor. Phys.*, 179:399–486, 2015. doi: 10.1007/978-3-319-18335-0_13.

[252] M van de Meent. Modelling emris with gravitational self-force: a status report. *Journal of Physics: Conference Series*, 840(1):012022, may 2017. doi: 10.1088/1742-6596/840/1/012022. URL `https://dx.doi.org/10.1088/1742-6596/840/1/012022`.

[253] James B. Hartle. Tidal Friction in Slowly Rotating Black Holes. *Phys. Rev. D*, 8:1010–1024, 1973. doi: 10.1103/PhysRevD.8.1010.

[254] Scott A. Hughes. The Evolution of circular, nonequatorial orbits of Kerr black holes due to gravitational wave emission. *Phys. Rev. D*, 61(8):084004, 2000. doi: 10.1103/PhysRevD.65.069902. [Erratum: Phys.Rev.D 63, 049902 (2001), Erratum: Phys.Rev.D 65, 069902 (2002), Erratum: Phys.Rev.D 67, 089901 (2003), Erratum: Phys.Rev.D 78, 109902 (2008), Erratum: Phys.Rev.D 90, 109904 (2014)].

[255] Scott A. Hughes. Evolution of circular, nonequatorial orbits of Kerr black holes due to gravitational wave emission. II. Inspiral trajectories and gravitational wave forms. *Phys. Rev. D*, 64:064004, 2001. doi: 10.1103/PhysRevD.64.064004. [Erratum: Phys.Rev.D 88, 109902 (2013)].

[256] Sayak Datta. Tidal heating of Quantum Black Holes and their imprints on gravitational waves. *Phys. Rev. D*, 102(6):064040, 2020. doi: 10.1103/PhysRevD.102.064040.

[257] Sayak Datta, Richard Brito, Scott A. Hughes, Talya Klinger, and Paolo Pani. Tidal heating as a discriminator for horizons in equatorial eccentric extreme mass ratio inspirals. *Phys. Rev. D*, 110(2):024048, 2024. doi: 10.1103/PhysRevD.110.024048.

[258] Thibault Damour and Gilles Esposito-Farese. Nonperturbative strong field effects in tensor - scalar theories of gravitation. *Phys. Rev. Lett.*, 70:2220–2223, 1993. doi: 10.1103/PhysRevLett.70.2220.

[259] Daniela D. Doneva and Stoytcho S. Yazadjiev. New Gauss-Bonnet Black Holes with Curvature-Induced Scalarization in Extended Scalar-Tensor Theories. *Phys. Rev. Lett.*, 120(13):131103, 2018. doi: 10.1103/PhysRevLett.120.131103.

[260] Hector O. Silva, Jeremy Sakstein, Leonardo Gualtieri, Thomas P. Sotiriou, and Emanuele Berti. Spontaneous scalarization of black holes and compact stars from a Gauss-Bonnet coupling. *Phys. Rev. Lett.*, 120(13):131104, 2018. doi: 10.1103/PhysRevLett.120.131104.

[261] Justin L. Ripley and Frans Pretorius. Dynamics of a $\mathbb{Z}_2$ symmetric EdGB gravity in spherical symmetry. *Class. Quant. Grav.*, 37(15):155003, 2020. doi: 10.1088/1361-6382/ab9bbb.

[262] Hao-Jui Kuan, Daniela D. Doneva, and Stoytcho S. Yazadjiev. Dynamical Formation of Scalarized Black Holes and Neutron Stars through Stellar Core Collapse. *Phys. Rev. Lett.*, 127(16):161103, 2021. doi: 10.1103/PhysRevLett.127.161103.

[263] Alexandru Dima, Enrico Barausse, Nicola Franchini, and Thomas P. Sotiriou. Spin-induced black hole spontaneous scalarization. *Phys. Rev. Lett.*, 125(23):231101, 2020. doi: 10.1103/PhysRevLett.125.231101.

[264] Shahar Hod. Onset of spontaneous scalarization in spinning Gauss-Bonnet black holes. *Phys. Rev. D*, 102(8):084060, 2020. doi: 10.1103/PhysRevD.102.084060.

[265] Carlos A. R. Herdeiro, Eugen Radu, Hector O. Silva, Thomas P. Sotiriou, and Nicolás Yunes. Spin-induced scalarized black holes. *Phys. Rev. Lett.*, 126(1):011103, 2021. doi: 10.1103/PhysRevLett.126.011103.

[266] Emanuele Berti, Lucas G. Collodel, Burkhard Kleihaus, and Jutta Kunz. Spin-induced black-hole scalarization in Einstein-scalar-Gauss-Bonnet theory. *Phys. Rev. Lett.*, 126(1):011104, 2021. doi: 10.1103/PhysRevLett.126.011104.

[267] Daniela D. Doneva, Stoytcho S. Yazadjiev, Nikolaos Stergioulas, and Kostas D. Kokkotas. Rapidly rotating neutron stars in scalar-tensor theories of gravity. *Phys. Rev. D*, 88(8):084060, 2013. doi: 10.1103/PhysRevD.88.084060.

[268] Nikolas Andreou, Nicola Franchini, Giulia Ventagli, and Thomas P. Sotiriou. Spontaneous scalarization in generalised scalar-tensor theory. *Phys. Rev. D*, 99(12):124022, 2019. doi: 10.1103/PhysRevD.99.124022. [Erratum: Phys.Rev.D 101, 109903 (2020)].

[269] Ivan Zh. Stefanov, Stoytcho S. Yazadjiev, and Michail D. Todorov. Scalar-tensor black holes coupled to Born-Infeld nonlinear electrodynamics. *Phys. Rev. D*, 75:084036, 2007. doi: 10.1103/PhysRevD.75.084036.

[270] Ivan Zh. Stefanov, Stoytcho S. Yazadjiev, and Michail D. Todorov. Scalar-tensor black holes coupled to Euler-Heisenberg nonlinear electrodynamics. *Mod. Phys. Lett. A*, 22:1217–1231, 2007. doi: 10.1142/S0217732307023560.

[271] Ivan Zh. Stefanov, Stoytcho S. Yazadjiev, and Michail D. Todorov. Phases of 4D scalar-tensor black holes coupled to Born-Infeld nonlinear electrodynamics. *Mod. Phys. Lett. A*, 23:2915–2931, 2008. doi: 10.1142/S0217732308028351.

[272] Avraham E. Mayo and Jacob D. Bekenstein. No hair for spherical black holes: Charged and nonminimally coupled scalar field with selfinteraction. *Phys. Rev. D*, 54:5059–5069, 1996. doi: 10.1103/PhysRevD.54.5059.

[273] S. Sen and N. Banerjee. On the absence of scalar hair for charged rotating black holes in non-minimally coupled theories. *Pramana*, 56:487–501, 2001. doi: 10.1007/s12043-001-0098-5.

[274] Daniela D. Doneva, Stella Kiorpelidi, Petya G. Nedkova, Eleftherios Papantonopoulos, and Stoytcho S. Yazadjiev. Charged Gauss-Bonnet black holes with curvature induced scalarization in the extended scalar-tensor theories. *Phys. Rev. D*, 98(10):104056, 2018. doi: 10.1103/PhysRevD.98.104056.

[275] Yves Brihaye and Betti Hartmann. Spontaneous scalarization of charged black holes at the approach to extremality. *Phys. Lett. B*, 792:244–250, 2019. doi: 10.1016/j.physletb.2019.03.043.

[276] D. Astefanesei, C. Herdeiro, A. Pombo, and E. Radu. Einstein-Maxwell-scalar black holes: classes of solutions, dyons and extremality. *JHEP*, 10:078, 2019. doi: 10.1007/JHEP10(2019)078.

[277] Carlos A. R. Herdeiro, Taishi Ikeda, Masato Minamitsuji, Tomohiro Nakamura, and Eugen Radu. Spontaneous scalarization of a conducting sphere in Maxwell-scalar models. *Phys. Rev. D*, 103(4):044019, 2021. doi: 10.1103/PhysRevD.103.044019.

[278] Jose Luis Blázquez-Salcedo, Carlos A. R. Herdeiro, Jutta Kunz, Alexandre M. Pombo, and Eugen Radu. Einstein-Maxwell-scalar black holes: the hot, the cold and the bald. *Phys. Lett. B*, 806:135493, 2020. doi: 10.1016/j.physletb.2020.135493.

[279] Wen-Kun Luo, Cheng-Yong Zhang, Peng Liu, Chao Niu, and Bin Wang. Dynamical spontaneous scalarization in Einstein-Maxwell-scalar models in anti–de Sitter spacetime. *Phys. Rev. D*, 106(6):064036, 2022. doi: 10.1103/PhysRevD.106.064036.

[280] Vitor Cardoso, Isabella P. Carucci, Paolo Pani, and Thomas P. Sotiriou. Black holes with surrounding matter in scalar-tensor theories. *Phys. Rev. Lett.*, 111:111101, 2013. doi: 10.1103/PhysRevLett.111.111101.

[281] Vitor Cardoso, Isabella P. Carucci, Paolo Pani, and Thomas P. Sotiriou. Matter around Kerr black holes in scalar-tensor theories: scalarization and superradiant instability. *Phys. Rev. D*, 88:044056, 2013. doi: 10.1103/PhysRevD.88.044056.

[282] Eric W. Hirschmann, Luis Lehner, Steven L. Liebling, and Carlos Palenzuela. Black Hole Dynamics in Einstein-Maxwell-Dilaton Theory. *Phys. Rev. D*, 97 (6):064032, 2018. doi: 10.1103/PhysRevD.97.064032.

[283] Richard Brito and Costantino Pacilio. Quasinormal modes of weakly charged Einstein-Maxwell-dilaton black holes. *Phys. Rev. D*, 98(10):104042, 2018. doi: 10.1103/PhysRevD.98.104042.

[284] Charles W. Misner and David H. Sharp. Relativistic equations for adiabatic, spherically symmetric gravitational collapse. *Phys. Rev.*, 136:B571–B576, Oct 1964. doi: 10.1103/PhysRev.136.B571. URL `https://link.aps.org/doi/10.1103/PhysRev.136.B571`.

[285] Qingyu Gan, Peng Wang, Houwen Wu, and Haitang Yang. Photon ring and observational appearance of a hairy black hole. *Phys. Rev. D*, 104(4):044049, 2021. doi: 10.1103/PhysRevD.104.044049.

[286] Qingyu Gan, Peng Wang, Houwen Wu, and Haitang Yang. Photon spheres and spherical accretion image of a hairy black hole. *Phys. Rev. D*, 104(2): 024003, 2021. doi: 10.1103/PhysRevD.104.024003.

[287] Aron Jansen, Andrzej Rostworowski, and Mieszko Rutkowski. Master equations and stability of Einstein-Maxwell-scalar black holes. *JHEP*, 12:036, 2019. doi: 10.1007/JHEP12(2019)036.

[288] Massimo Bianchi, Giorgio Di Russo, Alfredo Grillo, Jose Francisco Morales, and Giuseppe Sudano. On the stability and deformability of top stars. *JHEP*, 12:121, 2023. doi: 10.1007/JHEP12(2023)121.

[289] Pierre Heidmann, Nicholas Speeney, Emanuele Berti, and Ibrahima Bah. Cavity effect in the quasinormal mode spectrum of topological stars. *Phys. Rev. D*, 108(2):024021, 2023. doi: 10.1103/PhysRevD.108.024021.

[290] Alexandru Dima, Marco Melis, and Paolo Pani. Spectroscopy of magnetized black holes and topological stars. *Phys. Rev. D*, 110(8):084067, 2024. doi: 10.1103/PhysRevD.110.084067.

[291] Iosif Bena, Giorgio Di Russo, Jose Francisco Morales, and Alejandro Ruipérez. Non-spinning tops are stable. *JHEP*, 10:071, 2024. doi: 10.1007/JHEP10(2024)071.

[292] Alexandru Dima, Marco Melis, and Paolo Pani. Nonradial stability of topological stars. *Phys. Rev. D*, 111(10):104001, 2025. doi: 10.1103/PhysRevD.111.104001.

[293] Ibrahima Bah and Pierre Heidmann. Topological stars, black holes and generalized charged Weyl solutions. *JHEP*, 09:147, 2021. doi: 10.1007/JHEP09(2021)147.

[294] Ibrahima Bah and Pierre Heidmann. Bubble bag end: a bubbly resolution of curvature singularity. *JHEP*, 10:165, 2021. doi: 10.1007/JHEP10(2021)165.

[295] Umpei Miyamoto and Hideaki Kudoh. New stable phase of non-uniform charged black strings. *JHEP*, 12:048, 2006. doi: 10.1088/1126-6708/2006/12/048.

[296] R. Gregory and R. Laflamme. Black strings and p-branes are unstable. *Phys. Rev. Lett.*, 70:2837–2840, 1993. doi: 10.1103/PhysRevLett.70.2837.

[297] Sean Stotyn and Robert B. Mann. Magnetic charge can locally stabilize Kaluza–Klein bubbles. *Phys. Lett. B*, 705:269–272, 2011. doi: 10.1016/j.physletb.2011.10.015.

[298] Ibrahima Bah, Anindya Dey, and Pierre Heidmann. Stability of topological solitons, and black string to bubble transition. *JHEP*, 04:168, 2022. doi: 10.1007/JHEP04(2022)168.

[299] Yen-Kheng Lim. Motion of charged particles around a magnetic black hole or topological star with a compact extra dimension. *Phys. Rev. D*, 103(8):084044, 2021. doi: 10.1103/PhysRevD.103.084044.

[300] Pierre Heidmann, Ibrahima Bah, and Emanuele Berti. Imaging topological solitons: The microstructure behind the shadow. *Phys. Rev. D*, 107(8):084042, 2023. doi: 10.1103/PhysRevD.107.084042.

[301] Massimo Bianchi, Donato Bini, and Giorgio Di Russo. Scalar perturbations of topological-star spacetimes. *Phys. Rev. D*, 110(8):084077, 2024. doi: 10.1103/PhysRevD.110.084077.

[302] Wen-Di Guo, Qin Tan, and Yu-Xiao Liu. Gravitoelectromagnetic coupled perturbations and quasinormal modes of a charged black hole with scalar hair. *Phys. Rev. D*, 107(12):124046, 2023. doi: 10.1103/PhysRevD.107.124046.

[303] Wen-Di Guo and Qin Tan. Quasinormal Modes of a Charged Black Hole with Scalar Hair. *Universe*, 9(7):320, 2023. doi: 10.3390/universe9070320.

[304] David Pereñiguez. Black hole perturbations and electric-magnetic duality. *Phys. Rev. D*, 108(8):084046, 2023. doi: 10.1103/PhysRevD.108.084046.

[305] Edgardo Franzin, Stefano Liberati, and Vania Vellucci. From regular black holes to horizonless objects: quasi-normal modes, instabilities and spectroscopy. *JCAP*, 01:020, 2024. doi: 10.1088/1475-7516/2024/01/020.

[306] Marco Melis, Richard Brito, and Paolo Pani. Extreme mass ratio inspirals around topological stars. *Phys. Rev. D*, 111(12):124043, 2025. doi: 10.1103/zng8-9qrn.

[307] Massimo Bianchi, Donato Bini, and Giorgio Di Russo. Scalar waves in a Topological Star spacetime: self-force and radiative losses. 11 2024.

[308] Giorgio Di Russo, Massimo Bianchi, and Donato Bini. Scalar waves from unbound orbits in a topological star spacetime: PN reconstruction of the field and radiation losses in a self-force approach. *Phys. Rev. D*, 112(2):024002, 2025. doi: 10.1103/sycf-brn1.

[309] Massimo Bianchi, Donato Bini, and Giorgio Di Russo. Scattering angle in a topological star spacetime: A self-force approach. *Phys. Rev. D*, 112(4):044008, 2025. doi: 10.1103/cz6k-wqpn.

[310] Andrea Maselli, Paolo Pani, Vitor Cardoso, Tiziano Abdelsalhin, Leonardo Gualtieri, and Valeria Ferrari. Probing Planckian corrections at the horizon scale with LISA binaries. *Phys. Rev. Lett.*, 120(8):081101, 2018. doi: 10.1103/PhysRevLett.120.081101.

[311] Eric Poisson. Gravitational radiation from a particle in circular orbit around a black hole. i. analytical results for the nonrotating case. *Phys. Rev. D*, 47: 1497–1510, Feb 1993. doi: 10.1103/PhysRevD.47.1497. URL `https://link.aps.org/doi/10.1103/PhysRevD.47.1497`.

[312] Eric Poisson and Misao Sasaki. Gravitational radiation from a particle in circular orbit around a black hole. 5: Black hole absorption and tail corrections. *Phys. Rev. D*, 51:5753–5767, 1995. doi: 10.1103/PhysRevD.51.5753.

[313] Panagiota Kanti and John March-Russell. Calculable corrections to brane black hole decay. 1. The scalar case. *Phys. Rev. D*, 66:024023, 2002. doi: 10.1103/PhysRevD.66.024023.

[314] Songbai Chen, Bin Wang, Ru-Keng Su, and W. Y Pauchy Hwang. Greybody factors for rotating black holes on codimension-2 branes. *JHEP*, 03:019, 2008. doi: 10.1088/1126-6708/2008/03/019.

[315] S. Creek, O. Efthimiou, P. Kanti, and K. Tamvakis. Scalar Emission in the Bulk in a Rotating Black Hole Background. *Phys. Lett. B*, 656:102–111, 2007. doi: 10.1016/j.physletb.2007.09.050.

[316] Richard Brito, Vitor Cardoso, and Paolo Pani. Tidal effects around higher-dimensional black holes. *Phys. Rev. D*, 86:024032, 2012. doi: 10.1103/PhysRevD.86.024032.

[317] I. A. Stegun M. Abramowitz. *Handbook of Mathematical Functions*. GPO, 1964.

[318] J. A. Pons, E. Berti, L. Gualtieri, G. Miniutti, and V. Ferrari. Gravitational signals emitted by a point mass orbiting a neutron star: Effects of stellar structure. *Phys. Rev. D*, 65:104021, 2002. doi: 10.1103/PhysRevD.65.104021.

[319] Lee Lindblom, Benjamin J. Owen, and Duncan A. Brown. Model Waveform Accuracy Standards for Gravitational Wave Data Analysis. *Phys. Rev. D*, 78: 124020, 2008. doi: 10.1103/PhysRevD.78.124020.

[320] David D. K. Chow and Geoffrey Compère. Black holes in N=8 supergravity from SO(4,4) hidden symmetries. *Phys. Rev. D*, 90(2):025029, 2014. doi: 10.1103/PhysRevD.90.025029.

[321] Alexandru Dima, Pierre Heidmann, Marco Melis, Paolo Pani, and Gela Patashuri. The Great Impersonation: $\mathcal{W}$-Solitons as Prototypical Black Hole Microstates. 9 2025.

[322] Edward Witten. Instability of the Kaluza-Klein Vacuum. *Nucl. Phys. B*, 195: 481–492, 1982. doi: 10.1016/0550-3213(82)90007-4.

[323] Neil J. Cornish and Janna J. Levin. Lyapunov timescales and black hole binaries. *Class. Quant. Grav.*, 20:1649–1660, 2003. doi: 10.1088/0264-9381/20/9/304.

[324] Vitor Cardoso, Alex S. Miranda, Emanuele Berti, Helvi Witek, and Vilson T. Zanchin. Geodesic stability, Lyapunov exponents and quasinormal modes. *Phys. Rev. D*, 79(6):064016, 2009. doi: 10.1103/PhysRevD.79.064016.

[325] J. N. Goldberg, A. J. MacFarlane, E. T. Newman, F. Rohrlich, and E. C. G. Sudarshan. Spin-s spherical harmonics and $\eth$. *J. Math. Phys.*, 8:2155, 1967. doi: 10.1063/1.1705135.

[326] R. A. Breuer, M. P. Ryan, Jr., and S. Waller. Some Properties of Spin-Weighted Spheroidal Harmonics. *Proceedings of the Royal Society of London Series A*, 358(1692):71–86, December 1977. doi: 10.1098/rspa.1977.0187.

[327] Emanuele Berti, Vitor Cardoso, and Marc Casals. Eigenvalues and eigenfunctions of spin-weighted spheroidal harmonics in four and higher dimensions. *Phys. Rev. D*, 73:024013, 2006. doi: 10.1103/PhysRevD.73.109902. [Erratum: Phys.Rev.D 73, 109902 (2006)].

[328] Sam Dolan and Jonathan Gair. The Massive Dirac field on a rotating black hole spacetime: Angular solutions. *Class. Quant. Grav.*, 26:175020, 2009. doi: 10.1088/0264-9381/26/17/175020.

[329] Richard Brito, Vitor Cardoso, and Paolo Pani. Superradiance: New Frontiers in Black Hole Physics. *Lect. Notes Phys.*, 906:pp.1–237, 2015. doi: 10.1007/978-3-319-19000-6.

[330] Bernard F. Schutz and Clifford M. Will. BLACK HOLE NORMAL MODES: A SEMIANALYTIC APPROACH. *Astrophys. J. Lett.*, 291:L33–L36, 1985. doi: 10.1086/184453.

[331] Sai Iyer and Clifford M. Will. Black Hole Normal Modes: A WKB Approach. 1. Foundations and Application of a Higher Order WKB Analysis of Potential Barrier Scattering. *Phys. Rev. D*, 35:3621, 1987. doi: 10.1103/PhysRevD.35.3621.

[332] Massimo Bianchi, Giuseppe Dibitetto, Jose F. Morales, and Alejandro Ruipérez. Rotating Topological Stars. 4 2025.

[333] Pierre Heidmann, Paolo Pani, and Jorge E. Santos. Asymptotically Flat Rotating Topological Stars. 10 2025.

[334] Yasufumi Kojima. Equations governing the nonradial oscillations of a slowly rotating relativistic star. *Phys. Rev. D*, 46:4289–4303, Nov 1992. doi: 10.1103/PhysRevD.46.4289. URL `https://link.aps.org/doi/10.1103/PhysRevD.46.4289`.